NORTHWESTERN UNIVERSITY

Measurement of the Structure Function Ratio F_2^n/F_2^p in Muon-Nucleon Scattering at Low x and Q^2

A DISSERTATION

SUBMITTED TO THE GRADUATE SCHOOL
IN PARTIAL FULFILLMENT OF THE REQUIREMENTS

for the degree

DOCTOR OF PHILOSOPHY

Field of Physics

By
Panagiotis Spentzouris
EVANSTON, ILLINOIS
December 1994

ABSTRACT

Measurement of the Structure Function Ratio F_2^n/F_2^p in Muon-Nucleon Scattering at Low x and Q^2

Panagiotis Spentzouris

The ratio of the neutron to proton structure functions, F_2^n/F_2^p, from scattering of 470 GeV muons on liquid hydrogen and deuterium targets, is measured at very small-x and Q^2, using the Fermilab E665 spectrometer. The results presented cover the region $0.000004 < x < 0.3$ and $Q^2 > 0.001 GeV^2$, three orders of magnitude lower in x than previous fixed-target experiments, and with higher average Q^2 in the overlap region. The structure function ratio F_2^n/F_2^p is extracted from the ratio of the deuteron to proton single-photon-exchange cross-sections, $\sigma_{1\gamma}^d/\sigma_{1\gamma}^p$, assuming that $R^d = R^p$, where R is the ratio of the longitudinal to transverse polarization cross-sections of the virtual photon, and that the deuteron can be treated as a free neutron plus a free proton. With the above assumptions, $\sigma_{1\gamma}^d/\sigma_{1\gamma}^p = F_2^d/F_2^p$, where F_2^d is the per nucleon deuteron structure function, and $F_2^n/F_2^p = 2F_2^d/F_2^p - 1$. The single-photon-exchange cross-section ratio is obtained from the measured total cross-section using three largely independent techniques. The F_2^n/F_2^p ratio is found to be constant for $x < 0.01$, at $0.935 \pm 0.008 \pm 0.034$ ($\pm$ statistic $\pm$ systematic errors). The ratio of the per nucleon structure function of the deuteron to that of the proton for $x \leq 0.01$, is then $F_2^d/F_2^p = 0.968 \pm 0.004 \pm 0.017$. This means that the per nucleon structure function of the deuteron is smaller than the structure function of a free nucleon by $3.2\% \pm 1.7\%$. This result is consistent with recent predictions for nuclear shadowing effects in the deuteron. The variation of the ratio with $\ln Q^2$ is also examined, no significant dependence is found.

ACKNOWLEDGEMENTS

This thesis is about the work that I did over the past four years as a graduate student of Northwestern University, and as member of the E665 collaboration. On the other hand, my work for the DELPHI and E705/771 experiments as a graduate student of Athens University also contributed a lot to my physics education. In the following few lines, I shall try to acknowledge all of those with whom I have interacted and learned from over these past eight years in which I have been involved in experimental high energy physics.

I want to thank all the members of the group at the Athens University Nuclear Physics Laboratory for teaching me the basics of Particle Physics Research. Especially Dr. Efstratios Anassontzis and Prof. Pavlos Ioannou who introduced me to hardware, both design and implementation, during our work on the calibration system of the DELPHI Barrel RICH detector. Also Prof. Christine Kourkoumelis, my diploma thesis advisor, for helping me to complete my first major project, and for giving me the opportunity to work at CERN as an undergraduate.

During my involvement with E771, and more specifically with the Silicon Strip Detector Electronics System, I learned a lot about electronics and software (and also code organization and debugging techniques – or simply how to keep my cool when trouble comes) from Dr. Wolfgang Kowald of Duke University; I thank him for that, and for his friendship.

I thank Dr. Dimitri Dimitroyannis for his advice and support during the difficult period during which I was trying to decide if I should continue my studies in the field, and how to proceed in order to continue them. His enthusiasm and dedication during our long conversations played an important role in my decision. I thank him for that, and for being a good friend over all these years.

I would like to thank Prof. Jerry Rosen of Northwestern University for his help and support, which enabled my transfer from Athens University to Northwestern

University.

The successful operation of a high energy physics experiment like E665 requires the joint effort of many individuals; their work has contributed in many different ways, directly and indirectly, to the work that is presented in this thesis. I would therefore like to express my gratitude to the entire E665 collaboration, and especially to the physicists and the graduate students that were involved with the 1990/91 run of the experiment.

I would like to thank my boss, Prof. Heidi Schellman, both for being my advisor and for her leadership as the spokesperson of the experiment during and after the 1991 data taking period. By trusting me with major responsibilities on important projects like the alignment and the normalization, she helped me develop my judgement and self confidence. Interacting with her during my analysis was very useful; she was always open to discuss new ideas and she insisted on being cautious about systematic effects.

I have learned enormously from discussions with Dr. Don Geesaman and Dr. Harry Melanson on issues of analysis and of the physics of muon-nucleon (and nucleus) scattering; I thank them for sharing their enthusiasm for physics with the rest of us. I would also like to thank Don for his leadership during the initial phase of the 1990/91 run.

I wish to express my special thanks to Dr. Steve Wolbers for organizing the crunching and reconstruction of the E665 data; his contribution was invaluable to the experiment.

I would like to thank Prof. Mark Adams for his work on the Small Angle Trigger.

I enjoyed working with Dr. Bogdan Pawlik on understanding the alignment and developing a new technique for it. His contribution was very important, I thank him for that (and for sharing with me his good taste in Thai food and vodka).

I would like to thank Dr. Wolfgang Wittek for his overall contribution to the offline software of the experiment, Dr. Vassilio Papavassiliou for his work on the

trigger and for useful comments during various stages of my analysis, and Dr. Yin Fang Guang for many useful conversations on analysis issues. I thank Dr. David Jaffe for his work on calorimeter based analysis techniques.

I would like to thank Tim Carroll for his hard work on the SAT and on the PSA, and for sharing with me his equally distributed enthusiasm in jogging and beer drinking. I thank Rob Kennedy for his ideas about setting up the mechanics of the ratio analysis in the fastest way. I thank Arijit Banerjee, Janet Conrad, Bill Dougherty, Pat Madden and Mathias Wilhelm for their work on the experiment.

I wish to thank my friend and volleyball teammate Guo Rurngsheng for his work on the PSA/PSC and on the track fitting and pattern recognition, but mostly for his endurance and good humor in both aspects of our common activities, work and play.

Of my E665 collaborators, I left last in my acknowledgements the one closest to both my work and myself, my friend and comrade of the 1991 analysis, Ashutosh Kotwal. Our joint effort to understand both the physics and the detector through many hours of fruitful discussions, had a very significant contribution to the development of my analysis approach. The work which we did on the 1991 n-tuple software design and implementation was essential for the fast completion of both of our analyses. His work on the calorimeter trigger and calibration were of great importance to E665. For his contribution to the experiment, and for his friendship, I thank him.

I would like to thank the Greek community of Fermilab for making the transition to a foreign place easier. I would especially like to thank Penelope and George Fanourakis for making their house our home, and also for the feasts they provided. I wish the best of luck for them now that they are back in Greece; we will miss them.

I want to thank my volleyball teammates, the "Red Barbarians, Terror of the Prairie", for helping relieve some of the pressure of my graduate student life, and for winning the playoffs three years in a row.

Being away from home is difficult enough, add to it the nature of graduate student life and it can become unbearable. I would like to thank my wife, Linda Klamp

Spentzouris, for making my life happier. Her moral support has been essential to the completion of this thesis, and of course her proof reading very important. *Ευχαριστώ πολύ*.

I want to express my deepest gratitude to my parents *Ελλένη* and *Γεώργιος* for their love and support, especially during the very difficult last three years of my mother's illness. Their fighting spirit, optimism, and love for life kept me focused and helped me develop a positive attitude towards life.

This thesis is dedicated to my father and to the memory of my late mother.

Contents

List of Tables

List of Figures

Chapter 1

The Structure Function Ratio F_2^n/F_2^p in charged lepton-nucleon scattering

1.1 Introduction

The power of using lepton-nucleon scattering as a tool to study the structure of nuclear matter was established during the early days of particle physics. It stems from the fact that the electroweak field generated during the scattering process is weak enough to permit a perturbative treatment of its strength in powers of the electroweak charge. This allows the structure of the nuclear target to be probed using a known interaction mechanism and a well understood projectile.

In the 1950's, measurements of elastic electron-nucleus scattering at SLAC were used to determine the charge distributions of various nuclei [1]. The results revealed that the nucleon has a spatially extended charge distribution, providing evidence that it is not a point-like particle. The original measurements of high-energy electron-nucleon inelastic scattering in the late 1960's at SLAC showed that above the nucleon

resonance region the inelastic cross-section is independent of the four-momentum transfer squared from the probe to the target. This was a surprising result, since the resonance form factors fall rapidly as a function of the four-momentum transfer squared [2]. The interpretation of these results led to the quark-parton model [3], [4]. In this model and in the limit of large energy-momentum transfers, the nucleon inelastic cross-section is the incoherent sum of the elastic scattering from point-like constituents (partons). This model explained in a simple framework the scaling of the nucleon structure functions [1] as well as the behaviour of the difference of the structure functions of the neutron and the proton, which have been predicted using current algebra ([5] and [6] respectively). In the early 1980's the muon scattering experiments performed at CERN ([7] and [8]) verified the scaling violations predicted by the gauge field theory of the strong interactions, Quantum Chromo-Dynamics (QCD). The theory of QCD has been quite successful at explaining and predicting the behaviour of the strong interactions at short distance scales with respect to the nucleon size. The ability of QCD to calculate the cross-sections for processes involving hadronic matter depends on our knowledge of the momentum distributions of the constituent particles of the hadronic matter. These distributions are extracted from the compilation of structure function measurements using different probes on various nuclear targets.

In this thesis, the measurement of the structure function ratio of neutrons to protons from inelastic collisions of muons with hydrogen and deuterium is presented. The data for the measurement were taken during the Fermilab 1991 fixed-target period with the E665 apparatus [9]. The kinematic range covered is unique since it has never been probed before experimentally and it extends to a region where perturbative QCD calculations are not applicable and predictions can be made only by QCD phenomenology. The ratio measurement is a constraint on the parton distribution functions extracted from global structure function analysis and can be used as a test

[1] The structure functions scale if they depend only on dimensionless quantities

for the QCD phenomenology models. Furthermore, it provides information about nuclear shadowing in the deuteron, an effect which has been predicted by various models [10], [11] but has never been measured. Nuclear shadowing is the depletion of the per nucleon cross-section in composite nuclei as compared to the free nucleon and it has been observed in scattering from heavy nuclei targets.

This thesis is organized into six chapters and five appendices. In the remaining sections of this chapter a short discussion of the formalism of charged lepton-nucleon scattering is presented together with a summary of theoretical and phenomenological ideas concerning this process. In chapter two the E665 experimental apparatus is described. Chapter three contains a description of the event reconstruction program and describes the analysis performed to obtain the energy calibration of the calorimeter and the spectrometers of the apparatus. In chapter four, the physics analysis including systematic studies is presented. Chapter five contains the results, and a summary of the systematic effects. In chapter six, the physics results are summarized and compared with theoretical predictions from models that include shadowing effects in the deuteron. Chapter six also contains a discussion on the implications of the measurement, and the conclusions. Appendix A describes the analysis done to obtain the target normalization. Appendices B and C describe the data structures used in the normalization and physics analysis. Appendix D describes the measurement of the ratio of the elastic scattering cross-section of muons scattering off of atomic electrons of the deuterium target, to that same cross-section for the hydrogen target. Appendix E contains a glossary of terms that are specific to the 665 experiment, and a few acronyms commonly used in high energy physics.

1.2 Cross-section definitions and constraints

The kinematics of inelastic charged lepton scattering in the single photon exchange approximation are defined in figure 1.1. The diagram involves only the exchange

of a virtual photon since at energies relevant to this analysis the contribution of the Weak interactions is negligible. The kinematics of the interaction are described using the leading order Quantum Electro-Dynamics (QED) process; the effects of the higher order QED processes will be introduced as corrections to the single photon exchange approximation. In this approximation we can use our knowledge of QED

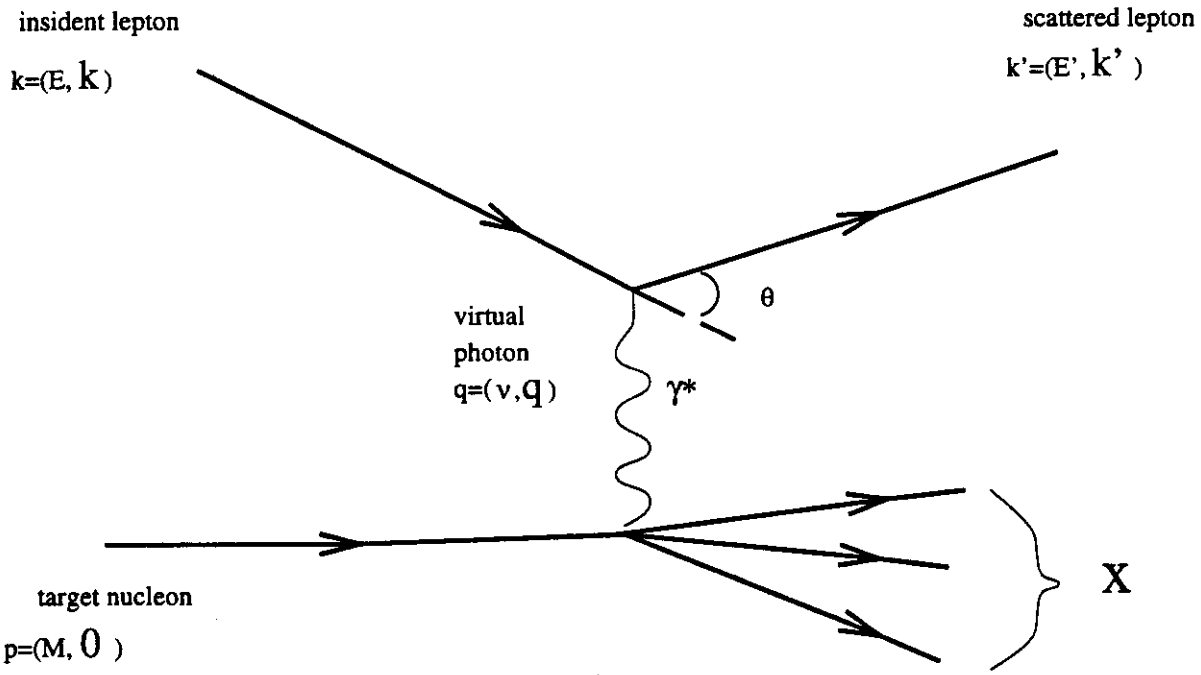

Figure 1.1: Charged Lepton-Nucleon scattering. Target rest frame.

field theory, the principles of gauge invariance and the parity conservation symmetry of the electromagnetic interaction to express the single photon exchange differential cross-section. Ignoring phase space factors, the inclusive cross-section can be written ($\hbar = c = 1$):

$$d\sigma \sim \frac{\alpha^2}{Q^4} L_{\mu\nu} W^{\mu\nu} \tag{1.1}$$

where the lepton tensor $L_{\mu\nu}$ is the product of the leptonic currents and it is calculable within the QED framework. Averaging over the spins of the initial state and summing

over the spins of the final state we obtain:

$$L_{\mu\nu} = 2(k_\mu k'_\nu + k'_\mu k_\nu - (k \cdot k' - m^2)g^{\mu\nu}) \tag{1.2}$$

where k and k' are the momenta of the lepton before and after the interaction respectively, and m is the lepton mass. Using the optical theorem, the hadronic tensor $W^{\mu\nu}$ is related to the product of the electromagnetic current of the hadron "leg" of the diagram in figure 1.1 (nucleon and final state X). By the optical theorem, the imaginary part of the forward scattering amplitude is proportional to the total cross-section. The application of the optical theorem for lepton-nucleon scattering is shown in figure 1.2 (see also [12]). The hadronic tensor $W^{\mu\nu}$ is computed to be

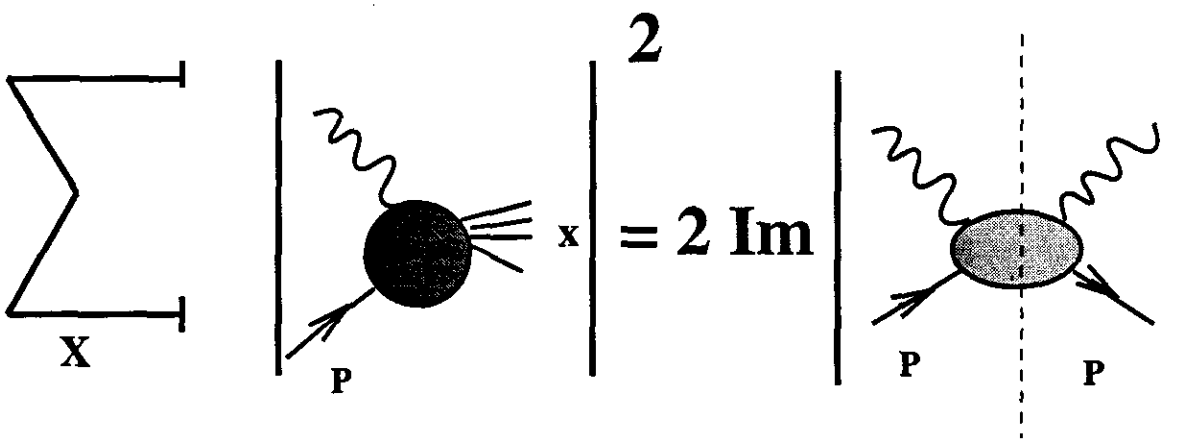

Figure 1.2: Optical theorem for lepton-nucleon scattering.

proportional to the matrix element of the time ordered product of the electromagnetic current operators $j^\mu_{em}(\xi)$ at space-time point ξ:

$$W^{\mu\nu} \propto Im\, i \sum_s \int d^4\xi \exp(iq\xi) < p,s \mid T j^\mu_{em}{}^\dagger(\xi) j^\nu_{em}(0) \mid p,s > \tag{1.3}$$

where T in the operator product denotes time ordering and s the spin of the nucleon. The nature of the electromagnetic interaction requires that $W^{\mu\nu}$ is gauge invariant and invariant under parity transformations. Because of these properties of the interaction the tensor $W^{\mu\nu}$ can be expressed in the most general form as [13]:

$$W^{\mu\nu}(p,q) = \frac{F_1(x,Q^2)}{M}\left(-g_{\mu\nu}+\frac{q^\mu q^\nu}{q^2}\right)+ \frac{F_2(x,Q^2)}{M(p\cdot q)}\left(p^\mu-\frac{p\cdot q}{q^2}q^\mu\right)\left(p^\nu-\frac{p\cdot q}{q^2}q^\nu\right) \quad (1.4)$$

where q^2 is the square of the four-momentum transfer to the target and $Q^2 = -q^2$, $x_{Bj} \equiv x = Q^2/(2p\cdot q)$ is the Bjorken scaling variable that measures the inelasticity of the process, M is the nucleon mass, and the functions $F_1(x,Q^2)$ and $F_2(x,Q^2)$ are the structure functions of the target. The invariant quantity $p\cdot q$ is proportional to the energy transfer ν in the target rest frame, $p\cdot q = M\nu$. The invariant mass of the final state hadronic system, W, is then $W^2 = M^2 + 2M\nu - Q^2$. In general the structure functions F_i can be expressed as a function of any two of the above Lorentz invariant kinematic variables. The tensor $W^{\mu\nu}$ has to satisfy the electromagnetic current conservation requirements:

$$q_\mu W^{\mu\nu} = 0$$
$$q_\nu W^{\mu\nu} = 0 \quad (1.5)$$

In order to explore potential kinematical singularities of the tensor $W^{\mu\nu}$ at the $Q^2 = 0$ limit we rearrange the terms of equation 1.4:

$$W^{\mu\nu}(p,q) = -\frac{F_1}{M}g^{\mu\nu}+\frac{F_2}{M(p\cdot q)}p^\mu p^\nu + \left(\frac{F_1}{M}+\frac{F_2}{M}\frac{p\cdot q}{q^2}\right)\frac{q^\mu q^\nu}{q^2}-\frac{F_2}{M}\frac{p^\mu q^\nu + p^\nu q^\mu}{q^2} \quad (1.6)$$

The last two terms of the expression 1.6 are singular in the limit $Q^2 \to 0$. Since the physical cross-section cannot be singular, the above behaviour forces us to introduce the following constraints on the structure functions F_i in the limit $Q^2 \to 0$:

$$\frac{F_1}{M}+\frac{F_2}{M}\frac{p\cdot q}{q^2} = O(Q^2) \quad (1.7)$$

$$F_2/M = O(Q^2) \quad (1.8)$$

These conditions have to be valid for arbitrary values of ν.

Contracting the leptonic and the hadronic tensors, inserting the phase space factors and using the expression 1.4 for $W^{\mu\nu}$, equation 1.1 of the differential electroproduction cross section in the single photon exchange approximation becomes:

$$\frac{d^2\sigma(x,Q^2)}{dQ^2dx} = \frac{4\pi\alpha^2}{Q^4}\left[\left(1-y-\frac{Mxy}{2E}\right)\frac{F_2(x,Q^2)}{x}+\left(1-\frac{2m^2}{Q^2}\right)y^2F_1(x,Q^2)\right] \quad (1.9)$$

where E is the energy and m is the mass of the incident lepton in the target rest frame, $y = \nu/E$ and α is the electromagnetic coupling constant. The expression 1.9 is completely general, and requires no assumptions about the nature of the interactions that define the structure of the hadronic tensor $W^{\mu\nu}$.

We can rewrite equation 1.9 using the structure function ratio $R(x,Q^2)$ instead of F_1. The structure function ratio $R(x,Q^2)$ is equal to the ratio of the cross-sections for the different polarizations of the virtual photon:

$$R(x,Q^2) = \frac{\sigma_L}{\sigma_T} = \frac{(1+4M^2x^2/Q^2)F_2}{2xF_1} - 1 \quad (1.10)$$

where σ_L and σ_T are the cross sections for the longitudinal and transverse virtual photon polarization states respectively. Now the differential cross section (1.9) becomes

$$\frac{d^2\sigma(x,Q^2)}{dQ^2dx} = \frac{4\pi\alpha^2}{Q^4}\frac{F_2}{x}\left[1-y-\frac{Mxy}{2E}+\left(1-\frac{2m^2}{Q^2}\right)\frac{y^2(1+4M^2x^2/Q^2)}{2(1+R)}\right] \quad (1.11)$$

Since real photons are only transversally polarized, σ_L and R should vanish as $Q^2 \to 0$, and the total cross-section should match the total real photoproduction cross-section.

1.3 Structure Functions in the Deep Inelastic Scattering limit

In the high energy limit, where $E \to \infty$, and with Q^2 fixed, integrating equation 1.9 "measures" the charged constituents (partons) of the nucleon. In order to aid

our intuitive understanding we identify kinematic conditions that permit an impulse approximation analysis of the lepton-nucleon inelastic scattering [14]. This leads to the parton model picture, which is a valid concept in the deep inelastic regime defined as the region where both Q^2 and $2M\nu$ are large and their ratio, x, is kept fixed. In this kinematic regime we can view the scattering process in an infinite momentum frame (see for example [15]), where the momentum P of the nucleon is very large ($P \rightarrow \infty$) and with a direction opposite to the virtual photon three-momentum vector. In this frame the transverse momentum ($k_\perp$) of the partons and the mass of the target nucleon are negligible. The partons share a finite fraction $0 < x_i < 1$ of P and move in the P direction. The lifetime of the parton states is much larger than the duration of the perturbing electromagnetic field of the interaction, so scattering from individual partons can be treated as incoherent for abrupt perturbations. The scattering off of each individual parton is elastic, so by using simple kinematics and the elasticity condition we find that the value of x_i for the momentum fraction of the scattered parton is equal to the Bjorken scaling variable x. The scattering cross-section can be expressed in terms of the probability distribution $q_i(x)$ of finding the parton i with fractional momentum x in the nucleon. If we calculate the elastic lepton-parton scattering matrix-element with the assumption that the partons are spin-1/2 particles, and then perform the integration over the phase space of the parton, we can derive simple relationships between the structure functions and the parton distribution functions ([15]):

$$F_2(x) = x \sum_i e_i^2 q_i(x)$$
$$F_1(x) = (1/2x) F_2(x) \qquad (1.12)$$

The second expression (Callan-Gross relation) can be used in equation 1.10 to obtain $R = Q^2/\nu^2$, which in the kinematic region where $Q^2 \ll \nu$ is $R \approx 0$. The measurement of a small R value at SLAC [16], led to the realization that the partons have to be identified with the fractionally charged spin-1/2 quarks postulated to explain the

particle multiplets of the hadronic spectrum ([17]).

The quark-parton model is a first order approximation to the correct strong interactions treatment in lepton-nucleon scattering. From purely kinematic arguments the interpretation of the Bjorken scaling variable x as the fraction of the momentum of the nucleon that the parton carries is only valid if $k_\perp, m_\perp \ll Q^2 \ll \nu^2$, where $m_\perp$ is the off-shellness of the parton during the interaction. Furthermore, the strong interactions of nuclear matter are indeed strong, which means that they will come into play, altering both the scaling picture and the postulate of a vanishing structure function ratio R.

1.4 Quantum Chromo-Dynamics and Structure Functions

Quantum Chromo-Dynamics (QCD) is the non-Abelian gauge field theory that describes the strong interactions. The fundamental particle fields are the quarks (fermions) and the gluons (vector bosons). The quantum number ("color") that the fundamental fields carry and exchange in order to interact has three different possible values. Both quarks and gluons carry color. The color transformations are described by the local gauge group $SU(3)$, the quarks are assigned to the fundamental ($\mathbf{3}$) representation of the group and the gluons to the adjoint ($\mathbf{8}$) representation. The QCD Lagrangian possesses, in addition to the non-Abelian $SU(3)$ gauge symmetry, the approximate flavor $SU(3)$ symmetry, since the constituent masses of the u, d and s quarks are roughly equal (the quarks come in different species, u, d, s, c, b and t "flavors"). The most important dynamical property of this non-Abelian gauge field theory is asymptotic freedom. If Q^2 represents some large momentum scale in the interaction, then the effective QCD coupling constant $\alpha_s(Q^2) \to 0$, as $Q^2 \to \infty$. This is a consequence of the antiscreening effect of the nonabelian coupling, which results in a decrease of the effective strength of the coupling as we go to short distances or large momentum

transfers.

The above property of QCD justifies the a priori assumptions of the parton model at large energy scales, since asymptotic freedom ($\lim_{Q^2\to\infty}\alpha_s = 0$) implies that in that regime the color interactions among the partons can be ignored. Furthermore, asymptotic freedom allows the use of perturbation theory (pQCD) to calculate large momentum transfer phenomena.

1.4.1 Perturbative Quantum Chromo-Dynamics

The next to leading order QCD diagrams (order α_s contribution) that have to be added to the simple leading order picture (figure 1.1) are gluon bremsstrahlung (figure 1.3), and photon-gluon fusion (figure 1.4). If we try to compute the contribution of these diagrams using massless quarks and gluons we will find that these correction terms diverge. In order to overcome this problem, we use the concepts of the factorization theorem in deeply inelastic scattering. The factorization theorem states that the contribution to the hadronic cross-section factorizes to a term that contains all short-distance contributions (large momentum scales) and a term that contains all the soft and collinear divergent contributions (long distance effects). Using these concepts, F_2 is given by

$$F_2 = \sum_k \int_0^1 d\xi C_2^i(x/\xi, Q^2/\mu^2, \mu_f^2/\mu^2, \alpha_s(\mu^2)) \times q_i(\xi, \mu^2, \mu_f) \qquad (1.13)$$

where k denotes any parton (quark, antiquark and gluon). The scale μ is the renormalization scale of the theory and μ_f the factorization scale which defines the separation between short and long distance effects. The hard-scattering functions $C_2^i(x/\xi, Q^2/\mu^2, \mu_f^2/\mu^2, \alpha_s(\mu^2))$ are calculable in perturbation theory and are non-divergent. They have no dependence on the characteristics of the hadron; they depend on the type of the interaction, the parton i, and the normalization and factorization scales. The parton distribution functions $q_i(\xi, \mu^2, \mu_f)$ are specific to the target hadron and contain all the divergencies of the cross-section, and the effects of the soft processes which determine the form of

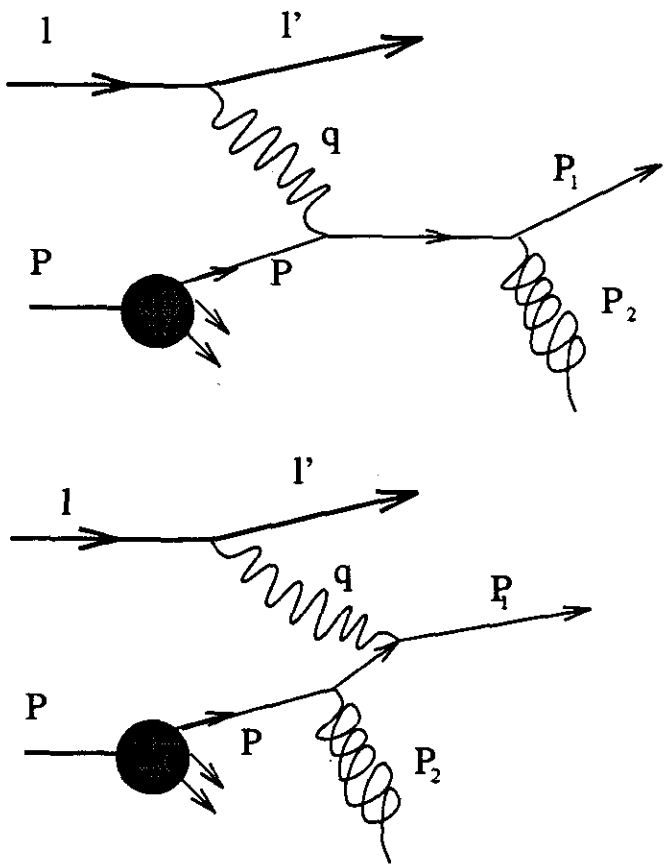

Figure 1.3: Gluon Bremsstrahlung.

the nucleon as a bound state of quarks; they are not calculable in perturbative QCD. However, they are universal and pQCD can predict their evolution with the scale μ. This evolution is most often described in terms of integro-differential equations [18] (to leading logarithmic approximation). These equations incorporate asymptotic freedom by phenomenologically using the running coupling constant α_s. In this approach the parton model is the lowest order approximation, with scale independent parton distributions which are modified by introducing a series of gluon emissions. Hard scattering with a momentum transfer Q probes the parton at a distance $\sim Q^{-1}$. When the parton wavefunction is resolved to small enough scales, it appears as a constituent parton, carrying a fraction of the original parton longitudinal momentum, plus a number of constituent gluons and $q\bar{q}$ pairs. Any of these constituents, if it carries a large fraction of longitudinal momentum, can initiate the hard scattering process. The contribution from the collinear and soft emissions becomes associated with the parton distribution functions. As a result, the effects of the QCD radiation originating because of the acceleration of the partons in the electromagnetic field are included in the description of the internal dynamics of the nucleon, which introduces the scale dependence of the parton distribution functions. The probability of a parton i of momentum fraction ξ to split because of gluon radiation into a parton j and a gluon, retaining a fraction $z = \xi/x$ of its original momentum, is denoted by $P_{i\to j}$, the "splitting function". Assuming that the transverse momenta of the emitted gluons are strongly ordered the integration over their phase space gives a leading contribution of the type $(\alpha_s \ln(Q^2/\mu^2))^2$ [12]. If only these leading terms are kept in the perturbative calculation of the evolution processes we obtain the leading $\ln(Q^2)$ approximation evolution equations [18]. The vertices which define the splitting functions that contribute to the evolution equations in this approximation are shown in figure 1.5. In the small-x limit the evolution equations [18] have to be modified in order to account for the appearance of large logarithmic ($\log(1/x)$) contributions. These powers of $\log(1/x)$ come from the fact that the integration over the longitudinal momentum

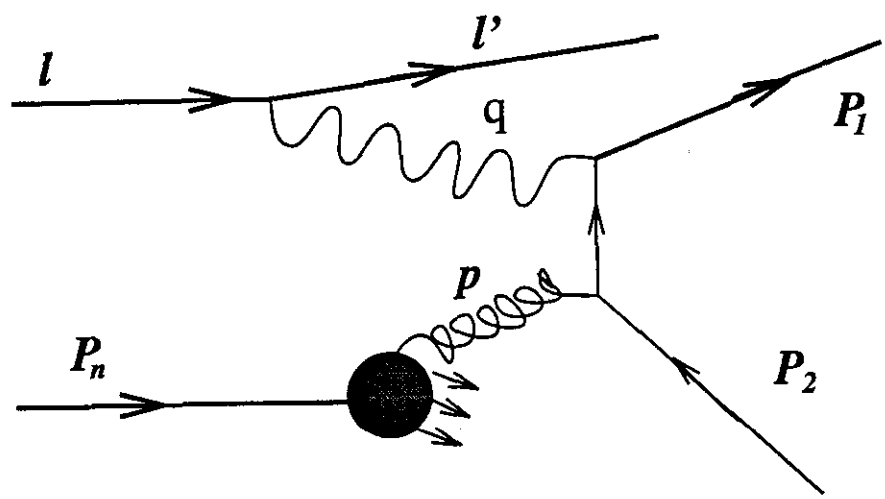

& diagram with: $P_1 \longleftrightarrow P_2$

Figure 1.4: Photon Gluon Fusion.

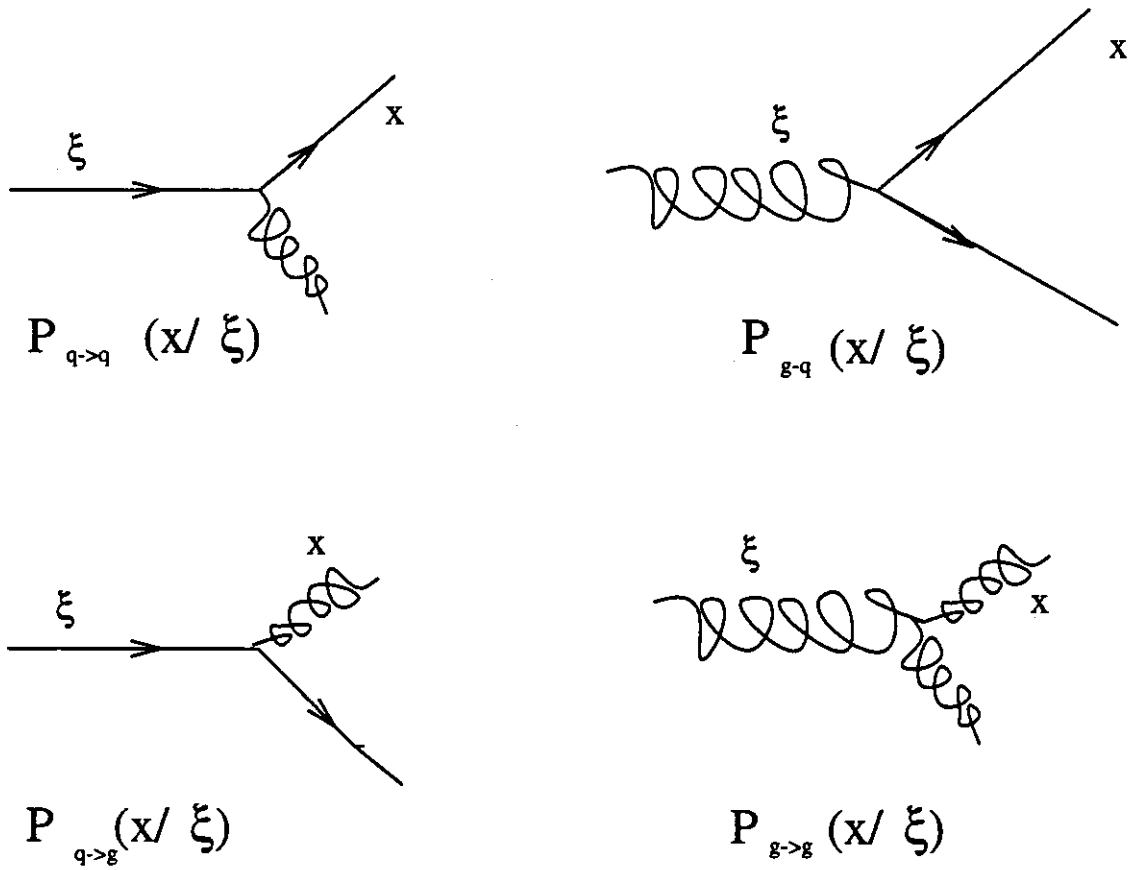

Figure 1.5: Vertices that define the Altarelli-Parisi splitting functions.

in the evaluation of the splitting functions becomes logarithmic. Depending on the number of terms that are kept in the double perturbative expansion in both $\log(1/x)$ and $\log(Q^2)$, different approaches are used to modify the Altarelli-Parisi equations (for a review see [12]).

The pQCD picture of the structure functions reveals the power of the structure function measurements: Measuring various combinations of different structure functions, by using different targets and different probes, at a given Q^2 scale [2], we can extract the parton distribution functions. We can then evolve them to any Q^2 scale and combine them with the calculable hard-scattering functions 1.13 in order to obtain the cross-sections for the corresponding processes at this Q^2 scale [3].

Since the factor governing the rate of the evolution of the parton distributions is $\sim \alpha_s(Q)$, when Q is large the evolution is slow and the leading $\log Q^2$ approximation of perturbative QCD is adequate to describe the interaction. Using this approximation the structure function $F_2(x, Q^2)$, to leading order in the perturbative QCD expansion, can be directly related to the quark- and antiquark momentum distributions, $q_i(x, Q^2)$ and $\bar{q}_i(x, Q^2)$:

$$F_2(x, Q^2) = x \sum_i e_i^2 \left[q_i(x, Q^2) + \bar{q}_i(x, Q^2) \right] \tag{1.14}$$

where i is the quark flavour and e_i the charge for the quark of flavor i. In this regime the quark and antiquark distributions exhibit approximate Bjorken scaling, mildly violated by the QCD logarithmic corrections. The evolution equations for these distributions with Q^2 as well as the relation (1.14) acquire corrections proportional to $\alpha_s(Q^2)$ in the next-to-leading $\log Q^2$ approximation, unless the factorization scheme used is the DIS scheme, where by definition 1.14 is valid to all orders [19]).

Having discussed the limitations of the pQCD picture of the structure functions, we can now concentrate on the expression for the F_2 1.14 and within the pQCD

---

[2] We can set for convenience $\mu_f^2 = \mu^2 = Q^2$

[3] In the above discussion we assumed that the hadronization process occurs on a longer time scale than that of the collision process and does not interfere with it

framework we will explore the behaviour of the structure functions for the neutron and the proton. To simplify the discussion (and the notation), we fix the energy scale ($\mu_f^2 = \mu^2 = Q^2 = const$), so in all the following relations the Q^2 dependence is implied but not explicitly shown. First let us split the contribution to the parton distribution functions into "valence" and "sea" quark contributions. The "valence" contribution corresponds to the portion of the number density of a flavor that contributes to the quantum numbers of the nucleon, while the "sea" contribution can be viewed as the gluon generated quark-antiquark pairs that carry the vacuum quantum numbers. In general we can write

$$\begin{aligned} q &= q_v + q_s \\ \bar{q} &= q_s \end{aligned} \tag{1.15}$$

We can also use isospin invariance to express the neutron and proton structure functions using the same parton distribution functions. Since the u, d quarks and the proton, neutron form isospin doublets, we have $u = u_p = d_n$, $d = d_p = u_n$, $s = s_p = s_n$. The heavy flavor contribution is omitted, since they can be resolved at scales above their production threshold $Q^2 \sim 4m_q^2$, where m_q^2 is the quark mass. (At $Q^2 = 10GeV^2$ the heavy flavor contribution is less than 1% of the total [24]). The structure functions can now be written:

$$\begin{aligned} F_2^p(x) &= x\{\frac{4}{9}(u(x) + \bar{u}(x)) + \frac{1}{9}(d(x) + \bar{d}(x) + s(x) + \bar{s}(x)) + ...\} \\ F_2^n(x) &= x\{\frac{4}{9}(d(x) + \bar{d}(x)) + \frac{1}{9}(u(x) + \bar{u}(x) + s(x) + \bar{s}(x)) + ...\} \end{aligned} \tag{1.16}$$

Imposing the conditions of equation 1.15 and remembering the spectroscopic flavor contents of the proton (valence quarks) we can assume that

$$\begin{aligned} u_v &= 2d_v \\ s_v = \bar{u}_v &= \bar{d}_v = \bar{s}_v = 0 \end{aligned} \tag{1.17}$$

Furthermore, if we assume that the sea quark distributions are flavor symmetric,

$u_s = \bar{u}_s = d_s = \bar{d}_s = s_s = \bar{s}_s = K$, and that at $x \to 0$ K dominates, then

$$\lim_{x \to 0} \frac{F_2^n}{F_2^p}(x) \to 1 \tag{1.18}$$

The justification of the "sea" domination at low x comes from the qualitative argument that the "sea" quarks are generated dynamically from gluon bremsstrahlung and the bremsstrahlung probability at a given momentum k behaves as dk/k, and hence like dx/x.

Using equation 1.16 we can also write an expression for the difference of the structure functions of the neutron and the proton:

$$\frac{F_2^p - F_2^n}{x} = \frac{1}{3}(u + \bar{u} - d - \bar{d}) \tag{1.19}$$

If we assume that the total number of $\bar{u}$ and $\bar{d}$ quarks inside the proton is the same, then integrating equation 1.19 over x and remembering the net valence quark flavor content of the proton (equation 1.17), we obtain:

$$S_G = \int_0^1 dx \, \frac{F_2^p(x) - F_2^n(x)}{x} = \frac{1}{3} \tag{1.20}$$

The above relation (1.20) constitutes the Gottfried sum rule [6]. Although this sum rule was introduced as a parton model sum rule, it has been proven to be almost exact; the pQCD corrections to S_G are very small [20]. This means that the pQCD evolution will not introduce any appreciably large difference to the value of the sum rule obtained at a fixed scale. The determination of the sum rule provides valuable information about the structure of the nucleon, since there is no a priori reason to believe that the total number of $\bar{u}$ and $\bar{d}$ quarks inside the proton is the same. If part of the quark "sea" is generated by a non-charge symmetric source then the "sea" does not have to be flavor symmetric (charge here refers to the electromagnetic charge and the masses are assumed to be similar).

1.4.2 Higher twist effects and target mass corrections

A rigorous analysis of the structure functions in the Bjorken limit can be done using the operator product expansion of the electromagnetic currents (expression 1.3 for the hadronic tensor) [21]. Such products contain singularities in their light-cone behaviour ($\xi^2 \to 0$, ξ space-time variable), which can be expanded as

$$j(\xi/2)j(-\xi/2) = \sum_{k,N} C_k^N(\xi^2)\xi^{\mu 1}...\xi^{\mu N}O^{kN}_{\mu 1...\mu N}(0) \tag{1.21}$$

where the operators O^{kN} (spin N operators) are non-singular and the coefficients C_k^N are singular as $\xi^2 \to 0$. Their behaviour can be found from dimensional counting [22]. If d_j and $d_{k,N}$ are the mass dimensions of J and O^{kN} respectively, then the mass dimension of C_k^N is $2d_j + N - d_{k,N}$, so that up to log terms

$$C_k^N(\xi^2) \xrightarrow{\xi \to 0} (1/\xi^2)^{1/2(2d_j - \tau_{k,N})} \tag{1.22}$$

where $\tau_{k,N} = d_{k,N} - N$ is called the "twist" of the operator O^{kN}, and it is the mass dimension of O^{kN} minus the spin of O^{kN}. The lowest twist (twist 2) dominates the light-cone expansion of the structure functions, this contribution comes from the processes described by the diagrams in figure 1.5. The expansion is done using operators that can create and annihilate partons in the proton wavefunction. The higher twist terms correspond to interactions between the struck quark and the spectator quark, the diagram is shown in figure 1.6. The coefficients of the expansion 1.21 depend on Q^2, this dependence comes from the operator rescaling and involves only logarithms of Q^2. The structure function F_2 is expanded in a sum of inverse powers of Q^2:

$$F_2(x, Q^2) = \sum_{n=0}^{\infty} \frac{C_n(x, Q^2)}{(Q^2)^n} \tag{1.23}$$

where the functions $C_n(x, Q^2)$ depend weakly (logarithmically) on Q^2. The leading twist terms are the $n = 0$ terms and the higher twists are the $n \geq 1$ terms. Thus equation (1.14) corresponds to the "leading twist" contribution to the F_2, which is a

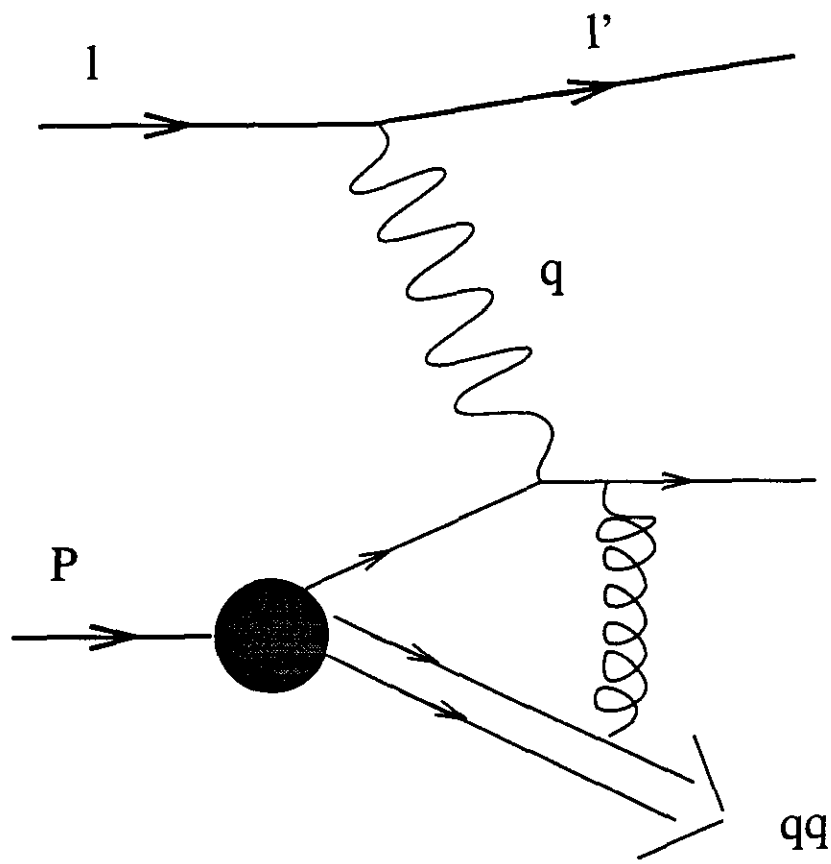

Figure 1.6: Higher twist diagram in Deep Inelastic Scattering.

good approximation for large values of Q^2. For moderately large values of Q^2 (of the order of a few GeV^2) contributions from the "higher twists" may become significant. The size of these terms cannot be calculated since this would require knowledge of the wave function of the bound state quarks. The higher twists are only corrections to the leading twist term (that corresponds to expression 1.14) in the large Q^2 region. Thus they cannot correctly describe the low nonperturbative Q^2 region, since the expansion of equation 1.23) gives a divergent series at low Q^2. In order to describe this region the expansion has to be summed beforehand at large Q^2, and then continued to the region of $Q^2 \sim 0$ [23].

In practice, in the analysis of experimental data which extend to low values of Q^2, the higher twist contributions can be extracted qualitatively in the following way:

$$F_2(x,Q^2) = F_2^{LT}(x,Q^2)\left[1+\frac{H(x)}{Q^2}\right] \tag{1.24}$$

where the F_2^{LT} is the leading twist contribution to F_2 and $H(x)$ is determined by fitting the data. This expression is not exact, since in principle the higher twist terms evolve differently with Q^2 than the leading twist term. On the other hand, since the leading twist term has a logarithmic Q^2 dependence the error will be small in this treatment.

Since the neutron and the proton have different net flavor contents, the higher twist coefficients should be different. Also the higher twist contribution to the structure function ratio, since it depends on the details of the nucleon wavefunction, should introduce a Q^2 dependence in the measurement.

There are two higher twist effects that are conventionally treated separately, the target mass corrections and the effect of the intrinsic transverse momentum of the parton ($k_\perp$). The correction for the effect of the target mass is of the order $\sim (xm/Q)^{2n}$, where m is the mass of the target nucleon. The correction from the intrinsic $k_\perp$ is of the order of $\sim (k_\perp/Q)^{2n}$. The first correction can actually be applied, since the target mass is known, whereas the average $k_\perp$ value can only be inferred from the

experiment.

1.5 Structure functions at low Q^2

As the value of Q^2 becomes smaller and smaller the partonic picture described in the previous section cannot predict the behaviour of the structure functions: the initial conditions of the evolution of the parton distribution functions are now determined by the form of the nucleon wavefunction at very large distance scales and are not calculable in pQCD. Equivalently, we can think of this as a consequence of the manifestation of a new scale length in the problem (that of the nucleon) which breaks the scale invariance. The Q^2 scale where this effect becomes significant is given roughly by the uncertainty principle: $\Delta l = 0.2/Q(GeV)fm$, where Δl is the spacial resolution of the probe (in fm units). Also, the Bjorken scaling which holds approximately at high Q^2 cannot be valid at low Q^2. This is a consequence of the conservation of electromagnetic current which requires that the structure function F_2 must vanish in the limit $Q^2 \to 0$ (equation 1.8), and of the intuitive argument that F_2 should be a continuous function. In the low Q^2 regime the interaction of the photon with the nucleon can be viewed through the transitions of the photon to virtual hadronic states which subsequently interact with the target nucleon. Models which describe the photon-hadron interaction in this fashion are the Vector Meson Dominance Models (VMD) and their generalizations (GVMD) [25].

In general, the wavefunction of a high energy physical (or virtual) photon can be represented as a superposition of a bare photon state and a hadronic component state. This hadronic component corresponds to the vector meson states having the same quantum numbers as the physical photon, thus enabling the photon to fluctuate to these states. The photon must be at a high energy state so that the mass of the vector meson is negligible. In this case the bare photon state is degenerate with any vector meson state that has the same quantum numbers with the photon ($J^{PC} = 1^{--}$

and zero electric charge) [25]. The transition to these virtual hadronic states will roughly occur during a fraction $\alpha(1/137)$ of the lifetime of the physical (or virtual) photon. The lifetime of the hadronic state is given by the uncertainty principle [25]:

$$\Delta t \sim 1/\|\Delta E\| \sim \frac{1}{\|\nu - (\nu^2 + Q^2 + m_v^2)^{1/2}\|} \sim \frac{2\nu}{Q^2 + m_v^2} \tag{1.25}$$

where m_v is the mass of the vector meson and the second approximation holds for large ν. Although these fluctuations occur during a small fraction of the lifetime of a virtual photon, they interact strongly with hadrons (with typical hadron-hadron cross-sections). In order to interact with the target nucleus, the virtual state has to propagate inside the nucleus for a time that is of the order of magnitude of the interaction time of the meson with the nucleus. This interaction time scale is given by the size of the target nucleus so for $Q^2 \ll \nu^2$ in equation 1.25 the interaction can occur (the speed with which the vector meson propagates is essentially the speed of light, so length and time scales are equivalent). When Q^2 is large, the formation time becomes shorter and the hadron-mediated interactions may become indistinguishable from the those of the bare photon term. The hadronic models are not (in principle) in conflict with the parton model description; they are describing a different kinematic domain. Actually, the generalization of the VMD models gives approximate scaling for the structure functions at large Q^2, which can be represented, for sufficiently large Q^2, in a form similar to the twist expansion of equation 1.23 [23, 26]. This indicates that the GVMD approach provides a phenomenological tool to estimate the higher twist contribution. This is similar to the way the target mass corrections are estimated, since their effect, the mass of the target, is known. The biggest advantage of VMD and GVMD models is that they allow us to use our knowledge of hadron-hadron interactions in order to express the F_2 structure functions.

The VMD model structure function F_2 in the most simple form is represented by a sum of the contribution of the vector mesons to which the photon fluctuates [25],

[27].

$$F_2\left(x,Q^2\right) \;=\; \frac{Q^2}{4\pi}\sum_v \frac{M_v^4\sigma_v(s)}{\gamma_v^2(Q^2+m_v^2)^2} \tag{1.26}$$

where $s = W^2$ is the center of mass energy squared of the interaction ($x = Q^2/(s + Q^2 - M^2)$), $\sigma_v(s)$ is the vector meson–nucleon total cross section for the vector meson v, m_v is the mass of the vector meson v and γ_v^2 is related to the leptonic width of the v [25]:

$$\frac{\gamma_v^2}{\pi} = \frac{\alpha^2 m_v}{3\Gamma_{e^+e^-}}. \tag{1.27}$$

If only the finite number of vector mesons is included in the sum (1.26), then the F_2 vanishes as $1/Q^2$ at large Q^2. Therefore, it does not contain the "leading twist" term [23]. The scaling can be introduced by including the infinite number of vector mesons in the sum. This is the Generalized Vector Meson Dominance (GVMD) model [25, 27].

Finally we should note that there are descriptions of the photon–hadron interactions that combine the VMD approach with that of pQCD in order to obtain the behaviour of the structure functions in both small and large Q^2 regions [28]. In this approach the photon interactions have two sources: a VMD photon–hadron interaction mechanism and a partonic mechanism. The partonic component is decomposed into two terms: the "direct" term which reflects the bare photon interactions with the partonic constituents of the hadron, and the "anomalous" term which corresponds to the interactions of the partonic constituents of the photon with the partons inside the hadron. In the latter case the photon coupling to its constituents is point–like. These partonic constituents of the photon correspond to the short lived $q\bar{q}$ fluctuations of the photon that do not have enough time to "dress" like vector mesons (these will be the short formation time states of the VMD description above). The main feature of the partonic mechanism is that it corresponds to the (semi) hard interactions which can be described by perturbative QCD. These highly virtual $q\bar{q}$ states at high Q^2 have small transverse size $\sim 1/Q^2$ and correspond to spatially small colour dipoles. The

reduced color dipole field results in a smaller dipole-nucleon cross-section. This is the idea of the 'shrinking-photon' or 'colour-transparency', which introduces scaling behaviour of the structure function in this mechanism [25]. The VMD part on the other hand contains both hard as well as soft components which cannot be described by perturbative QCD, and its contribution to the structure function is strongly Q^2 dependent (equation 1.26).

1.6 Regge Phenomenology

In the high energy limit Regge phenomenology is used to parametrize the cross sections of two–body scattering as functions of the center of mass energy W of the interaction [29]. The regime where this treatment is applicable is reached when all external masses and momentum transfers are much smaller than the scattering energy. The interaction is described by the exchange of particles, "Regge poles", with the appropriate quantum numbers. The Regge pole exchange is a generalization of the particle exchange; the poles are characterized by the same quantum numbers that identify elementary particles. The Regge poles formally describe poles of the partial wave amplitude in the crossed channel of the interaction in the complex angular momentum plane [23], [12]. The position of each pole is described by a trajectory function $\alpha(t)$, where t is the momentum transfer of the interaction. The value of the trajectory function for $t = 0$ is called the intercept. The Regge pole corresponding to the vacuum quantum numbers is called a pomeron. In the Regge approximation the high energy behaviour of the total cross sections is given by the following expression:

$$\sigma_{tot}(\sqrt{s}) = \sum_i \beta_i s^{\alpha_i - 1} \tag{1.28}$$

where $s = W^2$ is the center of mass energy squared of the colliding hadrons [4], α_i are the intercepts of the Regge poles, and β_i are their couplings [23]. The intercepts α_i are universal quantities, i.e. they are independent of the external particles or currents and depend only on the quantum numbers of the Regge poles which are exchanged in the crossed channel. Phenomenologically the energy dependence of the total hadronic and photoproduction cross sections can be described by two contributions: the (effective) pomeron with intercept α_P=1.08 (isoscalar pole exchange) and the Regge pole with the intercept $\alpha_R \sim 0.5$ (isovector pole exchange) [30].

The small-x regime of lepton-nucleon scattering ($x \to 0$) is the Regge limit for this process, since $x \ll 1 \Rightarrow Q^2 \ll 2M\nu$ (the momentum transfer characteristic for the process is much smaller than the scattering energy). In this limit the Regge parameterization of the total cross sections implies the following parameterization of the electroproduction structure function $F_2(x, Q^2)$ [23]:

$$F_2(x, Q^2) = \sum_i \beta_i(Q^2) s^{\alpha_i - 1} \tag{1.29}$$

In this limit $x \simeq Q^2/W^2$ and $x \ll 1$. Therefore the above parameterization (1.29) implies the following small x behaviour of $F_2(x, Q^2)$:

$$F_2(x, Q^2) = \sum_i \tilde{\beta}_i(Q^2) x^{1-\alpha_i} \tag{1.30}$$

where

$$\tilde{\beta}_i(Q^2) = (Q^2)^{\alpha_i - 1} \beta_i(Q^2) \tag{1.31}$$

If we use the phenomenological parameterization of the total cross section in terms of the pomeron and the isovector (A_2) pole exchange [30], we can rewrite equation 1.30 as $F_2(x, Q^2) \sim A(Q^2) + B(Q^2)\sqrt{x}$, where A is the pomeron contribution and B the A_2 contribution. At low Q^2 the behaviour of functions $\beta_i(Q^2)$ should be defined by

[4] In the case of lepton-hadron scattering this corresponds to the center of mass energy squared of the virtual photon-hadron system, since the virtual photon is viewed through its vector meson fluctuations

the photoproduction limit constraint (equation 1.8), so $\beta_i(Q^2) = O(Q^2)$ for $Q^2 \to 0$ and the F_2 in the low Q^2 region should smoothly join the photoproduction limit, $Q^2 = 0$. In this limit the total photoproduction cross section $\sigma_{\gamma p}(E_\gamma)$ is related to the structure function F_2 with the following expression:

$$\sigma_{\gamma p}(E_\gamma) = \lim_{Q^2 \to 0} 4\pi^2 \alpha \frac{F_2}{Q^2} \tag{1.32}$$

This limit should be taken at fixed $\nu = E_\gamma$ where $E_\gamma = \nu$ is taken as photon energy in the laboratory frame.

In the Regge limit the function $F_2^p - F_2^n$ is controlled by the A_2 pole exchange, since the pomeron contribution to the F_2 should be flavor independent. This interpretation, in a parton model picture of the structure functions, corresponds to the postulate that in the limit $x = 0$ the only contribution to the structure function difference is the valence quark contribution because of the light flavor symmetry of the sea. [5]. Thus, the difference $F_2^p - F_2^n$ should vanish in the limit $x = 0$ (for fixed Q^2):

$$F_2^p - F_2^n \sim x^{1-\alpha_{A_2}} \tag{1.33}$$

where $\alpha_{A_2} \approx 0.5$ is the A_2 reggeon intercept.

1.7 Electroweak Radiative Corrections

The structure function F_2 is defined in the single photon exchange approximation for charged lepton-nucleon scattering through the expression for the hadronic tensor $W^{\mu\nu}$ (equation 1.4). The F_2 can be extracted from the measurement of the inclusive cross-section in the above approximation; $\sigma_{1\gamma}$ given by equation 1.9. However, the experimentally measured cross-section, σ_{meas}, includes the contribution of all the higher order Quantum Electro-Dynamic (QED) processes beyond the Born level diagram of single photon exchange. In addition, the lowest order (Born level) electroproduction

[5] The Regge behaviour should reflect the parton model high-Q^2 interpretation of the F_2 [12].

cross section also has a contribution from the Z^0 boson exchange. This contribution cannot be separated experimentally from the single photon exchange contribution so it must be calculated. Since in the kinematic range covered by E665 the involved virtualities (Q^2) are small compared to the Z^0 mass squared, we will ignore the Z^0 contribution in the following discussion. Let us now concentrate on the experimentally measured cross-section σ_{meas}, and those higher order QED processes whose contribution has to be eliminated in order to obtain $\sigma_{1\gamma}$ and extract the F_2 structure function.

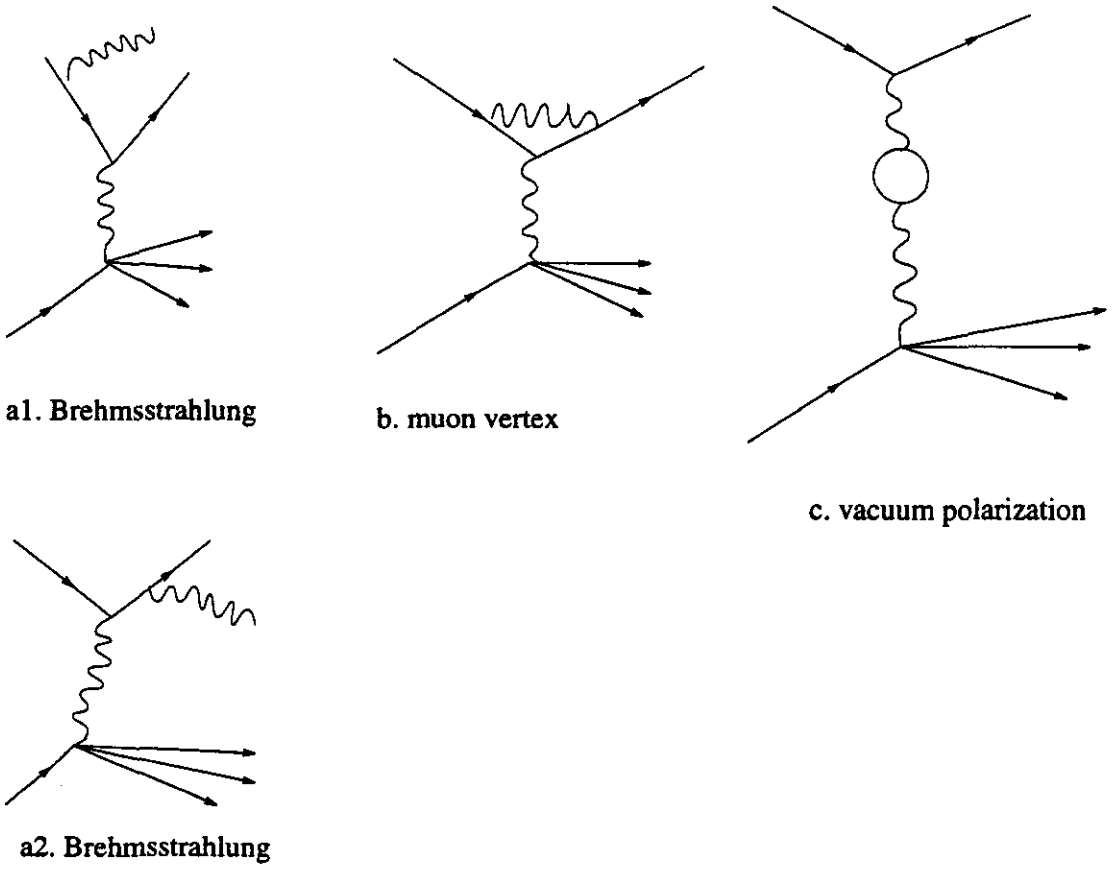

Figure 1.7: Electroweak radiative correction diagrams.

To simplify the discussion we will consider only the most important next-to-leading

order diagrams (order α^3). These diagrams are shown in figure 1.7[6]:

- the muon bremsstrahlung diagram, from either the incoming ($a1$) or the outgoing ($a2$) muon
- the muon vertex correction diagram (b)
- the vacuum polarization diagram (c)

The cross-section σ_{meas} now reads:

$$\sigma_{\text{meas}} \propto \|a0\|^2 + \|a1 + a2\|^2 + 2 \times Re\,[a0 \cdot (b^* + c^*)]$$

where $a0$ is the Born level amplitude. The two last terms of this equation are ill defined. All diagrams contain infrared divergences and diagrams b and c also contain ultraviolet divergences. The infrared divergences come from the fact that the bremsstrahlung photon is massless ($a1$ and $a2$) and from the limit where the momentum of the loops in diagrams b and c goes to zero. The ultraviolet divergences come from the limit where the momentum of the loops in diagrams b and c approaches infinity. Since the measured total cross-section is finite, these divergences have to cancel. The ultraviolet divergences cancel among the loop diagrams. Part of the infrared divergences of $a1$, $a2$ cancels the infrared divergences of the loop diagrams and the other part can be exponentiated, so that the total measured cross-section can be written:

$$\sigma_{\text{meas}} = K \times \sigma_{1\gamma} + \sigma_{tail} \tag{1.34}$$

These cancelations occur to all orders in α [31]. The correction factor K depends on the energy resolution parameter Δ, which is defined by our ability to resolve the emitted photon. A realistic detector has finite energy resolution Δ, which means that

[6]The other diagrams of order α^3 in the cross-section are suppressed compared to those described above. These suppressed contributions are from the target bremsstrahlung diagram, the hadron vertex correction diagram and the double-photon exchange diagram.

it cannot differentiate between single-photon exchange and the case where an extra photon with energy, $E_\gamma < \Delta$ was emitted. Thus, K contains the contribution of soft photon emission to the single-photon exchange cross section as seen by a detector with finite energy resolution. The total cross section does not depend on Δ, since σ_{tail} also depends on Δ (Δ defines what is hard and what is soft radiation).

The above interpretation leads to the conclusion that an experiment cannot measure $\sigma_{1\gamma}$ directly, since even when the final state can be completely reconstructed, the experimental resolution on the photon energy will require calculation of the K factor [7]. The effects of the higher order QED corrections account for a large fraction of the measured cross section, especially in the low x and high y region. There is a commonly used approach to eliminate this contribution, the description of which follows. Since the complete reconstruction of the final state is very difficult for practical applications, the kinematics are determined from the inclusive measurement of the incident and scattered lepton. Of course, this leads to the wrong interpretation of the measured event kinematics for radiative events. For example, any elastic scattering event accompanied by the emission of an energetic bremsstrahlung photon can be mistaken for an inelastic event, contributing to the measured cross-section at the reconstructed kinematic point. An inelastic event accompanied by radiation contributes to the cross-section at an *apparent* value of the kinematic variables that is different from the *actual* one. This can be seen schematically in figure 1.8, where the shaded triangle represents all the possible *actual* values of the kinematic variables that can contribute to an event measured with *apparent* kinematics $A(\nu, Q^2)$. The boundaries of this region are set by the elastic scattering constraint and the requirement that the radiated photon has a realistic emission angle ($\cos\theta_g$ between ± 1). To eliminate these effects the measured differential cross section is multiplied by a theoretically calculated correction factor. This is called a radiative correction procedure and the

[7] Strictly speaking $\sigma_{1\gamma}$ is only theoretically defined; the probability P to emit a photon with energy $E_\gamma \to 0$ is $P \to \infty$

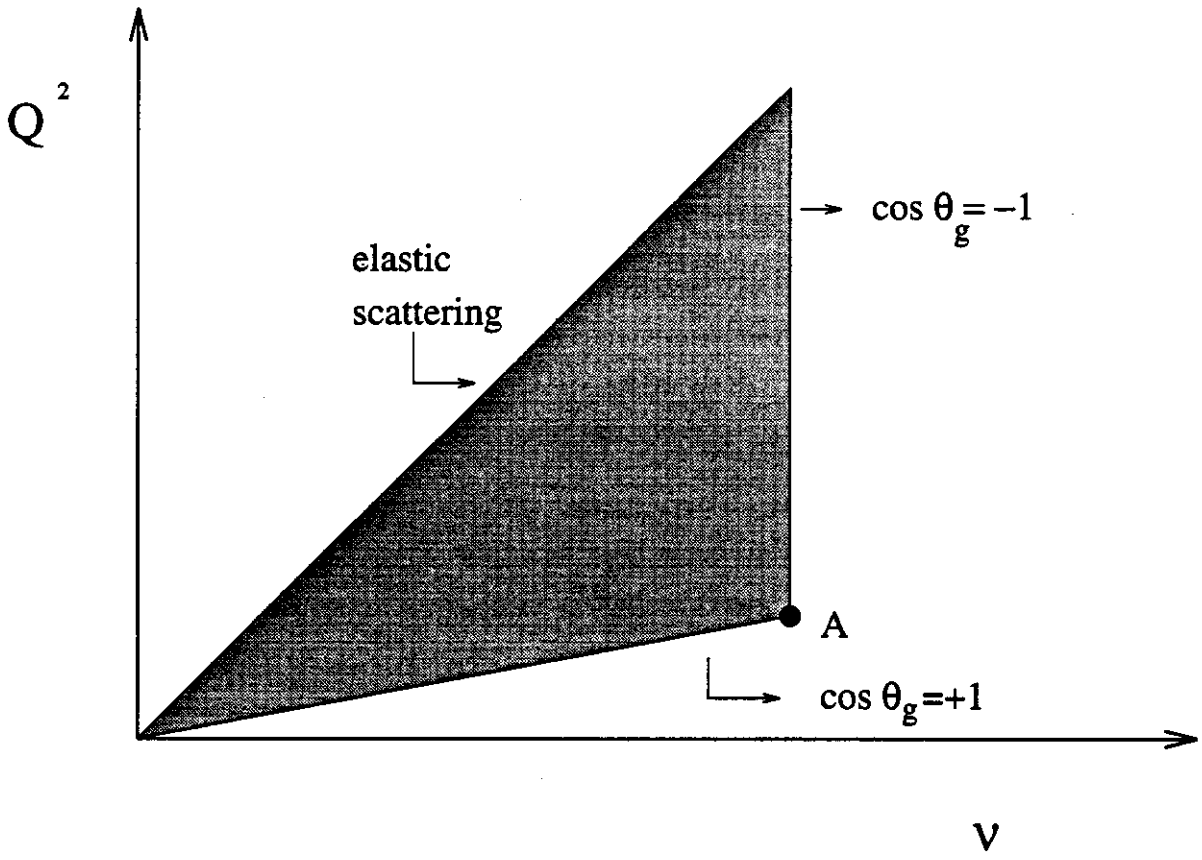

Figure 1.8: Radiative tail contribution to a measurement at an apparent Q^2, ν point.

radiative correction factor $\eta(x,y)$ is defined simply as the ratio of the calculated cross-sections: $\eta(x,y) = \frac{\sigma_{1\gamma}}{\sigma_{meas}}$. In general, for lepton-nucleus scattering the σ_{tail} term of equation 1.34 decomposes into three parts: $\sigma_{tail} = \sigma_{inelastic} + \sigma_{quasielastic} + \sigma_{coherent}$. The inelastic radiative tail corresponds to inelastic scattering from a nucleon, the quasielastic term corresponds to elastic scattering from a nucleon, and the coherent term to elastic scattering from the whole nucleus. All three contributions are accompanied by radiation. To calculate the first contribution the inelastic structure functions must be known, to calculate the second contribution the nucleon form factor is needed and to find the third contribution the form factor of the nucleus is needed.

1.8 Phenomenology of nuclear effects in the Deuteron at small-x

The determination of the quark structure of the nucleon is one of the most fundamental issues of both theoretical and experimental high energy physics. The deep inelastic scattering (DIS) of leptons from hydrogen has provided a wealth of information about the structure of the proton. However, in the absence of free neutron targets deuterium has been used in order to extract data on the neutron structure functions. Since the deuteron is a weakly bound nucleus, traditionally nuclear effects have been ignored in the treatment of DIS deuteron results (apart from Fermi motion corrections at high x). If such effects are present, the determination of nucleon parton distributions based on the nuclear/deuteron (or nucleon/deuteron) structure function ratios at small x may have to be modified. This includes the determination of the Gottfried sum rule, which is related to the question of flavour symmetry violation in the nucleon sea. A precise knowledge of the neutron structure function, F_2^n, is essential for the determination of the sum rule. Also, the extraction of information about nuclear effects in heavy nuclei as compared to a free nucleon is sensitive to nuclear effects in the deuteron, since in these measurements deuterium is used to represent

the isoscalar free nucleon combination.

1.8.1 Shadowing

The total lepton-deuteron cross section has been assumed to be the sum of the lepton-proton and lepton-neutron cross sections (apart from Fermi motion corrections at high x). The deviation from this simple relation, for any nucleus, in the region of small Bjorken x ($x \lesssim 0.1$) is known as nuclear shadowing. Experimentally nuclear shadowing has been observed as a deviation from unity in the the ratio of structure functions for lepton scattering from a heavy nucleus and from deuterium [32]. These results and corresponding later measurement [33], [34] showed a big decrease in the nuclear structure function per nucleon in the small x region, "shadowing" that was only weakly dependent on Q^2. The nuclear shadowing for heavy nuclei has been observed both in the low Q^2 (including photoproduction) and in the large Q^2 region.

Shadowing is expected to be a low x phenomenon. This can be understood in terms of the space–time picture of the interaction of the virtual photon with the nucleus [35]. Consider a nucleus with A nucleons having momentum p_A. In the infinite momentum frame where the momentum of the nucleons is very large $p = p_A/A$, the partons occupy longitudinal distances on the order $\Delta z_p \approx \frac{1}{xp}$. The nucleus in this frame occupies the Lorentz contracted distance $\Delta z_A \approx 2R_A\frac{M}{p}$, where R_A is the nuclear radius and M the nucleon mass. The average distance between the nucleons in this frame is $\Delta z = r\frac{M}{p}$, where r is the average distance between nucleons in the nucleus rest frame. We can identify three regions in x [23]:

- $x > \frac{1}{Mr} \Rightarrow \Delta z_p < \Delta z$. This region corresponds to the case where the partonic size is smaller than the average internucleon distance in the nucleus. In this region the shadowing is expected to be negligible since the partons exist within individual nucleons.

- $\frac{1}{2MR_A} < x < \frac{1}{Mr} \Rightarrow \Delta z_A > \Delta z_p > \Delta z$. This region corresponds to the longitudi-

nal size of the partons being larger than average distance between nucleons yet smaller than the longitudinal size of the nucleus. Here shadowing is expected to gradually set in with decreasing x.

- $x < \frac{1}{2MR_A} \Rightarrow \Delta z_p > \Delta z_A$. Here the partonic size is larger than the longitudinal size of the nucleus, thus shadowing is expected to be maximal.

In the last two regions the partons can no longer be regarded as belonging to individual nucleons since their longitudinal distances are larger than the average distances between nucleons, eventually exceeding the size of the nucleus. If we view lepton-nucleus inelastic scattering through the photon wavefunction fluctuations to vector meson states, the above regions can be defined through the relative size of the lifetime of the $q\bar{q}$ fluctuation of the virtual photon, $t_\gamma = \frac{1}{Mx}$ (see equation 1.25), and the characteristic distances r for the nucleon and R_A for the nucleus. From these we can see that nuclear shadowing again appears to be controlled by x; it is a small x phenomenon since $1/(Mr) \approx 0.1$.

1.8.2 Shadowing models

There are many models in the literature that attempt to explain shadowing for heavy nuclei. In this section we will describe some ideas that concern shadowing in the deuteron (some of these ideas are specific to the deuteron, some are inspired from more general shadowing models).

The lepton-deuteron inelastic cross section is related to the forward $\gamma^* D$ scattering amplitude via the optical theorem. In the impulse approximation the virtual photon interacts with only one of the nucleons in the nucleus. Of course, the total cross section receives a contribution from the double scattering diagram, in which both nucleons participate in the interaction. This contribution is the origin of the shadowing in a nucleus. Different models for shadowing correspond to different assumptions for the manifestation of the photon interaction, and also to different structural details for

the double scattering diagram.

In the region of low Q^2 (and for photoproduction) the natural mechanism for viewing nuclear shadowing is the multiple scattering of vector mesons in the nucleus. The vector mesons couple to either virtual or real photons and the interaction is described through the interaction of these vector mesons with the target (see equation 1.26). This model gives the following contribution from shadowing to the deuteron structure function F_2^D [23]:

$$\delta F_2^D = \frac{Q^2}{4\pi} \sum_v \frac{M_v^4 \delta\sigma_v^D}{\gamma_v^2 (Q^2 + M_v^2)^2} \tag{1.35}$$

where the cross section $\delta\sigma_v^D$ is the part of the vector meson – deuteron total cross section σ_v^D (normalized to a nucleon) which corresponds to multiple scattering:

$$\sigma_v^D = \sigma_v^N - \delta\sigma_v^D. \tag{1.36}$$

where σ_v^N is the vector meson – nucleon total cross section. The cross section which corresponds to multiple scattering can be obtained from the Glauber theory [36, 25]. The contribution of the double scattering process can be calculated using the Glauber formalism for hadron-deuteron scattering. The Glauber expansion of the cross-section gives the total vD cross section as a sum of the vN cross sections and a screening term arising from the double scattering off of both nucleons. The incident vector meson v scatters elasticaly on the first nucleon and then inelasticaly on the second. The phase of the amplitude for the first interaction at high energies is imaginary. This two–step amplitude is coherent and opposite in phase to the one–step amplitude where only one nucleon interacts. These arguments explain the negative sign of the term $\delta\sigma_v^D$ in equation 1.36. Formally the forward double scattering amplitude is given by [10], [37]:

$$\delta\mathcal{F}_{vD} = \frac{i}{2\pi|\mathbf{q}|} \int d^2\mathbf{k}_T \; S_D(\mathbf{k}^2) \; \mathcal{F}_{vp}(\mathbf{k}^2) \; \mathcal{F}_{vn}(\mathbf{k}^2), \tag{1.37}$$

where $\mathbf{q}$ is the momentum of the projectile, $\mathcal{F}_{vN}$ is the vector meson-nucleon scattering amplitude ($\mathrm{Re}\mathcal{F}_{hN} \ll \mathrm{Im}\mathcal{F}_{hN}$) and $S_D(\mathbf{k}^2)$ is the deuteron form factor. From the

optical theorem, $\sigma = \frac{4\pi}{|\mathbf{q}|}\,\mathrm{Im}\mathcal{F}$, we obtain

$$\delta\sigma_{vD} \;=\; -\frac{\sigma_{vN}^2}{8\pi^2}\int d^2\mathbf{k}_T\; S_D(\mathbf{k}^2) = -\delta\sigma_v^D \tag{1.38}$$

where $\delta\sigma_{vD}$ is the Glauber calculated double scattering contribution to the cross-section ($\delta\sigma_v^D$ in equation 1.36 is a positive defined term).

It follows from eq.(1.35) that the shadowing term which corresponds to the multiple rescattering at finite number of vector mesons has a strong Q^2 dependence and vanishes for large Q^2. If an infinite number of vector mesons is included in the sum, this together with the interference terms makes the Q^2 dependence much milder [26].

In the region of large Q^2 the parton model is expected to be applicable. In the parton model description of the forward $\gamma^* D$ scattering amplitude the photon has a point–like coupling to partons. This virtual Compton scattering on the deuteron can be expressed in terms of a multiple interaction series which includes the possibility of partons from different nucleons interacting with each other during the scattering process. The nuclear shadowing in the large Q^2 region may come from this multiple interaction term that includes partons from both nucleons. Different models for shadowing have different approaches for describing this term. A review of such models can be found in reference [33]. One description comes from the ideas of the parton recombination models [38, 39, 40]. There are two approaches that lead to shadowing using the parton recombination ideas. The first approach uses radiatively produced partons, and the fusion of quarks and gluons from different nucleons which introduces additional terms in the Altarelli-Parisi equations governing the QCD evolution of the parton distributions [39]. The second approach uses the recombination of partons in the initial state, which alters their momentum distributions [40]. An alternative description of the double interaction mechanism in the high energy limit can be given in terms of Pomeron ($\mathcal{P}$) exchange. If the momentum transfer between the photon and nucleon is small, the nucleon will most likely remain intact, in which case there will only be exchange of vacuum quantum numbers [10]. The virtual photon probes

the parton structure of the Pomeron, which is parametrized by the Pomeron structure function $F_{2\mathcal{P}}(x) \equiv \frac{Q^2}{4\pi^2\alpha}\sigma_{\gamma^* p}$. [41, 42] (defined in terms of the cross section for γ^*–Pomeron diffractive scattering).

There is another potential source of nuclear effects at high Q^2, that of the double scattering mechanism which involves the meson degrees of freedom of the nucleon [10]. In these models the physical nucleon state is expanded in a series that contains two-particle meson-baryon states in addition to the bare nucleon. These models lead to antishadowing corrections to F_2^D.

Finally, there are several models of shadowing that incorporate more than one of the above ideas (usually the VMD plus one of the partonic mechanisms and meson exchange), see [43, 10, 44] and also [33] for a review of shadowing models. In these models the VMD contribution is dominant at low Q^2, while the contributions from parton recombination and meson exchange have competing contributions as Q^2 increases.

1.9 Structure Function Ratio and Experiment

Within the framework of pQCD the measurement of the structure function ratio F_2^n/F_2^p is used to constrain the parton distribution functions when extracted from global structure function analyses. It is also used in the determination of the Gottfried sum rule 1.20, in order to minimize the systematic errors in the construction of the structure function difference that enters the sum rule. The Gottfried sum rule carries important information about the symmetry of the light flavor quark sea in the nucleon. Most of the contribution to the sum rule comes from the low-x values of the structure function difference, since it is weighted with $1/x$. In addition, the small-x value of the ratio contains information about shadowing effects in the deuteron.

In order to address the above issues, high precision/large statistics measurements of the ratio have been performed with both electron and muon beams at SLAC and

at CERN:

- SLAC experiments (e beam) [16]. The kinematic range covered was $0.5 < Q^2 < 30GeV^2$ with $x > 0.06$.
- BCDMS (μ beam) [8]. The kinematic range covered was $8.0 < Q^2 < 280GeV^2$ with $x > 0.06$.
- EMC experiment (μ beam) [7]. The kinematic range covered was $0.2 < Q^2 < 100GeV^2$ with $x > 0.002$.
- NMC (μ beam) [45, 46]. The kinematic range covered was $0.1 < Q^2 < 190GeV^2$ with $x > 0.002$.

These measurements are in good agreement, showing that the ratio is increasing with decreasing x, approaching but not reaching unity [8]. The logarithmic Q^2 dependence of the ratio has also been studied [45], showing negative slopes for $x > 0.1$ and no dependence for $0.004 < x < 0.1$. The results from NMC reach the lower x values and have very small systematic errors since this experiment was designed to measure the ratio by taking data with a complementary target system [45], thus reducing normalization and efficiency induced uncertainties. NMC defined $F_2^n/F_2^p \equiv 2(F_2^d/F_2^p) - 1$ and no nuclear corrections were applied (neither shadowing at small-x or Fermi motion at high-x). The values obtained are below unity, reaching $F_2^n/F_2^p = 0.976 \pm 0.017$ at the lowest x bin ($0.004 < x < 0.010$) [46]. Using the ratio measurement and the structure function F_2^d parameterization taken from a global fit [47] NMC measured the Gottfried integral 1.20, expanding the structure function difference as $F_2^p - F_2^n = 2F_2^d(1 - F_2^n/F_2^p)/(1 + F_2^n/F_2^p)$. The value obtained was $S_G(0.004 - 0.8) =$

[8]The SLAC results show some disagreement when plotted as a function of x with Q^2 averaged. This is understood as a smooth Q^2 dependence of the ratio at the higher x values, $x > 0.1$, explained by differences in the pQCD evolution and the higher twist contribution between the proton and the neutron structure functions

$0.221 \pm 0.008 \pm 0.019$, at a fixed Q^2 value of $4GeV^2$. For the unmeasured region $x > 0.8$, a smooth extrapolation of the measured points to the value of 0.25 at $x = 1$ was used, resulting in a contribution of 0.001 ± 0.001 to the sum rule. For the unmeasured region $x < 0.004$, a Regge inspired extrapolation was used, $F_2^p - F_2^n = \alpha x^\beta$. This form was fitted to the data resulting in $\alpha = 0.20 \pm 0.03$ and $\beta = 0.59 \pm 0.06$. These values were used to obtain the low-x contribution to the sum rule (0.013 ± 0.005). The final result of $S_G = 0.0235 \pm 0.026$ indicates violation of the sea flavor symmetry in the nucleon. Fermi motion effects are not expected to affect the sum rule. Also the fact that the Regge inspired fit is very close to the Regge theory expectation for free nucleon structure functions indicates that in the NMC regime there are no significant shadowing effects. Nuclear shadowing effects will lead to smaller $S_G(Q^2)$ than that determined experimentally assuming no shadowing [48, 43].

The above results show the importance of the structure function ratio at even smaller values of x than those previously measured. NMC is limited by the presence of the large muon-electron elastic background (muons scattering off of the atomic electrons of the target). Fermilab experiment 665 with electron identification using an electromagnetic calorimeter, and with specially designed low-x triggering, a higher energy muon beam and a target setup designed to reduce the systematic uncertainty of the ratio (see chapter 2) can probe this lower x region ($0.000001 < x$) with high precision [9].

At that point we should also mention another measurement relevant to the structure function ratio determination. In order to extract the structure function F_2 from the single photon exchange cross-section, information about R is needed (equation 1.11). From the form of expression 1.11 it can be seen that the single photon exchange cross-section ratio is equal to the structure function F_2 ratio if R is independent of the nuclear environment. The difference $R^p - R^d$ has been measured by [50, 51, 52]

[9] A measurement from an earlier run of E665, with no dedicated target setup [49], had low statistics and large systematic error and could not resolve any deviations of the ratio from unity

and the results show that this quantity is consistent with zero and that there is no x dependence.

Chapter 2

The E665 Experimental Apparatus

2.1 Introduction

The Fermilab Experiment-665(E665) was an open geometry, fixed-target muon-nucleon scattering experiment installed in the New Muon Laboratory, which was located at the end of the NM beamline of the Fermilab Tevatron. The location of the NM beam line in the fixed target area of the Fermi National Accelerator Laboratory (FNAL) is shown in figure 2.1. The main goal of the experiment was to study structure functions, structure function ratios and hadron production in inelastic muon scattering from various targets. The E665 experimental apparatus has been described in detail in references [9] and its upgrades in references [53], [54], [55], [56], [57]. It consisted of a beam spectrometer used to identify and momentum analyze the incoming muons (beam muons) and a forward spectrometer used to reconstruct the final state of the interaction. In the following discussion, the detectors and the detector related issues that were directly related to this analysis will be described.

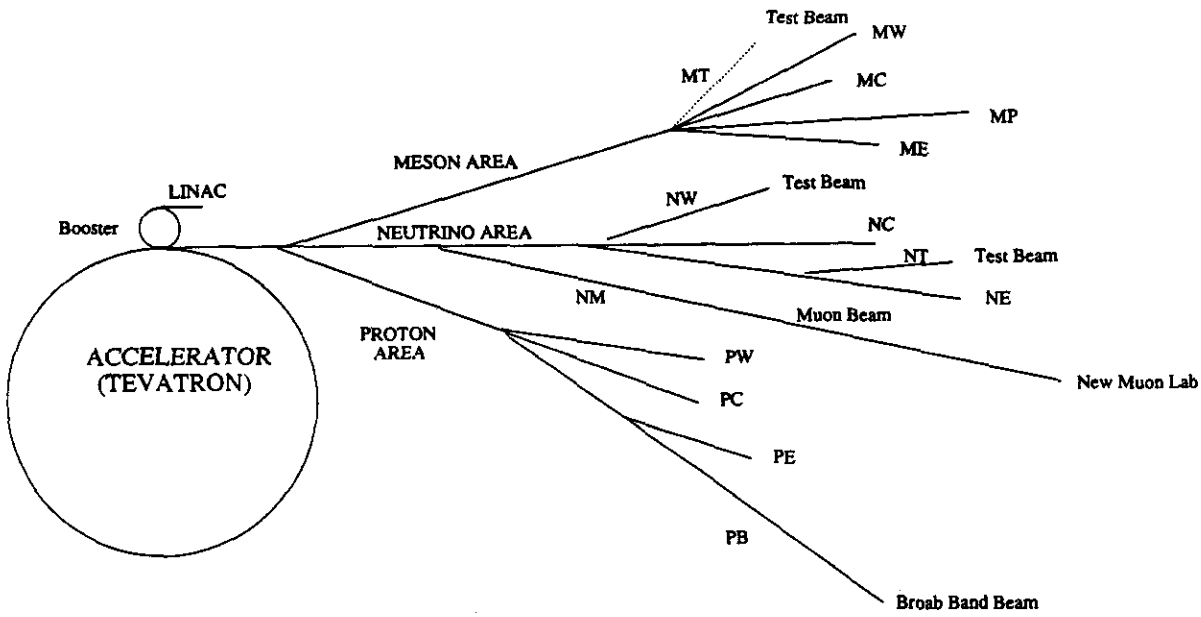

Figure 2.1: Fixed target areas at FNAL.

2.1.1 E665 Coordinate System

The global coordinate system of E665 was a right-handed Cartesian system with the X-axis defined along the direction of the muon beam. The Y-axis was defined on the horizontal plane, with Y increasing towards the left hand side, as one travels in the direction of the incoming beam. The Z-axis was defined as the perpendicular direction relative to the X-Y plane, with Z increasing with increasing altitude. The center of this coordinate system was nominally defined to be the center of the Chicago Cyclotron Magnet(CCM), the most upstream of the two forward spectrometer dipole magnets. The two powerful analysis magnets had the magnetic field along the Z-direction thus bending the charged particles only in the Y direction. For track reconstruction, the X-Y plane was then referred as the bending plane and X-Z plane was the non-bending plane.

The local coordinate system of each detector was described by a spatial vector $\vec{\Theta}$, which was defined to be perpendicular to the measuring elements, along the measuring

direction. The vector $\vec{\Theta}$ was expressed, in radians, in the global coordinate system using the rotation angles (α, β, γ) about the X-axis and two other axes, defined to be orthogonal in the plane of the the detector. The angle α was defined to be $\alpha = \pi/2$ for a chamber with vertical wire orientation; such a chamber measures the Y direction, so it was called a Y chamber. Chambers with wires aligned along the horizontal direction had $\alpha = \pi$ and measured the Z coordinate; these were the Z chambers. Chambers which were rotated with a positive angle from the vertical were called U chambers and those rotated with a negative angle were called V chambers.

2.2 The NM Beamline and the Beam spectrometer

2.2.1 NM Beamline

The beam spectrometer was located at the end of the NM beam line [58], which is shown in figure 2.2. The muons used by E665 were produced from the decay of secondary pions and kaons that originated from the interaction of primary 800 GeV protons with a beryllium target [9]. The protons were extracted from the FNAL Tevatron (a synchrotron with a diameter of 2km). Beam extraction lasted for was 23 seconds (one accelerator "spill"), during each 59 seconds, period of the accelerator "cycle", with about 4×10^{12} protons delivered per spill into the NM beam line. The secondary mesons and the non-interacting primary protons were momentum selected by a pair of dipole magnets. The protons were dumped in an absorber, while the selected mesons were transported through a 1.1km beamline with a succession of focusing and defocusing quadrupole magnets (FODO). In the transport line $\sim 5\%$ of the mesons decayed to produce muons. The muons remained in the transport line, while the hadrons that did not decay were absorbed in a beryllium absorber, located at the end of the 1.1km beamline. Downstream of the beryllium absorber

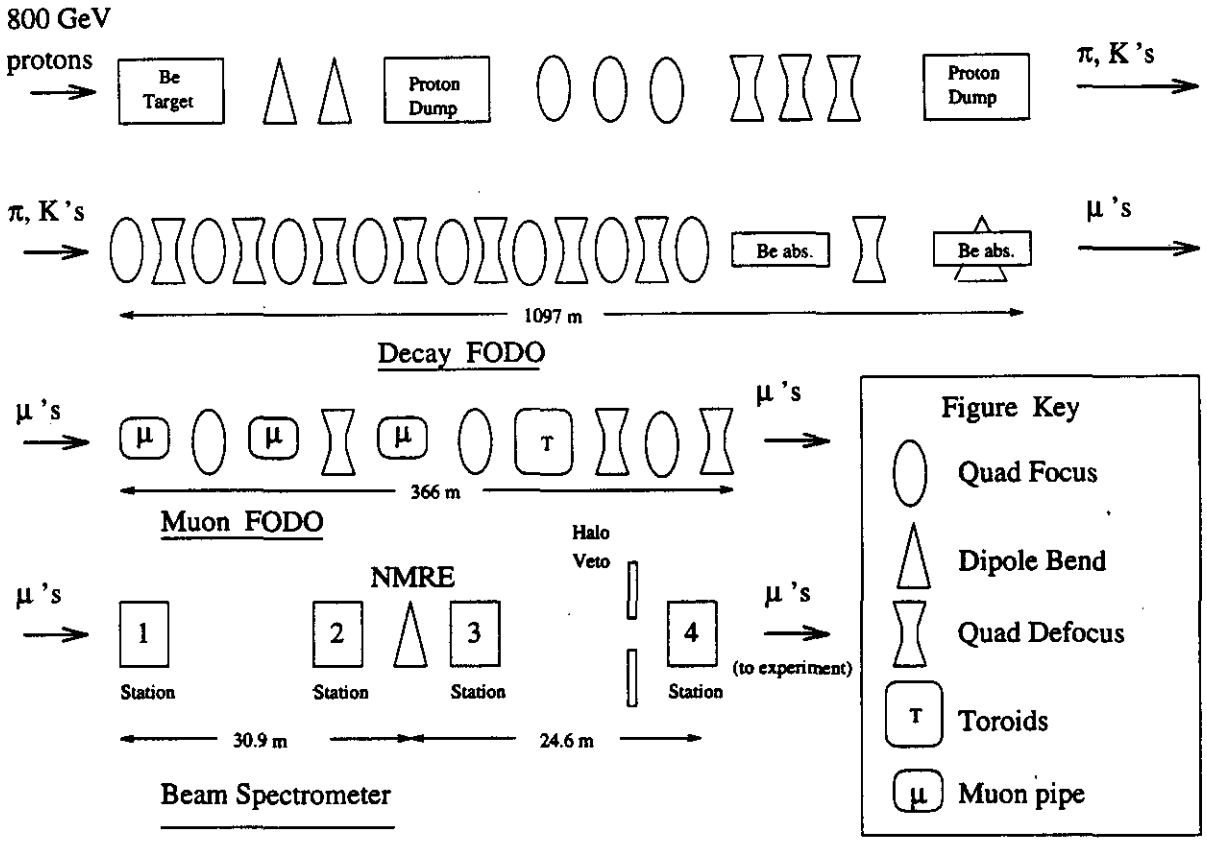

Figure 2.2: Schematic view of NM Muon beamline.

the phase-space of the transported muons was defined by a special magnetized steel pipe installed around the beam pipe. The result was that the number of muons that were not going to hit the experimental target ("halo muons") was reduced to a total of $\sim 20 - 30\%$ of the useful beam. The incident muon flux, the mean energy and the beam profile depended on the beam line momentum tune. During the Fermilab fixed-target-run of 1991 the average energy of the beam selected by the experimental triggers was $\sim 470 GeV$. The spatial transverse size of the beam was approximately 4cm in Z and 6cm in Y. The average incident muon flux was 1.7×10^7 muons per spill.

The secondary hadrons, as well as the decay muons, maintained the 53.1 MHz radio frequency (RF) structure of the accelerating voltage for the protons in the Tevatron. As a result, the muons were separated in 18.8 ns time intervals, with a jitter of 1 ns. This timing information was part of the experimental trigger logic. The occupation of these 18.8 ns time intervals, called "buckets", depended on the beam intensity. For normal experimental conditions about 1.3% of the RF buckets were occupied by muons; very few buckets contained more than one muon. At peak rates the RF bucket occupancy was $\sim 4.0\%$ and about 20% of the occupied buckets contained more than one muon. The apparatus was designed to accomodate this situation.

2.2.2 Beam Spectrometer

Before entering the experimental hall, the beam muons were tagged and momentum analyzed by the 55.5 meter long Muon Beam Spectrometer (figure 2.2). The beam spectrometer consisted of four stations of multi-wire proportional chambers (MWPC) and scintillator planes, and a dipole magnet which was referred to as NMRE. Two of the MWPC stations were upstream and two were downstream of NMRE. The magnet was nominally operated at 3350 amps, which corresponded to an effective P_t kick of 1.541 GeV, [59], see also section 3.2. The beam spectrometer wire chambers, referred

as PBTs, had a fine wire spacing of 1 mm. Each PBT detector had six planes that were organized into two independent (gas, high-voltage) sub-stations [9]. Each substation had three planes with different wire orientations: horizontal (Z), vertical (Y) and inclined (U or V). The sensitive area of the horizontal and vertical planes was 12.8 cm $\times$ 12.8 cm and of the inclined planes was 6.4 cm $\times$ 6.4 cm. The scintillator hodoscopes of each beam station (SBT) were aligned on both the vertical and horizontal planes, except for the second station which had only one horizontally aligned plane. All SBT planes consisted of thirteen small counters graded in width (except for the Z plane of the first station), in order to have an approximately equal rate per counter. The signals from these hodoscopes were used in the experimental trigger logic; they also provided the timing information to mask the PBT hits from beam tracks that were out-of-time (beams other than the one that caused the interaction to occur). Two beam halo monitoring systems, SVJ and SVW, were employed to detect the halo muons. The SVJ hodoscope was used for the halo that was very close to the muon beam, while the SVW, with larger scintillators than those of the SVJ, was used for the halo muons that were spread over a wider area. The in-time response from these two scintillator hodoscopes were used to veto the experimental triggers.

2.3 Targets

The target system setup for the 1990 and 1991 run periods was different than the original design for the experiment [9]. The new target system [60], [55], was an automatically controlled motorized stand [61], capable of holding three cryogenic liquid targets and a number of solid disc targets. During the 1991 running period only the cryogenic liquid targets were used for physics data taking. Figure 2.3 shows the schematic (not to scale) of the 1990/91 target setup. These targets were liquid hydrogen (H_2) and deuterium (D_2) and an evacuated vessel (the empty, or "MT" target) which was identical to the vessels of the two liquid targets. These three

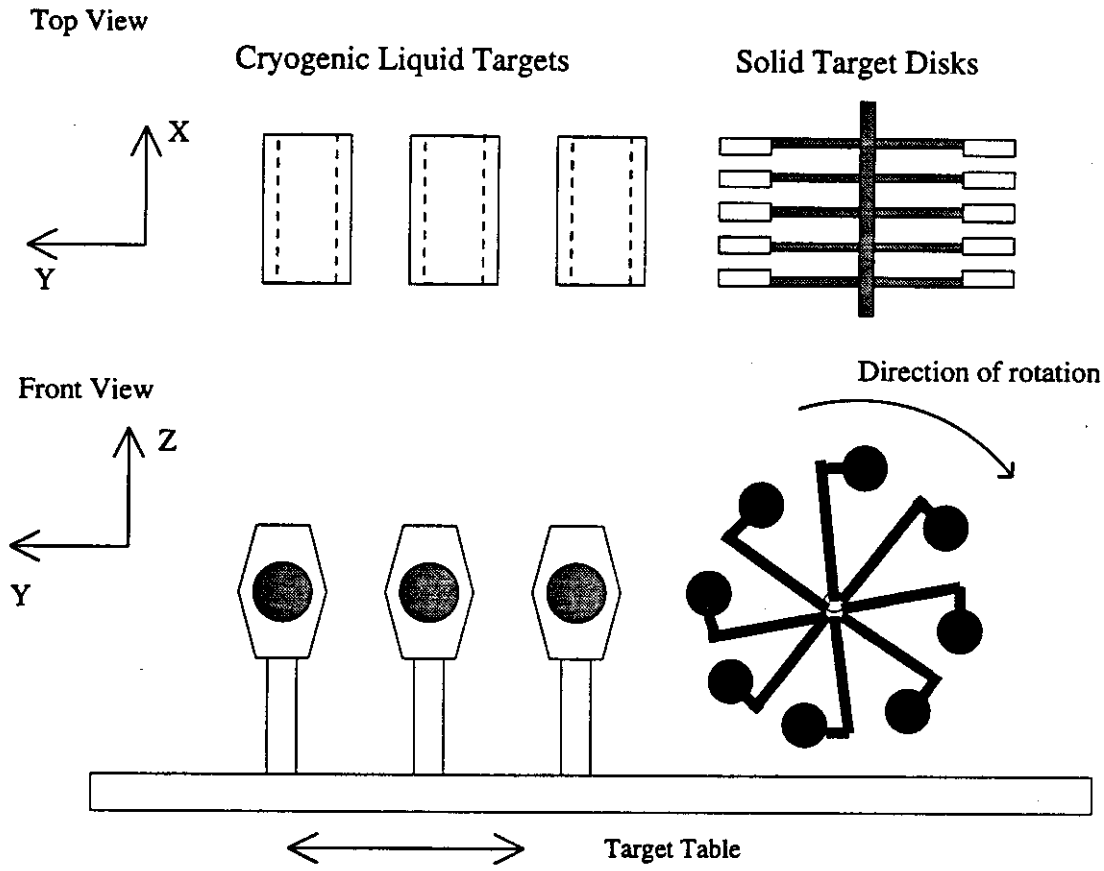

Figure 2.3: The E665 1990/91 target system.

targets were cycled into the beam at a rate such that each target was illuminated for the time period of a few accelerator spills before the next target was cycled into the beam. In each complete cycle, the number of spills for which each target was placed into the beam was 4, 2 and 1 for H_2, D_2 and MT respectively. Since the cycling period was very small compared to the expected time scale of time-dependent systematic effects, the target cycling greatly reduced the systematic error of the ratio measurement. The data from the empty target were used to subtract on a statistical basis the effect of the out-of-target scatters (chapter 4). The information of which target was in position for each spill was recorded on tape, as was the information about the condition of each target(pressure).

2.4 The E665 Vertex and Forward Spectrometer

The vertex and forward spectrometer of E665 (shown in figure 2.4) was an open geometry fixed-target spectrometer, built around two large aperture superconducting dipole magnets . These two magnets were operating with opposite polarities and with the field integral for each magnet set to be inversely proportional to the distance of the magnet from the front of the Muon Detection System. The result of this arrangement was that the position of the scattered muon on the front of the Muon Detection System was independent of the muon energy and depended only on the scattering angle (focusing condition). This condition was used in the design of the muon triggers of the experiment [9].

The first magnet, the CERN Vertex Magnet(CVM), was located immediately downstream of the target system and contained the Vertex Drift Chamber (VDC) centered in the one meter gap between two magnet poles [53], [55], [56]. The purpose of the VDCs was to improve the vertex resolution and reconstruct low momentum tracks. The CVM had a nominal operating current of 5000 amps with a corresponding field of 1.5 Tesla (P_t kick 2.60 GeV/c). The aperture of the magnet

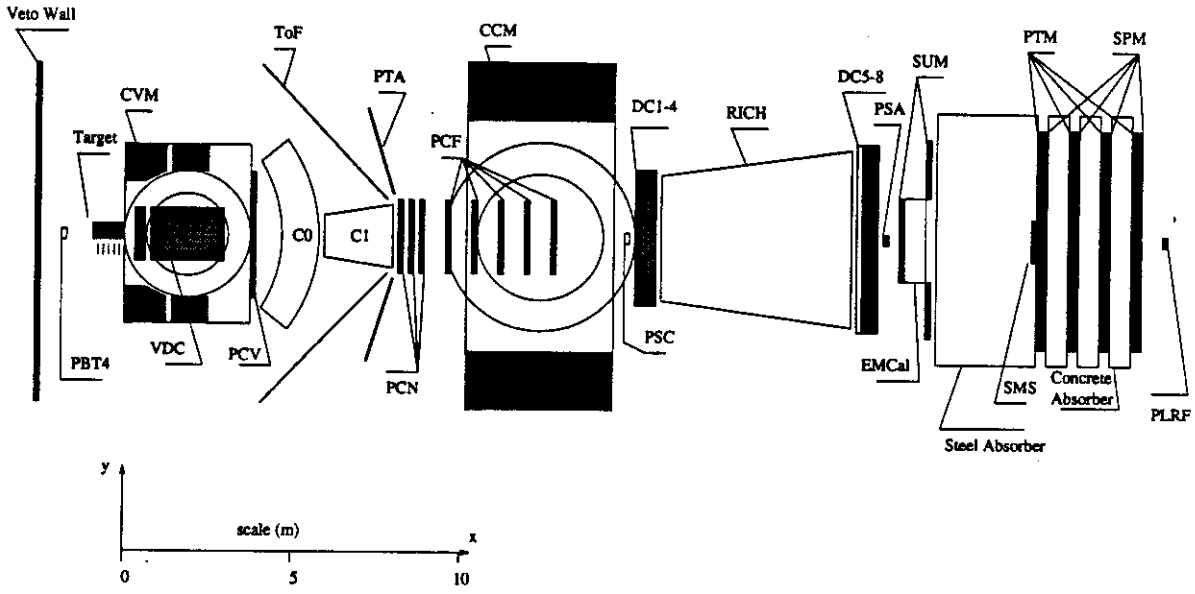

Figure 2.4: E665 Experimental Apparatus, Vertex and Forward Spectrometer.

was 2.0 × 1.0 meters ($Y \times Z$). The detectors located downstream the CVM magnet were the PCV and PC MWPCs, the TOF (Time-Of-Flight) hodoscope, and the PTA proportional tubes. The PCV information was very important in matching the tracks reconstructed in the VDCs with the rest of the spectrometer. The second magnet was the Chicago Cyclotron Magnet(CCM) which operated at 750.0 amps, with a corresponding field of 1.5 Tesla (P_t kick -4.06 GeV/c). The aperture of the magnet was 3.0 × 1.2 meters ($Y \times Z$). The PCF MWPCs were located inside the CCM, providing the most important measurement for the determination of the curvature of the track. Downstream of the CCM there were eight drift chamber (DC) planes. The central region of the DC was deadened and it was covered by the small multi-wire proportional chambers PSC and PSA. The PSC was very unstable during the 1991 run period so it was not used in the reconstruction of the 1991 data. Downstream of the PSA MWPC was the SSA hodoscope, which was installed before the 1990/91 data taking period and was used in the muon trigger logic [57]. The information from the DCs/PSA was very important to match the muons found in the Muon Detector with the corre-

sponding Forward spectrometer track and improved the momentum resolution of the reconstructed muon by a more than a factor of two. Downstream of all the tracking detectors, and just upstream of the iron hadron absorber was the electromagnetic calorimeter (the calorimeter is described in the next section). The Muon Detector was located downstream of the 3 meter thick iron hadron absorber ($\sim$ 18 interaction lengths). The muons, which were the only particles to traverse the iron absorber, were tracked by four stations of proportional wire chambers (PTMs). In between the stations a 91.4 cm thick concrete block provided shielding from electromagnetic showers induced by the penetrating muons. Each station also contained a plane of scintillation counters (SPM), which generated fast signals used in the muon triggering as part of the Large Angle Triggers (LATs) logic (section 2.5). A small hodoscope scintillator(SMS) was used for recovering the dead beam region of the PTM and the beam hole of the SPM, providing very good spatial and time resolution. The SMS detector was used in the muon Small Angle Trigger logic (SAT, see section 2.5). In order to improve the large angle muon triggers, the SVS detector (scintillator counters) was installed inside a 12 inch deep hole drilled into the downstream face of the hadron absorber, before the 1990/91 run period [54], [62] and used as a fixed beam veto. The SUM detector was installed upstream of the hadron absorber, in order to improve the timing resolution [54] of the positive muon requirement for the large angle triggers. This detector was also installed before the 1990/91 data taking periods. The PHI counters, placed at the most downstream point of the apparatus, provided the fast timing signal that was used to phase-lock the RF signal from the accelerator and set the trigger "clock" for the experiment. The characteristics of the different detectors of the forward spectrometer are summarized in table 2.1. A detailed description of these detectors can be found in [9], [55], [56], [57].

Table 2.1: Vertex and Forward Spectrometer Detectors.

Wire Chambers				
Name	Type	Aperture $Z \times Y$ (meters)	Number and Orientation of Planes	Wire Spacing (mm)
VDC	drift	0.70 × 1.20	16 (varius)	10.0
PCV	MWPC	1.00 × 2.80	Y,Z,2U,2V	2.0
PTA	prop. tube	2.00 × 2.00	Y,Z,V,U	12.7
PC	MWPC	2.00 × 2.00	(Y,Z,V,U)×3	3.0
PCF	MWPC	1.00 × 2.00	(U,V,Z)×5	2.0
PSC	MWPC	0.15 × 0.15	2Z,2Y/2U,2V	1.0
DCA	drift	2.00 × 4.00	4Z,2U,2V	25.4
DCB	drift	2.00 × 6.00	4Z,2U,2V	25.4
PSA	MWPC	0.13 × 0.13	2Z,2Y/2U,2V	1.0
PTM	prop. tube	3.60 × 7.20	(Y,Z)×2	12.7
Scintillation Counters				
Name	Aperture $Z \times Y$ (meters)	Thickness (mm)	Number and Orientation of Planes	Counters per Plane
SSA	0.13 × 0.13	12.7	1Z	12
SUM	3.00 × 6.00	25.4	2Y(3 sections)	5, 13
SVS	0.20 × 0.25	25.4	1 (various)	24
SMS	0.20 × 0.20	13.0	(Y,Z)×4	16
SPM	3.00 × 7.00	25.0	4Y (2 sections)	15
PHI	0.50 × 0.50	12.7	1 (various)	4

2.4.1 Calorimeter

The E665 Electromagnetic Calorimeter was a lead-gas sampling calorimeter [63], [9]. It was located downstream of the SUM detector, and just upstream of the hadron absorber. The calorimeter had twenty planes of approximately one radiation length thick lead (5 mm), interspersed with Iarocci proportional tube planes (the sum of all the material of a plane was one radiation length). The active area of the calorimeter was $3m \times 3m$. The proportional tubes have alternately Y and Z wires in consecutive planes. Each plane consisted of modules with eight wires of 1 cm spacing. The cathode planes were split into 1188 pads which were read out as towers summed over all planes. The pads had various sizes, 4 cm $\times$ 4 cm in the central 1 m $\times$ 1 m of the detector, 8 cm $\times$ 8 cm in the region of the detector between 1 m and 1.5 m, and 16 cm $\times$ 16 cm in the outer region.

2.5 Triggers

Triggering involves the online selection of events that are of some interest to the experiment, based on the event characteristics. In the case of a scattering experiment that studies structure functions, the interesting event property is simply scattering of the incoming particle off of the target material. In order to maximize acceptance and to control systematic uncertainties during the 1991 data taking period, E665 operated with a large variety of triggers. These triggers were divided into three different categories, according to the use of the data set that each one was sampling.

- Physics Triggers. These are the triggers that were designed to select muon-nucleon scattering events to be used for physics analysis.

- Normalization Triggers ("Rbeam" triggers). These triggers were designed to allow an unbiased measurement of the beam flux by a random sampling of the beam used in the Physics Triggers.

- Monitoring Triggers. These triggers were designed to study the performance of different elements of the Physics Triggers.

The trigger logic of the experiment was arranged in two levels. The Level One Trigger was used to generate the gates and strobes for the readout electronics of the detector. It used fast signals from scintillators to form a relatively broad definition of an acceptable interaction. The Level Two Trigger, if generated, formed a much stricter definition, using information from the MWPC and/or proportional tubes. The Level Two Trigger started the data acquisition, if it did not occur the apparatus electronics were cleared [9], [55].

The Physics Triggers were also subdivided into three categories:

- The Large Angle Triggers -LAT- (SVS, WAM, CVT, SVSWAM2) were formed by requiring the presence of a scattered muon with a trajectory that did not intersect a fixed central veto region. A detailed description of the LAT of the run period 1990/91 can be found in [55]. These triggers are not used in this analysis.

- The Small Angle Trigger -SAT- required the absence of an unscattered muon from a floating-veto area defined by the incoming beam. A detailed description of the SAT for the 1990/91 run period can be found in [57].

- The Calorimeter Trigger (CAL) used only the hadronic final state properties and fired on the spread of the calorimeter energy deposition. The CAL trigger is described in [64].

All triggers required the presence of an incoming beam muon, defined by an appropriate combination of the signals from the beam hodoscopes (SBT, SVJ and SVW). The trigger timing was set by the Phase-Locked RF signal.

In the following discussion the details of the Physics Triggers and the corresponding beam and monitoring triggers that are relevant in this analysis will be presented.

2.5.1 The Small Angle Trigger

Among the various triggers that were based on the scattering angle of the muon, the SAT had acceptance that covered the lowest values of Q^2 (down to 0.1 GeV^2). Since $Q^2 \cong 4EE' \sin^2(\theta/2)$, where θ is the scattering angle of the muon, the acceptance coverage of the low Q^2 kinematic region was achieved by triggering on events with small θ. Events that had scattering angle θ as low as 0.5 mrad could fire the SAT. This was possible because of the ability of the trigger to fire on events for which the scattered muon remained inside the nominal phase space of the muon beam. For fixed beam energy $(x_{Bj})_{min} \sim Q^2$, so the SAT acceptance at low Q^2 translated to small-x_{Bj} acceptance (down to 10^{-4}).

The SAT was a purely "veto" muon trigger. The veto condition was the presence of an unscattered muon inside an appropriately defined area. There was no positive signal requirement from the scattered muon. In order to obtain the small θ acceptance the veto was floating, sampling the beam phase space. The veto region was selected on an event-by-event basis by projecting the incoming muon trajectory, which was determined from the beam hodoscopes (SBT) to the focal plane of the two anti-parallel oriented analysing magnets. Elements from the SSA and SMS hodoscopes were used in the definition of this region. These elements were determined by high-speed trigger electronics (12 ns) that used the SBT hit combinations as input. In the SMS counters vetoes were defined separately in the Y and Z views (VY and VZ respectively). The logical "AND" of the signals from these views gave an SMS veto. The SSA veto was defined in the Z view only. The SAT veto was the logical "OR" of the SMS and the SSA signals.

The SAT beam (SATB) was defined by acceptable SBT hit combinations in the Y view (BY), using the planes SBT 2Y, 3Y and 4Y, and in the Z view (BZ), using the planes SBT 1Z, 3Z and 4Z. To eliminate the possibility of false triggers due to the presence of more than one muon in the same RF bucket or due to two muons in adjacent RF buckets, the SATB definition included two more components. The first

of these was the cluster module that required single hit clusters in SBT 3Y and 4Y (CY) and in SBT 1Z and 4Z (CZ), and the second was the no neighbor (NN) that required no muon in the preceding RF bucket.

The schematic representation of the SAT trigger is shown in figure 2.5 (from [57]). Tables with the number of counters, scintillator plane combinations and veto windows used in the SAT can be found in [57] and [65].

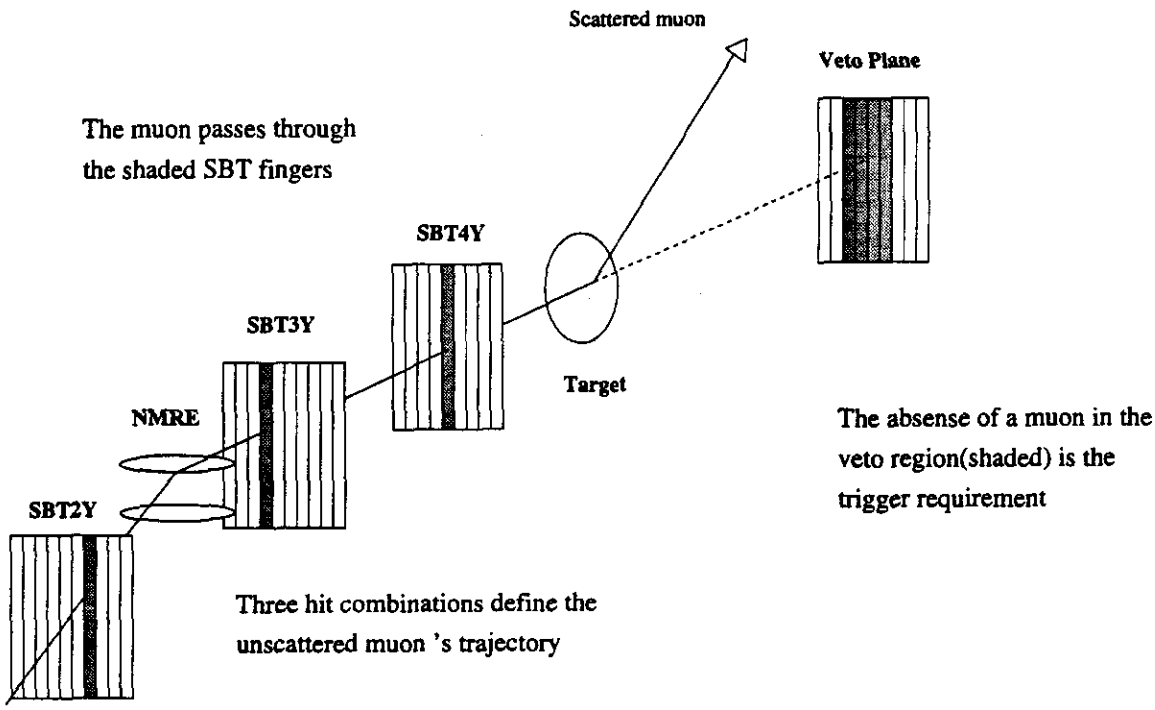

Figure 2.5: Small Angle Trigger Schematic Representation.

The complete trigger definition is:

$$SAT \equiv BY \bullet BZ \bullet CY \bullet CZ \bullet \overline{(VY \bullet VZ)} \bullet \overline{AZ} \bullet NN$$

The trigger acceptance was a strong function of the Y and Z coordinates of the beam and scattered muon in the veto planes. Furthermore, since the SSA veto element is in front of the hadron absorber, there was some dependence of the acceptance on hadron variables such as multiplicities and momentum distributions. This effect was

simply because of the non-zero probability that a final state hadron would hit the SSA within the veto window, and veto the event.

In the cross-section ratio measurement, the acceptance effects that depend on the muon variables are expected to cancel, since the geometrical acceptance is the same for all targets. On the other hand, given that the hadron distributions from different targets can be different, the SSA which was before the absorber, and was sensitive to final state hadrons can introduce a target dependent bias. In order to study the effects of the SSA veto, a monitoring trigger without the SSA requirement was implemented (SATPS). The SATPS was randomly prescaled (1/32) and the trigger definition was:

$$SATPS \equiv BY \bullet BZ \bullet CY \bullet CZ \bullet \overline{(VY \bullet VZ)} \bullet RPSRF \bullet NN$$

where RPSRF was a randomly prescaled copy of the Phase Locked RF signal.

The signal that corresponded to the beam muon definition used in the SAT, randomly prescaled ($1/2^{19}$), was used to define the SAT RBEAM trigger, known as RSAT. The definition for the RSAT was:

$$RSAT \equiv BY \bullet BZ \bullet CY \bullet CZ \bullet RPSRF \bullet NN$$

These triggers were recorded on tape providing an unbiased sample for systematic studies and a very efficient technique to normalize the cross-section measurements (section 4.2.1).

2.5.2 The Calorimeter trigger

The calorimeter trigger (CAL) was a positive trigger that used only the final state hadrons and triggered on the spread of the energy deposited on the electromagnetic calorimeter (it did not require the scattered muon and had no veto). It fired on the 3/4 coincidence of signals coming from the east,west,top and bottom halves of the calorimeter. In each of these sections (halves) the bitube analog signals were summed and discriminated to provide the inputs to the coincidence. The signals

from the four central bitubes in each view were not included since they were exposed to the beam. Hence the trigger required a spread in the energy deposition, which gave a very good rejection for electromagnetic backgrounds like muon-electron elastic scatters and hard target bremsstrahlung events (section 4.3.3). The four sections of the CAL trigger (A-D) are shown in figure 2.6. The Level One trigger was to discriminate the analog sum of all sections to 100 mV (the $mV \rightarrow GeV$ conversion factor was $5 - 10GeV/100mV$, depending on the fluctuations of the gas gain):

$$E = A + B + C + D > 100mV$$

The Level Two trigger was to discriminate the signal from each one of these sections to 175 mV:

$$(A > 175mV) \bullet (B > 175mV) \bullet (C > 175mV) \bullet (D > 175mV)$$

and form the 3/4 coincidence:

$$(A \bullet B \bullet C) \oplus (D \bullet B \bullet C) \oplus (A \bullet D \bullet C) \oplus (A \bullet B \bullet D) .$$

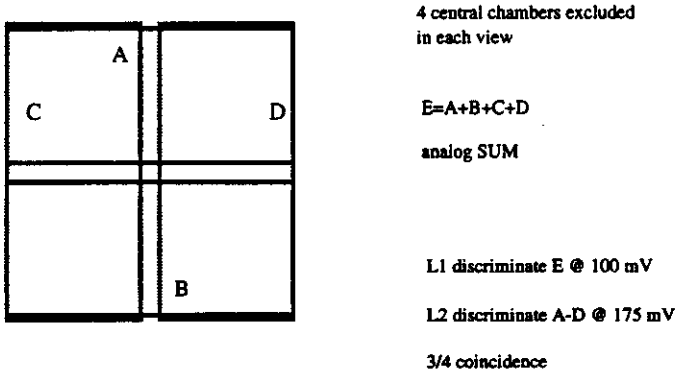

Figure 2.6: Calorimeter Trigger Schematic Representation.

The CAL acceptance changed with changes in the gas-gain. The time constant for these changes was much larger than the target cycling period, so there was no effect

in a ratio measurement. Another consideration was that some CAL signals might have been arriving too late to satisfy the Level-1 trigger timing; a modified version of the CAL (2/4 coincidence) was operated during the calorimeter calibration running to study this source of inefficiency.

The CAL beam (CALB) trigger was the coincidence of the LAT beam signal [55] and a 10 bucket no-neighbour on either side of the trigger RF bucket.

$$CALB \equiv SBT7/7 \bullet \overline{\sum SVJ} \bullet \overline{\sum SVW} \bullet NN$$

where SBT7/7 was the requirement for at least one hit in each of the seven SBT planes. The CAL RBEAM trigger (RCAL) was defined to be the coincidence of the CALB signal with the randomly prescaled ($1/2^{19}$) RF signal (PSRF): $RCAL \equiv CALB \bullet PSRF$

2.6 Data Acquisition

The E665 data acquisition system [66] was based on the FNAL VAXONLINE [67] and RSX-DA packages [68]. These articles refer to the original design and implementation of the data acquisition system for the 1987 data taking period. Before the 1991 data taking period a number of changes were made (some of the changes were made before the 1990 period) to both the hardware and the implementation of the system. An additional FASTBUS subsystem that used a DEC Micro Vax II for monitoring was installed in order to collect data from the VDC detector. The concatenation machine was upgraded to a DEC VaxStation 3200 and the off-line storage medium was changed from 6250 BPI nine-track open-reel tape to 8 mm video tape. To minimize the dead time during the 1991 data taking period, two tape drives were used synchronously.

The detector interfaces were standard CAMAC and FASTBUS electronics. The CAMAC crate controllers were linked by six parallel CAMAC branches (controlled by a JORWAY 411 branch driver) to the three DEC PDP 11/34s front end processors

(BISON 61, 64 and 65). There were two FASTBUS front-end systems for the CAL and the VDC detectors. The data which was read out in parallel from the front-end machines was stored in PDP bulk memory and LeCroy 1892 FASTBUS memory modules. The concatenation machine read out the buffers asynchronously, concatenated the information from the different sources and wrote the event on tape. Each of the tape drives was checked for a busy condition and the data event was written to the first available tape. The front-end machines were synchronized and prepared for data acquisition at the beginning of each spill with an interrupt.

The data on the tapes were organized in different files, the file size was the equivalent of a nine-track tape. Each event in a file was tagged with the Run Number, the Spill Number, the Event Number and the Time Stamp [69] and [70]. The Run Number was determined each time the data acquisition was started (new run); it was simply the previous Run Number plus one. The Spill Number counter was reset with every new run. For the 1991 version of the data acquisition, every time a run started a new file was opened, and when a run ended the tape logger waited for an End of Run Signal that signified that all buffers were cleared and closed the file. The End of Run Signal was always issued after the End of Spill signal. If a run crashed, restarting the system cleared the buffers. These improvements simplified beam normalization issues, since every file contained complete spills and there was no mixing between events of different run blocks. The event types written on tape and their characteristics are listed below:

1. Beginning Of Spill event, one from each PDP11. This type of event was written on both tapes.

2. End Of Spill event, one from each PDP11. This was written on both tapes.

3. Event During Spill (concateneted data event). These events were written on either one of the two tapes, depending on which drive was not busy.

4. Special End Of Spill event. This event contained the readout of the event scalers at the end of spill. It was written to either one of the two tapes.

5. Interspill events. These events contained monitoring information, including information about the magnets and targets. They were written to either one of the two tapes.

2.7 Beam Scalers

In order to measure the beam flux and monitor useful beam related quantities (like instantaneous luminosity, dead time and the performance of each scintillator component of the beam definition), two scaler systems were implemented. One set of scalers measured the beam flux accumulated during a spill and the other measured the beam flux between individual events. The information from the beam scaler systems was not directly used to normalize the relevant cross-sections in this analysis. The direct use of scaler information would have been to count the amount of live beam for each trigger and for each target. This method does not allow beam phase space selections to be implemented in a straight forward fashion; it depends on Monte Carlo studies to estimate the effects. In this analysis the RBEAM triggers were used for normalization and the the information from the scalers was only used in an indirect way, to verify and monitor the prescale factors for the RBEAM triggers (section 2.5).

2.7.1 Spill Scalers

The Spill Scaler implementation has been described in [71]. The spill scalers were read and cleared at the End of Spill and the information was part of the End of Spill event. The problem that existed during the 1990 data taken period caused by the loss of the End of Spill events [55] within file boundaries on a tape was corrected for the 1991 period (as described in the previous section). The 1991 version of the spill

scaler system was reliable.

2.7.2 Event Scalers

The Event scalers were read for each event as part of the normal during spill event. For the 1991 data taking period they were reset every time the corresponding trigger fired. The event scalers were also read and reset at the end of each spill and written on tape with the Special End of Spill event [72], [73], [69]. The event scalers were organized per trigger and they were scaling the physics beam corresponding to that trigger and also a beam definition common to all scalers, as a cross-check. There were two beam (and physics trigger beam) signals scaled for the scaler of each trigger; a gated signal scaled by an ungated scaler and an ungated signal scaled by a gated scaler (the scaler modules were actually inhibited, since they could understand inhibit but not gate logic). In addition, the spare modules were used for the second half of the run to count the coincidences among the various trigger beam definitions. The SPARE1G and SPARE1U modules as they appear in [72] (crate slots 16 and 17) were modified as follows:

- SPARE1G had the following inputs in spigots 0, 1, 2 and 3 respectively:
  1. $SATB \bullet LATB$
  2. $SATB \bullet LATB$ overflow
  3. $SATB \bullet CALB$
  4. $SAT \bullet CALB$ overflow
- SPARE1U had the following inputs in spigots 0, 1, 2 and 3 respectively:
  1. $LATB \bullet CALB$
  2. $LATB \bullet CALB$ overflow
  3. $LATB \bullet CALB \bullet SATB$

4. $LATB \bullet CALB \bullet SATB$ overflow

This information can be used to cross-normalize the beam counts for the various triggers.

Chapter 3

Offline Event Reconstruction

The Offline Event Reconstruction was the process by which the raw information of an event (data in the form of a set of uncorrelated detector hits) was converted into a set of tracks with well determined kinematics and calorimeter energy clusters. This process involved several stages: Unpacking and Decoding of the raw data, Pattern Recognition, Track Fitting, Muon Matching, Vertex Finding and Electromagnetic Calorimeter analysis. These basic analysis stages were incorporated into one computer program known as the PTMVE (the acronym PTMVE is deducted from the initial letters of the above described processes).

In order to perform the above tasks, each detector of the apparatus needed to be aligned and calibrated. The Offline Event Reconstruction was an iterative procedure, between alignment plus calibration and reconstruction of the data. The alignment and calibration of the apparatus were obtained by reconstructing the data from special data sets using initial alignment and calibration parameters, then these results were analyzed in order to improve the calibration and alignment parameters which were then used to reconstruct the data set again; and so on, until the procedure converged.

3.1 PTMVE

The first task that the PTMVE software performed was Decoding and Translation, a task where the encoded information from each detector was converted into detector hits corresponding to particle positions. The detector constants obtained by the alignment procedure described in the next section were used to do the translation. The next task was the Pattern Recognition (PR) stage, where the hits were associated with each other in groups that corresponded to track candidates. After the PR stage the Track Fitting (TF) task was performed, where the track candidates were fitted to obtain a momentum measurement for the tracks. The Muon Match (MM) task ran next, and matched the tracks fitted in the Forward Spectrometer with the line segments fitted in the muon detection system behind the steel absorber. The following stage was the Vertex Processor (VX) application, where tracks were fitted to vertices. The primary vertex included the incoming beam and the scattered muon. The Electromagnetic Calorimeter processor was the last task in the PTMVE chain. This task reconstructed calorimeter energy clusters induced by electromagnetic showers initiated by the passage of particles through the calorimeter. The PTMVE stages have been discussed in detail elsewhere, a short discussion and the corresponding references are given below.

3.1.1 Pattern Recognition

The Pattern Recognition (PR) used a straight line hypothesis for the trajectories in the magnetic field free regions and the non-bending view of the magnets, and a helical line hypothesis for the bending view inside a magnetic field. PR was performed by a number of different processors with different track requirements [56] and it was divided into three sections, the Beam Spectrometer PR, the Muon Detector PR and the Forward Spectrometer PR.

Beam Spectrometer PR. Two processors were used, the PB that found lines using the PBT information and the SB that determined if the tracks found in the PB were from the RF "bucket" coinciding with the trigger. The space-point finding algorithm for the PB is described in [74].

Muon Detector PR. Three processors were used, the PM that was used to find lines in the proportional tubes (PTM), the SM processor that was used to find lines in the SMS hodoscopes and the OV that allowed hits to be shared between the PTM and the SMS. Unlike the rest of the processors the Muon Detector PR gave 2-dimensional track segments as its final output (detectors with three or more views at the same X-coordinate allowed 3-dimensional track segments).

Forward Spectrometer PR (FSPR). FSPR ran in two phases with different sets of cuts, the muon phase and the hadron phase [56] (this reference contains a very useful flowchart of the FSPR stage). The muon phase FSPR searched for "stiff" tracks with strict target pointing criteria, while the hadron phase FSPR searched for softer tracks with looser cuts. The FSPR processors were:

1. DC: Used to find straight line segments in the DCs.
2. PC: Used to find straight line segments in the PCs.
3. MA: Used to link the segments found in PC and DC and pick up hits from the PCF.
4. PF: Extrapolated line segments to pick up PCF hits.
5. PS: Used to find PSA space points.
6. P2: Used to find PSC space points.
7. SF: Used to find the PCF space points and group them in five, four or three space point combinations, creating a line segment.
8. SN: Projected the lines obtained by the SF processor upstream, in order to use the PSC space points.

9. CF: Used to eliminate duplicate tracks by comparing the PCF to the PC hits on the existing line segments.
10. MS and M2: Extrapolated the line found in the PC and PCF to the PSA (MS processor) or to the PSC (M2 processor) to pick up space points and form a line containing all of the above information.
11. MD: Linked the line segments found in the PC and PCF with the DC information.
12. PV: Used to find the PCV space points.
13. MV: Projected all lines found in the FSPR into the PCV to pick up PCV space points.
14. UN: Performed the final comparison to eliminate duplicate tracks and stored the final results of the FSPR into permanent memory banks.

3.1.2 Track Fitting

At the Track Fitting stage the tracks found by the Pattern Recognition were fitted and the track parameters were determined. The results of the fit were expressed in terms of the coordinates of the track points (X, Y, Z), the slope of the tracks tangent at that point ($Y' = dY/dX$, $Z' = dZ/dX$) and the inverse momentum of the track (1/p). Since the length of the NMRE magnet was negligible with respect to the lever arm of the Spectrometer, the effect of the magnetic field was approximated with a constant impulse imparted to the track at the center of the magnet (p_t^{kick}) with a direction perpendicular to the magnetic field [75]. One straight line segment was fitted in the two PBT stations before the magnet and one segment was fitted in the two stations after the magnet. These lines were matched in the middle of the magnet (the X position of this point was determined during the alignment stage). The beam momentum was obtained from the bending angle between the two segments. For

the 1990/91 reconstruction the beam Track Fitting included the effects of multiple scattering by allowing the track to have kinks in the XY and XZ planes [76].

The Forward Spectrometer Track Fitting was performed using a quintic spline fit that used the full field map of CCM. The track momentum was determined by the track curvature in the CCM field. In addition to the five track parameters reported at a given value of the X coordinate, a full five by five covariance matrix for the errors on these parameters was reported. This matrix was modified in order to include the momentum dependent effects of multiple scattering [75].

3.1.3 VDC Pattern Recognition and Track Fitting

The Vertex Drift Chambers (VDC) were installed before the 1990 run period to increase the acceptance of the experiment to low momentum tracks and to improve the vertex resolution. The pattern recognition and track fitting (PRTF) for the VDCs was performed after the Forward Spectrometer PRTF, but before the muon matching and vertex finding processors were applied. The VDC hits along the forward spectrometer tracks were associated with these tracks during the VDC Pattern Recognition process.

The VDC PRTF had three processors: VA, VB and VD [56]. The VA processor projected the Forward Spectrometer tracks to the VDC layers in order to pick up hits. The VB processor used the leftover hits to fit VDC only tracks. The VD processor used the VDC only tracks found by the VB and projected them to the Forward Spectrometer in order to pick up hits and fit new tracks.

3.1.4 Muon Matching

The Muon Matching processor was applied after the Forward Spectrometer and the VDC Track Fitting. The purpose of this processor was to identify the Forward Spectrometer tracks that were due to muons, by matching them with lines reconstructed in the Muon Detector (PTM and SMS). If there was more than one muon found, the

processor made no attempt to decide which was the scattered muon. The matching procedure had three stages [57]: multiple scattering matching, intersection matching and ray trace matching.

Multiple Scattering Matching. All Forward Spectrometer tracks that contained information from detectors downstream of the CCM were projected behind the hadron absorber and were matched with the lines reconstructed in the XY and XZ views (separately) of the muon detector. The matching was performed by comparing the track parameters (position and slopes) at the same X coordinate and forming a χ^2 that had contributions from the errors on the Forward Spectrometer track, the muon detector line and the multiple scattering effect [57]. The χ^2 cut for the 1991 reconstruction was different than the one used for the 1990 reconstruction (as presented in [57]). For the 1991, the cut was $\chi^2 < 15$ separately for the slope and the position fits; this configuration was found to maximize the efficiency while minimizing the background [64].

Intersection Matching. At this stage the Muon Match accounted for the cases of muons suffering large angle scattering at a single scattering center, in the calorimeter or in the absorber. Intersections of the Forward Spectrometer tracks with the muon detector lines at positions upstream of the calorimeter and downstream of the absorber were also accepted.

Ray Trace Matching. This stage accounted for cases where there was no match with any Forward Spectrometer track that had information downstream of the CCM. Tracks with information up to the PCF chambers were tracked through the magnetic field behind the absorber and then the Multiple Scattering Matching algorithm was applied [57].

3.1.5 Vertex Finding

This stage of the PTMVE program was used to find the location of the interaction vertices [77]. The Vertex processor first found the $\mu\mu$ vertex, using the beam and scattered muons, ignoring any hadrons. Then it added the hadron tracks to the $\mu\mu$ vertex and performed a fit; this was the primary vertex of the interaction. The hadron tracks that intersected the primary vertex within some normalized distance were attached to this vertex. Finally the hadron tracks were used in a search for secondary vertices.

3.1.6 Electromagnetic Calorimeter

The Electromagnetic Calorimeter analysis was the last stage of the PTMVE program. The calorimeter information for each event was processed similarly to the spectrometer information (decoding and pattern recognition). The calorimeter data were decoded, the ADC channels were pedestal subtracted and noise suppressed and finally, the ADC counts were converted to energy per pad and energy per wire (this corresponds to the decoding/translation phase). The next step was to apply the calorimeter clustering algorithm (pattern recognition phase) in order to combine neighboring pads into calorimeter energy clusters [78] and [79].

3.2 Alignment and Calibration of the Apparatus

The alignment of the apparatus involved the determination of the position of each wire (or counter) of a chamber (or hodoscope) plane in three dimensional space. The calibration of the apparatus involved the determination of the energy scale of the spectrometer and the energy response of the calorimeter. The first task was twofold, since there were two spectrometers (the Beam and the Forward spectrometers) and the energy scale had to be determined in a consistent way for both. The analysis of

the data from the 1987 period and the preliminary analysis of the 1990 data suffered from disagreement between the momentum measurement of the two spectrometers [55]. For the reconstruction of the complete 1990 data set and for the 1991 data set a different alignment procedure was developed. This procedure was completed in four stages:

1. The beam spectrometer was aligned with the NMRE magnet off [86].

2. The NMRE magnet was calibrated using primary protons from the Tevatron [87], [59].

3. The forward spectrometer was aligned with respect to the beam spectrometer [80].

4. The momentum measurement from the two spectrometers was verified to be in agreement [81].

After the completion of the first alignment, the beam and the forward spectrometers were aligned on a regular basis for monitoring purposes and the alignment procedure was applied every time a detector system had to be moved for maintenance. In addition to the alignment, the drift chambers of the apparatus had to be calibrated, in order to determine their resolution. This was an independent procedure that used the alignment information as a starting point [82], [83]. The results of the alignment of each period were used in the form of special text files, "levella constant " files, that were read by the reconstruction software of the experiment during the offline analysis.

The electromagnetic calorimeter was aligned and its energy response calibrated after the alignment and calibration of the two spectrometers. This procedure involved the analysis of data taken with electron beams of various energies and various magnet settings [84], [85].

3.2.1 Beam Spectrometer Alignment

The alignment of the beam spectrometer was performed using special data sets that were obtained using the LATB trigger, with the NMRE magnet turned off and with the empty vessel target (the spectrometer and the trigger definition are described in chapter 2). The purpose of the alignment process was to determine the position of the PBT wire chambers with respect to a set of four reference planes. These reference planes were defined to be four PBT planes that belonged to two different PBT stations. The two planes from each station (doublet) were measuring along the Y and Z directions, so that a space point could be reconstructed from each of the two doublets (the X position of all chamber planes was determined using surveyor measurements). The alignment procedure was iterative and consisted of three steps:

1. For events with a single incoming muon in the Beam spectrometer, the four reference planes were used to reconstruct a straight line track (since there was no interaction and no magnetic field).

2. For each chamber the residuals of the closest hits to this line were fitted across and along the wire orientation, using a linear fit.

3. The results from the fit were used to adjust the Θ coordinate of the first wire of each chamber, the α angle (the angle of the plane with respect to the beam axis measured from the direction of a wire), and to check the wire spacing.

4. A new "levella constant " file was created and the procedure was repeated using this file as input, until the values obtained from the fits became the same as the the input values.

The success of the alignment procedure depended on the following:

- The precision of the relative alignment of the four reference planes. The survey values were taken for the positions of the reference planes.

- Since the track fitting software for the beam spectrometer was only taking care of Y view bends, the coordinate system defined by these reference planes had to coincide with the one defined by the bending view of the NMRE magnet.

Furthermore, the β and γ angles of all chambers (these are the angles that measure how perpendicular the chambers were to the beam) were ignored in the alignment process. This approximation was justified since these angles were indeed of negligible magnitude.

In order to satisfy the above requirements, the survey information was used to choose the reference planes from the substations that had the smallest relative α angle and were most parallel to the NMRE magnet. The reference planes used to align the spectrometer for the 1990-1991 data taking period were the PBT2Y2,PBT2Z2 and PBT4Y1,PBT4Z1 planes (where the convention for the plane acronyms is "detector name", "station number", "measuring direction" and "substation number") [86]. To verify the accuracy of the surveyor's measurements on the reference planes, a series of consistency checks were performed:

1. After the alignment with the nominal set of reference planes converged, an alignment iteration was performed with a different set of reference planes in order to obtain information about a possible relative α angle between the nominal reference planes. The result of the analysis confirmed the surveyor's measurements.

2. Data taken with the NMRE magnet on were used to find the bending plane of the NMRE magnet with respect to the coordinate system defined by the PBT reference planes (software coordinate system). The cross product of the vectors defined by the reconstructed track segment upstream and downstream of the NMRE magnet was used to measure the relative α angle of the NMRE plane with respect to the XY plane of the software coordinate system. The effect found was negligible; the relative angle was on the order of 1 mrad, resulting in an effective Z view kink from the NMRE magnet on the order of 3×10^{-5}

(Z is the non-bending view of the NMRE in the software coordinate system) [86]. The track segment fits upstream and downstream of the NMRE magnet were also used to find the X-position of the centre of the magnet. This was by definition at the point where the two track segments intersected. The X_r position found was different ($\sim$ 3 cm) from the one used by the track fitting software and it was corrected [86].

The results of the alignment together with documentation on the run conditions were included in the corresponding "level1a constant " files.

3.2.2 Forward Spectrometer Alignment

The forward spectrometer alignment method was based on the same ideas used to align the beam spectrometer. A reference track was reconstructed, and for each detector plane the residual distance of the closest hits to that track along and across the wires was minimized. The results from this minimization were used to adjust the Θ of the first wire and the α coordinate of each plane [80].

Since the forward spectrometer had the large Multi Wire Proportional Chambers (MWPC) PCV, PC and PCF and also the drift chambers DCA-B and VDC, the alignment for the forward spectrometer had to be performed in several stages:

PCV, PC, PCF, PSC, PSA, SMS .

- Reference tracks used: Tracks reconstructed using the beam spectrometer only. The RLAT trigger was required and a single track in the spectrometer. A straight line was fitted using PBT stations 3 and 4 and it was extrapolated from PBT4 to the forward spectrometer.
- Magnet settings : Both NMRE on and NMRE off data were used in order to illuminate as many wires as possible. Both CCM and CVM magnets were off.

At this stage the Θ corrections for the first wire of all chambers and the α corrections for only the PSC and the PSA (small MWPC) were determined. Since the region of the chamber illuminated by the beam tracks was small for the large MWPC compared to the size of the chamber, α corrections for these chambers were measured using muon HALO data.

Note that SMS scintillator array was treated as a wire chamber, with the "wire" position defined to be the center of the counter, the "wire spacing" defined to be the width and the resolution equal to $\frac{wirespacing}{\sqrt{12}}$.

DC, PTM, α for PCV,PC,PCF .

- Reference tracks: Tracks reconstructed using the PCV-PC-PCF detectors (straight line fit was applied). The HALO muon trigger was required and a single track in the event.
- Magnet settings : CCM and CVM off, NMRE either on or off.

This stage was designed to determine α and Θ corrections for the DC and PTM and α for the large MWPC. If α corrections were necessary for the MWPC, the previous step had to be repeated.

VDC and PCV Θ .

- Reference tracks: Tracks reconstructed using the beam spectrometer only. The RLAT trigger and a single track in the spectrometer were required. The track was extrapolated using the magnetic field maps of the CCM and CVM magnets.
- Magnet settings : all magnets on, nominal current value.

In this stage α and Θ for the VDC central region chambers were determined. The chambers in the outer region were not illuminated by the RLAT trigger data and were moved by the same amount as the corresponding inner chambers.

The Θ coordinate of the PCV chambers was also changed during this step since the PCV chambers were mounted on the yoke of the CVM magnet and the chamber moved when the magnet was powered.

VDC using wide HALO trigger .

- Reference tracks : The tracks were reconstructed using the PCV-PCN-PCF-DC detectors.
- Magnet settings : NMRE was either on or off, CVM and CCM were on.

This step was designed to determine α and Θ for all the VDC chambers. It required the alignment of the rest of the forward spectrometer chambers.

The results of all alignment runs of the forward spectrometer were tabulated in the "levella constant " files, together with comments and relevant information about each run.

3.2.3 Absolute Energy Scale - Proton Calibration

Experiments that use charged lepton beams are very sensitive to energy calibration effects, as the cross section is a strong function of Q^2 ($\sim Q^4$ and $Q^2 \sim 4EE'\sin^2(\theta)$). In order to determine the absolute calibration of the beam and the forward spectrometers, on November 1 and 2 of 1991, E665 ran primary protons from the Tevatron into the Muon Lab. The momentum of the primary protons during the calibration run had a magnitude of $P_{proton} = 800.6 \pm 2\ GeV$. This value was determined using the set and readback values of the main Tevatron dipoles [87].

The data were taken running the NMRE dipole magnet (Beam spectrometer) at four different currents. The results from these measurements were used to determine the transverse momentum kick (P_T^{kick}) of the NMRE magnet at the nominal current value ($P_T^{kick}(3350)$, NMRE ran at 3350 Amps during normal data taking). The P_T^{kick} was the effect of the magnetic field as approximated in the track fitting program,

which assumed that a constant impulse was imparted to the track at the center of the magnet. The analysis of the data was performed using the standard pattern recognition and track fitting software of the experiment (PTMVE), after the full alignment procedure was applied. Each event with a single proton reconstructed in the beam spectrometer was processed, resulting in a momentum distribution which was then fitted to a gaussian. The mean value of the gaussian fit (P_{fit}), together with the P_T^{kick} value used in the track fitting software ($P_T^{kick}(fit)$) and the proton momentum given by the accelerator were combined to obtain the $P_T^{kick}(3350)$ value. The magnetic field was scaled using either the current readout of the magnet or the magnetic field value as measured with a Hall probe:

$$P_T^{kick}(3350) = \frac{P_T^{kick}(fit)}{P_{fit}} \frac{A(3350)}{A(read)} P_{proton}$$

where A is either the current readout or the Hall probe information for the different currents. Both methods gave consistent results, and the $P_T^{kick}(3350)$ value was found to be 1.515 ± 0.004 GeV. The total error had contributions from the error in the proton momentum determination and from the quantization of the NMRE magnet readout [59].

3.2.4 Relative Energy Calibration of Beam and Forward Spectrometers

The relative energy calibration of the Beam and the Forward Spectrometers depended on the quality of the detector alignment and on the accuracy of the magnetic field maps of the spectrometer magnets. Since the response of the NMRE magnet (Beam Spectrometer) was calibrated using the Tevatron primary protons and the Forward spectrometer was aligned using reference tracks reconstructed in the Beam Spectrometer, the measurement of the momentum of the primary protons from the Forward Spectrometer (P_{fs}) was used to verify the relative calibration of the two spectrometers [81]. Beam trigger events, with one reconstructed track in the Beam Spectrometer

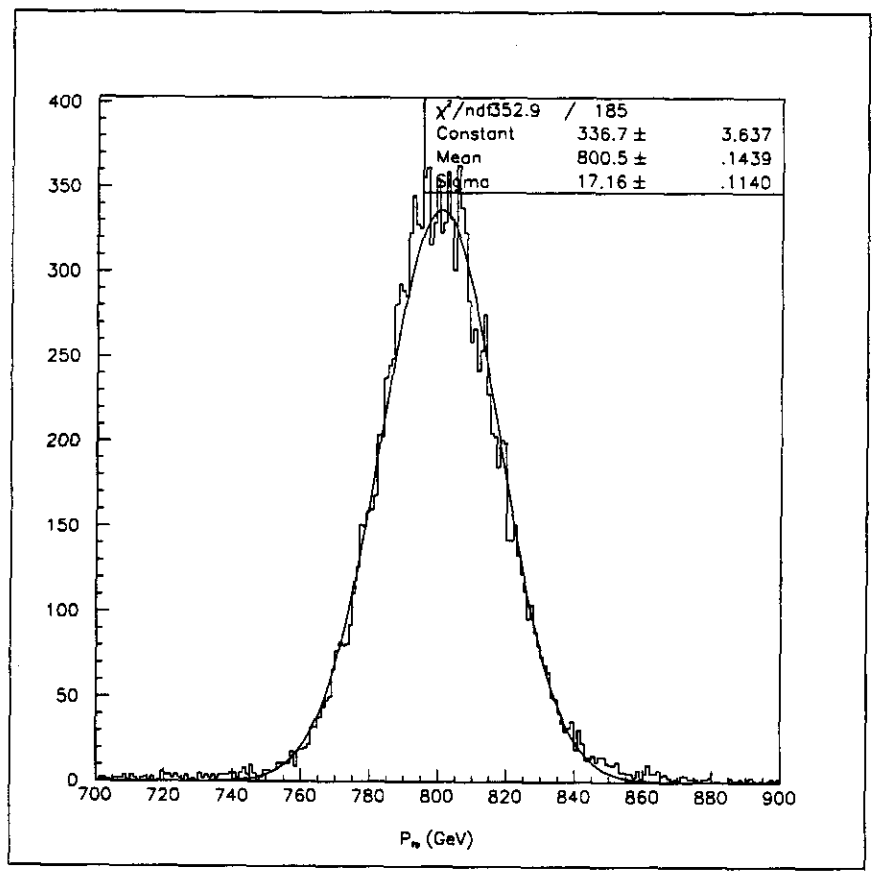

Figure 3.1: Proton Calibration Forward Spectrometer momentum measurement.

and one in the Forward Spectrometer, were used to obtain the P_{fs} distribution shown in figure 3.1. The gaussian fit of this distribution resulted in a mean value of 800.5 GeV, with a sigma of about 17 GeV. This result is consistent with the accelerator value of 800.6 ± 2 GeV, quoted for the primary protons.

In addition, in order to verify both the validity of the alignment procedure and its stability over the various alignment runs, the difference of the momentum measured with the beam to that measured with the forward spectrometers, was measured for Rbeam triggers (straight through beams). This was done during normal data taking with an incoming muon beam. The measurement was performed as a function of the run block number, thus covering all different alignment periods. This difference, which is simply the kinematic variable ν for these non-interacting beams, is shown in figure 3.2. The resulting systematic error (miscalibration) of the relative momentum scale of the two spectrometers is less than 0.5%.

3.2.5 Calorimeter Alignment and Calibration

The E665 Electromagnetic Calorimeter used gas-filled proportional chambers that were read-out by a FASTBUS ADC system. Thus its energy response was dependent on the ADC pedestals, the amplifier gains and on the gas gain fluctuations. The gas gain was a function of pressure, temperature, high voltage and gas composition. During the physics data-taking period and between accelerator spills, these quantities were recorded [79] and were used offline to perform the relative calibration of the data [88] (removing any time dependence of the calorimeter response). The absolute scale of the calorimeter response was determined using data taken with an electron beam [85]. The electron data were also used to determine the position of the centre of the calorimeter (the calorimeter alignment) [84].

ADC calibration. Amplifier gains and ADC pedestals were determined by measuring the response of all channels at several test pulse heights during the interspill

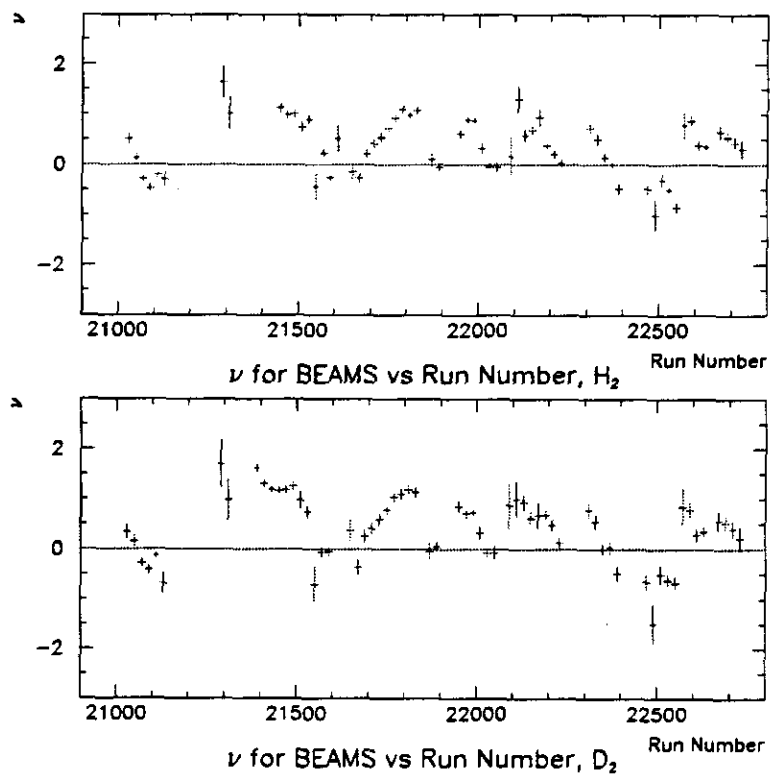

Figure 3.2: Difference of the Beam and Forward Spectrometer Reconstructed beam momentum as a function of Run Block.

period. The pedestal measurement corresponds to zero input charge. The data collected were analyzed offline and the results were used by the Calorimeter Analysis Software in the form of run block dependent text files that were read during the reconstruction of the calorimeter information of the physics data.

Gas Gain. There were two gas gain monitors (GGM) that were inserted in the path of the gas before and after the calorimeter. These GGM were proportional tubes, with a Fe^{55} gamma ray source mounted inside. The gas flowed through the GGM and the pulse height information was recorded on tape. There were two monitors in order to detect any gas contamination due to a leak in the calorimeter. The gas gain was corrected for dependence on the following variables:

- Temperature: There were twenty temperature sensors at various locations in the calorimeter, including one in each GGM. During the offline calibration a mean temperature was obtained from all the working monitors and the gas gain was corrected according to the variation of this mean value.
- Pressure: There was one pressure sensor through which the gas flowed before it fanned out to the calorimeter planes. The gas gain was corrected according to the readings of this sensor.
- High Voltage: The cathode high voltage was provided by Droege power supplies and the output voltage of each power supply was monitored and recorded on tape. These values (which were very stable during the run) were used to compute a plane-by-plane correction.
- Gas composition: The variation of the gas gain over the entire 1991 run period was large, the minimum and maximum gains during the run differed by about a factor of two [89]. The cause of these large variations was identified to be the change of the gas composition over the run. To correct for this time dependence of the gas gain, the remaining variation

after temperature and pressure corrections was parametrized as a piece-wise linear function of time. The gas gain was corrected according to the results of this fit and the gas gain variations were reduced to the $\sim$ 2% level [89]. The variations remained large for the boundaries of the time periods that the calorimeter gas was contaminated ($\sim$ run blocks 21300 and 21900). There was also an unexplained large change of the gas gain between run block 22000 and run block 22500 [89].

The alignment and the absolute energy calibration of the calorimeter were obtained using electron beam calibration data. These data were taken in two modes:

1. "position sweep" mode, where the beam was of fixed energy and the beam was swept over the calorimeter face. This mode was used for the determination of the position of the center of the calorimeter.

2. "energy sweep" mode, where the energy of the electron beam was varied and the beam was aimed at a few spots on the calorimeter. This mode was used for the energy calibration.

To check the stability of the calorimeter performance during the 1991 run data taking period, the average calorimeter energy and the average number of calorimeter clusters were plotted as a function of time (run block number). The results are shown in figure 3.3 for the average number of clusters and in figure 3.4 for the average calorimeter energy. The fluctuation is larger than the value obtained in the calibration procedure, but the important feature for this analysis is that the fluctuation is the same for both the hydrogen and the deuterium targets. The average calorimeter energy is not the same for the two targets because of the differences in the electromagnetic background content of the two data sets (see chapter 4), but the fluctuations of the average calorimeter energy, as a function of run block, are the same for both targets. The pattern of these fluctuations follows in an exaggerated fashion

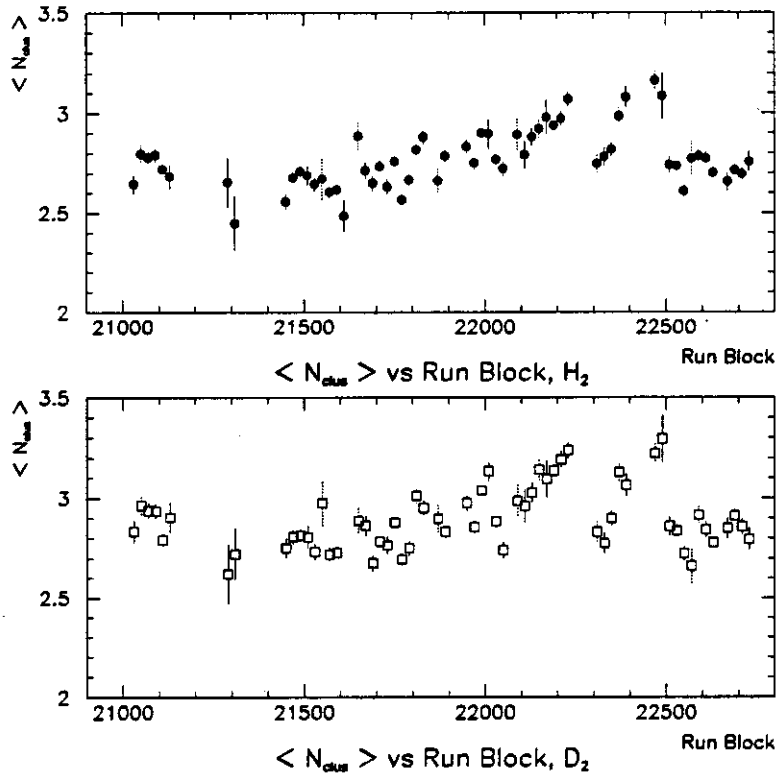

Figure 3.3: Average number of calorimeter energy clusters as a function of Run Block.

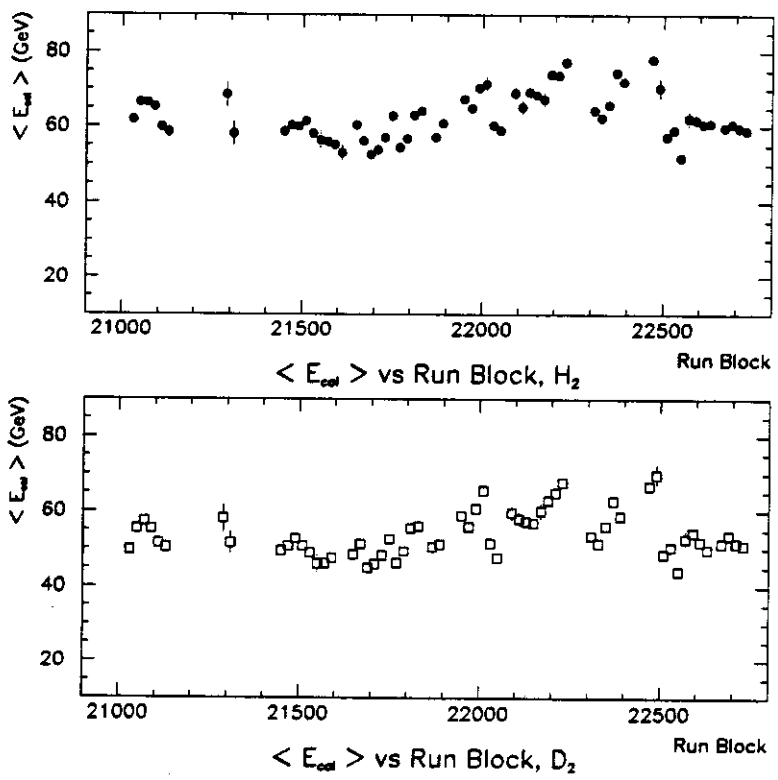

Figure 3.4: Average calorimeter energy as a function of Run Block.

the gas gain run dependence as seen by the gas gain monitor in [89], including a level difference of the average calorimeter energy in between run blocks 22000 and 22500. The event selection and the procedure followed to obtain the calorimeter alignment can be found in [84]. Since this alignment used reconstructed electron tracks it had to be performed after the alignment of the spectrometer chambers. The position of the centre of the calorimeter was found to be -10.2 mm in Y and -7.2 mm in Z, with Y and Z being measured in the global E665 coordinate system.

The event selection and the method used to obtain the absolute energy scale for the calorimeter can be found in [85]. The electron beam momenta used were as high as 45 GeV and the calorimeter response was found to be linear within that range. The proportionality constant that related the calorimeter energy to the electron energy was used to set the energy scale. The pad energy resolution in the energy range of the calibration was measured to be: $\sigma_E/E = 0.38 \pm 0.11/\sqrt{(P)}$, where E is the energy of a calorimeter cluster associated with an electron track of momentum P.

The calorimeter response became nonlinear for electromagnetic showers with energies above 75 GeV. The space charge that developed was so large that it distorted the accelerating electric field of the proportional tubes. This effect is known as "saturation" of the electromagnetic calorimeter. The non-linearity was parametrized using a data sample of electron tracks that was defined by selecting elastic muon-electron scattering events from the physics data sample (muons scattered off of the atomic electrons of the targets), but the correction was not part of the standard calorimeter calibration of the experiment.

3.3 Data Production - Run 1991

The data of the 1991 run period were analyzed with PTMVE version 23.09 and 23.10 [90], [91] on the Fermilab CPS farms [92]. The PTMVE program was split into three different classes of processes in order to adapt to the multi-processing CPS

environment [93]. The class 1 process handled the event input, the class 2 processes did the event reconstruction in parallel and the class 3 process handled the output of the processed data. For the 1991 data production there were a number of changes made to the three classes of CPS processes as they are described in [93]. The changes were made to improve both the speed of the PTMVE itself and the speed and accuracy with which physics analysis could be done on the PTMVE processed data.

- BYTE-swapping was rewritten in the assembly and c programing languages.

- The flow of the ptmv was modified to stop processing events as soon as it was known that the event was to be discarded:

  1. For events with either no Beam or no Y view or Z view scattered muon projections after Pattern Recognition, there was no further processing.
  2. After the Muon Match, if there were no muon candidates processing was stopped.
  3. After the Vertex fitting, if the event had $\nu < 20$ and $\theta < 0.0003$ rad there was no further processing.

- The n-tuple [1] and normalization database files produced by PTMVE were re-designed.

- The calculations related to the n-tuple and the n-tuple filling were moved from class3 to class2, in order to gain speed.

In addition, since the PSC detector was very unstable during the 1991 run period, the P2 and M2 processors were turned off.

[1] N-tuples are Hbook objects. Hbook is a CERN developed histogram package.

3.3.1 Normalization data base and analysis n-tuples

In addition to writing the acceptable reconstructed events on tape, the PTMVE software produced the normalization data base and analysis n-tuple disk files. Since the 1991 data sample was large (about 1000 raw data tapes), this form of output was designed to minimize the time and maximize the accuracy of the structure function and structure function ratio analysis. The analysis presented here was based on the normalization data base and the analysis n-tuple output of the PTMVE.

The normalization data base files were produced by a software package that ran as a part of the class1 PTMVE process [69]. For every raw data tape processed by the PTMVE, one of these plain text files was produced. Each file contained four different type of records: one header record that included the tape number (written at the beginning of the file), one summary record that contained a summary of the statistics and the errors reported during processing (this was written at the end of the file), a record that contained magnet and target conditions information (written once per spill) and a record that contained scaler information (written once per spill). Each record had as a tag the run number and the spill number of the corresponding spill. The great advantage of the normalization data base was that it maintained the event order, since it was created by the class1 PTMVE (the standard output tapes did not maintain the event order since the class2 processors were processing events asynchronously). This was important because of the dual tape output of the 1991 data acquisition system: the events from a spill were written to two tapes and in order to use the per event scalers and compare them to the spill scalers on a spill by spill basis, both tapes had to be processed at the same time, with the events in the correct order. The processing of the normalization data base files two at a time was much easier than the processing of the PTMVE output tapes. The procedure is described in [94], the files were combined using the run and tape number information and the per spill records of each file were combined using the spill number tags. All the 1991 run normalization data base files were combined to create an easy to use

normalization n-tuple [94]. The contents of the normalization database are described in B.

The 1991 analysis n-tuples were designed to provide all the information needed to perform a structure function analysis. Each n-tuple file included two different n-tuples, one for the physics triggers and one for the Rbeam triggers. Both n-tuples contained all the detector information on the Beam and Forward Spectrometer reconstructed muons (detector hits on the track) and the reconstructed kinematics with their errors. The physics trigger n-tuple also contained calorimeter information, the charged track multiplicity and other final state variables and detector related quantities (the n-tuple contents are given in C). The information in both n-tuples was in the form of packed bitted words, so the n-tuples served as a mini-DST for the structure function analysis. In order to be included as an entry to the n-tuple, the physics trigger events were required to pass cuts, while there was no requirement for the Rbeam trigger n-tuple (the cuts are described in C).

3.3.2 Reconstruction Performance

The PTMVE program calculated errors on the reconstructed kinematic variables which were deduced from the track fitting and the vertex fitting errors. These errors corresponded to the experimental resolution on the measurement of the kinematic variables. The resolution of the reconstructed event kinematics of a ratio measurement is important both as an absolute number (it affects the scale of the kinematic variables), and as a relative number between the different targets (it can bias the ratio measurement). Since the experiment ran for a long period of time, changes in the performance of any detector system during that time can introduce a time dependence of the apparatus resolution and a time dependent overall reconstruction efficiency. This time dependence is not expected to affect the ratio measurement because of the small period of the target cycling into the beam ($\sim$ 1 spill). There are efficiency and acceptance issues that depend on the event topology which can intro-

duce differences in the performance of the PTMVE for different targets (for example different hit multiplicities); these issues will be studied in the analysis chapter. In this section the calculated errors of some important quantities are studied both as a a function of Run Block (time dependence) and integrated over time, and the results for the two liquid targets are compared.

The beam spectrometer resolution is shown in figure 3.5. It was better than 0.5% and was the same for both targets. The muon vertexing efficiency was measured using a sample of elastic muon-electron scattering events from the physics data sample (muons scattered off of the atomic electrons of the targets) and it was found to be $\sim$ 87% and the same for bot targets [95] and [96]. The dependence on x of the

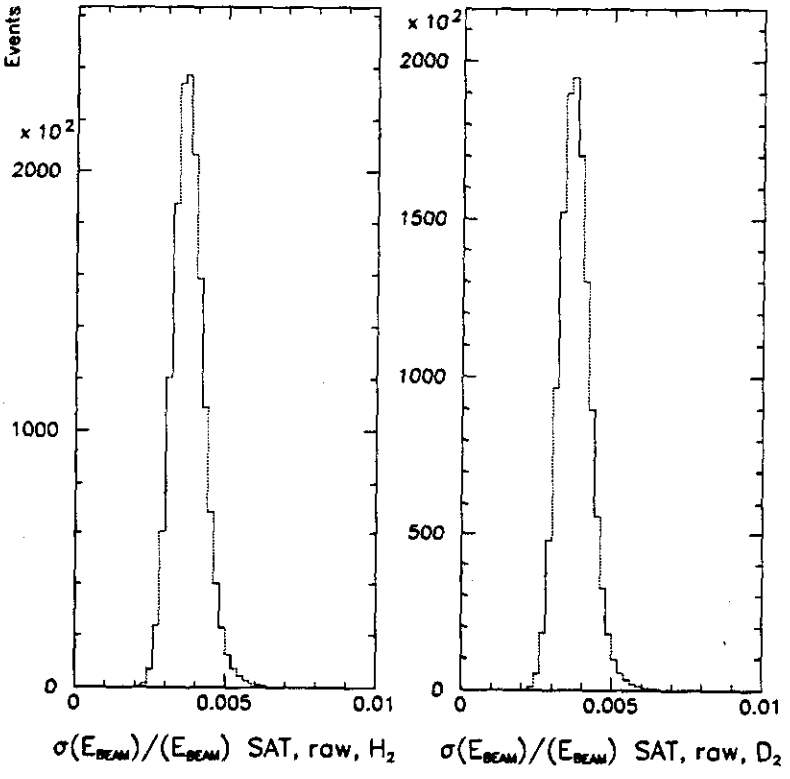

Figure 3.5: Fractional error of the reconstructed Beam momentum.

logarithm of the relative error in x is shown in figure 3.6. Even at the smallest x values the error is better than $\sim$ 20% and it is the same for both targets. Figure 3.7 shows the logarithm of the relative error in ν as a function of ν and figure 3.8 shows the logarithm of the relative error in Q^2 as a function of Q^2; in both cases the results for the two targets are in good agreement. The time dependence of the

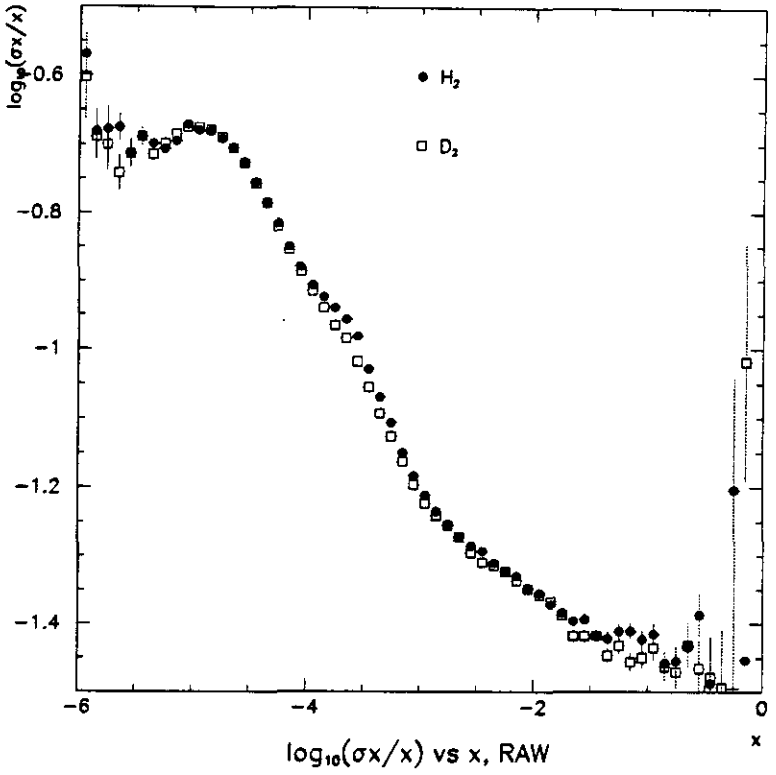

Figure 3.6: Fractional error on the reconstructed Bjorken x variable.

logarithm of the fractional error on Q^2 is shown in figure 3.9, where this quantity is plotted as a function of the Run Block number. The time dependence is the same for both targets. These results are from the SAT trigger and the fluctuations observed correlate with the performance of the PSA detector, that covered the small angle region after the CCM magnet. The time dependence for the PSA chamber is shown

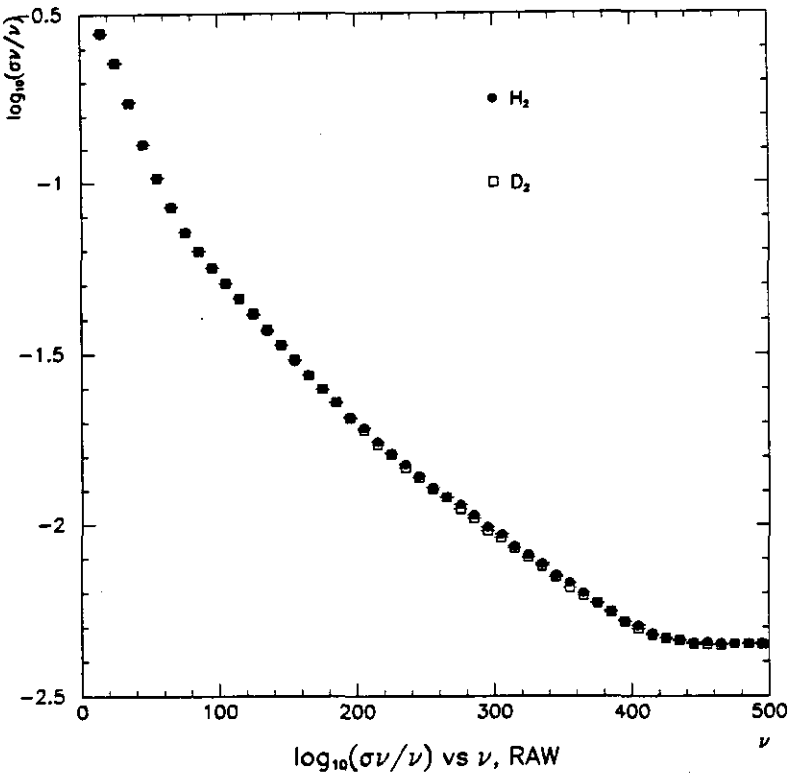

Figure 3.7: Logarithm of the fractional error of the reconstructed ν variable.

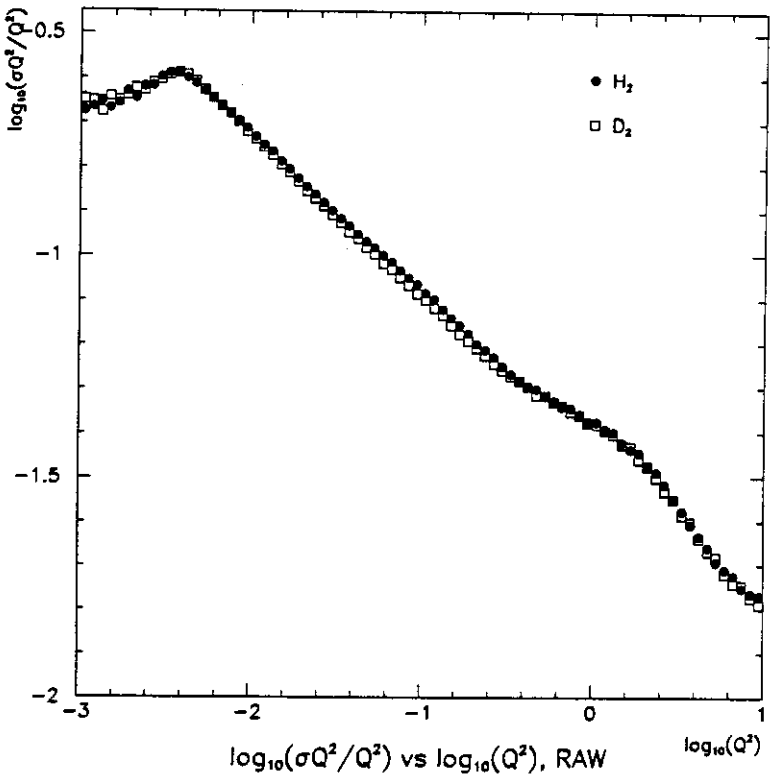

Figure 3.8: Logarithm of the fractional error of the reconstructed Q^2 variable.

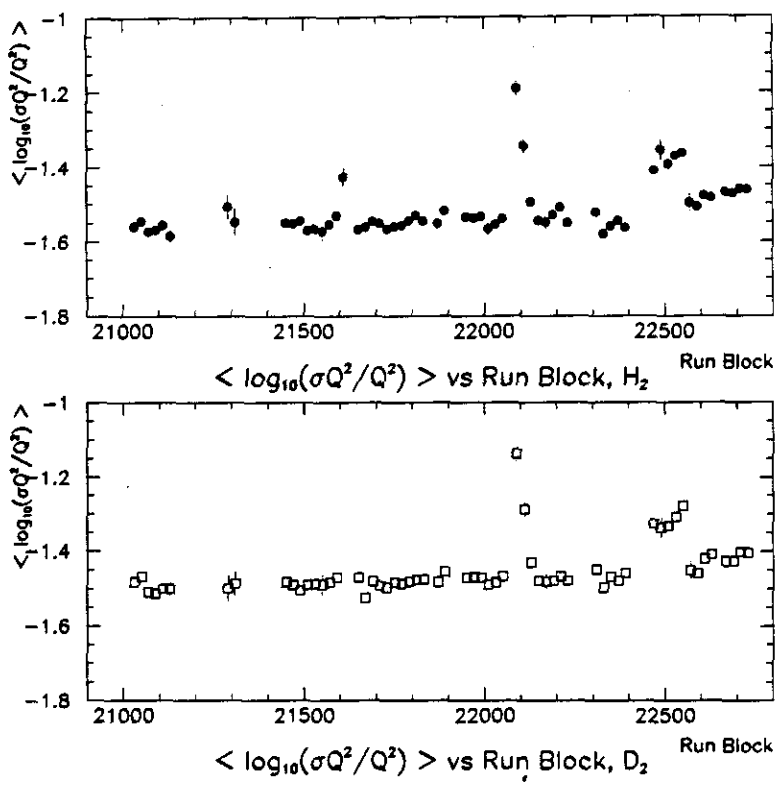

Figure 3.9: Logarithm of the fractional error of Q^2 as a function of the Run Block number.

in figure 3.10. The average fraction of reconstructed forward spectrometer muons with PSA information is plotted as a function of the Run Block number. This is not an absolute efficiency plot, since a reconstructed muon was required, it shows the efficiency fluctuations during the run, assuming that all other parameters were stable (trigger, beam tune, etc). There is a good correlation between the PSA performance and the experimental resolution. Because of these large resolution effects only muons that were found in the PSA or the DCs were used in this analysis (see chapter 4) . The

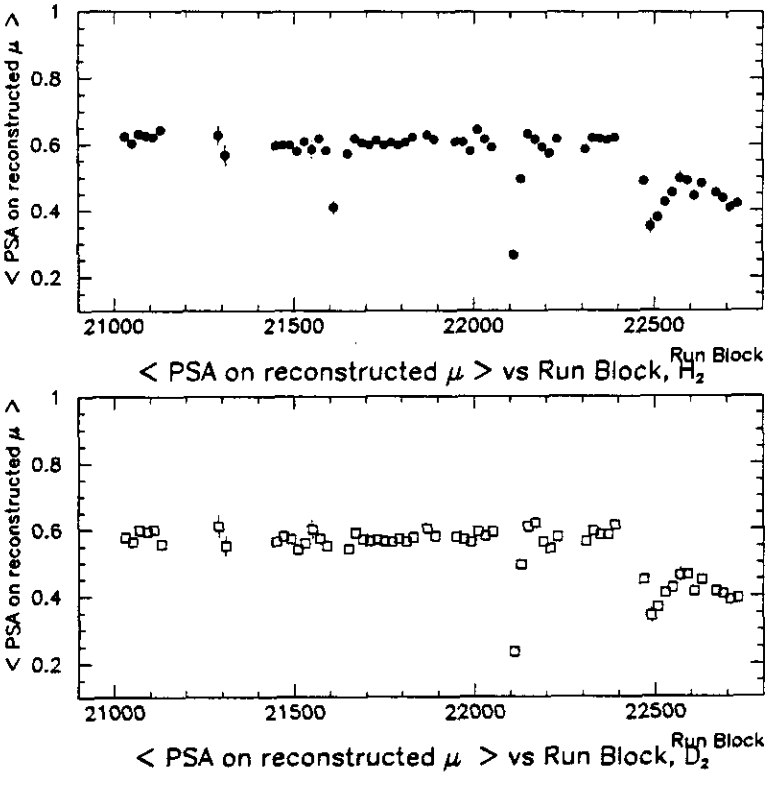

Figure 3.10: Average number of forward spectrometer muons reconstructed with the PSA as a function of the Run Block number.

electromagnetic calorimeter was very important in removing background processes for the structure function ratio measurement. The performance of this detector was very

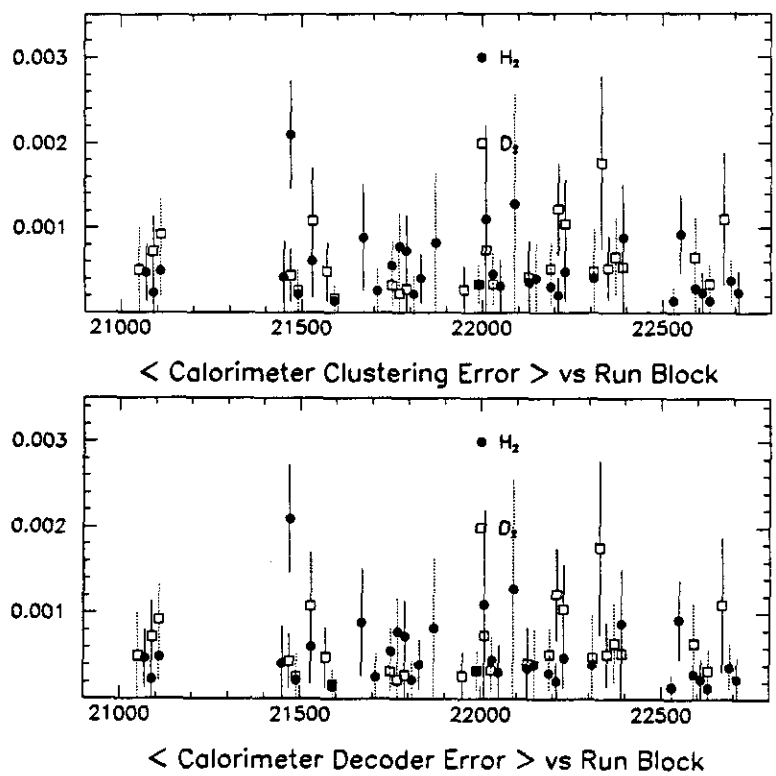

Figure 3.11: Calorimeter Clustering errors (top) and Decoding errors (bottom) as a function of the Run Block number.

good during the 1991 data taking period. The fraction of events with a clustering algorithm failure (top plot) and calorimeter decoder failure (bottom plot) are shown in figure 3.11. The error occurrence was negligible and of the same frequency for both targets. In order to verify the overall stability of the performance of the detector and

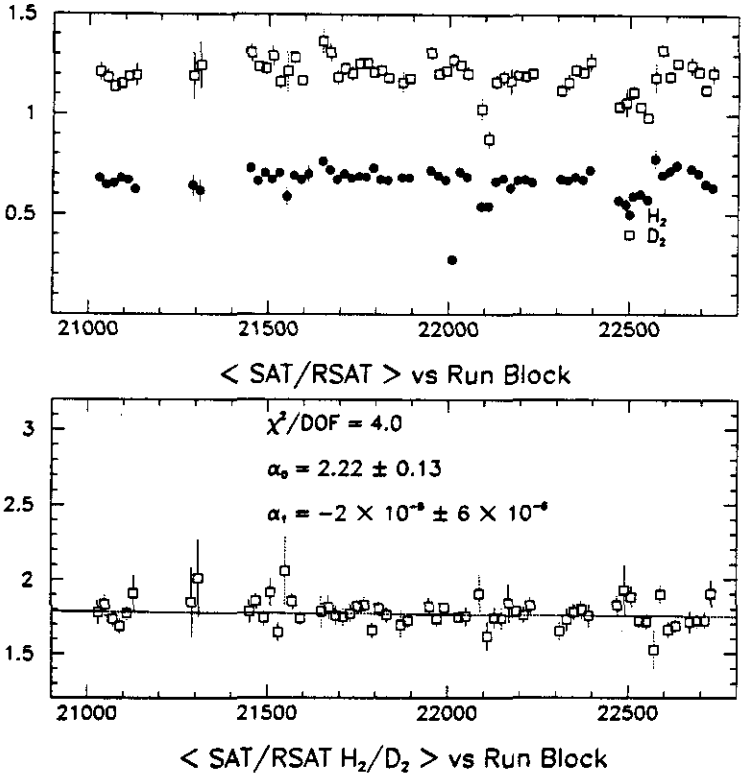

Figure 3.12: Average number of SAT/RSAT for H_2 and D_2 (top) and their ratio (bottom), as a function of the Run Block number.

the reconstruction software during the 1991 data taking period, the average number of physics triggers (SAT) per random beam trigger (RSAT) are plotted as a function of the Run Block number. The results are shown in figure 3.12 for both the H_2 and the D_2 targets (top plot) and their ratio (bottom plot). The ratio was fitted to a straight line with zero time dependence as a result (the α_1 fit parameter is shown in

the figure).

3.4 Simulation Software

3.4.1 The E665 Monte Carlo programs

The E665 Monte Carlo event simulation was divided into two phases: the event generation (stage-one Monte Carlo) and the detector simulation (stage-two Monte Carlo).

The stage-one Monte Carlo (MC1) simulated the interaction of an incoming beam muon with the nuclear matter of the experimental targets. The events were generated with scattered muon kinematics determined by the acceptance-rejection method according to a parameterization of the single-photon exchange muon-nucleon inelastic cross-section. The beam phase space was not simulated, the MC1 stage used reconstructed Rbeam trigger events as input. The muon kinematics were smeared to take into account the effects of the higher order Quantum Electro Dynamics (QED) processes using the GAMRAD program [97], [98]. The same program (GAMRAD) also simulated the emission of radiative photons due to these higher order QED processes (bremsstrahlung photons from the radiative elastic, resonance and inelastic states). The hadronic final state generation was simulated using the LUND hadron generator [99], using the Lund string fragmentation model and Parton Distribution Functions that were used to calculate the cross-section distribution of the different possible final state exclusive processes at the parton level. The tracking of the particles through the detector, taking into account the magnetic field and the interactions with the material of the apparatus, was done using the GEANT package [100], customized with a complete description of the E665 geometry and materials of the detectors.

The stage-two Monte Carlo (MC2) simulated the response of the detector. The track information at the positions of the different detector systems was used to produce wire-chamber hits, taking into account wire-chamber efficiencies and simulating

the effects of electronic noise [101].

The specifics associated with the Monte Carlo production for the run 1991 data analysis validation are given here. The Monte Carlo event generation used Lepto version 5.2 and Jetset version 6.3 from the LUND package and GEANT version 3.15. The structure functions used to generate the inclusive cross-section were constructed using the NMC F_2 parameterization for the high W^2 inelastic region [47], the low W^2 inelastic region parameterization from reference [103], the resonance region parameterization from [102] and the extrapolation of [104] to small-Q^2 for high W^2. The method of construction for the input F_2^p used in the event generation is described in reference [105]. The GAMRAD program used the Mo and Tsai formalism for radiative processes in lepton-nucleon interactions. The numerical integration for W was performed in 35 bins and for θ in 8×30 bins (equ. A24 of [106]). The resolution parameter Δ (soft photon emission) was set to 400 MeV. The elastic form factors used in the cross-section calculations were from [107]. The final state hadrons were generated using the Parton Distribution Functions (PDFs) from the GRV set HO citegrv. In principle, the same PDFs used in the hadronic final state generation should used to construct the F_2 used in the inclusive construction generation. Since the E665 acceptance went lower in Q^2 than any other previous experiment there were no valid PDF parametrizations for the kinematic region covered by E665. The F_2 used covered the whole E665 kinematic region and used the same data (NMC) that were included in the GRV fit for the higher Q^2 region. The efficiency measurement of the chambers and their implementation to the MC2 is described in [64]. In the same reference a description of the upgrades to the trigger simulation done for the 1991 Monte Carlo production.

The MC events were processed using the same analysis chain that was used for the data and they were analyzed using the same n-tuple form.

Chapter 4

Analysis

4.1 Introduction

4.1.1 Cross-section formulation

Cross-section measurements involve a counting of the number of scattering events per incident beam flux per unit number of scattering centers in a unit area in a region of the kinematical phase space. If the apparatus registers N_{meas} events in a given elementary cell $\Delta(\omega)$ of the kinematic domain, the experimental cross-section is:

$$\frac{\Delta\sigma}{\Delta(\omega)} = \frac{AN_{meas}}{N_{Avg}N_{beams}\rho L\Delta(\omega)} \tag{4.1}$$

where A is the atomic weight of the target, L is the length and ρ is the mass density of the target, N_{beams} is the number of incident beam particles required to produce N_{meas} interactions and N_{Avg} is Avogadro's number.

The quantities appearing in equation 4.1 have to be determined, so the extraction of the cross-section involves the following measurements:

- Beam counting (N_{beams}).
- Target composition (ρ).

- Acceptance determination (N_{meas},N_{beams}).
- Efficiency (hardware) measurement (N_{meas},N_{beams}).
- Efficiency (software) measurement (N_{meas},N_{beams}).
- Calibration, energy scale ($\Delta(\omega)$).
- Resolution (N_{meas}).

From the measured quantity $\frac{\Delta\sigma}{\Delta(\omega)}$ we want to extract the one-photon exchange cross-section. The experiment measures the total cross-section within its acceptance, which includes contributions from other processes (background) that need to be removed.

4.1.2 Experimental cross-section

The total measured cross-section, assuming no experimental losses (perfect acceptance and resolution), can be expressed as:

$$\sigma_{tot} = \sigma_{1\gamma} \times K_{sum} + \sigma_{rad-inel} + \sigma_{quasi} + \sigma_{coh} + \sigma_{\mu-e} \tag{4.2}$$

where $\sigma_{1\gamma} \equiv \sigma_{Born}$ is the 1γ exchange cross-section we want to extract, $\sigma_{radinel}$ corresponds to inelastic muon-nucleon scattering with the emission of external bremsstrahlung photons, σ_{quasi} corresponds to the coherent muon-nucleon elastic scattering and σ_{coh} corresponds to the muon-nucleus coherent elastic scattering. The K_{sum} factor takes into account the contribution of soft photon emissions, as well as vertex and vacuum polarization corrections. [1] In order to obtain a common reference between experiments it is customary to take the effects of the higher order electromagnetic processes into account as a correction to the experimental observed cross-section. The $\sigma_{\mu-e}$ term of equation 4.2 is the contribution of the muon electron elastic scattering to the total

[1] See page 28, chapter 1

measured rate and it is not part of the muon-nucleon scattering cross-section, since it corresponds to a different process. The cause of this contribution is muons that scatter elastically off of the atomic electrons of the target material. Since this is an elastic process, its contribution appears at the value of x_{bj} ($x_{bj} = m_e/m_p = 0.000544$) that the elasticity constraint dictates. The following formulation of the radiative correction procedure requires the separation of the $\mu - e$ elastic events from the total measured event yield.

Realistic experiments do not have perfect acceptance and resolution. In order to substitute σ_{exp}, the total measured experimental cross-section, for σ_{tot} of equation 4.2 we have to correct for these experimental losses, because of the finite resolution and acceptance effects. These losses are not independent of the production cross-section (σ_{tot}), so the extraction of σ_{Born} from the total measured event rate has to take into account all effects simultaneously. This can be easily seen in the expression that relates the measured event rates to the Born cross-section. In a given reconstructed (x_{Bj},Q^2) bin, after removing the $\mu - e$ contribution, and for a given target i, the number of events from that target N^i_{events} (with $x \equiv x_{Bj}$) is:

$$N^i_{events} = \int_0^\infty \iint_{DQ^2Dx} L^i(PHS_{bm}) \{ \iint_{DQ_t^2 Dx_t} K^i(x, Q^2, x_t, Q_t^2)\, A^i(x_t, Q_t^2) \times \frac{d^3\sigma_{Born}}{dx_t dQ_t^2 dE_{bm}}\, dx_t dQ_t^2 \}\, dx dQ^2 dPHS_{bm} \qquad (4.3)$$

where,

1. x_t, Q_t^2 are the true (unsmeared by experimental effects) values of the measured x_{Bj},Q^2 variables.

2. $L^i(PHS_{bm})$ is the overall normalization factor, where PHS_{bm} are the beam phase space variables: the energy (E_{bm}), 3-momenta and position of the incoming μ and position of the interaction vertex.

3. $K^i(x,Q^2,x_t,Q_t^2)$ is a smearing function, which includes effects such as resolution and radiative corrections.

4. $A^i(x_t,Q_t^2)$ is the overall acceptance and efficiency factor, including the reconstruction efficiency. It is a function of the true variables because of effects that depend on the cross-section (charged track multiplicity effects for example). Acceptance is usually determined as a function of the measured variables x_{Bj},Q^2.

The total number of events counted by the experiment when target i is in position (N^i_{total}) is expressed:

$$N^i_{total} = N^i_{events} + N_{bgnd} \tag{4.4}$$

where the number N^i_{events} corresponds to equation 4.3, evaluated for the target i and is the number of events that originated in the target, while N_{bgnd} is the number of events from out of target scatters that occurred while target i was in position. Since in the experiment we measure N^i_{total} in order to use equation 4.3 to extract the single-photon-exchange cross-section we need to estimate N_{bgnd}.

4.1.3 Cross-section ratio measurement

In the measurement of the cross-section ratio, as opposed to the absolute cross-section measurement, the effects of some of the terms appearing in equations 4.1 and 4.3 are minimized. Taking a ratio results in much smaller corrections from the effects of quality/resolution cuts and acceptance, efficiency losses. The biggest contribution to the systematic uncertainty cancellation in the cross-section ratio measurement comes from the use of cycling H_2,D_2 and empty vessel targets. The following statements are based on the effects of target cycling:

- Since the period of the target rotation is much smaller than the time scale of chamber performance changes (mostly chamber aging), any time dependence in the reconstruction efficiency cancels in the ratio.

- After beam phase space cuts the geometrical acceptance is the same for both targets. The beam phase space cuts are imposed to assure that the beam used transverses the target in its full length and the same cross sectional area is seen by the beam for both targets.

As a result of these cancellations in the ratio measurement, we can simplify equation 4.3. We can choose the x,Q^2 bins so that the resolution part of the kernel K(x,Q^2,x_t,Q_t^2) is a smooth function peaking in the corresponding bin, and such that we can substitute A(x,Q^2) in place of A(x_t,Q_t^2). If A(x,Q^2) is a smooth function with little variation in each bin, and is the same for both targets, it can be pulled out of the integral and cancels in the ratio. This is an exact solution only if A(x,Q^2) is constant, because even if it is the same function for both targets, the cross-sections and the smearing kernels could be different. Since A(x,Q^2) includes the trigger acceptance the validity of this cancelation is subject to detailed checks, which will be presented in the following sections.

As a consequence of the acceptance cancellation, the cross-section ratio measurement reduces to the determination of the L(E_{bm}) factor (beam counting, target composition), the integration of the K(x,Q^2,x_t,Q_t^2) kernel and the measurement of the event yield in each (x_{Bj},Q^2) bin. Of course, the effects of the trigger acceptance have to be studied. The kernel integration can either be performed formally using a kernel that includes radiative correction factors or the radiative events can be removed from the measured N_{events} that enter equation 4.3. In this case, only the smearing part of the kernel needs to be included in the integration.

4.1.4 Out of target event rejection

Another important issue is the rejection of the events that originate outside of the target volume when the target is in place (N_{bgnt} events in equation 4.4). In order to remove these events it is not sufficient to simply impose the requirement that the

reconstructed vertex position be within the target, due to the finite resolution of the vertex position measurement. Instead of a vertex position cut, the data from the empty target vessel [2] are used to remove the out of target events on a statistical basis. The event yield from the empty target, properly scaled with the relative luminosity to the liquid target, and for every kinematic variable examined, is subtracted bin by bin from the event yield of each liquid target:

$$N^i_{corr} = N^i - \frac{N^i_{beams}}{N^{Mt}_{beams}} N^{Mt}$$

where i refers to events either from H_2 or D_2, N^i_{corr} is the corrected for out-of-target contribution event yield, N^i the uncorrected event yield, N^i_{beams} the number of incident muons required to produce N^i events, N^{Mt} the number of events from the empty vessel and N^{Mt}_{beams} the number of incident muons required to produce N^{Mt} events. The same selection criteria apply to both the liquid target and the empty vessel events. The X_{Vtx} distribution (in meters) for the three targets is shown in figure 4.1 . The target position is between -13.0 m and -12.0 m in the E665 coordinate system. For this method to work, the beam has to be well contained in the target volume. The out of target events are beams that scatter from components of the apparatus that are not part of the moving target system, so their contribution is the same independently of which target is in place. If the beam aperture is not contained within the target then some beams will scatter from the side of the target vessel. These events will not be properly accounted for by the empty target subtraction technique unless the x-y position of the liquid and empty targets is exactly the same. Unfortunately, this was the case for the run 91 data taking, with the beam scraping the target vessel. This is shown in figure 4.2, where the Y_{Vtx} and Z_{Vtx} position are plotted for all interaction points with X_{Vtx} in the target volume. The enhancement towards the negative Y_{Vtx} axis is due to the beam scattering from the vessel wall. This is not an asymmetry of the beam phase space. In figure 4.3 the position that the

[2] this method has a general applicability, it is not unique to the ratio measurement

beam intercepts the last plane of the last beam station (PBT4) is plotted and shows no asymmetry. To correct for this problem, the beam phase space of the accepted events is selected so that the target volume traversed by the beam is defined by a cross-sectional area of the x-y plane that is well contained in each target, through the full length of the target. The X_{Vtx} distribution for both liquid targets after the empty target subtraction procedure is applied shows no residual background (figure 4.4, the event yield per target was scaled with the relative luminosity before the subtraction).

4.2 Normalization

4.2.1 Beam counting

The determination of the beam flux requires the counting of beams available for interaction during the live-time of the experiment. In this analysis we use randomly prescaled BEAM triggers (Rbeam) to sample the beam. The Rbeam triggers were formed by a coincidence of the physics trigger beam signal [3] and a randomly prescaled RF signal. On the average, every 2^{α} BEAM trigger is selected and recorded on tape, where α is the prescale exponent that controls the prescale factor P_{fact} of the hardware random number generator (the module allows α to be changed). In order to determine the total beam flux P_{fact} must be measured.

The Rbeam trigger normalization method is very powerful since it has the advantage of providing all the information needed to account for beam reconstruction losses and beam phase space cuts. Since for this data analysis the requirement is that the beam for the physics trigger events is reconstructed and beam phase space cuts are applied, a simple beam counting with scalers will overestimate the actual flux. When the same selection criteria are applied on Rbeam events, the effect of these requirements in the cross-section normalization cancels. If $\epsilon_{Rbeam}(Y)$ is the fraction

[3] RBEAM triggers, section 2.5

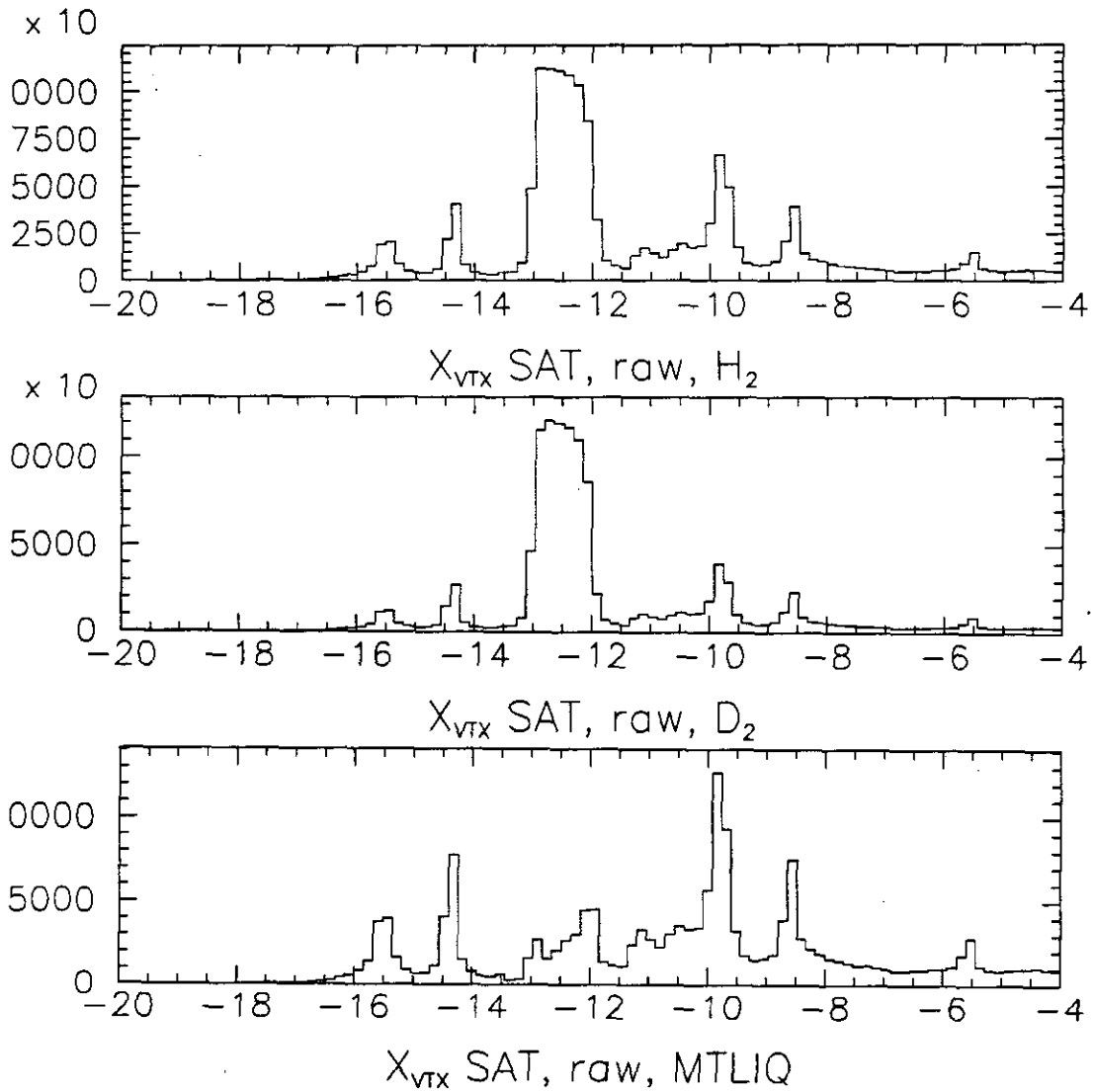

Figure 4.1: X_{Vtx} position for the 3 targets

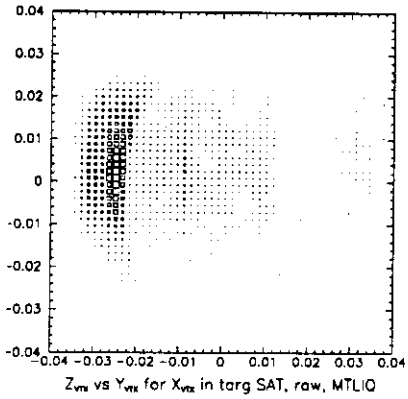

Figure 4.2: Empty target Z_{Vtx} vs Y_{Vtx} for X_{Vtx} in target

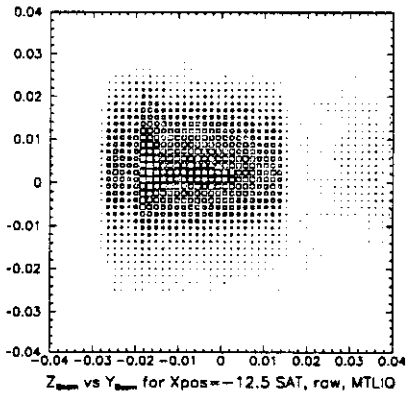

Figure 4.3: Empty target Z_{beam} vs Y_{beam} at PBT4

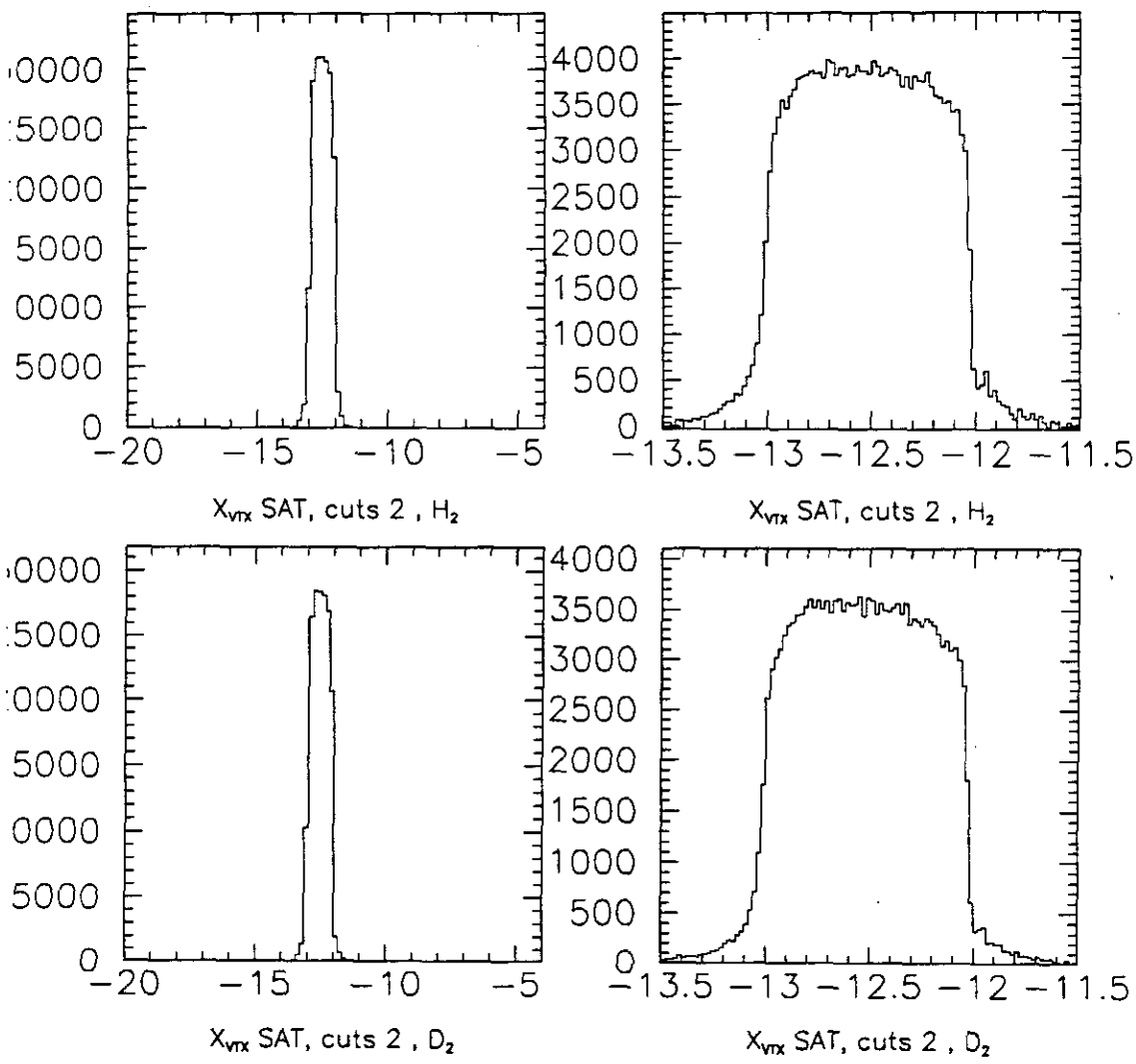

Figure 4.4: X_{Vtx} after empty target subtraction

of Rbeam events rejected by the above requirements in a bin Y of the beam phase space, the same fraction $\epsilon_{Rbeam}(Y)$ of physics trigger events will be rejected due to the failure of the beam of each event to pass these same requirements. The cross-section can be written: $\sigma \sim N_{events}/N_{Rbeams} = (\epsilon_{Rbeam}(Y)N_{events})/(\epsilon_{Rbeam}(Y)N_{Rbeams}) = N_{eventsCut}/N_{RbeamsCut}$, where $N_{eventsCut}$ and $N_{RbeamsCut}$ the number of physics and Rbeam trigger events after the selection criteria and N_{events} and N_{Rbeams} the numbers before these criteria.

The prescale factor is measured by comparing the number of BEAM triggers from the normalization event and spill scalers, integrated over some period of time, to the number of Rbeams over the same time period:

$$P_{fact} = \frac{N_{Beams}^{scaler}}{N_{Rbeams}}$$

The quantity

$$\log_2(\frac{N_{Beams}^{scaler}}{N_{Rbeams}})$$

corresponds to the prescale exponent α, where N_{Beams}^{scaler} is the total number of BEAM triggers from the scalers and N_{Rbeams} is the number of Rbeams recorded on tape. To perform the measurement, information from both the spill scalers and event scalers (integrated per spill), is used. This information is part of the spill database for Run 91, described in reference [69] and in chapter 2. The results from some of the scaler channels are shown in figures 4.5, 4.6 and 4.7.

The mean value of the prescale factor as a function of run block is evaluated in twenty Run Block intervals. To keep the statistical errors on the measurement Gaussian, the average number of Rbeams with its error and the average number of Beams with its error are measured in each interval and then the prescale factor ratio is formed. For the cross-section ratio measurement the relevant quantity is the ratio of the prescale factors for the two targets. The target rotation of once per spill makes it hard to create conditions that will give different P_{fact} for the two targets. This assumption is checked by measuring P_{fact} per target and then taking the ratio of the

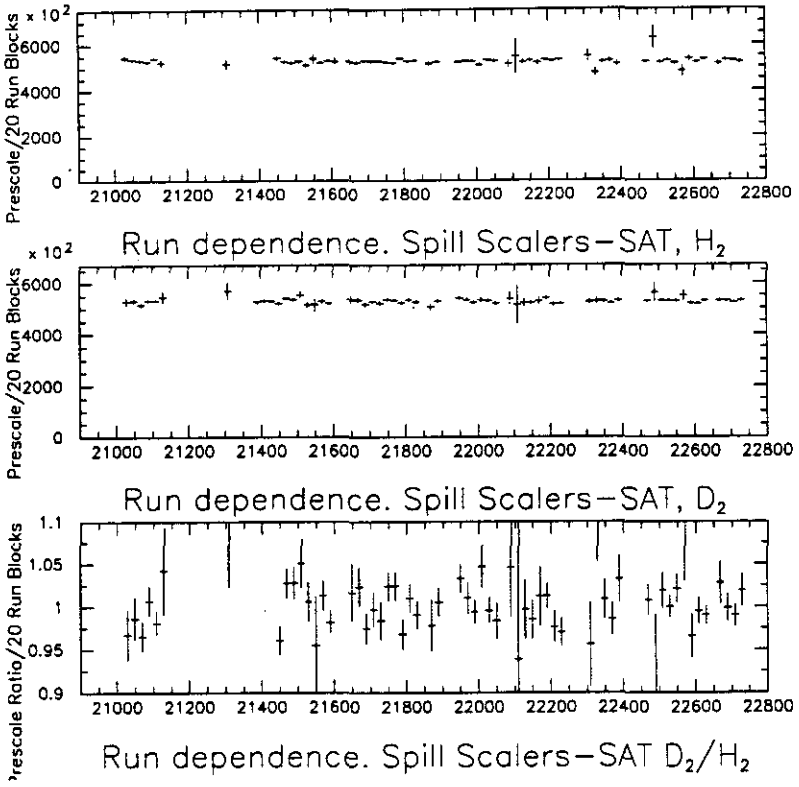

Figure 4.5: P_{fact} for SAT from the Spill Scalers

two quantities. Since different triggers have different beam definitions and different hardware associated with them , the prescale factors for the SAT and CAL triggers that are used in this analysis are measured separately.

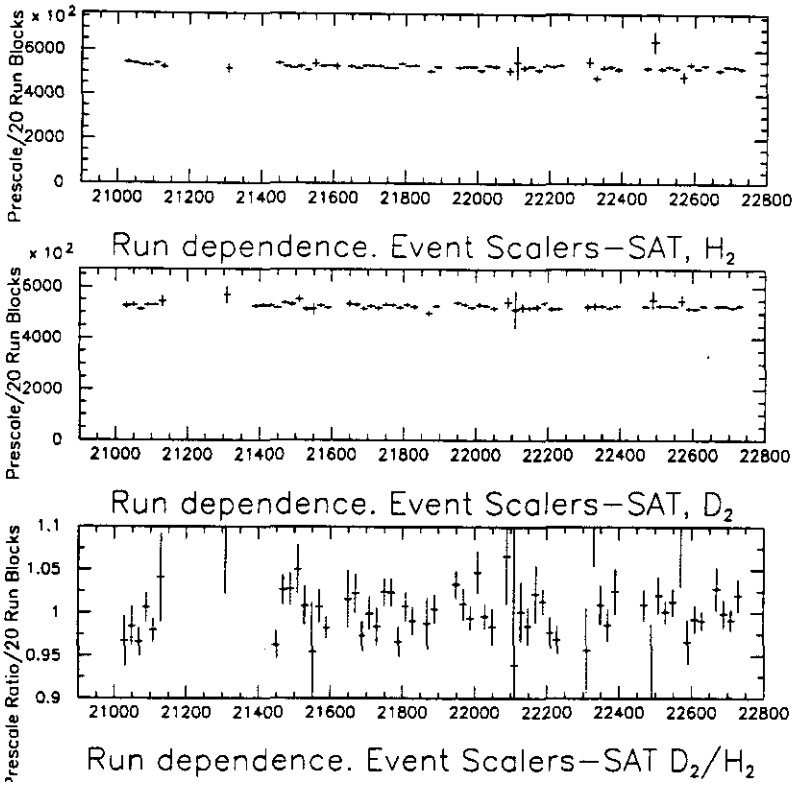

Figure 4.6: P_{fact} for SAT from the Event Scalers

The average value of the prescale factor for each target and of their ratio is determined by a flat line fit over the time dependence of each quantity. The error from the fit is the systematic error assigned to the beam normalization procedure. The prescale factor ratio measurement shows good agreement between the two targets and has no time dependence. The results are summarized in Table 4.1, Table 4.2 and Table 4.3. The average value of the prescale factor integrated over the whole run is also given ($< P_{fact} >$) with its statistical error.

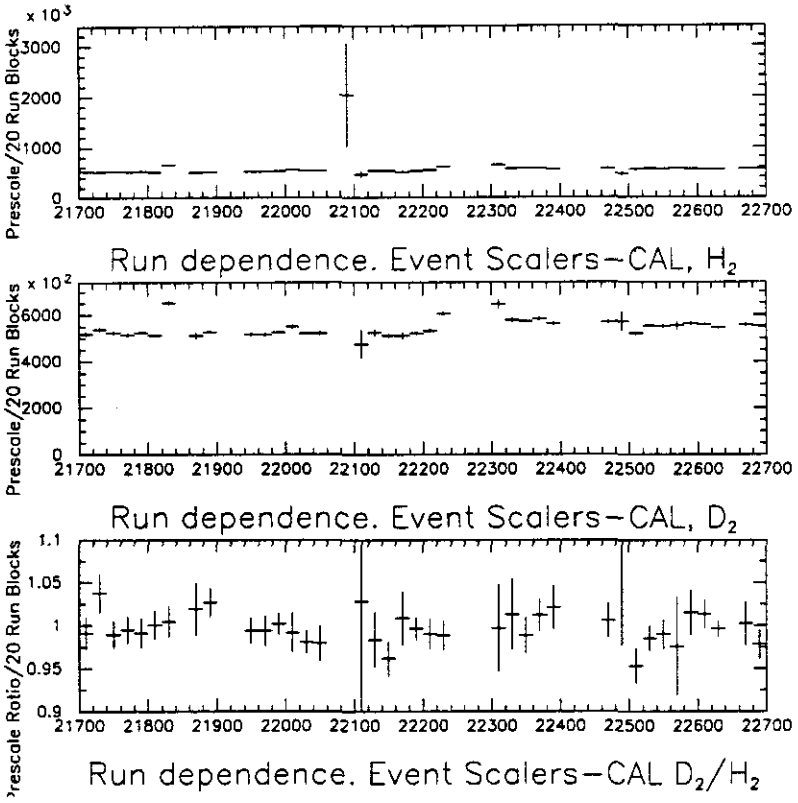

Figure 4.7: P_{fact} for CAL from the Event Scalers

Table 4.1: Prescale factor measurement for SAT from the Spill Scalers

	P_{fact}	$\delta_{P_{fact}}$ from fit	χ^2	α	$< P_{fact} >$	$\delta_{<P_{fact}>}$
H_2	526800	840		19.007	526993	840
D_2	526200	894		19.005	526991	840
D_2/H_2	0.9992	0.0025	1.33		0.9999	0.0025

Table 4.2: Prescale factor measurement for SAT from the Event Scalers

	P_{fact}	$\delta_{P_{fact}}$ from fit	χ^2	α	$< P_{fact} >$	$\delta_{<P_{fact}>}$
H_2	526900	840		19.007	527108	840
D_2	526300	894		19.005	526451	894
D_2/H_2	0.9990	0.0025	1.34		0.9988	0.0024

Table 4.3: Prescale factor measurement for CAL from the Event Scalers

	P_{fact}	$\delta_{P_{fact}}$ from fit	χ^2	α	$< P_{fact} >$	$\delta_{<P_{fact}>}$
H_2	536200	1049		19.03	539428	1010
D_2	542100	1146		19.04	544297	1074
D_2/H_2	0.9955	0.0030	0.74		1.0090	0.0028

The same result is obtained, for both the spill and the event scalers, from all the different scaler channels used. The measured values agree with the setting of the prescale factor in the hardware. Due to the design of this Random Prescaler the agreement does not have to be absolute, but the above result confirms what has been observed in the previous data–run of the experiment. Since each different Rbeam trigger uses a different channel of the prescaler, the prescale factor can have different deviations from the hardware set value for different triggers. This is the reason why separate measurements are done for each different trigger.

The final check on the accuracy of the determination of the relative beam normalization is done using the out-of-target events [108]. These events correspond to scattering from the material outside the target vessel, which remains the same when the targets are interchanged. The ratio of the cross–section for the out-of-target events when target i is in position, over the cross–section for the out-of-target events when target j is in position ($i \neq j$), is examined. If the beam counting is correct this ratio must be one, since the amount of material in both cases is the same. In order to perform that check the following procedure is applied:

- The ratios of the event yields for all three targets are formed as a function of the position of the vertex along the beam direction (X_{vtx}).

- The ratio is then fitted to a flat line for the events originated downstream of the target. This is done to avoid effects of the target material in the acceptance, since the targets have different interaction lengths and the tracks from the upstream of the target events have to penetrate the target.

- The ratio is then multiplied with the inverse of the ratio of the Rbeam triggers that correspond to these event yields, in order to form the cross–section ratio.

The event selection for the physics and Rbeam triggers is the same with the event selection for the physics analysis, as described in the following sections. Of course

the restriction for the X_{vtx} position has been removed, in order to collect the out-of-target events and the Y_{vtx} and Z_{vtx} cuts are less tight (± 0.04), in order to increase the statistics. The fiducial volume required for the beam penetration is defined to match the above values of the accepted vertex position.

The results for the CAL trigger beam counting are presented in figure 4.8. The number of Rbeams on each target after the selection criteria is 308014 on H_2, 152067 on D_2 and 51919 on the empty vessel. The ratios examined are D_2/H_2 and $H_2/MTliq$

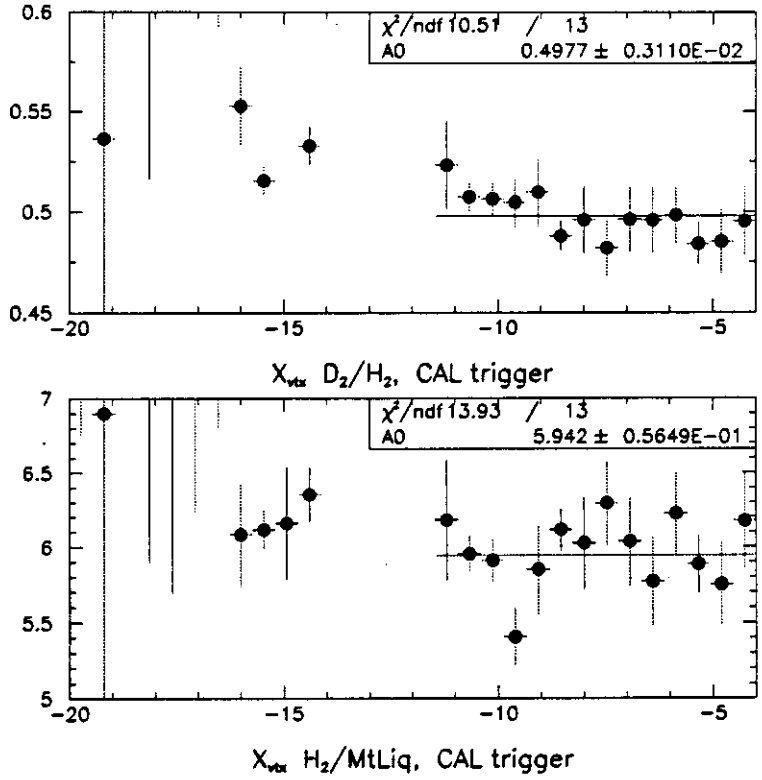

Figure 4.8: Out-of-target normalization.

and the fits are done for the events downstream of the target, as shown in figure 4.8. The results from the fit are: $D_2/H_2 = 0.49768 \pm 0.00311$ and $H_2/MTliq = 5.9420 \pm 0.05648$. After correcting for the relative luminosities the cross-section ratios are:

$\sigma_{D_2}/\sigma_{H_2} = 1.0080 \pm 0.0064$ and $\sigma_{H_2}/\sigma_{MTliq} = 1.0015 \pm 0.0099$, where the errors include the contribution from the error on the fit and the statistical error on the beam count. This result confirms the accuracy of the relative normalization to the 1% level.

4.2.2 Target Composition and Density

The target densities are derived indirectly from the measurement of the saturated vapor pressure in the cryogenic liquid reservoir. The vapor pressure was measured by a pressure to voltage transducer and recorded on tape as a function of time. Offline the raw pressure was adjusted according to the pressure transducer calibration data. The saturated vapor pressure was converted to density assuming equilibrium conditions and by relating the measured pressure to temperature and the temperature to density.

The chemical composition was determined using a boil-off test. The D_2 target was contaminated with HD molecules, which complicated the density determination for D_2 from the measured pressure since this pressure is related to the mixture of the unpure D_2 target. An iterative procedure was followed to find the densities using the information from the chemical analysis, the molar densities and the chemical properties of D_2 and HD. The density determination analysis, including the conversion formulas (pressure–temperature and temperature–density), results and the error estimate are described in **Appendix A**. The contribution to the error of the cross–section ratio measurement from the systematic uncertainty due to the target composition and the density determination are also included. Note that there are two periods for the HD contamination of the D_2 target. These will be called Sample I and Sample II .

4.3 Beam Selection

The beam selection criteria are imposed in order to minimize problems in three different components of the σ_n/σ_p measurement: kinematic resolution, relative normal-

ization and out of target event rejection. As discussed in the normalization section, the same criteria apply for both the physics and the Rbeam triggers. The description of the beam selection requirements is given in the following paragraphs.

Reconstruction. All beam muons used in this analysis must be reconstructed. This is a quality cut on the resolution/accuracy of the kinematic variables.

Single Intime Beam. The incoming muon is required to be the only muon in the event and to be in the same RF bucket in which the trigger fired. The SBT schintilator planes are used to obtain the timing information on the beam muon. The requirement is that all the SBT counters intersected by the beam found in the PBT wire chambers fired. At least six SBT planes must be intersected. With this requirement the events selected will have one beam associated with the event and one and only one beam present in the spectrometer, avoiding systematic effects at the reconstruction level (assigning the wrong beam or forward spectrometer muon to the event).

Beam Phase Space. The beam muons entering the experimental hall have a wide spectrum of energy. The distribution has a mean value $\sim$ 465 GeV and long tails (figure 4.9).

Since the cross-section depends on the energy of the incoming particle and our beam is not monoenergetic, the accepted beam muons are required to have an energy in the range of 380 GeV to 650 GeV inclusive. There is also another reason why the very low momentum beams are removed. They might suffer the effect of multiple Coulomb scattering in the beam spectrometer, an effect that is not taken into account in the beam momentum calculation. In addition, in order to take into account the correct amount of target material in the cross-section normalization, each beam is required to traverse the target in its full length. Also to successfully deal with the out-of-target scatters (page 103), the events originated on the target vessel walls (radial dimension) must be eliminated.

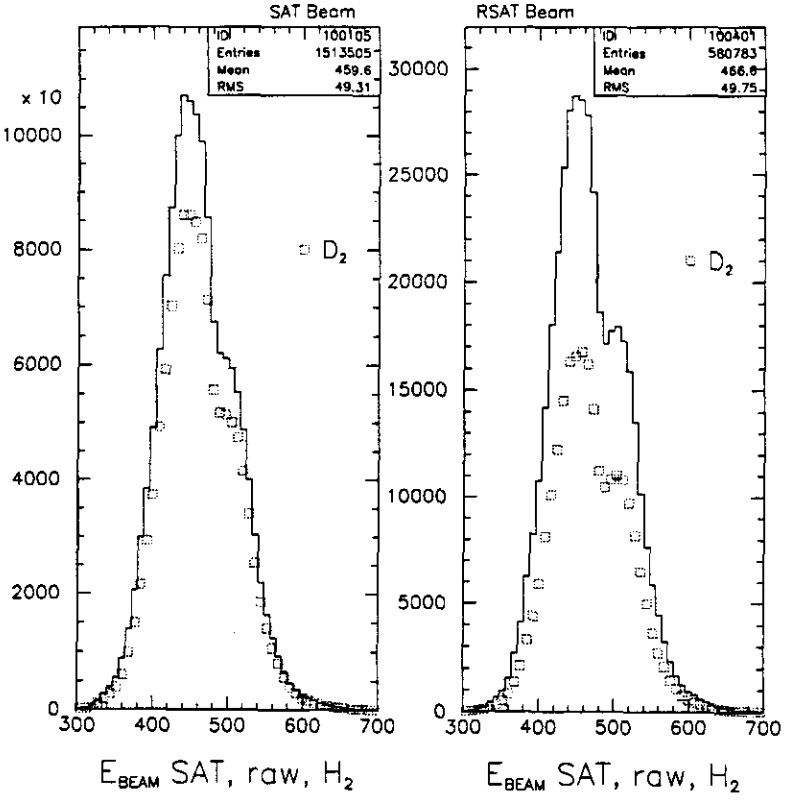

Figure 4.9: Raw Beam Energy

The above requirements result to a fiducial volume cut that further restricts the acceptable beam phase space. The beam should transverse the target in the box defined by:

1. $-0.015m \leq Y_{beam} \leq 0.015m$ at $X_{beam} = -13.0m$ and at $X_{beam} = -12.0m$
2. $-0.020m \leq Z_{beam} \leq 0.026m$ at $X_{beam} = -13.0m$ and at $X_{beam} = -12.0m$

The Y_{beam}, Z_{beam} beam particle coordinates are measured at PBT station 4 ($X_{beam} = -12.5m$) and then since the target is in an essentially magnetic field free region a straight line extrapolation is used to find where the track intercepts the upstream and downstream target faces. The track slopes used in the extrapolation are those determined by the offline reconstruction/fitting process.

This cut results to a $\sim 30\%$ rejection of beams, but it is necessary since in the 91 data taking period the beam was not centered in the target.

Software Simulation. In order to avoid systematic effects due to electronic noise, each beam has to satisfy in software its corresponding definition, using the information from all trigger elements that form that definition. This means that the combination of hodoscope elements that defines the beam in the hardware is verified in software, using the latch information. The software package for the SAT trigger simulation, which is the most complicated since it has to simulate the SAT floating veto, is described in [65].

The fraction of Rbeam events passing the beam definition cuts for RSAT trigger is listed in Table 4.5 (Sample I) and Table 4.6 (Sample II) and for RCAL trigger in Table 4.7 (only Sample II data for CAL trigger). The boundary between the two samples is run block 21601 (September 6, 1991), and it is defined by the change in the D_2 target composition (page 116). In the above tables the fraction of events that belong to runs identified as problematic is also shown for completion. The criteria for a run block to be marked as bad are based on the target and magnet condition,

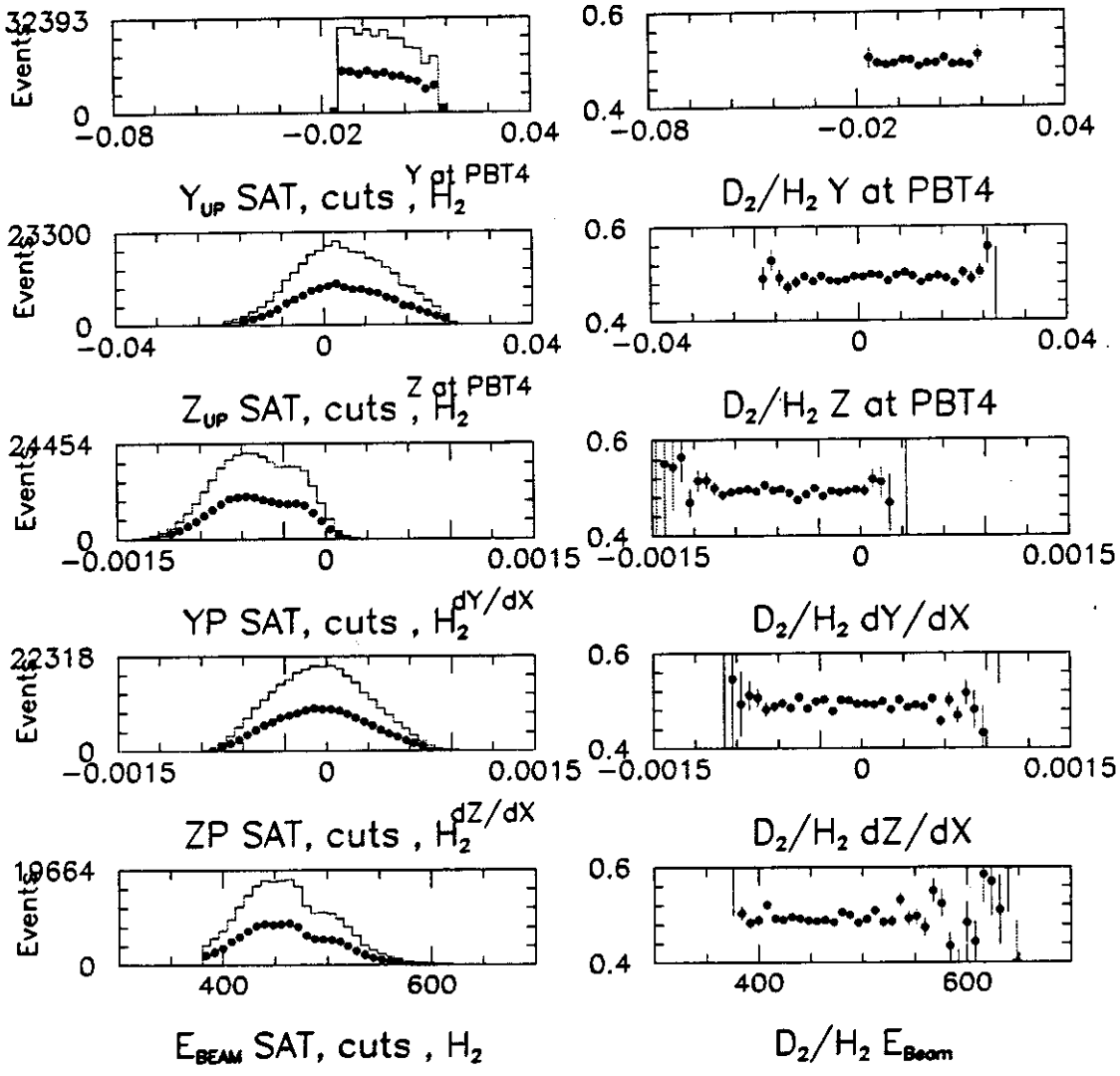

Figure 4.10: Beam Phase Space RSAT. Left hand side H_2 (line) and D_2 (bullets) superimposed. Right hand side D_2/H_2

information taken from the 91 spill database [69] and listed in Table A.1. During these run blocks the data are taken only on one target. Since during the 1991 run the H_2 target had more problems than the D_2 target, the requirement that both targets were operational removed more D_2 than H_2 data. Another category of bad runs are the runs that the chambers were filled with unclean gas mixture. Table 4.4 lists the rejected run blocks. Also events that the calorimeter reported some decoder error

Table 4.4: Run blocks removed from the σ_n/σ_p analysis

Run block range	Comment
21125-21330	Bad Gas I
21305-21428	no H_2 target
21449-21463	no H_2 target
21296-21298	NMRE magnet high
21600-21643	no D_2 target
21885-21943	Bad Gas II
21990-22015	no H_2 target

are removed from both the physics sample and the Rbeams. Each line of the tables is inclusive, each cut is applied to the events passing the previous cut. The results

Table 4.5: Number of RSAT passing Beam Cuts. Sample I

Cut	H_2		D_2		Empty Liquid	
	Events	Fraction	Events	Fraction	Events	Fraction
Total	147755	100 %	116345	100 %	29933	100 %
Acceptable Run	146455	99 %	72120	62 %	24218	81 %
No CAL error	146362	99 %	72086	62 %	24206	81 %
Reconstructed and E_{beam} range	132805	90 %	65169	56 %	21770	73 %
Target Penetration	92222	62 %	45188	39 %	15067	50 %
Single Beam	87670	59 %	42939	37 %	14292	48 %
Trig. Simulation	82520	56 %	40402	35 %	13488	45 %

for the beam selection cuts applied on the physics triggers are listed in Tables 4.8 and 4.9 for SAT trigger Sample I and Sample II respectively and in Table 4.10 for the CAL trigger.

The beam selection criteria should result in a sample of selected Rbeam or physics trigger events that have the same distributions of the beam related variables for H_2

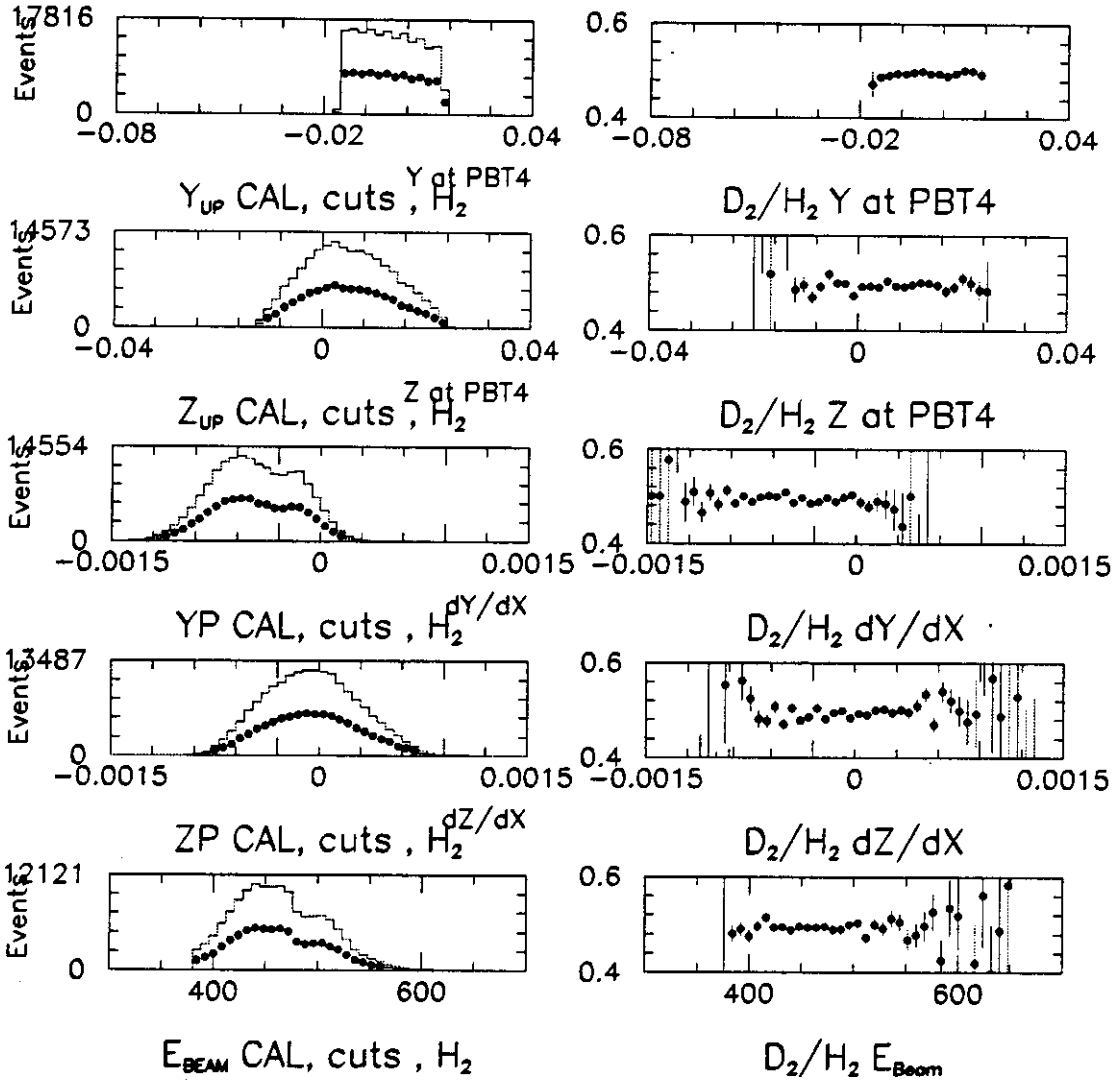

Figure 4.11: Beam Phase Space RCAL. Left hand side H_2 (line) and D_2 (bullets) superimposed. Right hand side D_2/H_2

Table 4.6: Number of RSAT passing Beam Cuts. Sample II

Cut	H_2		D_2		Empty Liquid	
	Events	Fraction	Events	Fraction	Events	Fraction
Total	433028	100 %	219580	100 %	78572	100 %
Acceptable Run	422384	98 %	208780	95 %	71498	91 %
No CAL error	422244	98 %	208717	95 %	71466	91 %
Reconstructed and E_{beam} range	369190	85 %	182717	83 %	62516	80 %
Target Penetration	268661	62 %	133075	61 %	45623	58 %
Single Beam	257045	59 %	127268	58 %	43636	56 %
Trig. Simulation	252537	58 %	125144	57 %	42870	55 %

and D_2. The distributions of the position at a fixed plane (PBT4), the slopes and the beam energy are compared and the ratio D_2/H_2 is formed for each one of them. The results for RSAT triggers are shown in figure 4.10 (full sample) and for RCAL in figure 4.11. There is no dependence of the ratio in any of the examined variables. The beam illuminating both targets is the same after the beam phase space cuts.

4.3.1 Physics Trigger Event Selection

After reconstruction, a series of selection cuts are imposed to the physics trigger sample that is used in the ratio analysis. These cuts are applied in addition to the beam selection criteria described in the previous section. The beam selection cuts are applied to the reconstructed beam of each physics trigger event. The selection criteria that used to define the physics event sample are described below.

Table 4.7: Number of RCAL passing Beam Cuts. Sample II

Cut	H_2		D_2		Empty Liquid	
	Events	Fraction	Events	Fraction	Events	Fraction
Total	423573	100 %	215664	100 %	77143	100 %
Acceptable Run	412049	97 %	203664	94 %	69420	90 %
No CAL error	411917	97 %	203596	94 %	69396	90 %
Reconstructed and E_{beam} range	360980	85 %	178025	83 %	60870	79 %
Target Penetration	213353	50 %	105194	49 %	36052	47 %
Single Beam	205439	49 %	101395	47 %	34725	45 %
Trig. Simulation	202790	48 %	100062	46 %	34271	44 %

Trigger. SAT or CAL trigger fired (hardware).

Allowed kinematic region. The kinematic region is selected based on resolution, trigger acceptance and radiative correction effects that will be closely examined in the following paragraphs. The kinematic variables are restricted in the following regions:

1. $Q^2 > 0.1 GeV^2$ for the SAT trigger events and $Q^2 > 10^{-3} GeV^2$ for the CAL trigger.
2. $0.1 \leq y_{bj} \leq 0.8$
3. $0.0001 \leq x_{bj} \leq 0.99$ for the SAT trigger events and $0.00001 \leq x_{bj} \leq 0.99$ for the CAL trigger.
4. $\nu > 40\ GeV$
5. $\theta_{scat} > 0.001 rad$ for SAT and $\theta_{scat} > 0.0001 rad$ for the CAL trigger

Table 4.8: Number of SAT passing Beam Cuts. Sample I

Cut	H_2		D_2		Empty Liquid	
	Events	Fraction	Events	Fraction	Events	Fraction
Total	435476	100 %	472753	100 %	57002	100 %
Acceptable Run	431788	99 %	284865	60 %	45288	79 %
No CAL error	431222	99 %	284491	60 %	45242	79 %
Reconstructed and E_{beam} range	409194	94 %	269573	57 %	42943	75 %
Target Penetration	290538	67 %	196273	42 %	27127	48 %
Single Beam	270796	62 %	182867	39 %	25260	44 %
Trig. Simulation	255432	59 %	172574	37 %	23844	42 %

The CAL trigger is accepted for lower Q^2 and θ_{scat} than the SAT because it does not trigger on the scattered muon, so its acceptance is not limited by the angular resolution of the SAT trigger elements.

Vertex Cuts. This fiducial volume cut for the vertex is the equivalent to the fiducial volume defining the target penetration requirement for the beams. The X coordinate is restricted to a range of two target lengths (it includes the target region plus half a target length on each end of the target). This will take care of vertex resolution effects in the empty target subtraction scheme that removes the out of target events on a statistical basis. The Y and Z coordinates are restricted to a range that excludes the scatters from the vessel walls (see page 103 for a more detailed discussion). The accepted range is :

1. $-13.5m \leq X_{vtx} \leq -11.5m$

Table 4.9: Number of SAT passing Beam Cuts. Sample II

Cut	H_2		D_2		Empty Liquid	
	Events	Fraction	Events	Fraction	Events	Fraction
Total	1078029	100 %	755290	100 %	113574	100 %
Acceptable Run	1054813	98 %	714719	95 %	102974	91 %
No CAL error	1053533	98 %	713716	95 %	102857	91 %
Reconstructed and E_{beam} range	1014653	94 %	687373	91 %	99228	87 %
Target Penetration	738126	68 %	519773	69 %	63433	56 %
Single Beam	695027	64 %	489337	65 %	59660	53 %
Simulation	682678	63 %	480967	64 %	58379	51 %

2. $-0.015m \leq Y_{vtx} \leq 0.015m$
3. $-0.020m \leq Z_{vtx} \leq 0.026m$

Resolution cuts. This selection removes events where the kinematic variables are not well measured.

1. The muon must have chamber information after the CCM magnet (either the drift chambers or the PSA on the scattered muon fitted track. This is the most important of these cuts. It assures that the fit of the scattered muon track is well constrained after the bending magnets.
2. $\nu/\delta_\nu > 4$
3. $\delta_\nu < 15GeV$
4. $\delta_{x_{bj}}/x_{bj} < 0.5$. This cut applies only to the CAL trigger due to the fact that the measured scattering angles are very small compared to the SAT

Table 4.10: Number of CAL passing Beam Cuts. Sample II

Cut	H_2		D_2		Empty Liquid	
	Events	Fraction	Events	Fraction	Events	Fraction
Total	463533	100 %	393721	100 %	41581	100 %
Acceptable Run	447903	97 %	358034	91 %	37028	89 %
No CAL error	445905	96 %	356442	90 %	36843	89 %
Reconstructed and E_{beam} range	438479	95 %	350644	89 %	36215	87 %
Target Penetration	263061	57 %	215844	55 %	19523	47 %
Single Beam	248746	54 %	204400	52 %	18427	44 %
Simulation	246160	53 %	202289	51 %	18240	44 %

trigger.

5. χ^2 vertex probability > 0.001. The vertex used is that of the incoming beam, the scattered muon and all the fitted hadron tracks.

6. Positive scattered muon. Any negative scattered muon is considered to be a failure of the pattern recognition.

The kinematic variables are shown in figures 4.12 and 4.13 for the SAT trigger and 4.14 and 4.15 for the CAL trigger, the arrows correspond to the cut values. The effect of each cut on the data is tabulated in tables 4.11, 4.12 and 4.13. The first entry is the number of events after the beam selection criteria applied (from tables 4.5, 4.6 and 4.7).

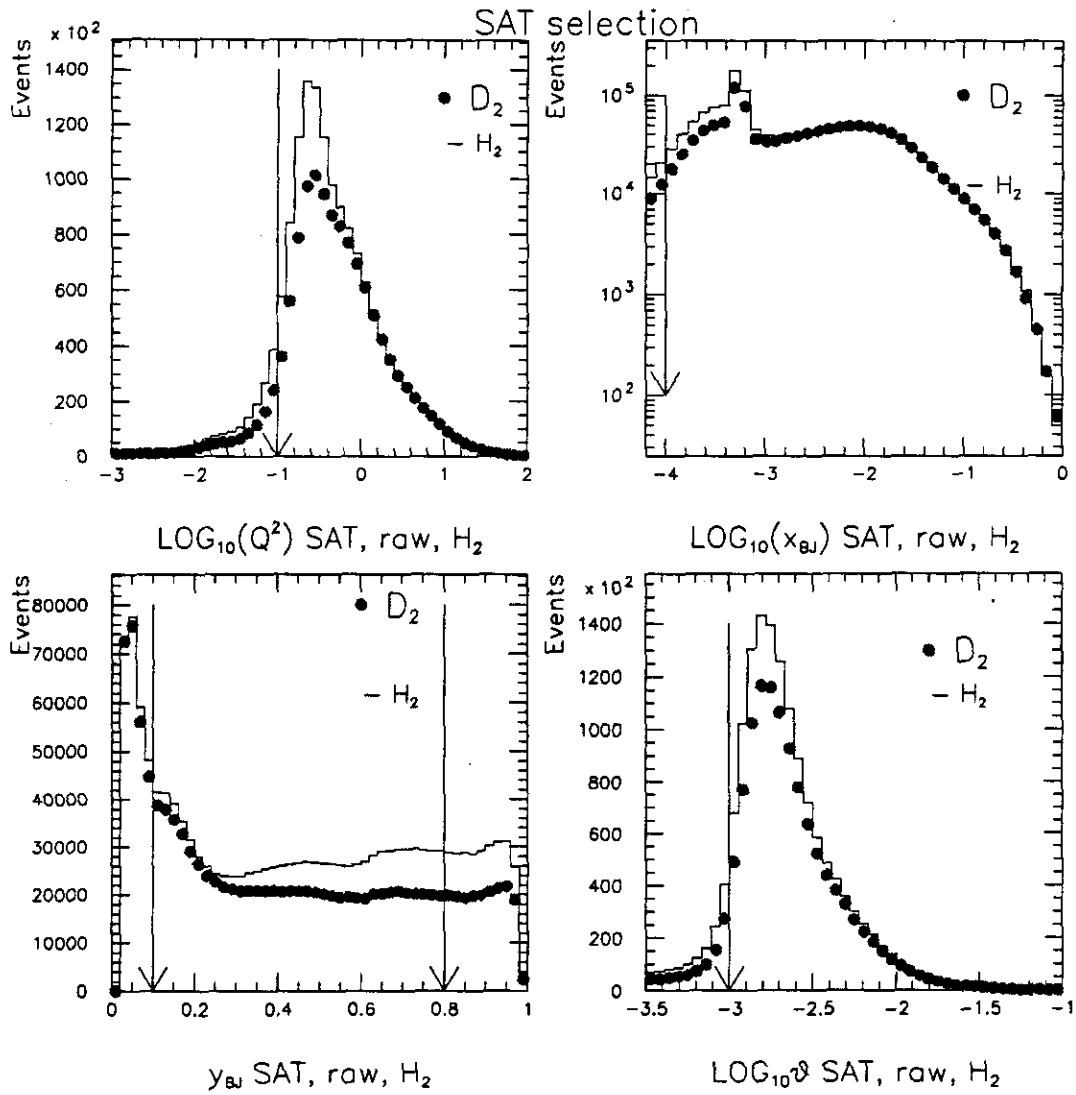

Figure 4.12: SAT trigger selection for D_2 (squares) and H_2 (histogram)

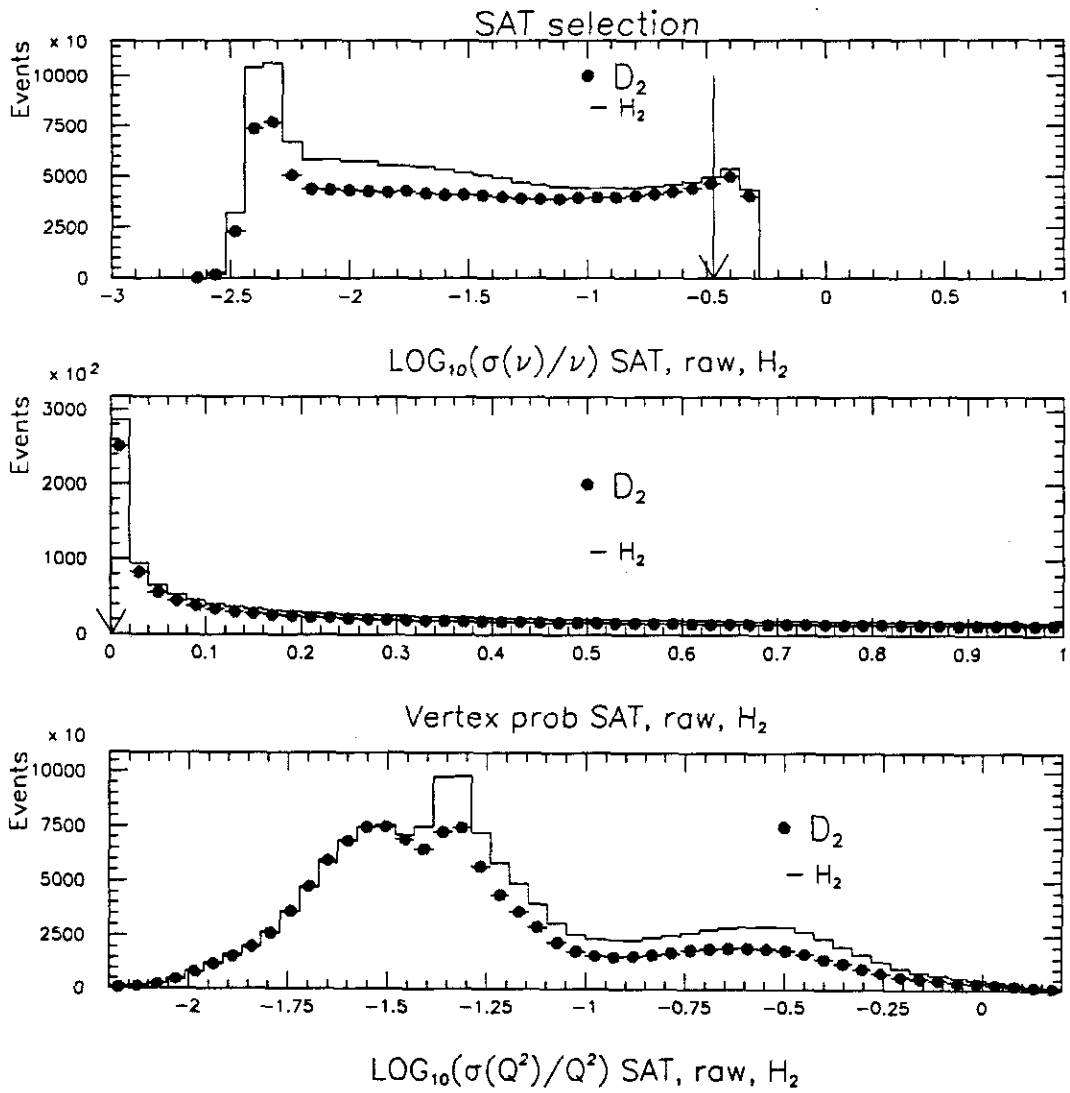

Figure 4.13: SAT trigger selection for D_2 (squares) and H_2 (histogram)

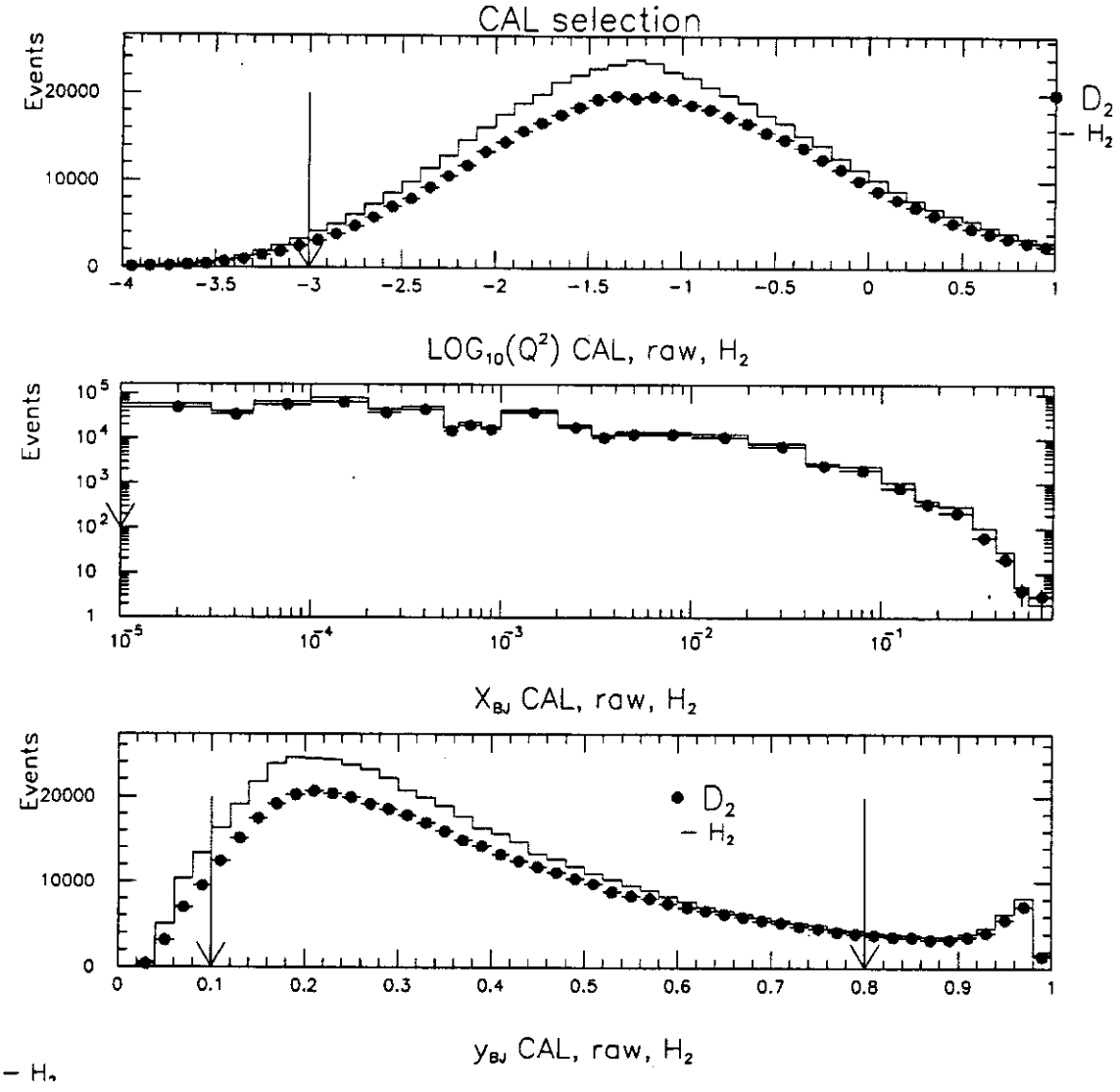

Figure 4.14: CAL trigger selection for D_2 (squares) and H_2 (histogram)

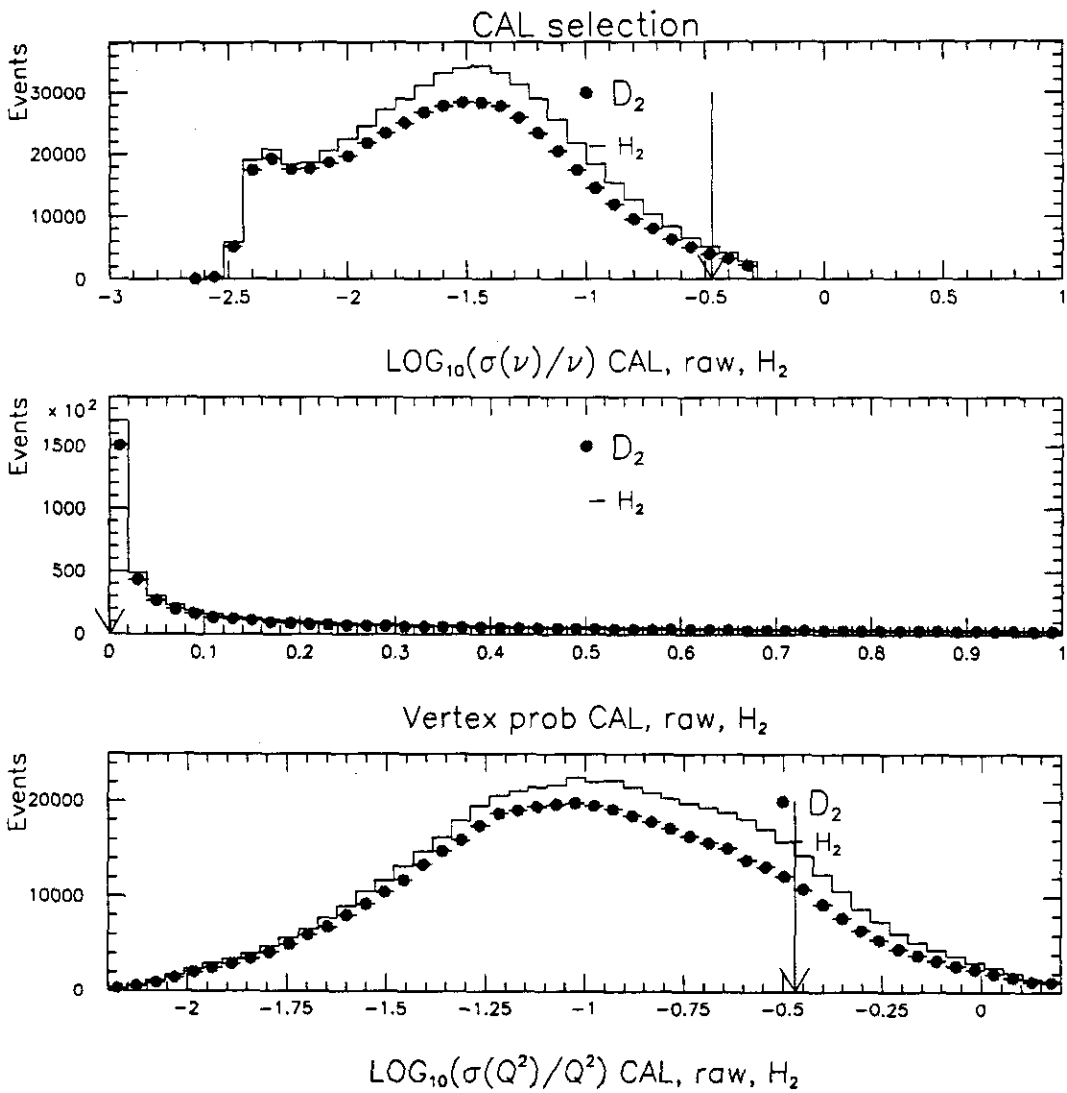

Figure 4.15: CAL trigger selection for D_2 (squares) and H_2 (histogram)

Table 4.11: Number of SAT passing Event Selection. Sample I

Cut	H_2		D_2		Empty Liquid	
	Events	Fraction	Events	Fraction	Events	Fraction
Total after Beam Cuts	255432	100 %	172574	100 %	23844	100 %
Resolution	174448	68 %	119051	68 %	15137	64 %
Vertex in Target	74816	29 %	65193	37 %	974	5 %
Kinematic	54722	22 %	48120	22 %	634	2 %

4.3.2 Monte Carlo validation

The use of a Monte Carlo program for any kind of correction requires that the detector and the triggers have been well simulated. This has to be checked before we use the Monte Carlo to correct the data distributions. We have to demonstrate that all inclusive distributions from reconstructed Monte Carlo are similar to the measured distributions (data). This is not enough since even if all one-dimensional distributions are equal, the multivariate distribution need not be the same. In this analysis we will make the assumption that if all one-dimensional distributions show agreement between the data and the Monte Carlo, then the Monte Carlo describes the data reasonably well.

To compare Data and the Deep Inelastic Scattering (DIS) Monte Carlo, the $\mu - e$ events have to be removed from the Data, since the Monte Carlo does not include them. Another way to do the comparison would be to mix DIS Monte Carlo with $\mu - e$ Monte Carlo events. For the Data and Monte Carlo comparison, and only for that, events are removed if:

Table 4.12: Number of SAT passing Event Selection. Sample II

Cut	H_2		D_2		Empty Liquid	
	Events	Fraction	Events	Fraction	Events	Fraction
Total after Beam Cuts	682678	100 %	480967	100 %	58379	100 %
Resolution	425821	62 %	302911	63 %	33151	57 %
Vertex in Target	208454	30 %	182310	38 %	2431	4 %
Kinematic	150048	22 %	132299	28 %	1524	2 %

Table 4.13: Number of CAL passing Event Selection. Sample II

Cut	H_2		D_2		Empty Liquid	
	Events	Fraction	Events	Fraction	Events	Fraction
Total after Beam Cuts	246160	100 %	202289	100 %	18240	100 %
Resolution	195473	79 %	161364	80 %	14324	77 %
Vertex in Target	103936	42 %	106690	53 %	1285	7 %
Kinematic	91073	38 %	93674	45 %	1078	6 %

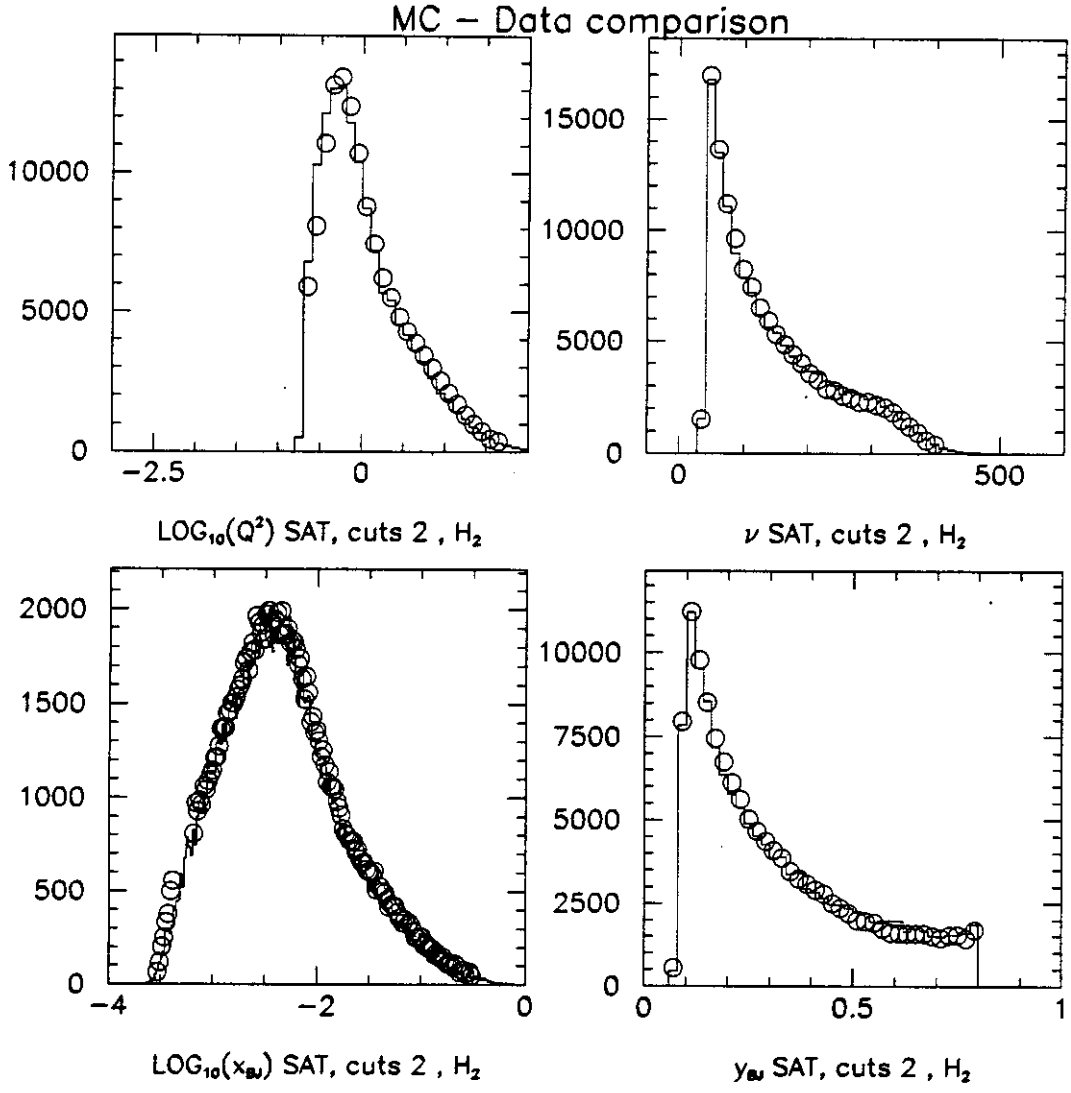

Figure 4.16: Monte Carlo validation.

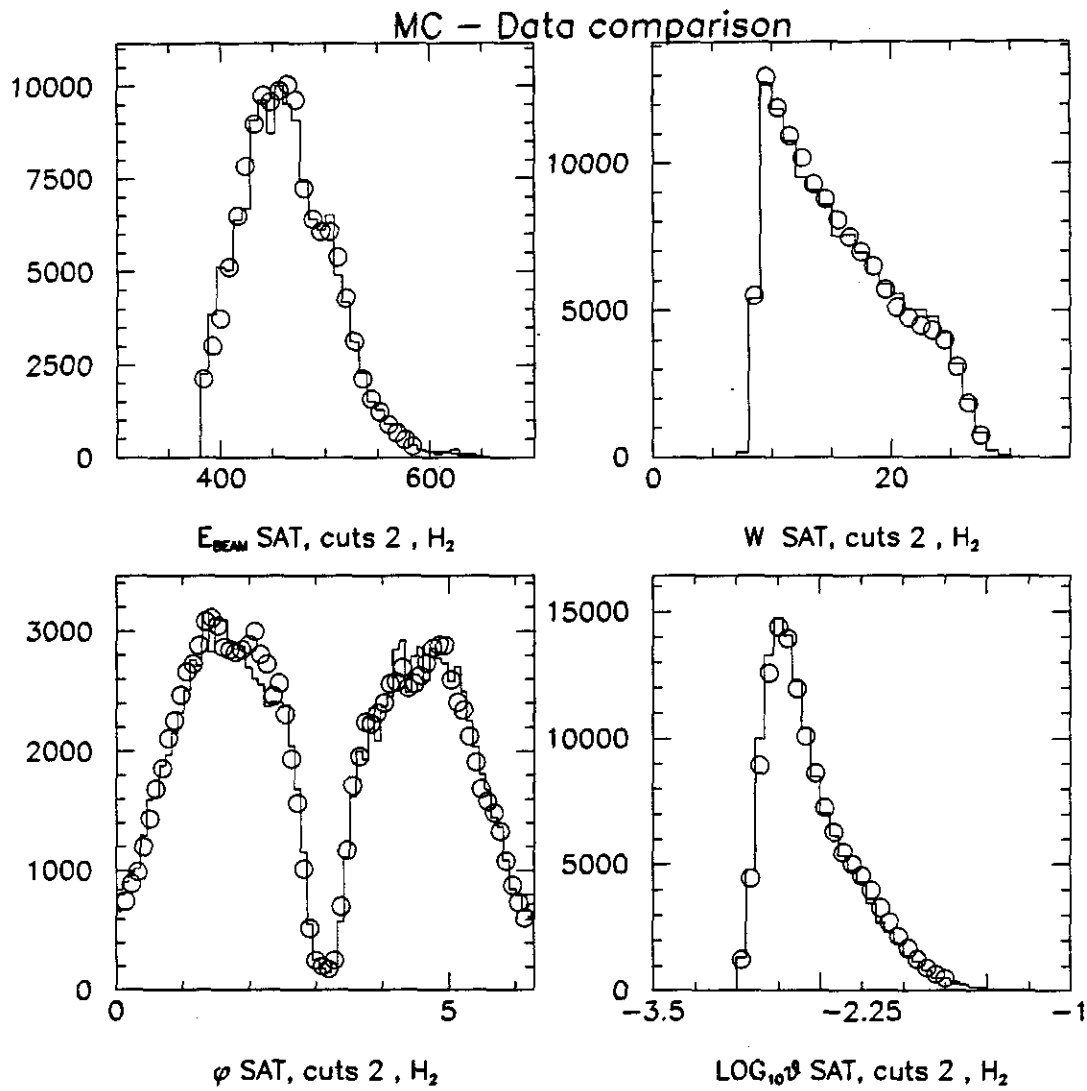

Figure 4.17: Monte Carlo validation.

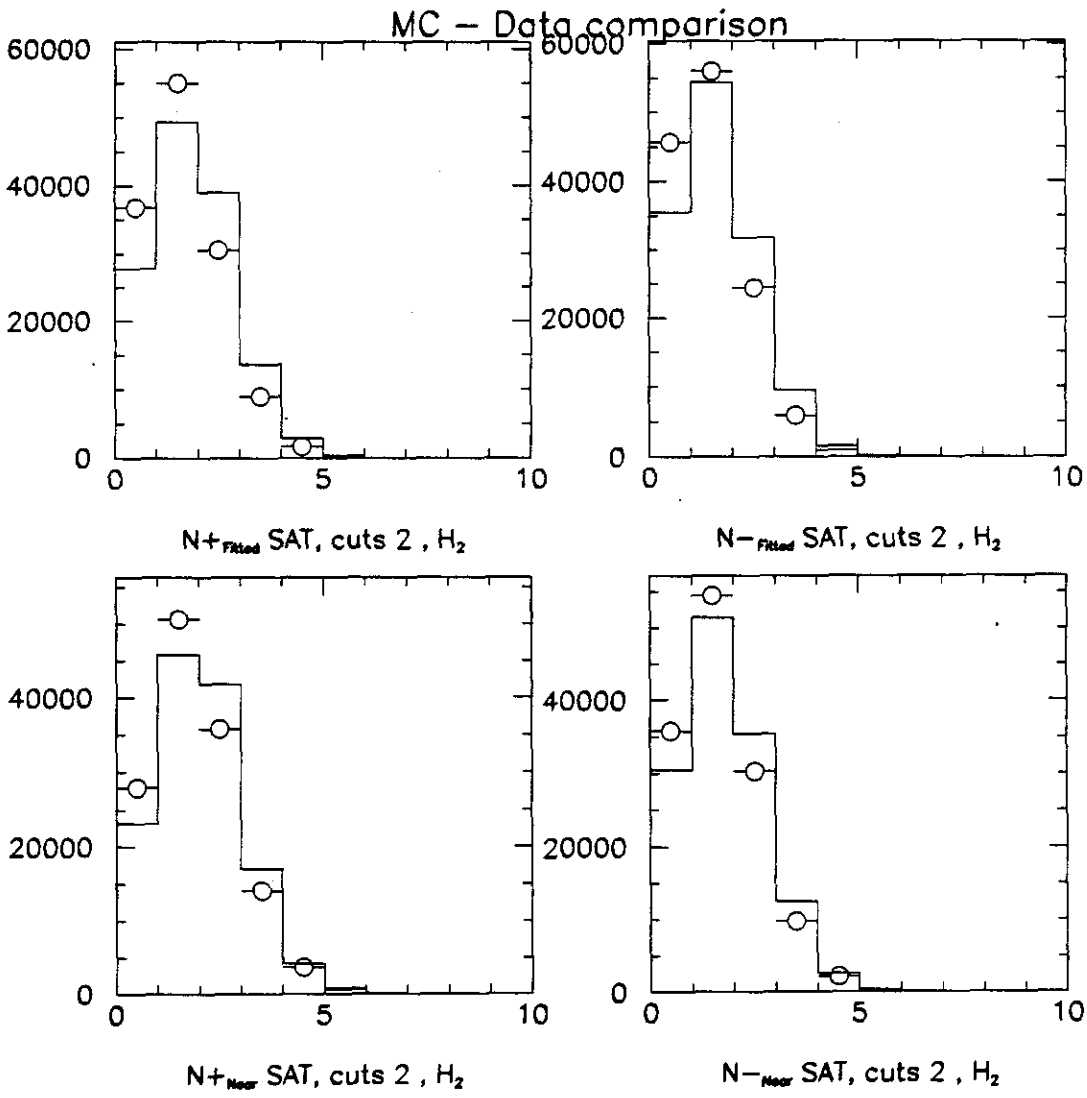

Figure 4.18: Monte Carlo validation.

1. $0.00042 \leq x_{bj} \leq 0.00060$. Remove the $\mu - e$ bin.

2. No positive tracks and only 1 negative track having a calorimeter cluster associated with it and momentum $> 0.90 \times \nu$

Also since the MC events are generated with $Q^2 > 0.2 GeV^2$ the same cut was applied to the Data. The Monte Carlo events were generated with beam distributions and hardware efficiencies that sample the run period as a function of time [64]. This is not absolutely necessary for the ratio measurement because of the cycling targets that cancel time dependent effects. The comparison for some of the inclusive distributions is shown in figures 4.16 - 4.18. The plots are normalized to the total number of entries. The open symbols are for the data points and the histogram for the Monte Carlo. The agreement is very good, apart from the multiplicity distributions in figure 4.18. This disagreement is not a problem with the physics generator, it is rather a problem with the sigmas used in the track fitting from the Monte Carlo. This results to a discrepancy between the track multiplicity distributions from Data and the Monte Carlo, since more Monte Carlo tracks appear to be fitted to the primary vertex. This is supported by the fact that the agreement between Data and the Monte Carlo is much better for the class of tracks defined as near tracks (plot of N_{near} distribution, second raw of plots in figure 4.18). These tracks are classified according to their absolute distance from the vertex rather than the normalized distance to the vertex (using the sigma of the fit).

4.3.3 Trigger acceptance-efficiency

We will define the acceptance of the trigger as the fraction of the total events of any type in some region of the kinematic domain that the trigger registers in that region; assuming that the hardware has no inefficiencies. For a positive muon trigger that triggers on the presence of the scattered muon, this acceptance is the same for all classes of events. For veto muon triggers with a veto in front of the steel absorber,

like the SAT trigger or for hadronic final state triggers like the CAL trigger, the previous statement is not by definition correct. Assuming that an event of type i is produced with some probability P_i and detected with probability D_i, then the ratio $A_i = D_i \cdot P_i/P_i$ is the acceptance A_i for that type of event in that domain (where i can be a DIS event, a radiative event, a $\mu - e$ event or even a class of DIS events with certain topology, and so on). The trigger acceptance A(x_{bj},Q^2) for the inclusive sample will then be:

$$A(x_{bj}, Q^2) = \frac{\sum_i P_i D_i}{\sum_i P_i} \tag{4.5}$$

with $\sum_i P_i$ normalized to the total number of produced events. The trigger efficiency is defined to be the combined effect of the scintillator efficiency, noise, timing and false vetoes caused by showers in the steel absorber.

What we are interested in for the cross-section ratio measurement is the differences in trigger acceptance and trigger efficiency between the two targets. Furthermore, we are measuring the process muon-nucleon scattering, so the $\mu - e$ elastic scatters should be excluded. This is not just a matter of definition, because we are normalizing the event yields per nucleon and the number of electrons per nucleon on H_2 is two times that of the D_2. Also the acceptance for this process is different from the acceptance for DIS or radiative events. The CAL trigger is designed to exclude $\mu - e$ events and the SSA veto element of the SAT is preferably vetoing these events because of the electron being in the same plane as the beam and scattered muons. Using the notation of equation 4.5, both $P_{\mu-e}$ and $D_{\mu-e}$ are different between the two targets, and also $D_{\mu-e}$ is different from the D_i of DIS and radiative events. We can see that this contribution should be excluded from the $A(x_{bj}, Q^2)$ measurement. The SAT acceptance for $\mu - e$ from the Monte Carlo is shown in figure 4.19 and should be compared with the same plot for muon-nucleon scattering from figure 4.21. The $\mu - e$ elastic is not a problem if we are using the Monte Carlo to determine the geometric acceptance of the trigger, since the process can be trivially excluded. It becomes important for the CAL trigger studies, since the CAL trigger is not simulated. In

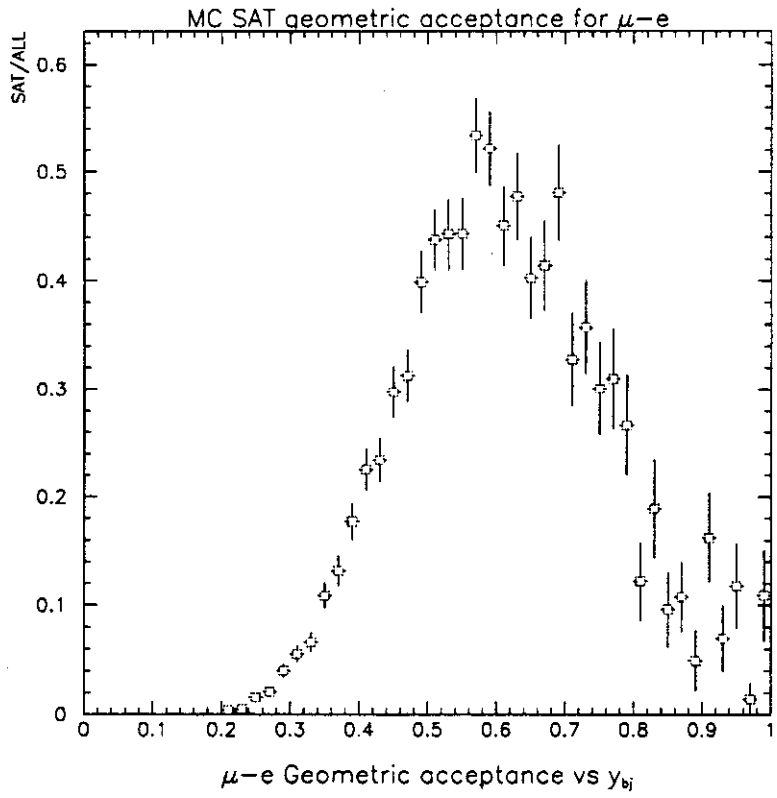

Figure 4.19: y_{bj} $\mu - e$ SAT trigger acceptance from MC.

that case we use a sample of selected events from all the muon triggers and this selection excludes the $\mu - e$ elastic. It is also important when we use monitoring triggers (like SATPS) to examine the effect of the SSA veto on the SAT trigger. Due to the target cycling, the efficiency effects cancel to a very good approximation in the ratio. The acceptance effects on the ratio are examined separately for the SAT and CAL triggers.

SAT trigger There is no argument to support the idea that the geometrical acceptance of the trigger is different for each target, given that the beam phase space cuts constrain the beam to be well inside the target. What is different is the effect of the SSA veto in front of the steel absorber. This means that differences in the topology of the final state will result in acceptance differences, given that a final state particle can veto the event. The acceptance behind the absorber should not have any target dependent effects, since it just depends on the muon characteristics. We check the acceptance effects on the two targets from Monte Carlo. The quantity

$$\frac{SATevents}{ALLevents}$$

is plotted as a function of x_{bj} and y_{bj} and then the ratio is examined for differences. The results are shown in figures 4.20 and 4.21. Note that the only event selection that defines the numerator of the previous expression is the SAT trigger requirement. To the level that the Monte Carlo correctly simulates the final state from the two targets, there is no difference in the trigger acceptance between H_2 and D_2. This is only in the kinematic region above $x_{bj} > 10^{-3}$ and $Q^2 > 3GeV^2$, where the parton distributions used in the Monte Carlo generation are constrained by the data entering the global fits. For the region of lower x_{bj} and Q^2 the only check of the validity of the simulation is the agreement between Data and the Monte Carlo in a comparison of the final state quantities.

In order to enhance our understanding of the SAT trigger, we use Data from the SATPS monitoring trigger. The SATPS has the same definition as the SAT

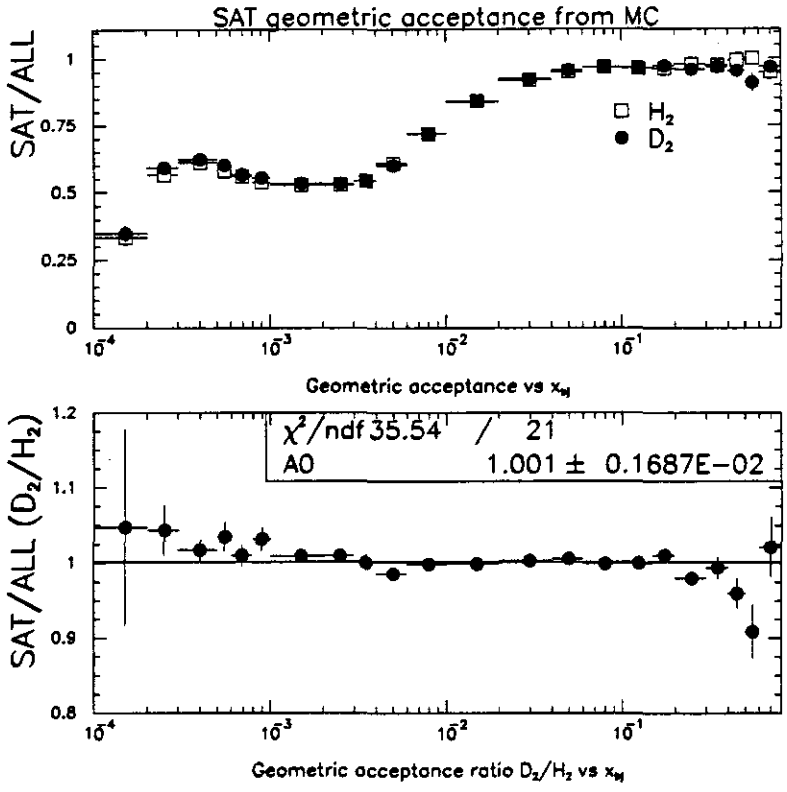

Figure 4.20: x_{bj} SAT trigger acceptance from MC.

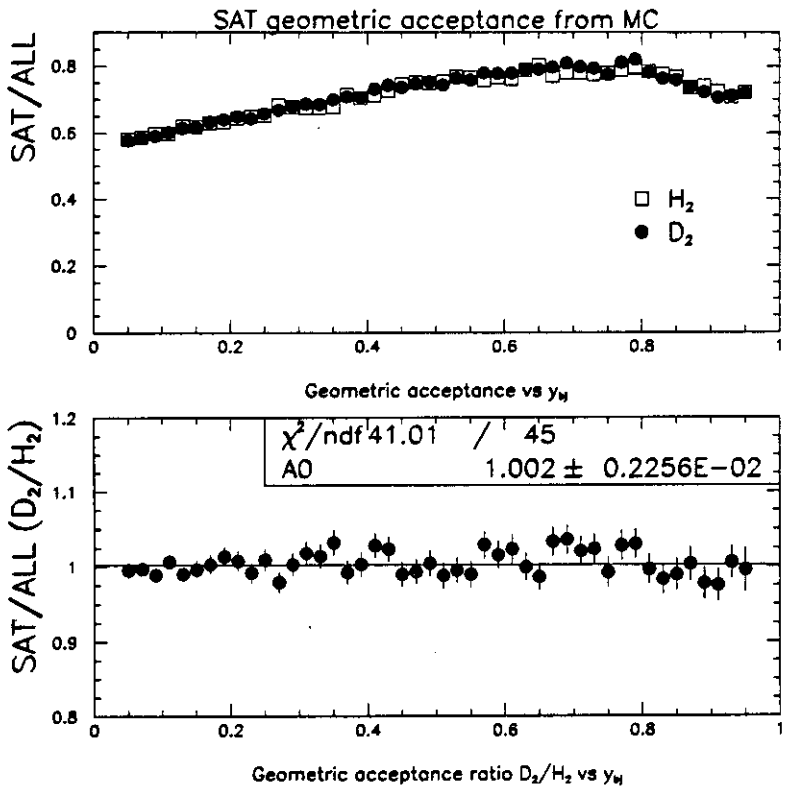

Figure 4.21: y_{bj} SAT trigger acceptance from MC.

but with no SSA veto (see section 2.5). We define a clean sample of SATPS events and we form the quantity

$$\frac{SAT \odot SATPS}{SATPS}$$

Given that the only difference between the two triggers is the SSA veto, we can study its effect on the ratio of the acceptances for the two targets. The SATPS monitoring sample is defined applying the same physics trigger event selection described previously. Also we apply the calorimeter based selection that will be described in the next section, in order to remove the electromagnetic background, which has different acceptance than the inelastic events. This background includes $\mu - e$ elastic scatters and hard target bremsstrahlung events. Since these cuts are applied, the conclusions about the acceptance effects of the SAT trigger in the σ_n/σ_p ratio measurement from this measurement are bound to be useful only for a sample defined with the exact same cuts. Using the formalism of equation 4.5 we see that this statement applies to the subset of processes i that the selection is retaining in the sample. The results for different kinematic quantities are shown in figures 4.22 and 4.23. The fit on the x_{bj} dependence of the ratio of acceptances is done for the points below 10^{-3}. The answer is consistent with no dependence ($\sim 1\% \pm 1\%$).

CAL trigger The calorimeter trigger acceptance depends on the performance of the E665 calorimeter and its time dependence. This is because the gas gain changes its response as a function of time, while the voltage threshold that determines the trigger remains constant. This should not introduce any effect in the cross-section ratio measurement, since the event samples from the two targets are composed of the same statistical mixture. The CAL acceptance is checked versus a sample selected from the muon triggers SAT,SATPS,SVS using the quantity:

$$\frac{CAL \odot (SATPS \oplus SAT \oplus SVS)}{(SATPS \oplus SAT \oplus SVS) \odot RCAL}$$

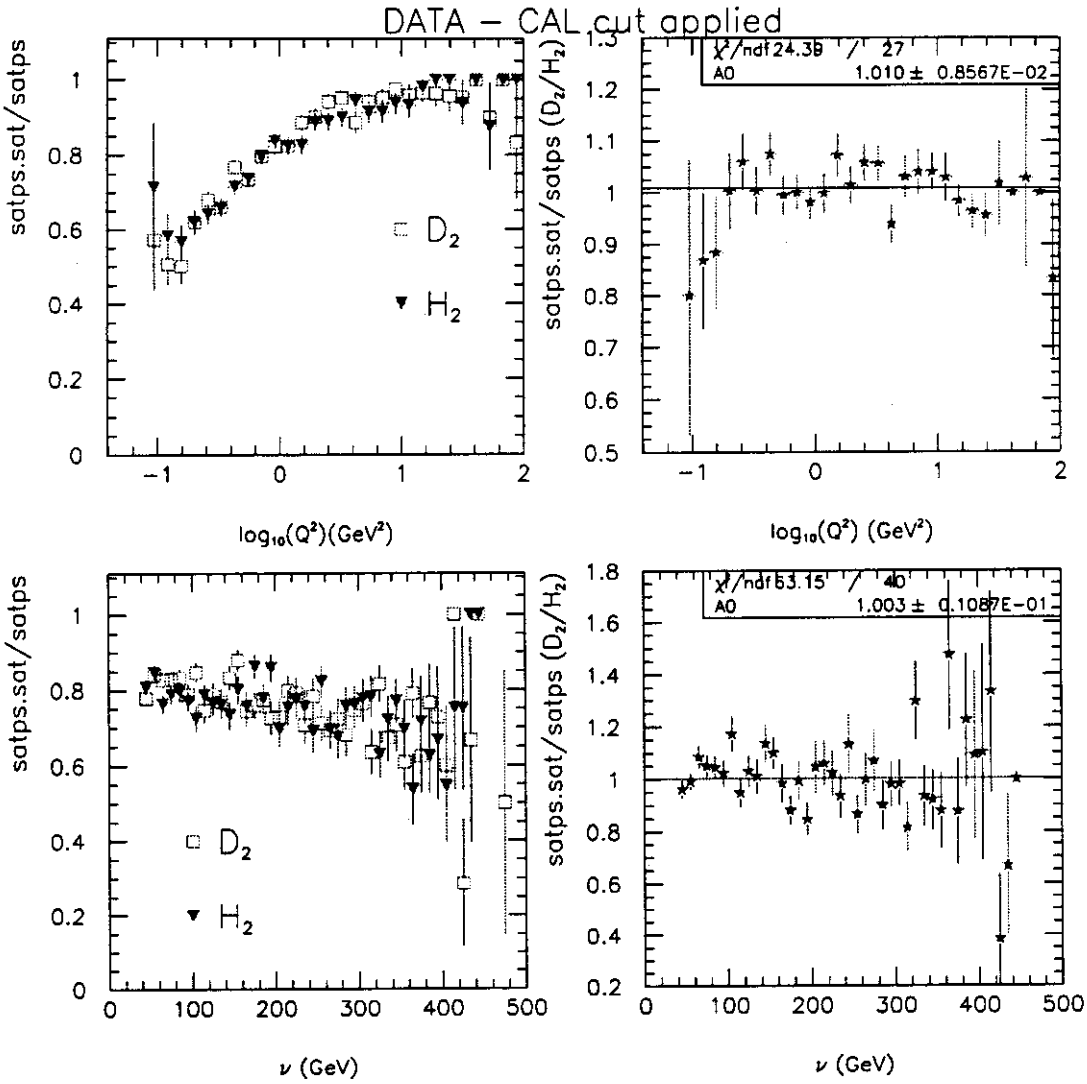

Figure 4.22: SAT trigger acceptance from Data and SATPS trigger.

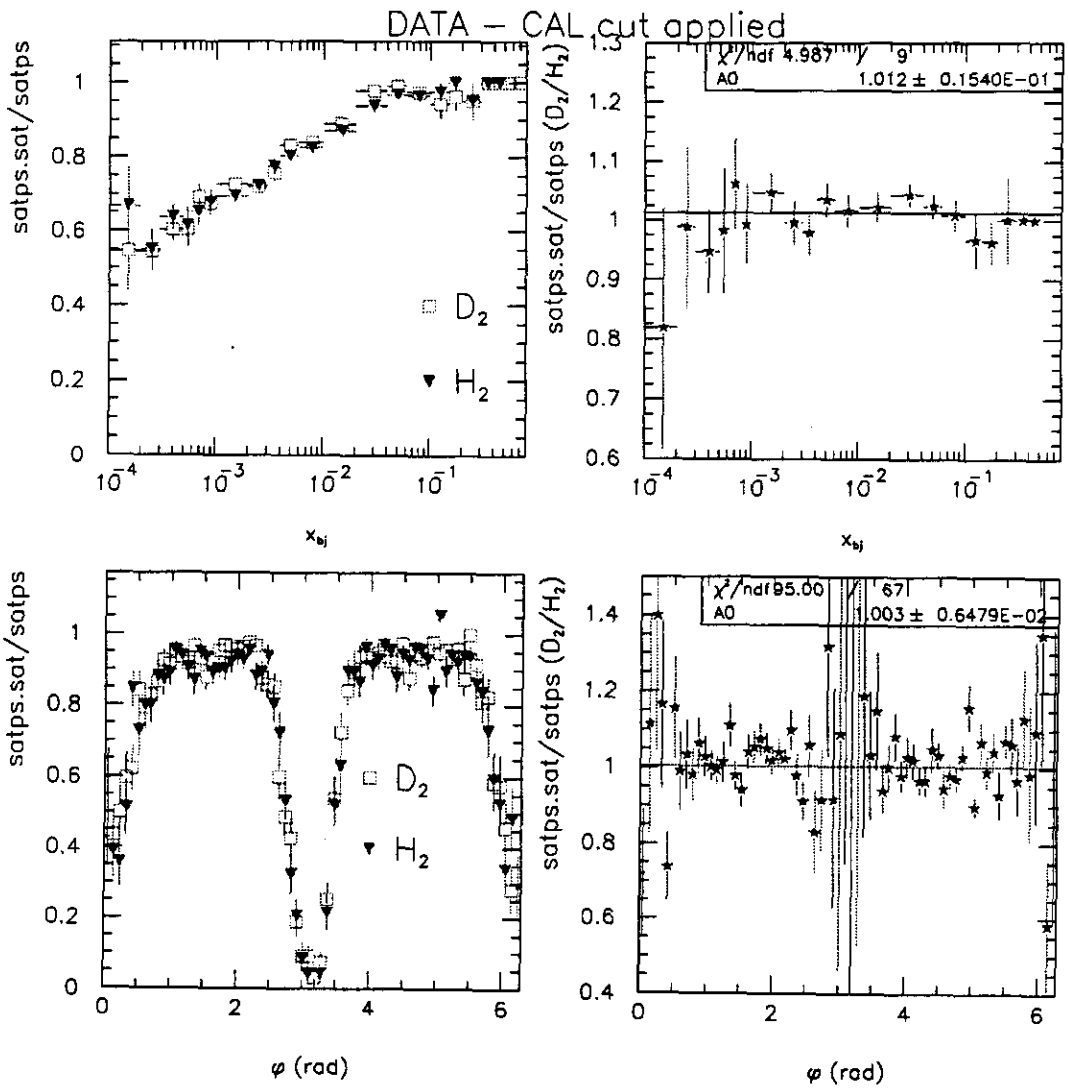

Figure 4.23: SAT trigger acceptance from Data and SATPS trigger.

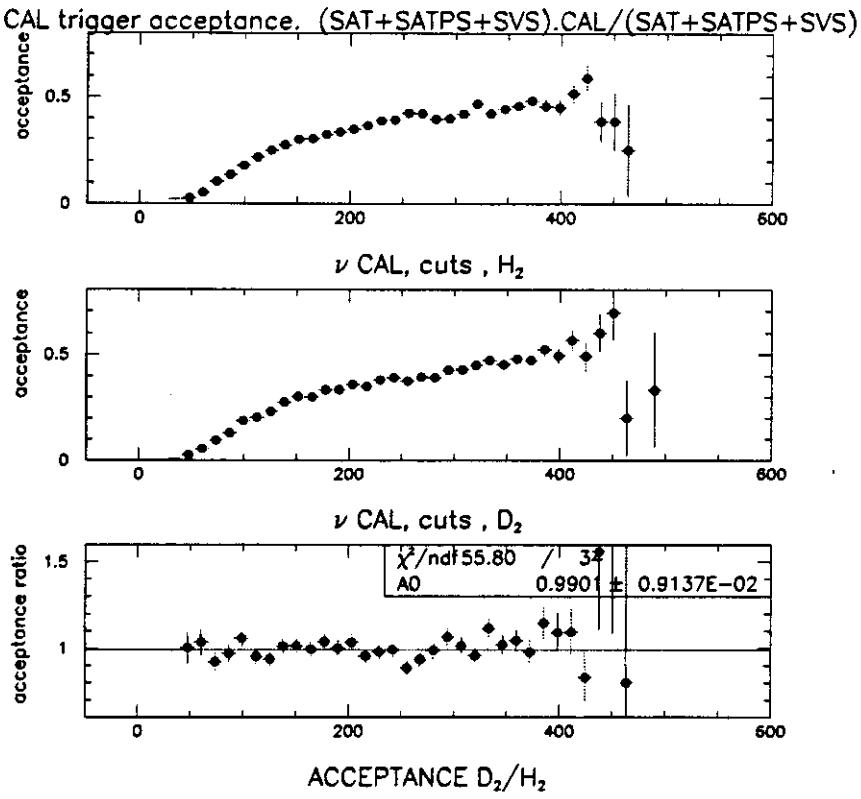

Figure 4.24: ν CAL trigger acceptance from Data (muon triggers).

The RCAL requirement in the denominator means that the beam for all events has to satisfy the calorimeter beam definition (RCAL). The requirements (selection criteria) that define this test sample are the same requirements that are used to define the SATPS sample used for the SAT trigger studies (kinematic plus calorimeter cuts) and are described in the previous paragraph.

The calorimeter trigger by construction excludes $\mu - e$ elastic and hard target bremsstrahlung events by triggering on the topology of the hadronic final state. To the approximation that inelastic, $\mu - e$ and bremsstrahlung event topology do not differ between the two targets, the trigger should not bias the ratio. We still have to establish that we can relate the partial cross-section ratio with the total cross-section ratio; this will be done in the following section. The two targets have similar lengths in radiation lengths, but D_2 is ~ 2 times longer in interaction lengths, so the distribution of secondary particles is different. Also the D_2 contributes coherent (from the nucleus) radiative events to the total cross-section, while H_2 does not have that component. The most important effect here is that of the difference in secondary interactions. The calorimeter trigger will fire if there is electromagnetic activity with some spread out of the scattering plane above some threshold. The source of these charged tracks or neutrals is not a parameter of the design. To the extent that we have established that the muon triggers are not sensitive to these effects, the results presented in figures 4.24 and 4.25 for the CAL trigger acceptance show that down to x_{bj} of 10^{-4} the CAL trigger is not introducing any bias to the ratio measurement. One way to understand this insensitivity of the calorimeter trigger to the difference in secondary interactions between the two targets is to assume that the secondary particles produced by rescattering in the target have the same probability to fire the calorimeter trigger as the primary particle that produced them, if it were not rescattering in the target. Assuming then that the primary particles from both targets have the same probabilities to fire the trigger, we end up with zero

net effect from the differences in interaction lengths. From the formulation of

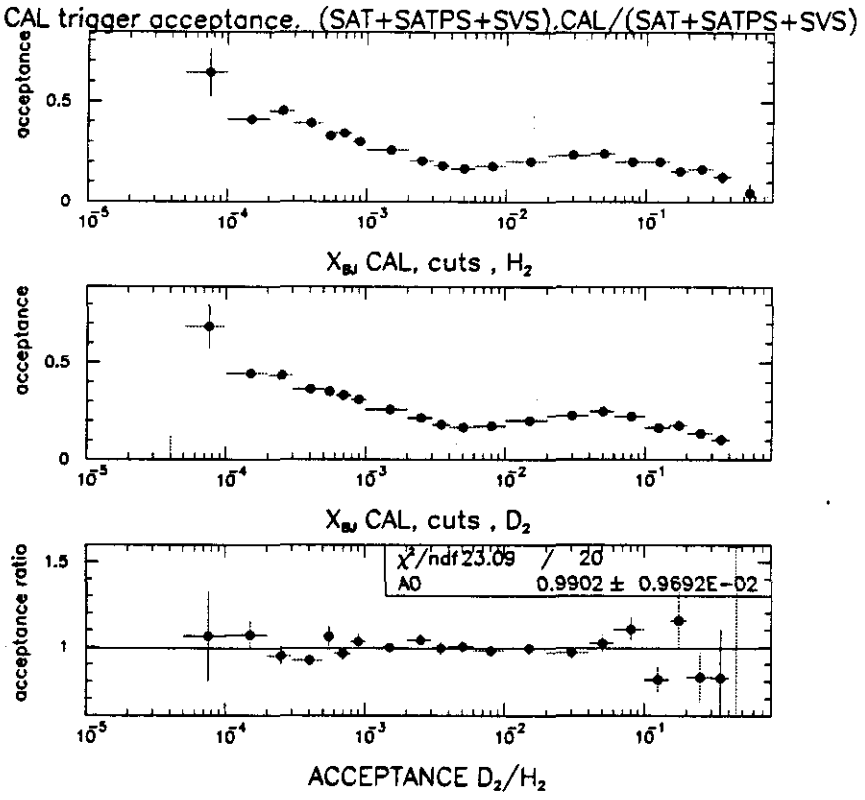

Figure 4.25: x_{bj} CAL trigger acceptance from Data (muon triggers).

equation 4.5 we see that for the components of the total cross-section that the trigger is sensitive to, the acceptance is the same.

4.4 Radiative Correction Application

4.4.1 Electromagnetic Background and Inclusive measurements

Our objective is to measure σ_n/σ_p, the ratio of the total neutron cross-section over the total proton cross-section in the single photon approximation. The only procedure that maintains a priori the definition of $\sigma_n^{measured}/\sigma_p^{measured}$ as the total cross-section ratio is the application of calculated radiative corrections. This statement is true under the condition that the trigger used to select the sample has no bias based on the final state (in the ratio measurement acceptance biases to a large extend factorize and cancel). If this is not true then the radiative correction method fails to the level that the initial, uncorrected sample is biased. Assuming that the measured total cross-section ratio is not biased, the problem of this method is that it requires the knowledge of the structure functions in the allowed region for photon radiation (see chapter 1). The data presented in this analysis extend to a region that the structure functions are not yet measured, complicating the radiative correction procedure. Another problem of course are the $\mu - e$ elastic events. They have to be removed, but the only cut that would be compatible with radiative corrections is a cut that is 100% efficient and 100% pure, since radiative correction techniques apply to total event rates.

A different approach will be to identify and remove all radiative events, on an event-by-event basis, using the final state event properties. Experiment 665 has an Electromagnetic Calorimeter that allows identification of electrons and photons above its energy resolution cutoff. Furthermore, the Calorimeter trigger (triggering on the properties of the hadronic final state) has extended acceptance on the kinematic plane as compared to the acceptance of the muon triggers, and it is designed to exclude bremsstrahlung and $\mu - e$ elastic events. By definition any method that uses a cut or a trigger that selects events based on the topology of the event is not measuring the total cross-section. In order to use these techniques, corrections have to be applied on the

measured cross-sections. These corrections are based on the acceptance and efficiency studies for the selection, determined from Monte Carlo studies. Complementary to the Monte Carlo studies, another check for the calorimeter trigger is the study of the hadronic final state properties from the Data. This simply means the comparison of the distributions of the hadronic final state variables that the trigger probability depends on, between the two liquid targets, and that as a function of the kinematic variables. If these distributions are the same, then to the extent that they define the trigger probability, the trigger performance is similar for the two targets.

Our strategy for the measurement will be to use the calculated radiative corrections technique in the region that is applicable. Then we will extend the range of the measurement using the other two techniques in the region where the systematic errors are minimized. Fortunately this region corresponds to the small-x_{Bj} region, since there the cross-sections of the proton and the neutron are similar and cancellations of systematic effects are expected in the ratio measurement.

4.4.2 Application of the Method

In order to identify the non-radiative part of the cross-section in the cross-ratio measurement we use three different techniques. The first two involve the SAT muon trigger and the third the CAL trigger.

SAT and Radiative correction calculated This method is applied by correcting the Data in an event by event basis using weights calculated at the exact kinematics of the event. The radiative correction factors were calculated according to the prescription of Mo and Tsai [106] and Tsai [109]. These weights correspond to the fraction of the deep inelastic scattering cross-section over the total cross-section. The computer program FERRAD [110], version 35, was used to perform the numerical integrations. This program has been developed by members of the EMC and NMC collaborations. A detailed description of

the program can be found in Reference [111]. The structure functions F_2^d and F_2^p are essential input in the calculation. The structure functions used in this analysis were constructed using the NMC F_2 parametrization [47] for the high W^2 inelastic region, the low W^2 inelastic region parametrization from [103], the resonance region parametrization from [102] and the extrapolation of [104] to small-Q^2 for high W^2. The construction of the input F_2^p used in the radiative correction calculation (and also in the Monte Carlo generation) is described in [105]. The elastic form factors used in the calculation were from [107].

The numerical integration (from equ. A24 of [109]) in W was performed in 280 bins and for θ in 8×30 bins. The resolution parameter Δ (soft photon emission cutoff) was 500 MeV. The size of the radiative corrections on the ratio D_2/H_2 is shown in figures 4.26, 4.27 and 4.28, as a function of y_{bj} in x_{bj} bins. The procedure was applied as follows:

- The radiative correction factors were calculated in a y_{Bj} and x_{Bj} grid (30×30), for H_2 and D_2 targets.
- The Data were corrected in an event by event basis using the correction factor from the above grid. For each event a three by three table in y_{Bj} and x_{Bj} was defined from the closest points of the grid to the measured y_{Bj} and x_{Bj} of the event. The weight for the event was found by interpolation in that table.
- The empty target contribution was measured separately for each target, using the event per event weight technique. This means that the empty target data were used two times separately, with different weights (once for each of the H_2 and D_2 targets) and the corresponding yields were subtracted from those of the liquid targets. To quantify this, let us examine the contribution in the event yield in a kinematic bin when target j is in position in front of the beam (j can be either the H_2 or the D_2 target).

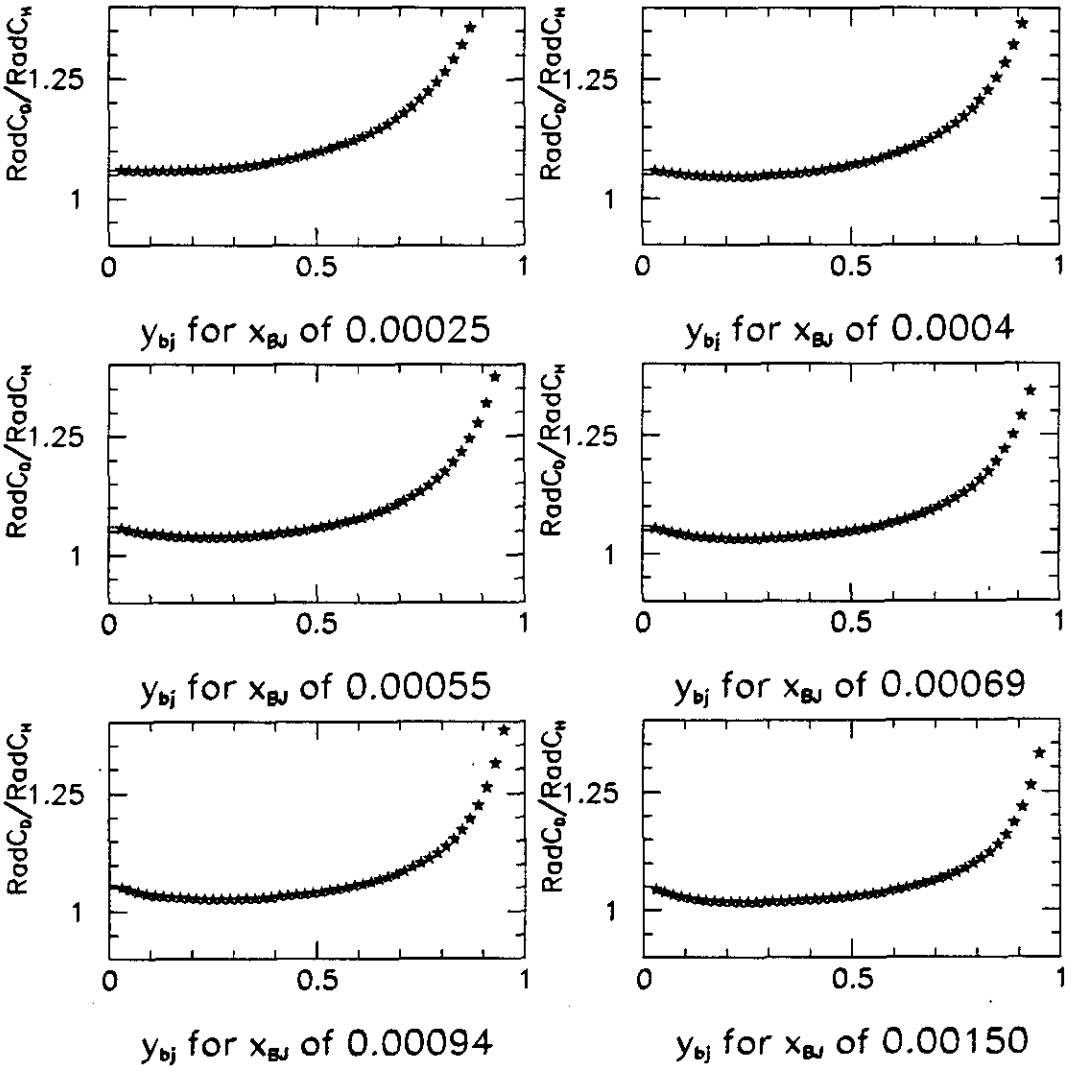

Figure 4.26: Radiative Correction Ratio (D_2/H_2).

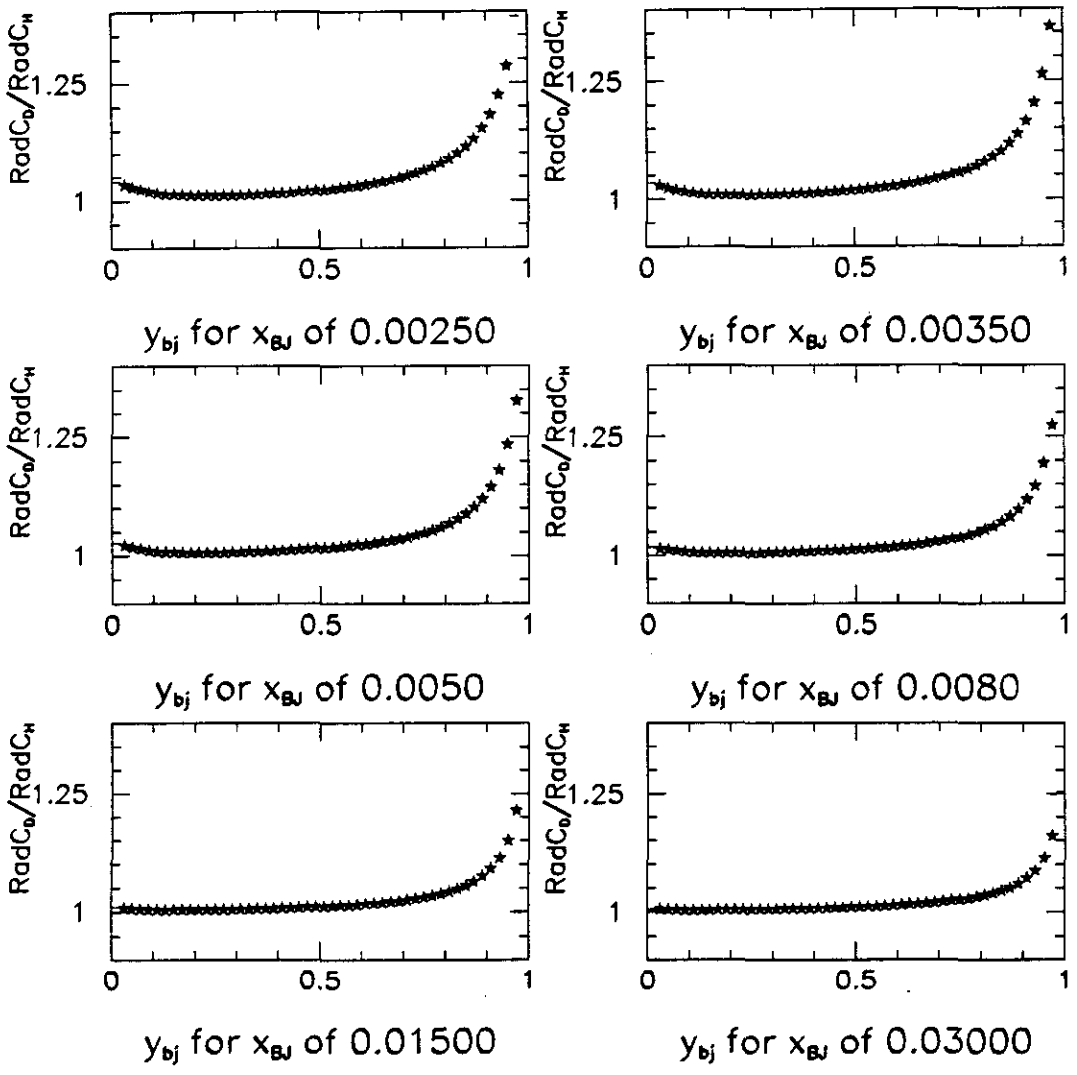

Figure 4.27: Radiative Correction Ratio (D_2/H_2).

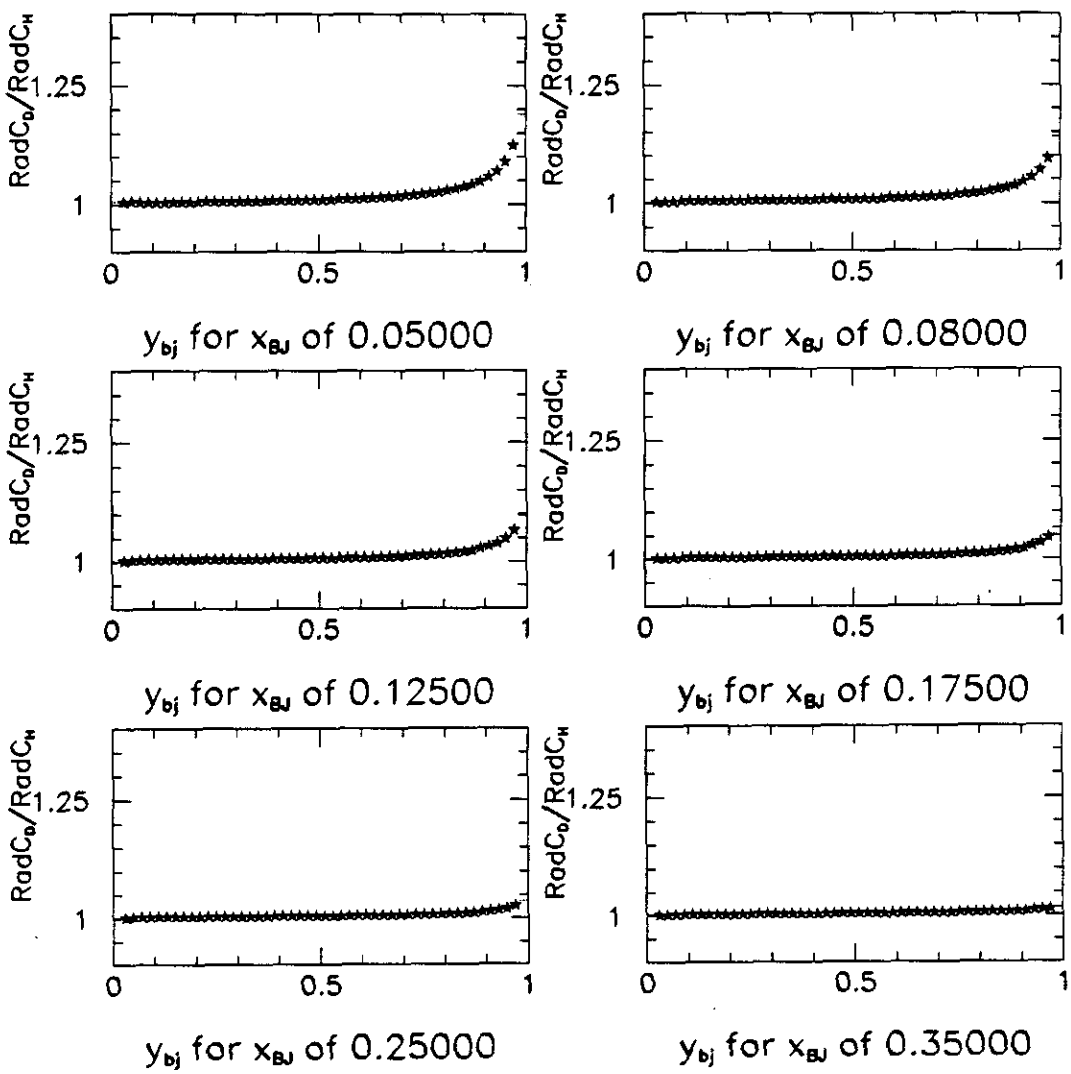

Figure 4.28: Radiative Correction Ratio (D_2/H_2).

The number of events (N^j_{corr}) counted when target j is in position and after the radiative corrections, is given by the following expression:

$$N^j_{corr} = \sum_i^N w^i_j + \sum_i^{Nbg} w^i_j$$

were w^i_j is the weight for each i event in the kinematic bin, N the number of events coming from the j target, and Nbg the number of events coming from outside of the target when j target is in place (this will correspond to the empty target contribution, scaled with the relative luminosity). We determine the contribution to N^j_{corr} from the out-of-target events using the measured event yield from the empty target and the radiative correction weights for target j. If $\overline{Nbg}$ is the number of events from outside of the target when the empty target is in place, the number of the empty target events after the radiative correction weights are applied (N^{MT}_{corr}) is given by the formula:

$$N^{MT}_{corr} = \sum_i^{\overline{Nbg}} w^i_j$$

When the relative fluxes are scaled $\overline{Nbg} \equiv Nbg$ and the subtraction will give the in target events, when target j is in place in front of the beam.

The radiative correction method with calculated weights does not deal with the $\mu - e$ elastic contribution.

SAT and Calorimeter Selection The calorimeter cuts are based on the topology of the hard target bremsstrahlung and the $\mu - e$ elastic events (the electromagnetic (EM) background). From the kinematics of these processes, all the activity in the event is concentrated on the plane defined by the incoming and outgoing (scattered) muon 3-vectors, as opposed to a typical DIS event that has no preference on that plane. The event characteristics are discussed in the

following paragraphs. The standard E665 Monte Carlo is used to study these characteristics, with either the $\mu - e$ or the DIS (plus EM radiation) generators.

The simplest case of a muon-electron elastic event is an event with only the scattered muon and the scattered electron in the final state. Since the process is elastic the electron track will be approximately coplanar with the incoming and outgoing muon tracks. For the purposes of this analysis the plane defined by the muon in-muon out vectors is identical with the bending plane of E665 spectrometer. This is true because within the acceptance of the detector for $\mu - e$ events (figure 4.19) and for E665 beam energies, the scattering angles of the muon and the electron are smaller than $\sim 4.8 mrad$ [112]. We want to project the event to the calorimeter front face, which is $\sim 13.5m$ from the interaction point, so the two planes will be very close. The result is that the spectrometer magnets preserved this coplanarity, since the bending angles were much larger than the scattering angles for the process.

For the $\mu - e$ elastic events that pass the trigger requirement the electron will reach the electromagnetic calorimeter $\sim 100\%$ of the time (from the $\mu - e$ Monte Carlo). The calorimeter in this case will report one large cluster of energy with its centre on the muon in-muon out plane. The size of the cluster is defined with respect to the ν of the event (normalized cluster energy, $z_{clus} = E_{clus}/\nu$). There are more complicated cases of muon-electron elastic events. These belong to the categories of radiative muon-electron scattering, where the electron is accompanied with a hard target bremsstrahlung from the muon, and events where the electron produces an electromagnetic shower as it passes through the experimental apparatus. To higher orders of complexity, a combination of the two previous cases can occur and also the bremsstrahlung photon can introduce showers with pair production. The first case of the more complicated muon-electron elastic event is not modeled in the $\mu - e$ Monte Carlo. The topology of this type of event is not expected to have different properties from the ones

discussed above for the simple $\mu - e$ case. This is because the emission angle of the bremsstrahlung photon with respect to the incoming or the outgoing muon (initial or final state bremsstrahlung) is roughly $\sim \sqrt{m_\mu/E}$ or $\sim \sqrt{m_\mu/E'}$, so the event is still planar in the bending plane (muon bending angle much bigger than the scattering and the photon emission angles), with large calorimeter activity on that plane. The second case is the most common case and it is modeled in the $\mu - e$ Monte Carlo. The fraction of these events corresponds to $\sim 93.7\%$ of the muon-electron events that pass the trigger selection. The event is still planar and the calorimeter activity large on the plane, since the shower has the direction of the electron (as the Monte Carlo studies suggest).

The simplest case of a hard target bremsstrahlung event is an event with only the scattered muon and a hard photon in the final state. For kinematic reasons the bremsstrahlung events are also planar on the muon in-muon out plane (given that the emission angle of the bremsstrahlung photon with respect to the incoming or the outgoing muon is $\sim \sqrt{m_\mu/E}$ or $\sim \sqrt{m_\mu/E'}$). The calorimeter will report one large cluster of energy with its centre on the muon in-muon out plane. Since the reported energy loss of the muon (ν apparent) includes the effect of the bremsstrahlung emission, and since the actual ν that is transferred to the target is very small because of the cross-section dependence on ν (see chapter 1, section 1.7), the normalized cluster energy (z_{clus})is very close to 1. The E665 Monte Carlo also models the cases of more complicated bremsstrahlung events, where the photon converts to an electron-positron pair and creates a shower.

The calorimeter cut design is based on the properties of the background processes discussed above. Its definition uses the normalized energy of the largest calorimeter cluster (E_{clus1} / ν) and the quantity Z_{flow}, which measures the spread of the EM energy out of the magnetic bend plane. For each event Z_{flow} is defined:

$$Z_{flow} = \frac{\sum_{Nclus} Z_{clus}^2 E_{clus}}{ECAL_{total}}$$

The sum is over all the clusters in the EM Calorimeter. Z_{clus} is the vertical distance of the center of the cluster from the center of the Calorimeter, E_{clus} is the energy of the cluster and $ECAL_{total}$ is the total EM energy in the calorimeter. The quantity $\log_{10} Z_{flow}$ is shown in figure 4.29 for both liquid targets. The histogram shows the distribution before the calorimeter cut and the solid symbols the distribution after the cut described below. The cut is a 2 dimensional

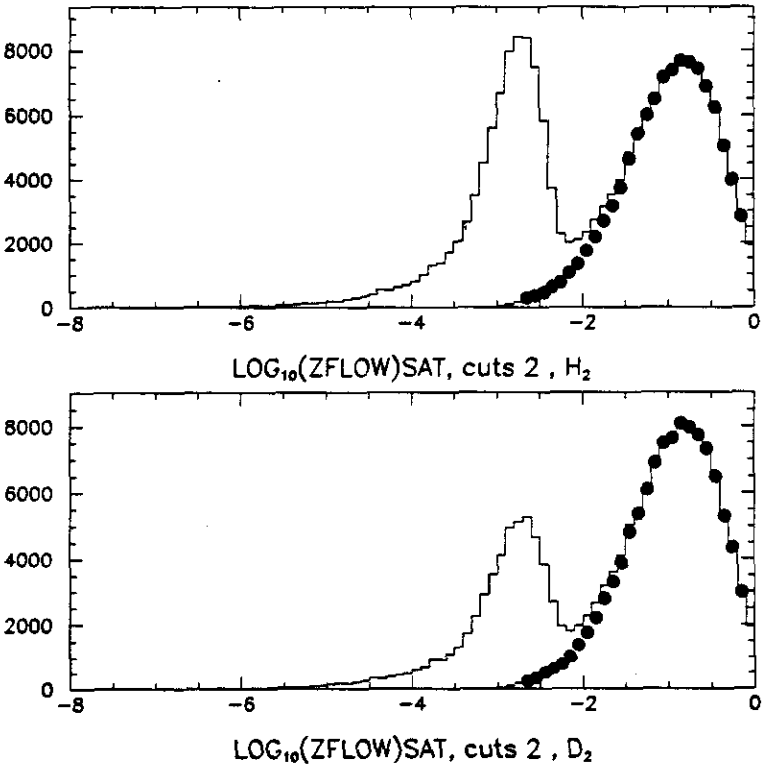

Figure 4.29: $\log_{10}(Z_{flow})$. Solid symbols after the calorimeter cut.

cut and the event is removed if :

$$E_{largest\ cluster}/\nu > 0.27 \times (\log(Z_{flow})) + 0.8$$

Figure 4.30 shows the effect of this cut. The events that are removed are seen to be clearly separated from the inelastic events.

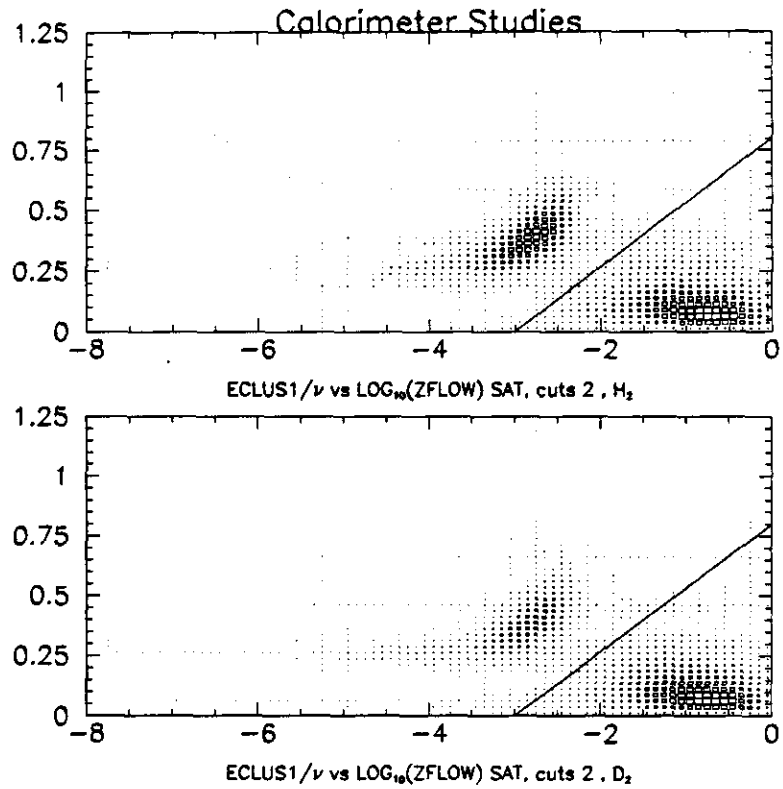

Figure 4.30: E_{clus1} / ν vs $\log_{10}(Z_{flow})$. SAT trigger

The effect of this selection on events with different charged track multiplicities is shown in figures 4.31 and 4.32, for 0, 1, 2 and more than 3 charged track multiplicity in the event, where the quantity $ECAL_{total}/\nu$ is plotted for each selection. The histograms are the distributions before and the solid symbols after the calorimeter cut. Note that as part of the calorimeter selection events

with zero calorimeter energy are included in the final sample, except if there was a calorimeter hardware error reported. In this case the event is removed. The fraction of the calorimeter hardware errors is 0.0006 and stable as function of run block, as has been reported in chapter 2. The calorimeter selection

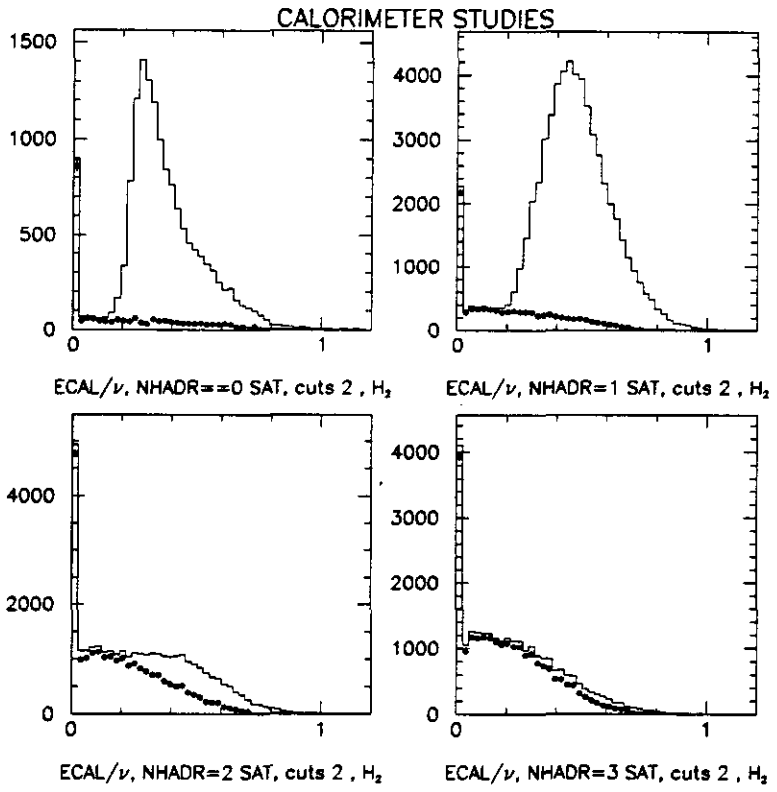

Figure 4.31: $ECAL_{total}/\nu$ for different charged multiplicities. Solid symbols after calorimeter cut. H_2 target

as a radiative correction technique has the advantage of removing the $\mu - e$ elastic events. This can be seen qualitatively in figures 4.33 and 4.34. In figure 4.33 the x_{Bj} distributions of the events from the two liquid targets are plotted without the calorimeter selection. The large $\mu - e$ peak centered at $x_{bj} \sim m_e/m_p = 0.000544$ can be easily identified. A double gaussian plus a

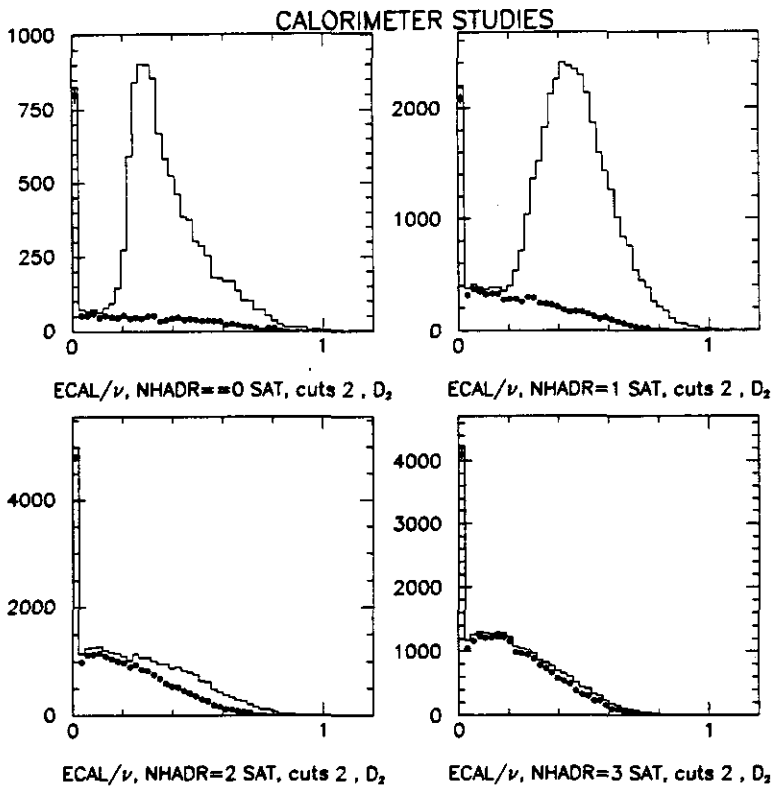

Figure 4.32: $ECAL_{total}/\nu$ for different charged multiplicities. Solid symbols after calorimeter cut. D_2 target

first degree polynomial function is used to fit the $\mu - e$ signal and the muon-nucleon inelastic "background". In figure 4.34 the x_{Bj} distributions are shown after the calorimeter selection has been applied. A fit is performed using the same function as in the case of no calorimeter cut. The values obtained by the fit without the calorimeter selection are used as the initial guess for the fit parameters after the calorimeter selection has been applied. There is no indication of a residual $\mu - e$ signal after the calorimeter selection. On the

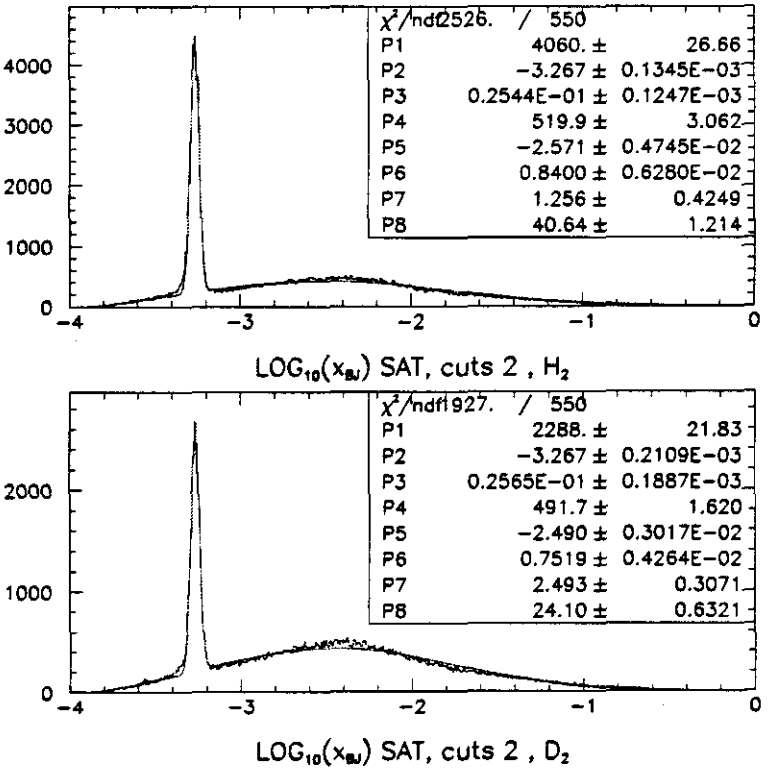

Figure 4.33: $\log(x_{bj})$ distribution before the calorimeter cut. H_2 target top plot, D_2 target bottom plot.

other hand the calorimeter selection only removes a fraction of the DIS radiative events, since the topology of these type of events is similar to that of a non

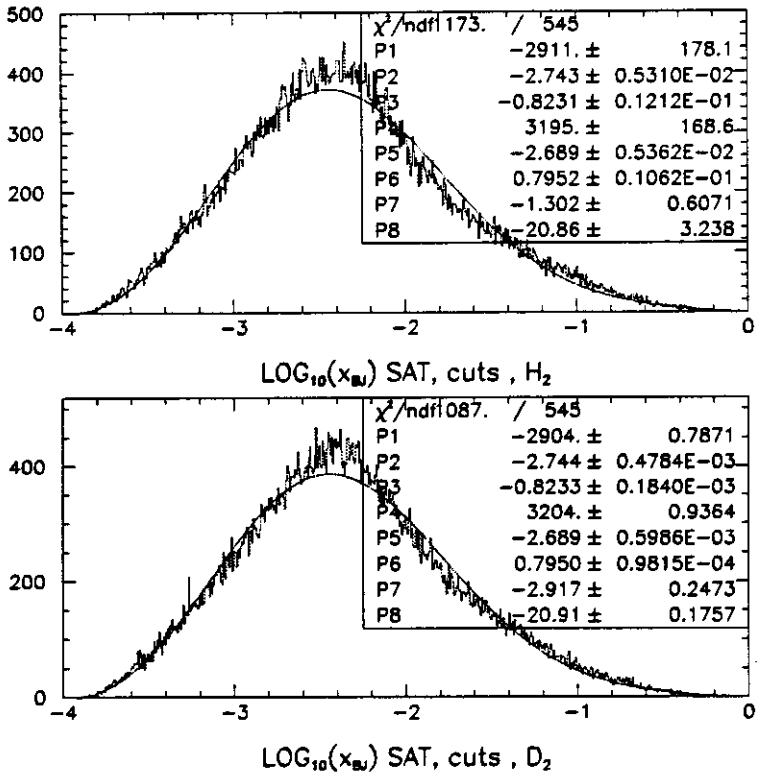

Figure 4.34: $\log(x_{bj})$ distribution after the calorimeter cut. H_2 target top plot, D_2 target bottom plot.

radiative DIS event. To complete this method a correction from the Monte Carlo is required, for the inefficiencies and the impurities of the selection. This study is presented in the next section.

Calorimeter (CAL) trigger The CAL trigger is a hadronic final state trigger, selecting events based on the spread of the calorimeter deposited energy (see section 2.5). The CAL trigger selects events based on the same ideas that defined the calorimeter selection above. In addition, since it does not require the scattered muon in order to trigger, it spans a larger region of the Kinematic space. In figure 4.35 the calorimeter quantities that define the offline calorime-

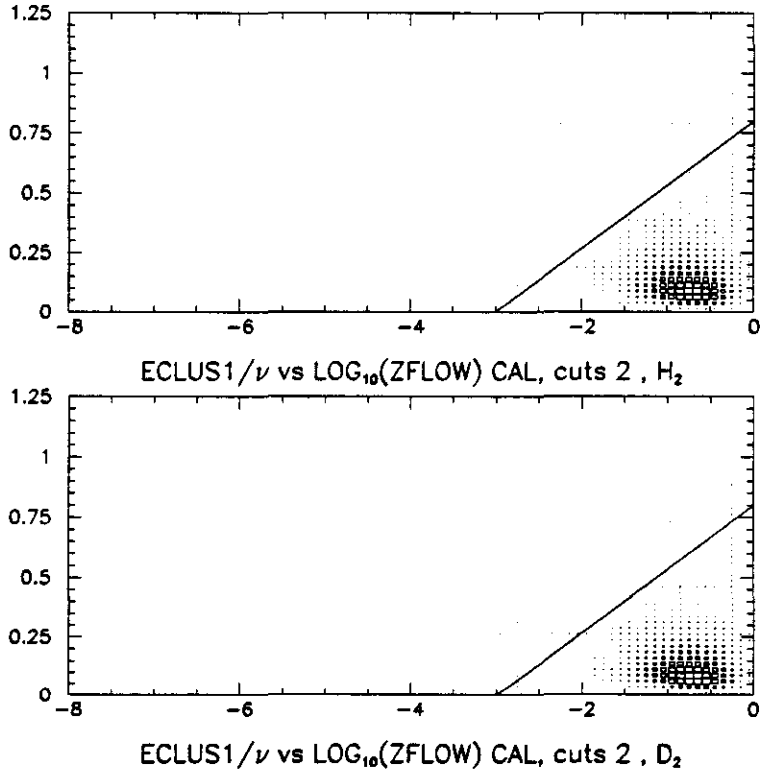

Figure 4.35: E_{clus1} / ν vs $\log_{10}(Z_{flow})$. CAL trigger

ter selection are plotted for both targets and from the calorimeter trigger. The

events selected with this trigger are compatible with our offline definition of DIS events, based on the event topology.

4.5 Uncertainties on the Radiative Correction Techniques

4.5.1 Calculated Radiative Corrections

From the three Radiative Correction techniques discussed in the previous section, the systematic effects for the first one (Calculated Radiative Corrections) has been discussed in detail in the literature [115], and in the E665 internal reports [113], [114]. The conclusion is that assuming that the input structure functions used are realistic, the effects on the ratio measurement due to uncertainties on the theoretical model and the numerical integration are less than 0.5%. In these studies comparisons of the different theoretical approaches and their implementations are used to estimate the quoted uncertainty. Since E665 has a calorimeter an attempt was made (reference [116]) to estimate this uncertainty from the comparison of the absolute bremsstrahlung event rate, as measured with the calorimeter, to the one calculated by FERRAD. The same event weighting technique that is used in the DIS analysis was applied, but this time the weights were the fraction of the bremsstrahlung over total cross-section. The event selection for the bremsstrahlung events was the calorimeter cut described in the previous paragraph inverted (the negative requirement becomes positive). In addition all events with $0.00042 \leq x_{bj} \leq 0.00060$ were removed in order to remove the $\mu - e$ elastic contribution explicitly, since it has a similar calorimeter signature to the bremsstrahlung events. The agreement between the calculated and the measured rates was at the 5% level. This uncertainty was dominated by the contamination of the bremsstrahlung sample with deep inelastic scatters and the error on the Monte Carlo correction applied to remove them. Similar results have

been reported by EMC [117] for the same comparison of calculated versus measured absolute bremsstrahlung event rates. The conclusion of these checks can be summarized with the following statement: The Calculated Radiative Corrections technique is self consistent with 0.5% uncertainty on the ratio, while it has been checked experimentally and found correct with an uncertainty at the 5% level on the absolute rate measurement.

4.5.2 Electromagnetic Selection and SAT trigger

The E665 Monte Carlo is used to study the EM selection (calorimeter cuts) from the SAT data sample. The efficiency for the $\mu - e$ elastic rejection is measured in a straight forward manner. E665 Monte Carlo events, generated with the $\mu - e$ elastic process generator, and reconstructed with the standard pattern recognition filters, are subjected to the standard chain of physics analysis cuts. The quantities that define the calorimeter cut from this sample are plotted in figure 4.36. The line drawn represents the cut selection. The $\mu - e$ elastic rejection is $\sim 99.994\%$ efficient.

In order to measure the purity of the cut (what fraction of DIS events are removed) and its efficiency in removing radiative events, the E665 Monte Carlo with the DIS generator plus higher order EM processes (as described in chapter 2) is used. Before we continue with this study some Monte Carlo terminology definitions are needed:

- True variables are the generated variables, before reconstruction.
- At the true level the kinematic variables can be either calculated from the scattered muon or from the virtual photon. In the first case, if there is radiation, then the kinematic quantities will not correspond to the 4-momentum transferred between the target and the muon. We define:
  1. Apparent are the kinematic quantities determined from the scattered muon.
  2. Actual are the kinematic quantities determined from the virtual photon.

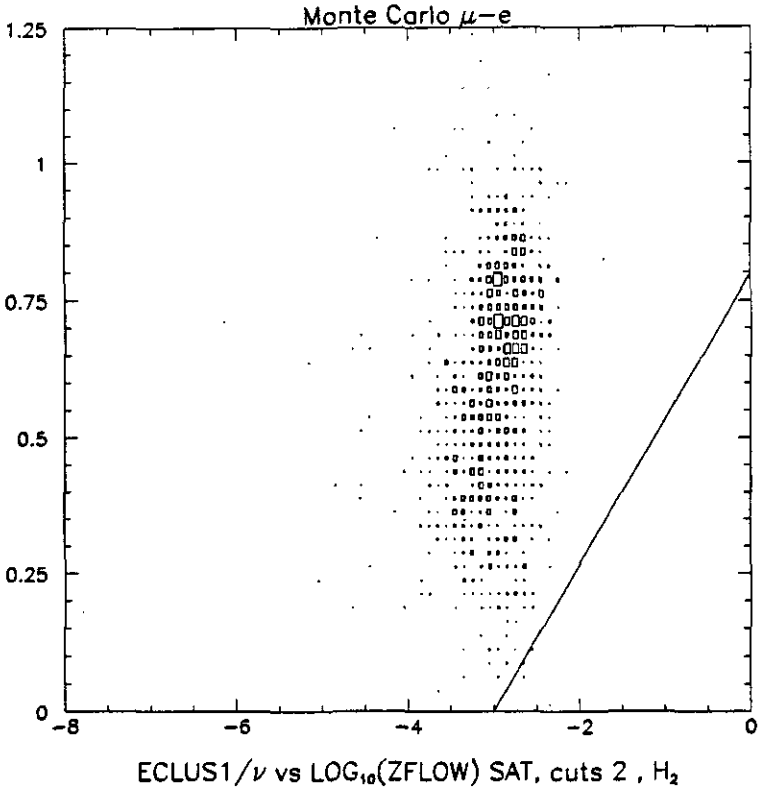

Figure 4.36: E_{clus1} / ν vs $\log_{10}(Z_{flow})$. $\mu - e$,SAT trigger.

- Following these definitions, the radiative events at the Monte Carlo analysis level are tagged using the condition: $\nu_{actual} < \nu_{apparent}$, where the subscript refers to the way that ν was determined. Since the radiative photon spectrum in the E665 Monte Carlo starts at 400 MeV, this is the lower limit in the difference of the two quantities for a radiative event. There is a slight mismatch if one wants to compare final state quantities between data and Monte Carlo, since the calorimeter resolution cutoff is higher than 400 MeV (minimum 1 GeV for a cluster). The calorimeter "sees" radiative photons above 5 GeV, while the Monte Carlo tagged spectrum starts at 0.4 GeV. This difference has no effect in the calorimeter cut studies. The radiative events can be further categorized as radiative DIS events and coherent (only for D_2) or quasielastic radiative events. The true actual mass of the hadronic final state (W^{true}_{actual} is used to differentiate between the 2 categories:

  1. $W^{true}_{actual} < 4.0$ GeV. Resonance region. Coherent or Quasielastic event.
  2. $W^{true}_{actual} > 4.0$ GeV. Continuum. Radiative DIS event.

We will use the above definitions to investigate the effects of the calorimeter cut on each different type of event. In figure 4.37 the composition of the event sample is shown, as a function of x_{Bj}, before and after the calorimeter cut for both targets. The top curves on each plot are the fraction of the radiative events to the total number of events after the selection. The bottom curves are the DIS event fraction to the total. The fractions before the calorimeter cut are plotted with open symbols, and after the cut are plotted with solid symbols. The EM selection minimizes the contamination of the sample with radiative events. To go one step further in our study we need to quantify and determine the fraction of radiative events before and after the cut, and the fraction of DIS lost due to the cut. Let us write an expression for the total measured cross-section, using the extra information that the calorimeter can provide (identification of the radiative events) and then try to relate it with the terms in

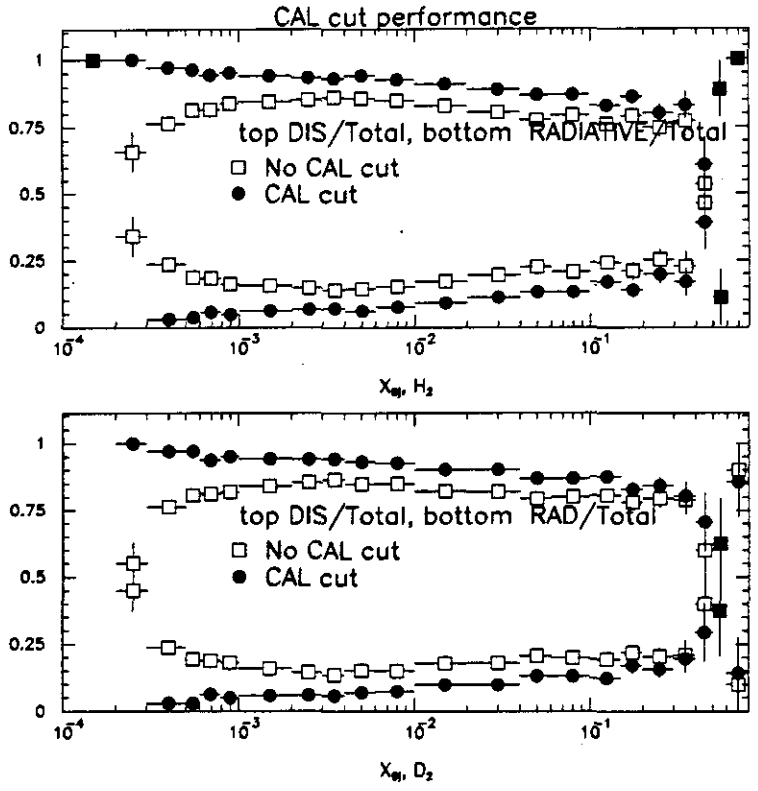

Figure 4.37: MC: Radiative/Total (top), DIS/Total (bottom) event fraction as a function of x_{Bj}.

equation 4.2 ($\sigma_{tot} = \sigma_{1\gamma} \times K_{sum} + \sigma_{radinel} + \sigma_{quasi} + \sigma_{coh} + \sigma_{\mu-e}$). Define $\sigma^{measured}_{nonradiative}$, $\sigma^{measured}_{radiative}$ and $\sigma^{measured}_{\mu-e}$ as the non-radiative, radiative and $\mu - e$ event cross-sections as tagged by the calorimeter. Then the total cross-section measured by the experiment is:

$$\sigma_{exp} = \sigma^{measured}_{nonradiative} + \sigma^{measured}_{radiative} + \sigma^{measured}_{\mu-e} \tag{4.6}$$

When we apply the calorimeter cut analysis we remove the $\sigma^{measured}_{radiative}$ and $\sigma^{measured}_{\mu-e}$ contributions. Since the $\sigma^{measured}_{\mu-e} = \sigma_{\mu-e}$ according to the Monte Carlo results presented above, we will drop the $\mu - e$ terms from the two relations. The measured quantities with the calorimeter selection can be related to the unbiased event rates with the following formulas:

$$\begin{aligned} \sigma^{measured,i}_{nonradiative} &= (1 - \lambda_i + \epsilon_i)\sigma^i_{1\gamma} \times K_{sum} \\ \sigma^{measured,i}_{radiative} &= \sigma^i_{radinel} + \sigma^i_{quasi} + (\lambda_i - \epsilon_i)\sigma^i_{1\gamma} \times K_{sum} \end{aligned}$$

where λ is the fraction of non-radiative cross-section lost to the total non radiative cross-section (which is $\sigma_{1\gamma} \times K_{sum}$), ϵ is the fraction of radiative events kept to the total non radiative cross-section, and the index i (i=1,2) indicates the different liquid targets. What we measure is $\sigma^{measured,D}_{nonradiative}/\sigma^{measured,H}_{nonradiative}$, which with the help of the above expressions gives:

$$\frac{\sigma^D_{1\gamma} \times K_{sum}}{\sigma^H_{1\gamma} \times K_{sum}} = \frac{\sigma^D_{1\gamma}}{\sigma^H_{1\gamma}} = \frac{\sigma^{measured,D}_{nonradiative}}{\sigma^{measured,H}_{nonradiative}} \times \frac{1 - \lambda_H + \epsilon_H}{1 - \lambda_D + \epsilon_D} \tag{4.7}$$

We will evaluate λ and ϵ as a function of x_{Bj} from the Monte Carlo and then we will use the values that correspond to the x_{Bj} region where the calorimeter cut method is applicable. The dependence of ϵ in x_{Bj}, for the two targets, is shown in figure 4.38. Also shown is the value obtained from a flat line fit for $x_{Bj} < 0.005$ (0.0058 ± 0.0023 for H_2 and 0.0056 ± 0.0021 for D_2). The $1 - \lambda$ x_{Bj} dependence is shown in figure 4.39, with the value of the flat line fit for the same x_{Bj} region (0.0606 ± 0.0023 for H_2 and 0.0658 ± 0.0022 for D_2, these are the λ values). Using these four values in equation 4.7 we obtain a value of 0.9949 ± 0.0025 for the expression $\frac{1-\lambda_H+\epsilon_H}{1-\lambda_D+\epsilon_D}$. This means that

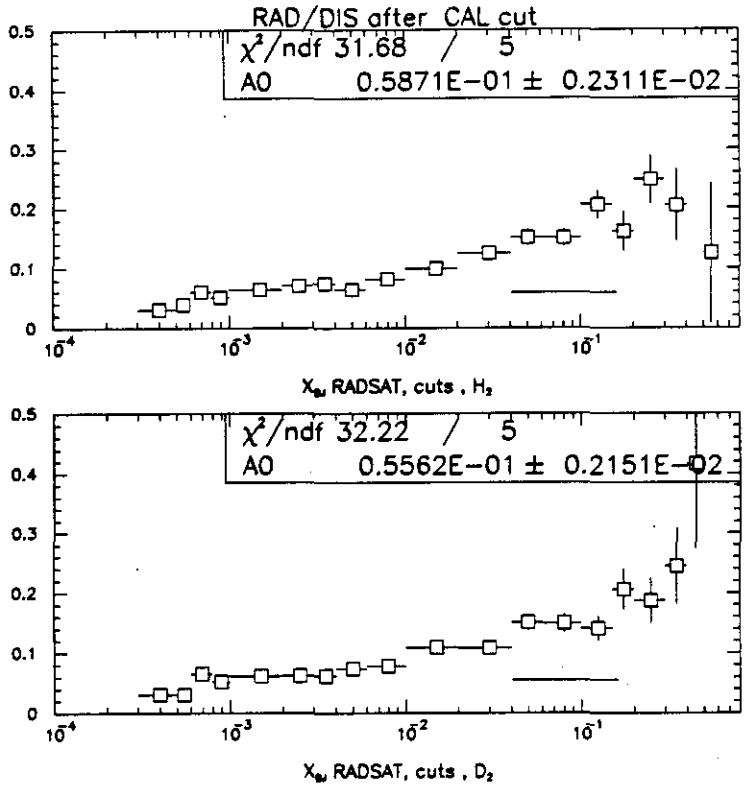

Figure 4.38: ϵ as a function of x_{Bj}.

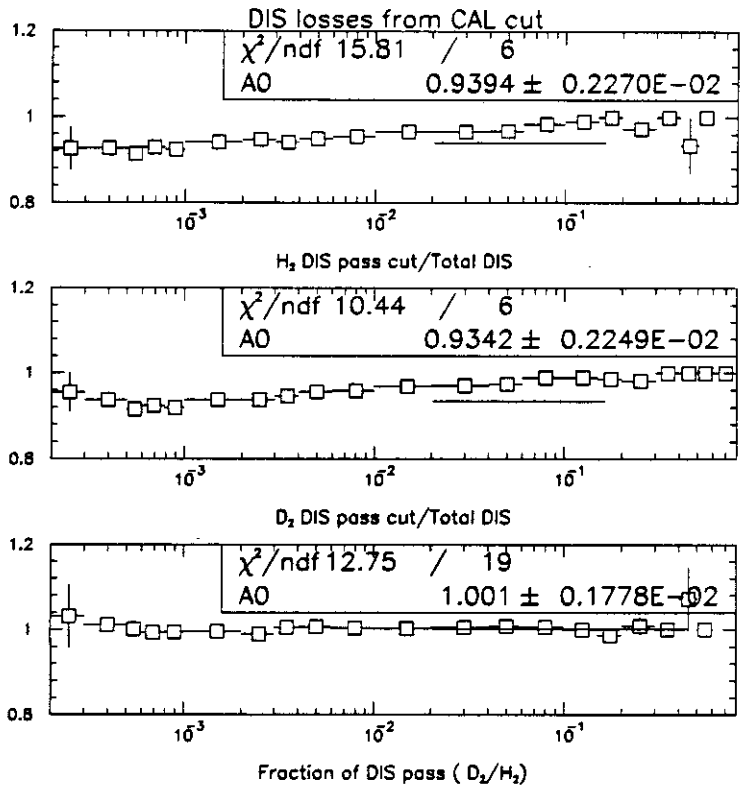

Figure 4.39: $1 - \lambda$ as a function of x_{Bj}.

below x_{Bj} of 0.005 the correction on $\frac{\sigma^D_{1\gamma}}{\sigma^H_{1\gamma}}$ from the calorimeter cut is $0.51 \pm 0.25\%$ of the measured ratio.

This very small bias from the calorimeter cut in the region of small-x_{Bj} is coming from the fact that the calorimeter selection is very efficient in removing the coherent and quasielastic radiative events. It is not efficient in removing the radiative DIS events, but in the small-x_{Bj} region the F_2 differences are small for the two targets, and the radiative DIS rate is proportional to F_2. Most of the estimated correction on the calorimeter cut is due to the presence of radiative DIS events in the final sample. This can be seen in figures 4.40 and 4.41 for H_2 and D_2 respectively. The top plots are showing the number of radiative events before (histogram) and after the calorimeter selection, as a function of W_{actual}. The bottom plots are showing the fraction of the radiative events after the calorimeter cut to the total number of radiative events, also as a function of W_{actual}. In the resonance region there are no radiative events left, while in the DIS continuum region the cut has no significant effect. There is another contribution to the total cross-section that the calorimeter selection can not remove: the vertex and lepton self energy corrections. These are multiplicative corrections to the single-photon-exchange cross-section and they are of the order of $\sim 1\%$ [114]; since these corrections are combined with the residual effect from the shoft photon radiation, the magnitude of the correction depends on the infrared cutoff [4]. The vertex and lepton self energy corrections cancel in the measurement of the cross-section ratio.

4.5.3 Calorimeter Trigger

There are two categories of effects that we have to investigate in order to understand the CAL trigger. The first is acceptance biases, and in this category effects such as secondary interaction differences are included. We have studied these effects in

[4] These effects are discussed in chapter 1, section 1.7

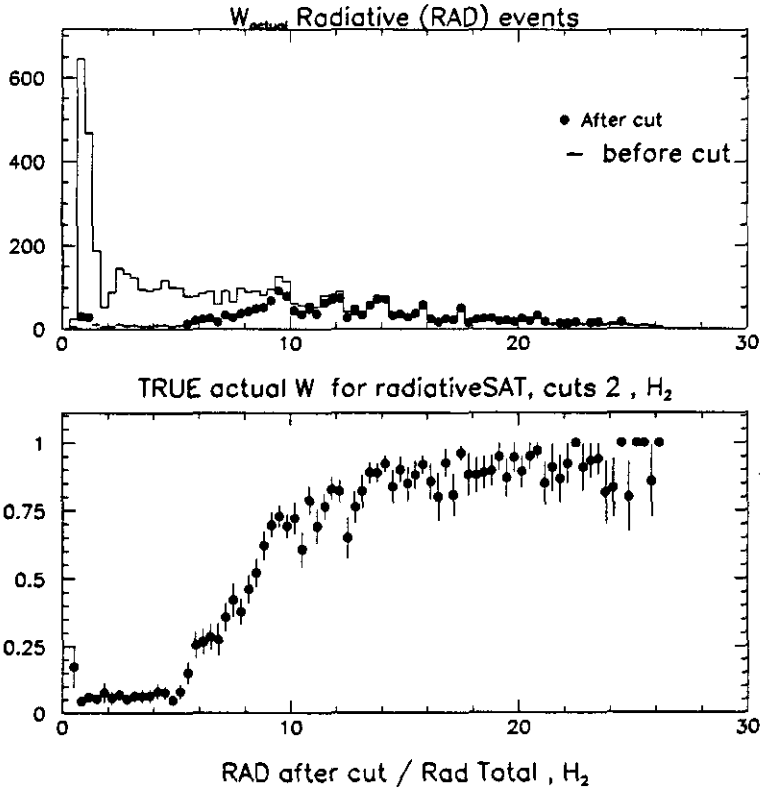

Figure 4.40: MC: Calorimeter Selection as a function of W_{actual}. H_2

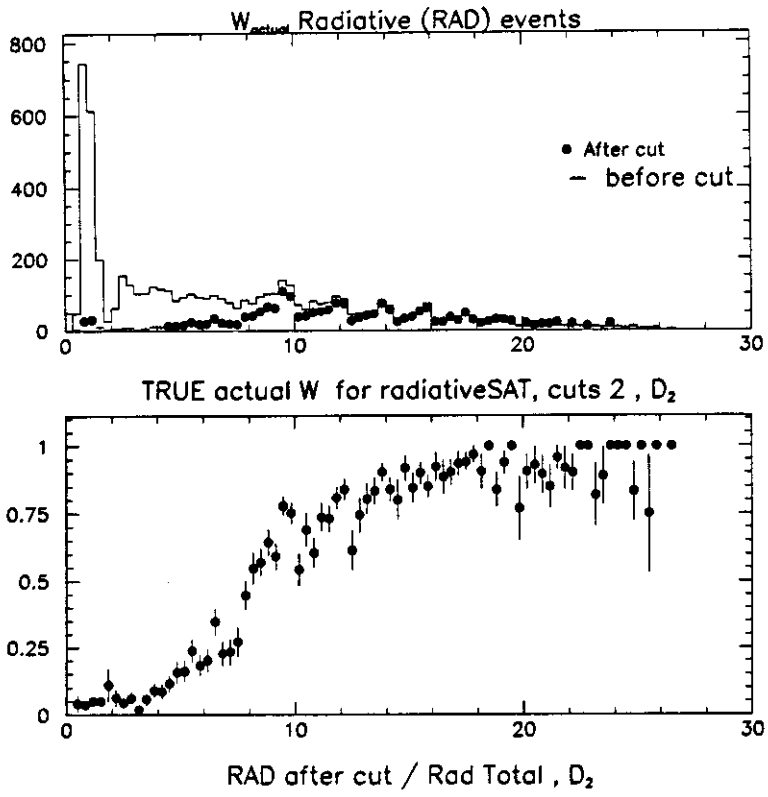

Figure 4.41: MC: Calorimeter Selection as a function of W_{actual}. D_2

Section refs-trig in the region of overlap with the muon triggers. Assuming that we can smoothly extrapolate our results to the kinematic region where there is no overlap with other triggers, we see no effect on the ratio. The second category corresponds to the trigger bias in terms of the fraction of the total cross-section of each target that the trigger can "see". The calorimeter trigger, for example, does not fire on events that do not have particles reaching the calorimeter detector. In order to prove that there is no bias on the ratio, we have to establish that the losses are the same for the two targets. This is not a trivial statement for the high x_{bj} region, since this is the valence quark dominated region in the cross-section, and the neutron and proton are different. There is no reason to expect that the fraction of each type of event produced (tagged with its final state properties), will be the same. For x_{bj} values low enough that the cross-section is sea dominated the hadronic final states should be similar. We will study the final state differences for the two targets in that region.

The implication discussed in the previous paragraph is not an acceptance problem. Even if for a given type of event the trigger probability is the same for both targets, the probability to produce such an event does not need to be the same. In that case the fact that the trigger will not fire at all for certain types of events biases the results obtained with that trigger. What we want to establish here is that the fraction of the total non-radiative cross-section that corresponds to $\sigma^{measured}_{nonradiative}$ for the CAL trigger is the same for the two targets. Since the CAL is triggering on the hadronic final state if the event topology is similar then the above argument is supported. The ratio (H_2/D_2) of the average values of the final state quantities that the calorimeter trigger probability depends on is presented in figures 4.42 and 4.43, as a function of x_{bj}. The average quantities plotted as a function of x_{bj} are E_{clus1}, Z_{flow}, $E_{cal} - E_{clus1}$, the number of positive N_+ and negative N_- tracks and N_{clus}, the number of calorimeter clusters. The ratios are then fitted to a flat line for $x_{bj} < 0.005$. All results deviate from unity by order of 1% except for the ratio of the charged track multiplicities, for which the deviation is approximately double. The tracks used to

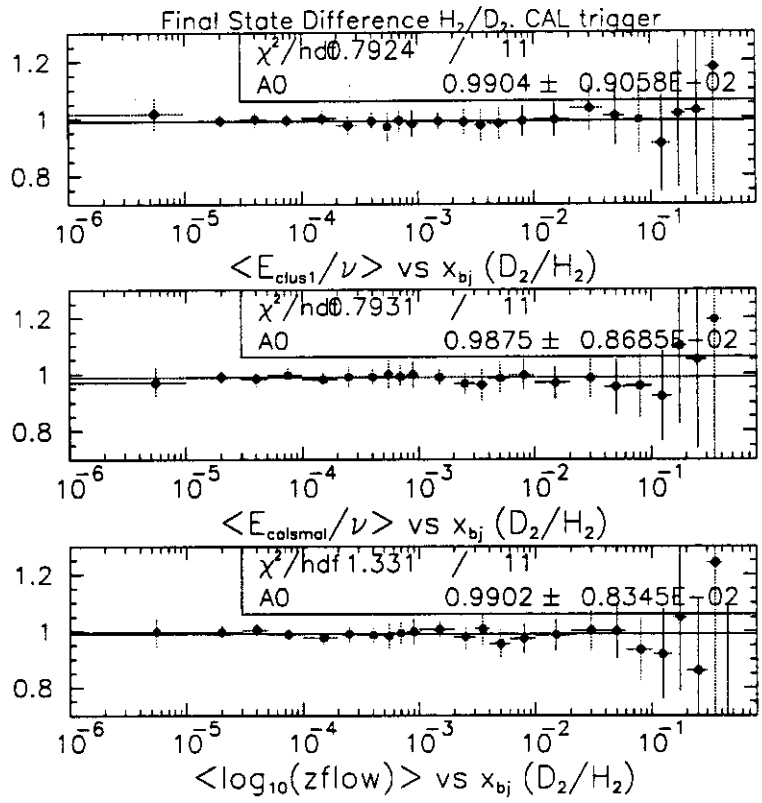

Figure 4.42: D_2 - H_2 hadronic final state comparison 1. CAL trigger

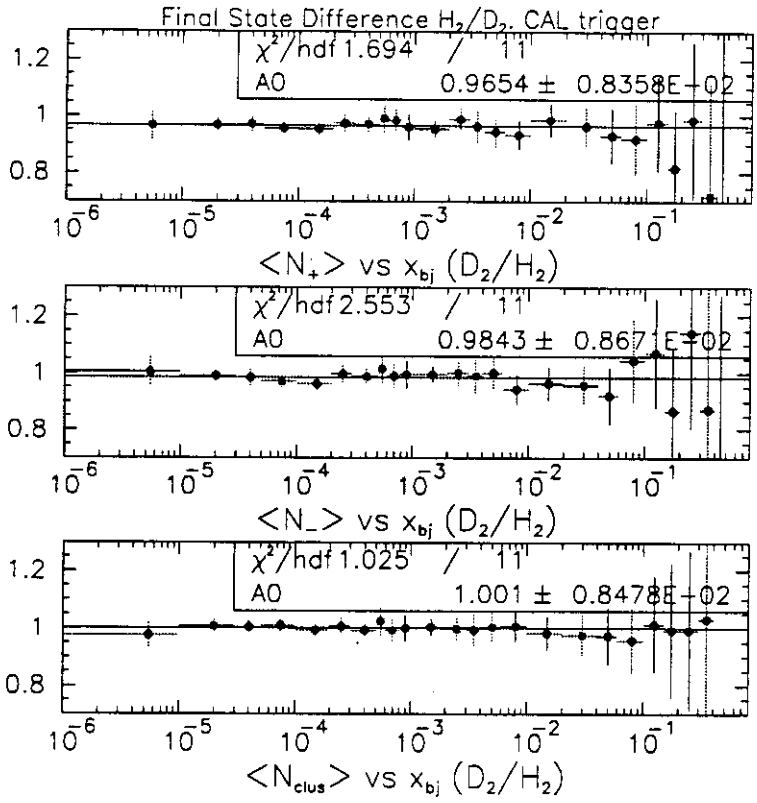

Figure 4.43: D_2 - H_2 hadronic final state comparison 2. CAL trigger

form this ratio are tracks associated with the primary vertex. Since the D_2 target has double the interaction lengths of the H_2 target, secondary interactions will reduce the number of tracks fitted to the vertex for the D_2 events as compared to the events from H_2. This means that the difference in multiplicities does not have to be a difference in the production probability from the two targets. It can be the effect of the difference in interaction length between the them. This is an acceptance problem which we have already studied in Section 4.3.3 where we saw no overall acceptance difference. In order to examine that hypothesis we plot the same ratios for events

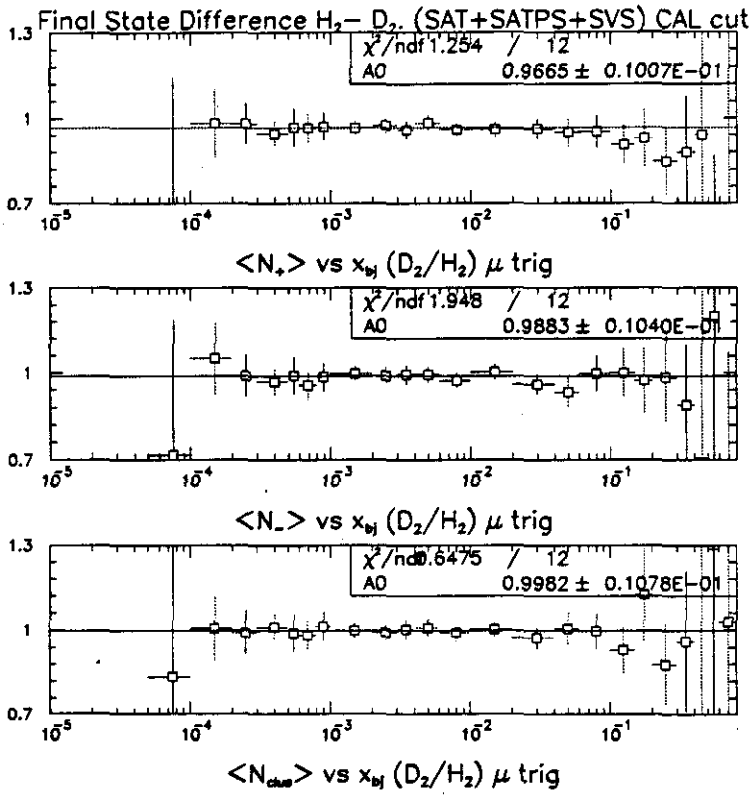

Figure 4.44: D_2 - H_2 hadronic final state comparison 2. Muon triggers

from the combined muon triggers data sample, with calorimeter cuts applied. We perform the same fits and the results are similar. These results support the idea that

the larger differences seen in the multiplicity ratios for the calorimeter trigger are not due to the difference of the cross-section fraction that the trigger "sees" between the two targets.

4.6 Validation of the Reconstruction of the Event Kinematics

Since the ratio measurement extends to very small values of the kinematic variables it is important to verify the precision with which the Pattern Recognition reconstructed the event kinematics.

A straight forward method to check for biases due to the reconstruction techniques is to reconstruct Monte Carlo events and compare the reconstructed values of the kinematic variables with the values of the true event kinematics. For any kinematic variable X we define the normalized residual NR:

$$NR(X) = \frac{X_{apparent} - X_{reconstructed}}{\sigma(X)}$$

where $X_{apparent}$ is the value of the apparent kinematic variable generated by the Monte Carlo, $X_{reconstructed}$ is the value of the variable reconstructed by the Pattern Recognition and $\sigma(X)$ is the uncertainty in this reconstructed value computed by the Pattern Recognition. We use the apparent kinematics because here we want to study the smearing effects due to reconstruction only (the definition of the apparent true Monte Carlo kinematics can be found in the previous section). If the uncertainty $\sigma(X)$ describes correctly the instrumental uncertainties and there are no reconstruction biases, the distribution of the NR variable should follow a normal distribution. In figure 4.45 the distribution of NR is examined for the θ and ν variables as a function of θ and ν respectively, and in figure 4.46 the distribution of NR for Q^2 and x_{Bj} is examined as a function of Q^2 and x_{Bj} respectively. For each bin of the kinematic variables the mean value and the spread of the NR distribution is shown. The results

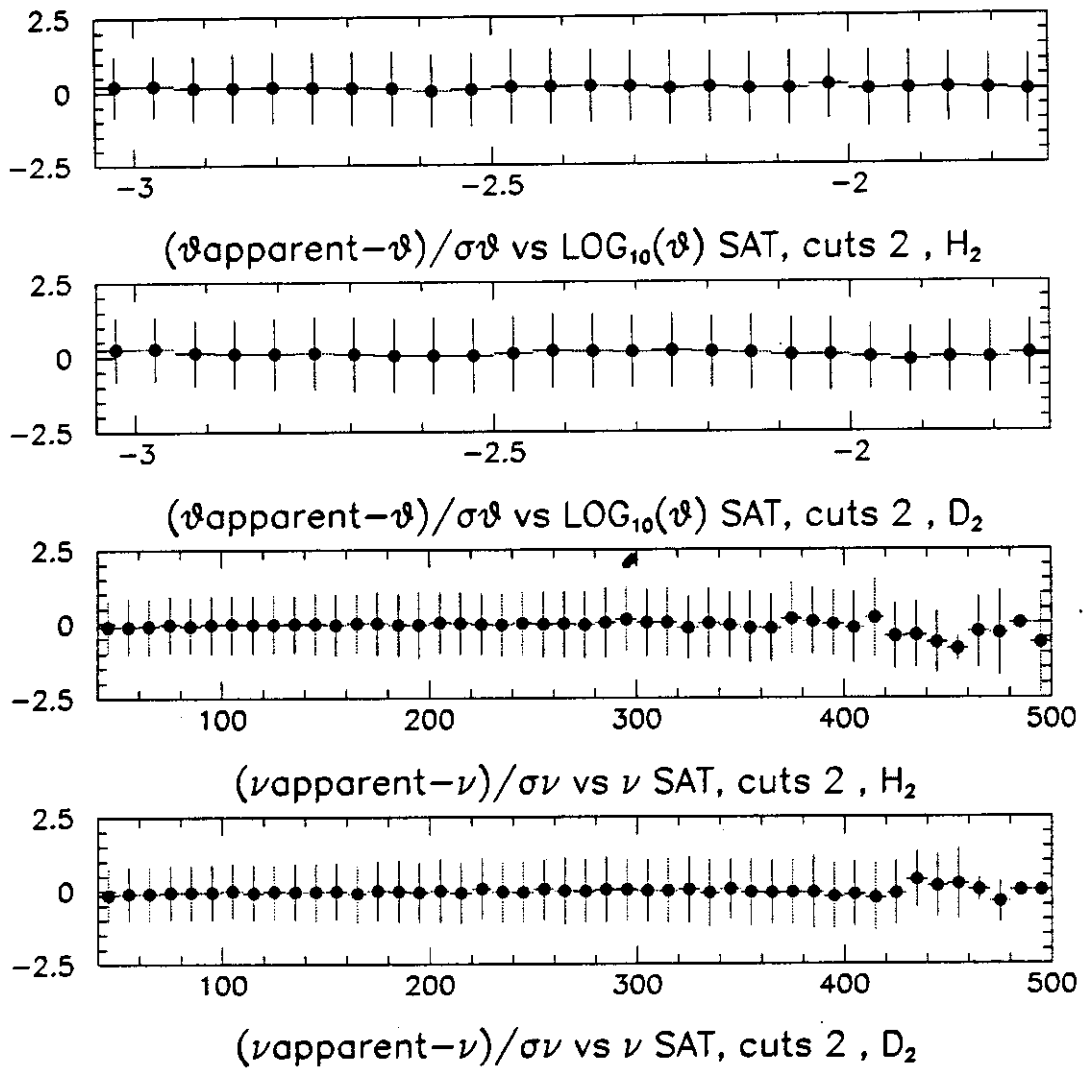

Figure 4.45: The mean and the standard deviation of the normalized residual distribution for θ and ν versus θ and ν respectively.

are shown separately for the hydrogen and the deuterium targets. The distributions are flat, all the points are close to zero and the standard deviations in each bin are close to unity. In figures 4.47 and 4.48 the mean value of the NR distribution is plotted together with the error of the mean rather than the spread, as a function of θ and ν, and Q^2 and x_{Bj} respectively. There is no significant systematic deviation from zero.

In addition to the use of Monte Carlo events, Rbeam events are used in order to check that the apparatus does not introduce any target dependent bias in the reconstructed event kinematics. In principle, straight through beams should not have a reconstructed scattering angle. Apparent small non-zero scattering angles can be introduced due to small alignment problems. Small angles can also be induced from multiple scattering in the target. Since the two liquid targets are similar in radiation lengths (there is a 14% difference) the multiple scattering effects should be approximately the same in the ratio measurement. In figure 4.49 the top plot shows the $\log(Q^2)$ distribution of the reconstructed Rbeam triggers from the H_2 and D_2 targets. The events are selected using the standard beam phase space cuts described in the previous sections. In addition, one forward spectrometer muon reconstructed in the PSA chamber is required. The bottom plot of in figure 4.49 shows the ratio of the $\log(Q^2)$ distributions from the two targets. The ratio is fitted to a linear function in $\log(Q^2)$. The result of the fit shows no target dependent reconstruction bias. The total number of Rbeam trigger events with reconstructed kinematics is 762425 from a total of 961226 Rbeam triggers for H_2 (79.3%), and 561309 from a total of 447887 for D_2 (79.7%).

4.7 Detector Smearing Effects

The finite resolution of the detector smears the muon kinematics as they appear after the effects of electromagnetic radiation (apparent kinematics). Although the

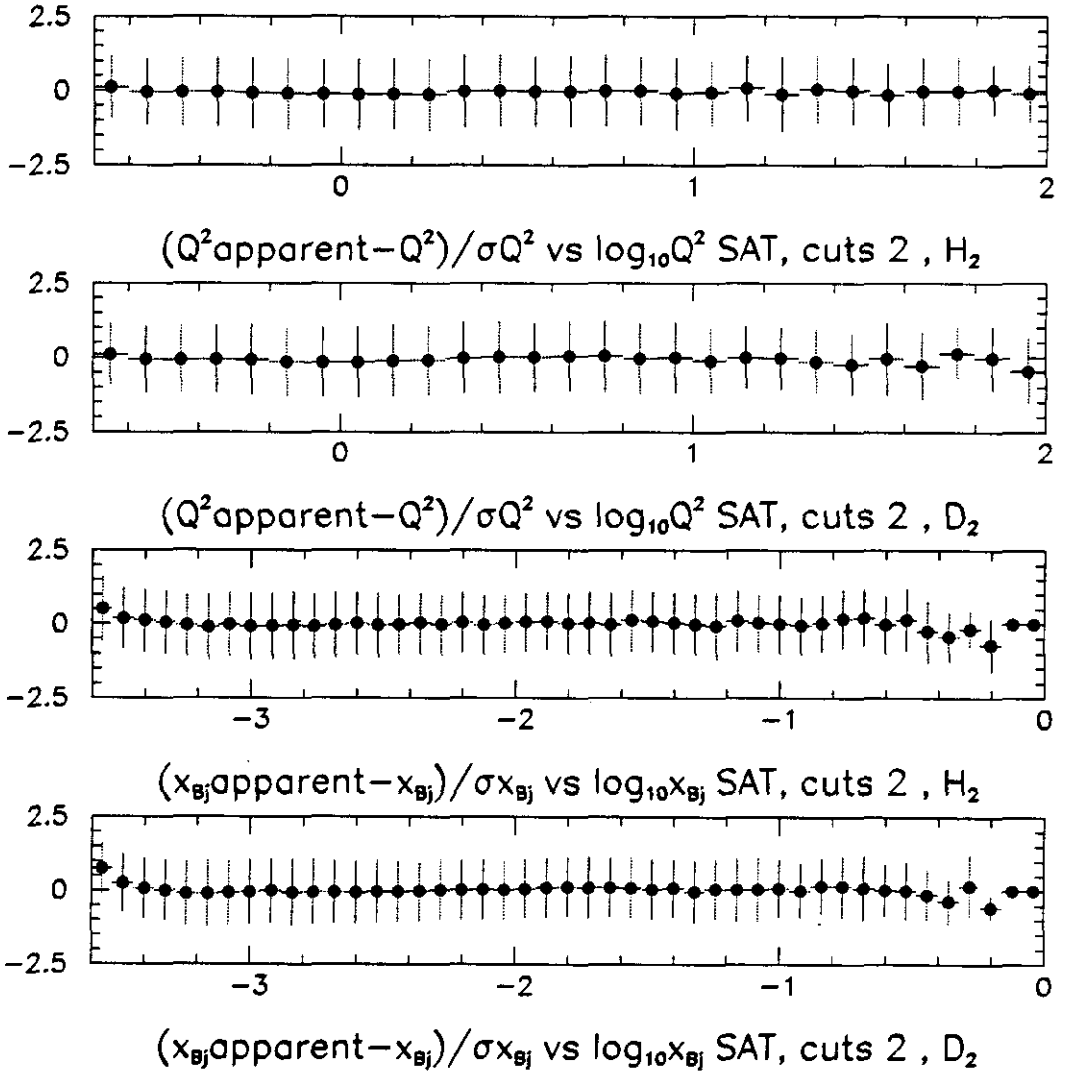

Figure 4.46: The mean and the standard deviation of the normalized residual distribution for Q^2 and x_{Bj} versus Q^2 and x_{Bj} respectively.

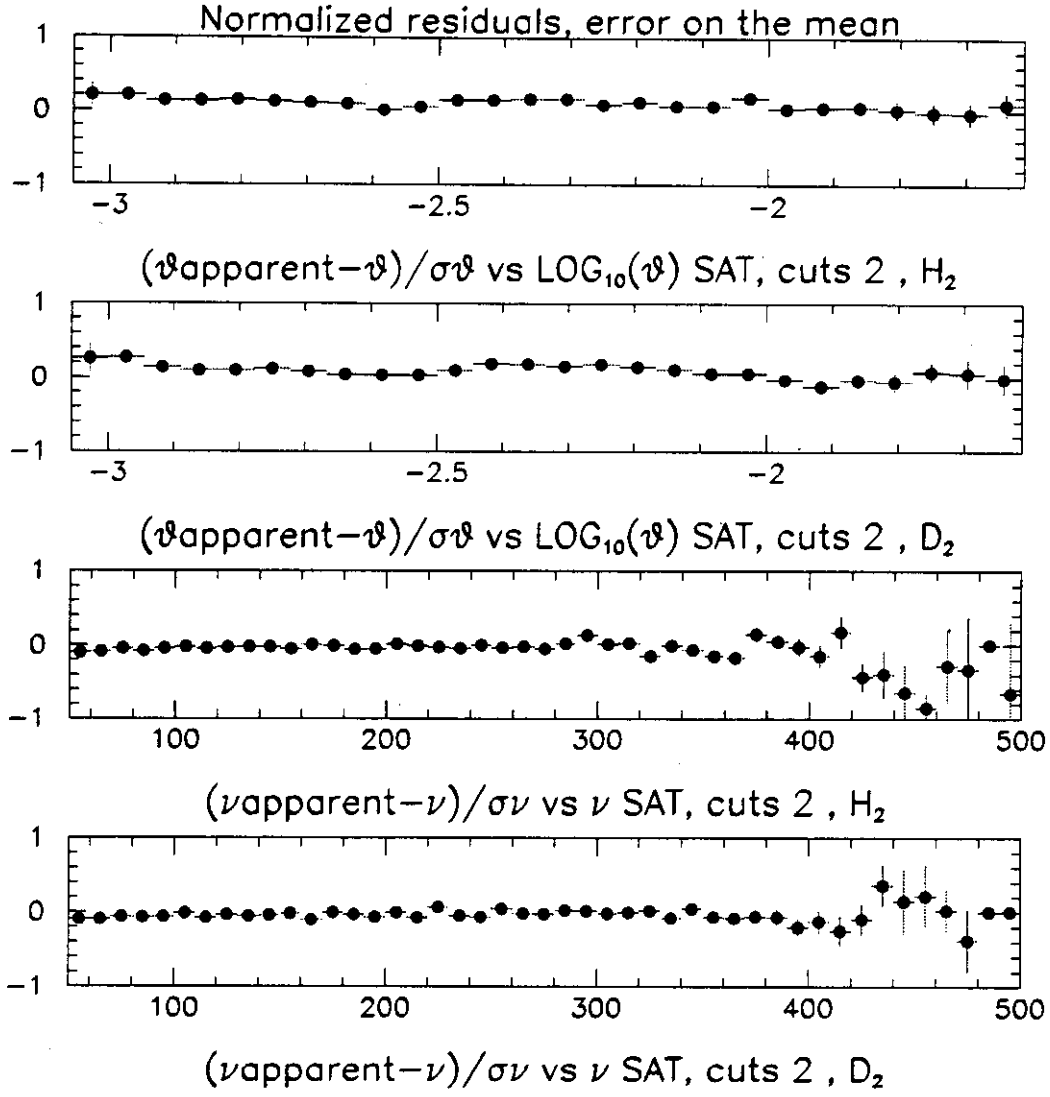

Figure 4.47: The mean and the error of the mean of the normalized residual distribution for Q^2 and x_{Bj} versus Q^2 and x_{Bj} respectively.

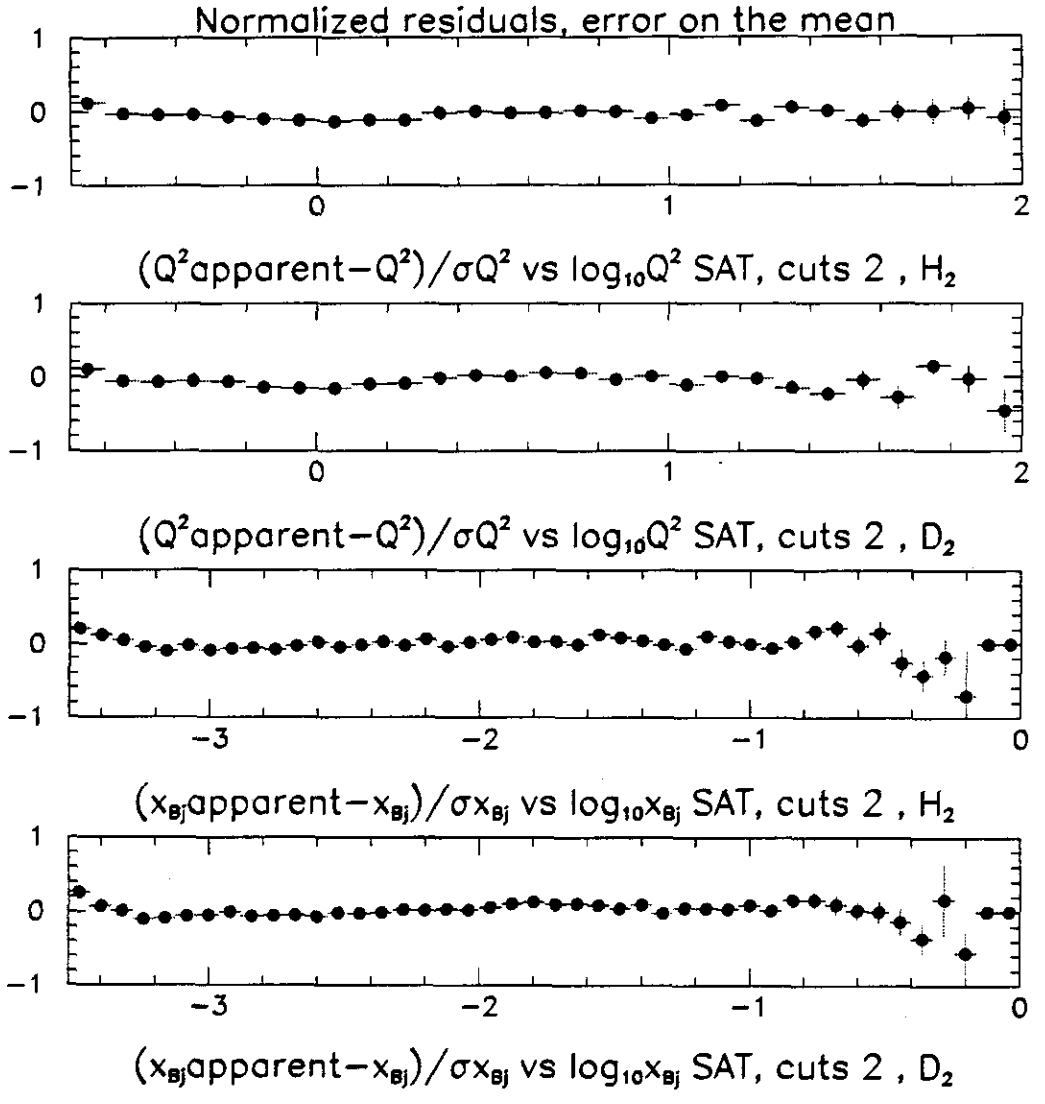

Figure 4.48: The mean and the error of the mean of the normalized residual distribution for Q^2 and x_{Bj} versus Q^2 and x_{Bj} respectively.

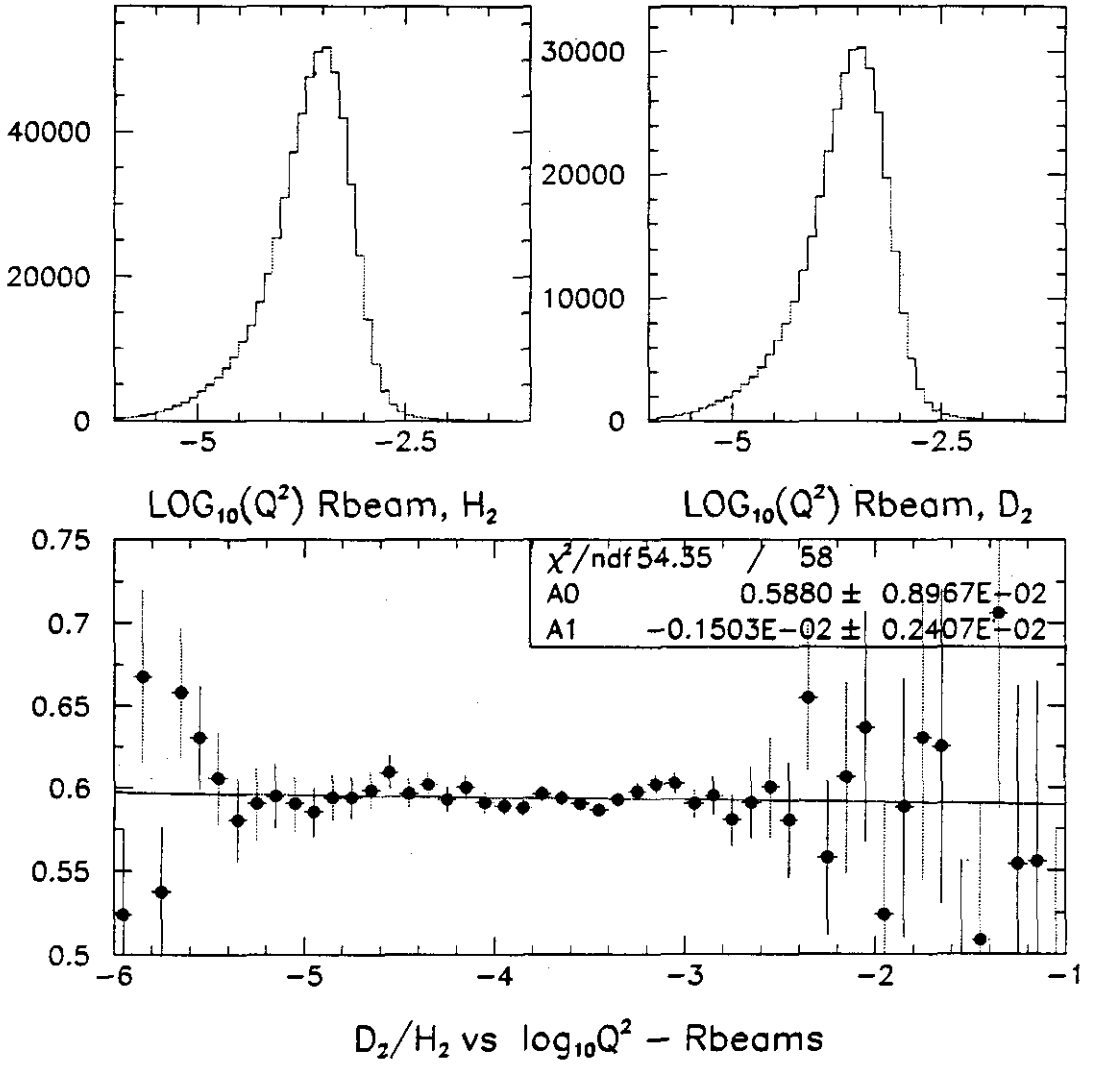

Figure 4.49: Reconstructed Rbeam $\log(Q^2)$ distributions from the H_2 and D_2 targets (top plot), and the $\log(Q^2)$ distribution of the ratio D_2/H_2 (bottom plot).

resolution of the detector is similar for the hydrogen and the deuterium targets, the apparent kinematic distributions are different for the two targets, so detector smearing could introduce a systematic effect on the extraction of the single-photon-exchange cross-section from the total measured cross-section (see equation 4.3). In order to verify that there is no systematic effect introduced by the detector smearing, reconstructed Monte Carlo events are used. The detector smearing function is evaluated by comparing the apparent muon kinematics at the true level with the apparent muon kinematics after the detector simulation and the reconstruction has been applied.

The total number of events in each reconstructed kinematic bin has contributions from two sources:

1. The events that were generated with true kinematics in the bin, and remained in the same bin after reconstruction.

2. The events that were smeared into the bin due to detector resolution.

The smearing function in a kinematic bin is defined as: $(smearingfunction)^{-1} = N_{true}/N_{recin} + N_{true}/N_{smearin}$, where N_{true} is the number of events generated with their true kinematics in that bin, $N_{smearin}$ is the number of events that smear into that bin, and N_{recin} the number of events that remained in the bin after reconstruction. The error on the first fraction is binomial, the error on the second is gaussian. The total error is the quadratic sum of the two. In figure 4.50 the $(smearingfunction)^{-1}$ is presented as a function of X_{Bj} for the H_2 and the D_2 targets (two top plots). The ratio of the two is presented in the bottom plot of the figure; there is no significant effect on the ratio due to detector smearing.

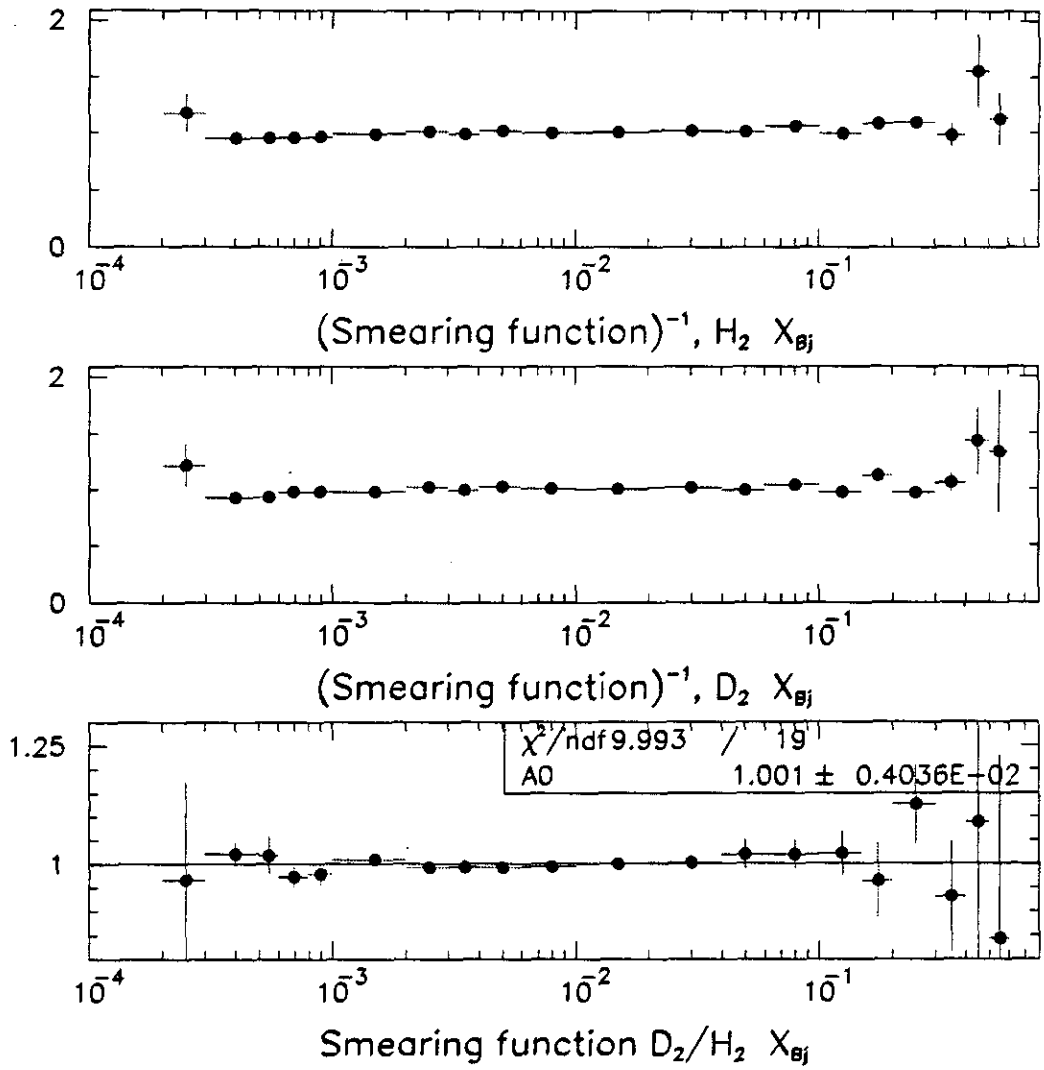

Figure 4.50: The detector smearing as a function of X_{Bj} for the H_2 and the D_2 targets (two top plots) and for the ratio D_2/H_2 (bottom plot).

Chapter 5

The neutron to proton structure function ratio-Results

In this chapter the final results of the measurement of the neutron to proton structure function ratio are presented. The dependence of the ratio on the Bjorken scaling variable x is examined, averaged over Q^2. This measurement has high statistics and small systematic uncertainty and covers the region $0.000004 < x < 0.3$. These are the first high precision results in the region below $x = 0.0004$. In addition, the dependence of the ratio on Q^2 for fixed x is presented.

In the extraction of the structure function ratio the assumption is that there are no nuclear effects in the deuteron, $F_2^d = \frac{1}{2}(F_2^n + F_2^n)$, and that the structure function ratio R is the same for hydrogen and deuterium, $R^d = R^p$. The assumption $R^d = R^p$ is supported by the existing experimental results (see the discussion at the end of chapter 1). With the above assumptions, the cross-section ratio $\sigma_{1\gamma}^n/\sigma_{1\gamma}^p$, is equal to the structure function ratio F_2^n/F_2^p (see equation 1.11).

The structure function ratio is obtained using three largely independent analysis techniques to extract the single-photon-exchange cross section from the measured event rates. The first two techniques use data obtained with the Small Angle Trigger

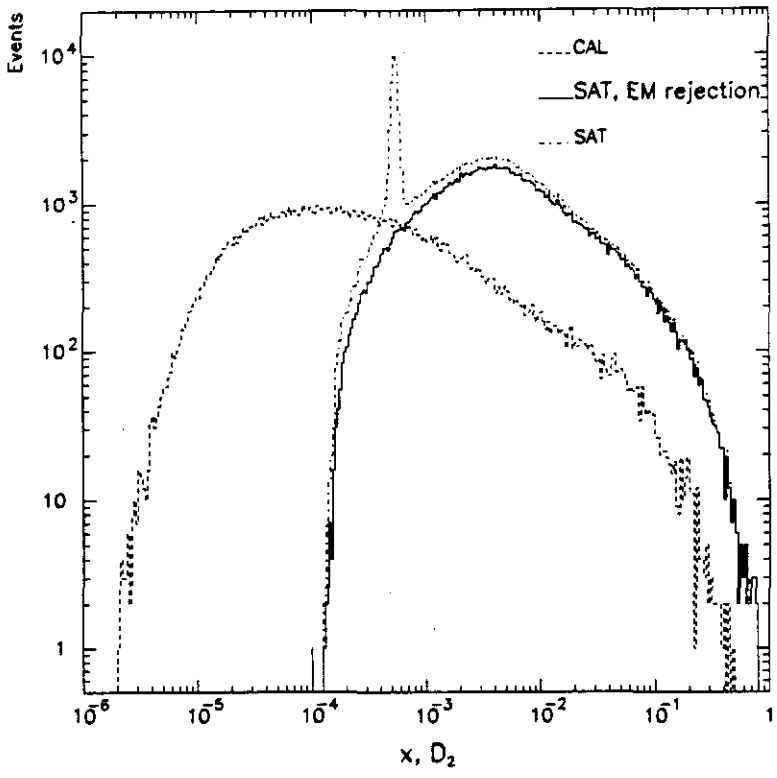

Figure 5.1: The x distribution for D_2. SAT trigger before and after the EM rejection and CAL trigger.

(SAT) and either calculated radiative corrections or calorimeter based event selection. The third analysis technique uses the calorimeter (CAL) trigger (section 4.4.2).

5.1 The final sample

In this section the final statistics for each one of the three analysis techniques and for each target are presented. Both the number of incident muons and the final number of events after all cuts are summarized.

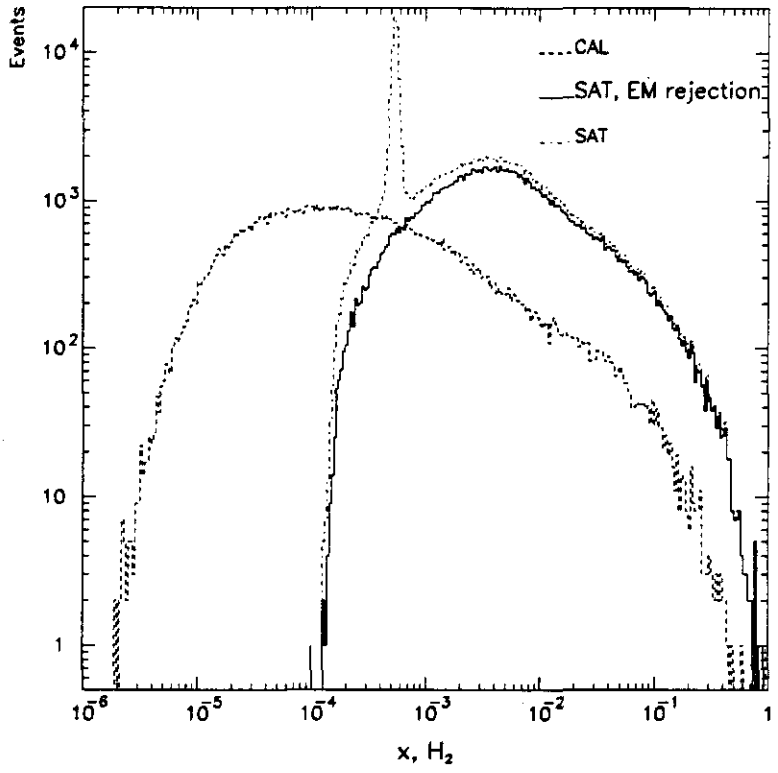

Figure 5.2: The x distribution for H_2. SAT trigger before and after the EM rejection and CAL trigger.

The complete data sample for the muon Small Angle Trigger (SAT), before any

beam phase space cuts were applied, was obtained from 3.05×10^{11} muons incident on the H_2 target. For the D_2 target there were 1.76×10^{11} muons, and for the liquid empty target (MT) there were 0.57×10^{11} muons. After applying the beam selection criteria described in chapter 4, the number of useful beam muons on each target was 1.75×10^{11} on the H_2 target, 0.87×10^{11} on the D_2 target, and 0.30×10^{11} on the MT target. The calorimeter (CAL) trigger data, without any beam cuts, were obtained from 2.22×10^{11} muons on the H_2 target, 1.13×10^{11} muons on the D_2 target, and 0.40×10^{11} muons on the MT target. After the beam selection, for the CAL trigger there were 1.06×10^{11} muons on the H_2 target, 0.52×10^{11} muons on the D_2 target and 0.18×10^{11} muons on the MT target. These beam rates were calculated using the measured prescale factors tabulated in Tables 4.1-4.3 and the Rbeam counts from tables 4.5-4.7. The resulting total number of events for the different analysis techniques and for each target is summarized in table 5.1. The first column gives the total number of SAT events after the kinematic selection, the second column gives the total number of SAT events after the Electromagnetic (EM) background rejection cuts, and the last column gives the total number of CAL trigger events (the three analysis techniques are described in chapter 4). The SAT event yield includes the contribution from both Period I and Period II samples [1]. The x distribution of the events for the three analysis techniques is shown in figure 5.2 for the H_2 target and in figure 5.1 for the D_2 target. The large effect of the muon-electron elastic scattering contribution is shown in the SAT sample with only the kinematic selection. The SAT data set with EM rejection and the CAL trigger data set show no effect, in agreement with the studies presented in chapter 4.

[1]The division of the data in two periods because of the change in the D_2 target composition is described in appendix A. The CAL trigger was active only during Period II

Table 5.1: Final statistics per target

Target	Total number of events		
	SAT kinem. cut	SAT EM selection	CAL kinem. cut
H_2	205112	122354	91073
D_2	180751	126841	93674
MT	2160	1367	1078

5.2 The x dependence of the ratio

In order to study the x dependence of the ratio, the data were averaged over Q^2. The ratio is extracted using equation A.13, with the target composition corresponding to each data period determined by using the procedure described in appendix A (the results are tabulated in table A.3).

The event yields from the two liquid targets are corrected for the contribution of the out-of-target interactions and the target vessel interactions. This is done by subtracting the empty target vessel data scaled with the relative beam fluxes, as described in chapter 4. The relative beam fluxes were calculated from tables 4.5-4.7; and for Period I SAT were $H_2/MT = 6.1452$, $D_2/MT = 2.9989$, and $H_2/D_2 = 2.0491$. For Period II SAT they were $H_2/MT = 5.8967$, $D_2/MT = 2.9146$, and $H_2/D_2 = 2.0231$. The relative beam fluxes for the beam definition of the CAL trigger were $H_2/MT = 5.9201$, $D_2/MT = 2.9275$, and $H_2/D_2 = 2.0223$. The size of the correction due to the empty target subtraction is of the order of $5 - 8\%$ of the uncorrected event yield.

The results of the structure function ratio measurement, F_2^n/F_2^p, as a function of x, obtained using each of the different analysis techniques, are shown in figures

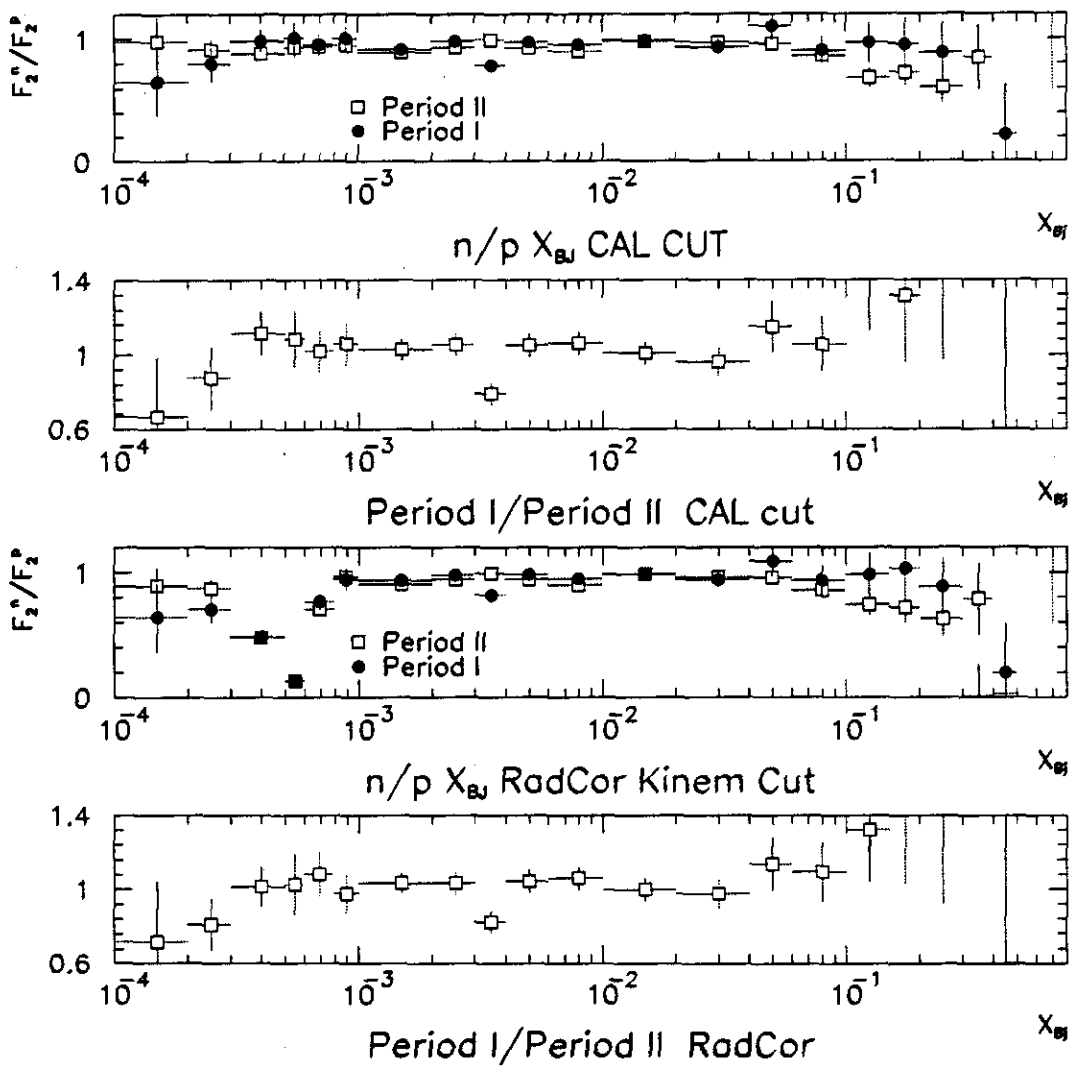

Figure 5.3: The ratio as a function of x from SAT. Comparison of Period I-II.

5.3- 5.6. The F_2^n/F_2^p ratio measurements obtained from each of the two periods of the SAT data sample are compared in figure 5.3. Both the EM rejection method and the radiative correction calculation technique are shown. The ratio of the F_2^n/F_2^p measurement from the two periods is also shown as a function of x for each one of the two analysis techniques. The overall differences are within the normalization uncertainties of the target composition determination discussed in appendix A. The results from the two SAT periods are combined by taking the weighted average of the structure function ratio in each x bin. The weighted average of the structure function

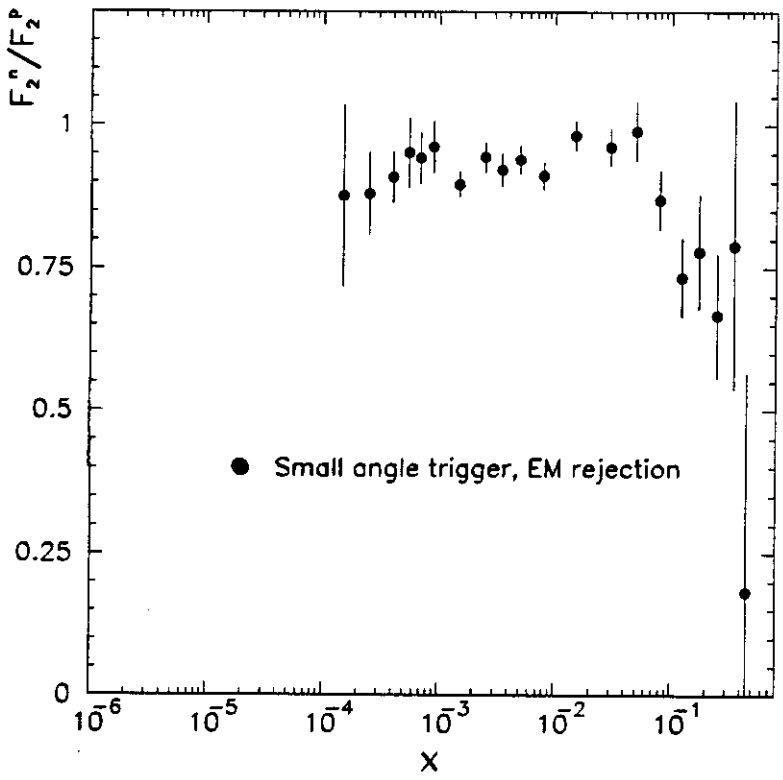

Figure 5.4: The ratio as a function of x from SAT. EM rejection.

ratio, $r \equiv F_2^n/F_2^p$, in each bin of the x variable is given by $r = \sum_i (r_i/s_i^2)/\sum_i (1/s_i^2)$, where r_i and s_i are the ratio and the statistical error on the ratio for period $i = I, II$.

The uncertainty on each value of r is given by $s = 1/\sum_i(1/s_i^2)$. The results from the combined SAT sample using the EM rejection technique are shown in figure 5.4. The combined SAT results using the calculated radiative correction technique are shown in figure 5.5. Because of the large muon-electron elastic scattering effect, which can be identified at the value $x \sim 0.00055$, the calculated radiative correction method breaks down below x of 0.0008. Finally, the ratio obtained with the CAL trigger technique is shown as a function of x in figure 5.6.

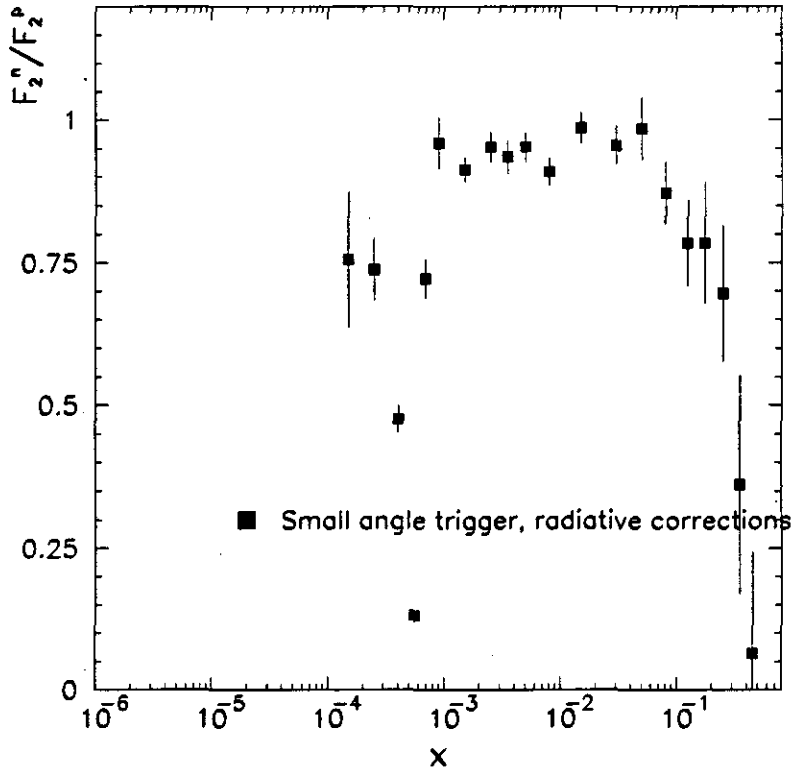

Figure 5.5: The ratio as a function of x from SAT. Calculated radiative corrections.

The results of the three analysis techniques, including the event yields for each target, are listed in tables 5.3- 5.7. The first column of these tables gives the bin edges of each x bin, the next six columns give the event yields for the three targets

before and after the empty target correction, and the last two columns give the F_2^n/F_2^p ratio and the statistical error on the measurement. The results from the SAT with the EM rejection technique are given in tables 5.3 and 5.4 for the SAT periods I and II respectively. The results from the SAT with the calculated radiative correction technique are tabulated in tables 5.5 and 5.6, one table for each of the two periods. The structure function ratio results as a function of x obtained with the CAL trigger are given in table 5.7. The averaged results of both SAT based analysis techniques are presented in table 5.8. In this table the combined F_2^n/F_2^p ratio and the statistical error from each technique is given for each x bin. Since the F_2^n/F_2^p ratio has been obtained assuming no nuclear effects in the deuteron, the corresponding ratio of the per nucleon structure function of the deuteron to that of the proton, F_2^d/F_2^p, can be extracted from the tabulated results using the simple relation

$$F_2^d/F_2^p = \frac{F_2^n/F_2^p + 1}{2}$$

while the error of the F_2^d/F_2^p measurement is half the error of the F_2^n/F_2^p measurement.

The systematic uncertainty and its sources are summarized in table 5.2 for each one of the three analysis techniques. The systematic uncertainty includes the effects of relative normalization (chapter 4 and appendix A), the trigger acceptance differences for the different targets, the calorimeter event selection, and the calculated radiative corrections. The trigger acceptance differences are caused because of hadronic final state differences that affect the veto element of the SSA in front of the muon absorber, and the performance of the CAL trigger. The analysis of the contribution from different sources to the systematic uncertainty is presented in chapter 4). The total systematic uncertainty of each method is obtained by adding in quadrature the values of the systematic errors that are relevant to the method. The resulting total systematic error is less than 3.5% in the region of applicability of each analysis technique (see chapter 4 and table 5.2). In addition, an independent check of the systematic uncertainty on the ratio has been performed using the muon-electron

elastic scattering events. The result of this study is presented in appendix D and is consistent with the value of the systematic uncertainty quoted here.

Table 5.2: Summary of the systematic errors on ratio.

Analysis technique			Source
CAL	SAT and EM rejection	SAT and radiative corrections	
$x < 10^{-3}$	$x < 10^{-2}$	$8 \times 10^{-4} < x$	
$\pm 0.5\%$	$\pm 0.5\%$	$\pm 0.5\%$	Beam NRM
$\pm 0.85\%$	$\pm 0.85\%$	$\pm 0.85\%$	Target
		$< \pm 0.5\%$	Rad. Cor.
	$< 2.0\%$	$< 2.0\%$	SAT veto
	0.6%		CAL cut
$< 3.5\%$			Final state

The final F_2^n/F_2^p results from each one of the three different methods are compared in figure 5.7. The ratio value from each method is plotted in the x region where the systematic errors for this method are minimized. There is very good agreement between the results from the different techniques in the region of overlap. The systematic uncertainty of the result is represented by the shaded band at the bottom of the plot. The x dependence of the structure function ratio measurement is also compared with the results from the NMC experiment [46]. The NMC results shown are also averaged over Q^2, and the assumptions made in the extraction of the structure function ratio are the same as those made in this analysis (no nuclear effects in the deuteron, and R^d=R^p). The agreement between the two experiments is very good. The value of the ratio is systematically below unity in the whole x region that the data cover and it is constant for $x < 0.01$ (the flat line drawn at the value

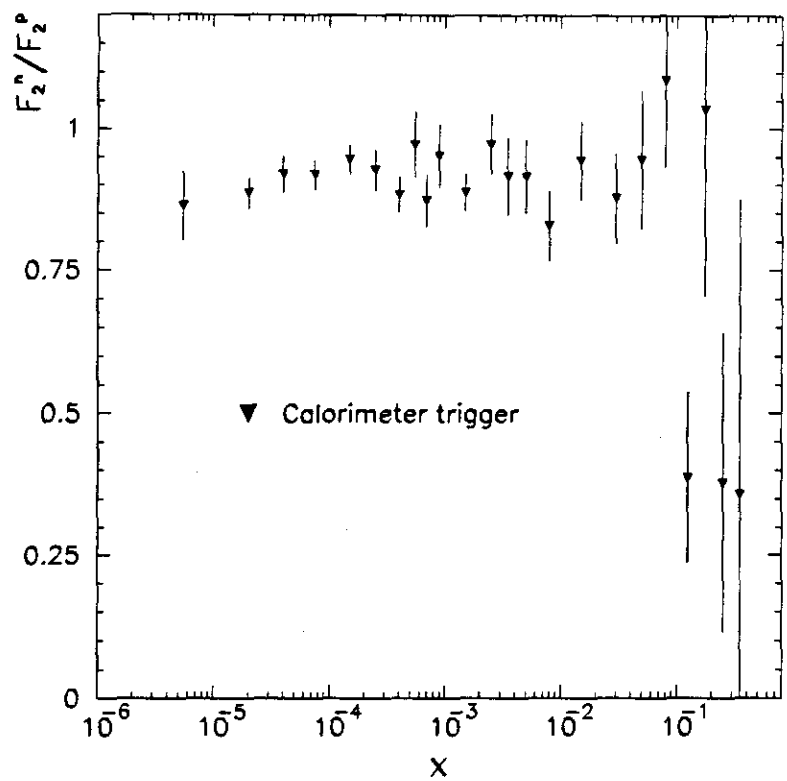

Figure 5.6: The ratio as a function of x from CAL trigger.

$F_2^n/F_2^p = 1$ is to guide the eye). The average Q^2 values in each x bin for the E665 data are larger than the corresponding NMC values [118] in the x bins where both

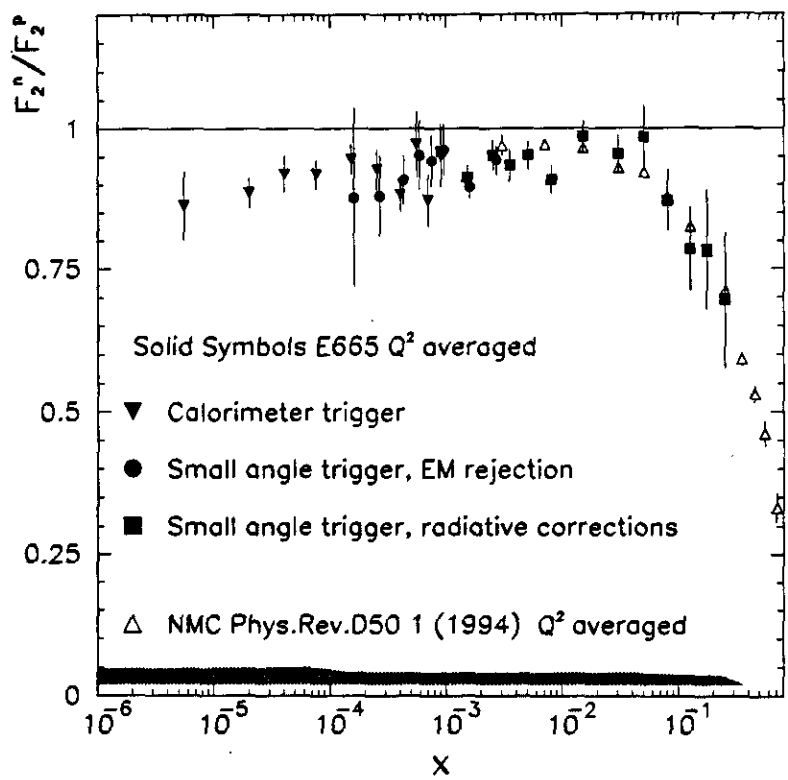

Figure 5.7: The ratio as a function of x. Comparison of the three techniques.

experiments have data. The average Q^2 values per bin are given in table 5.9. The agreement of the measurement from the two experiments indicates that there is no significant Q^2 dependence of the ratio in the region of overlap in x. The measured Q^2 dependence from the E665 data is discussed in section 5.3.

Table 5.3: F_2^n/F_2^p averaged over Q^2 as a function of x. SAT with EM rejection, Period I

x	Event yield			Empty subtracted		F_2^n/F_2^p	error
bin center	H_2	D_2	Empty	H_2	D_2		stat.
0.000150	100	87	2	88	81	0.65	0.28
0.000250	448	427	7	405	406	0.80	0.14
0.000400	1187	1275	10	1126	1245	0.98	0.09
0.000550	666	715	8	617	691	1.01	0.12
0.000695	1160	1231	9	1105	1204	0.95	0.09
0.000895	1196	1262	19	1079	1205	1.00	0.09
0.001500	4897	5052	49	4596	4905	0.91	0.04
0.002500	3634	3814	53	3308	3655	0.98	0.05
0.003500	2925	2829	26	2765	2751	0.78	0.05
0.005000	3838	4059	44	3568	3927	0.97	0.05
0.008000	4054	4249	45	3777	4114	0.95	0.05
0.015000	3780	3965	58	3424	3791	0.99	0.05
0.030000	2304	2389	26	2144	2311	0.93	0.06
0.050000	913	1006	15	821	961	1.10	0.11
0.080000	815	816	14	729	774	0.90	0.11
0.125000	389	400	7	346	379	0.96	0.16
0.175000	186	199	1	180	196	0.95	0.21
0.250000	142	146	1	136	143	0.89	0.24

Table 5.4: F_2^n/F_2^p averaged over Q^2 as a function of x. SAT with EM rejection, Period II

x	Event yield			Empty subtracted		F_2^n/F_2^p	error
bin center	H_2	D_2	Empty	H_2	D_2		stat.
0.000150	242	260	2	230	254	0.98	0.19
0.000250	1178	1229	8	1131	1206	0.91	0.08
0.000400	3249	3301	34	3049	3202	0.88	0.05
0.000550	1769	1837	20	1651	1779	0.93	0.07
0.000695	3128	3256	36	2916	3151	0.94	0.05
0.000895	3314	3468	38	3090	3357	0.95	0.05
0.001500	13346	13620	138	12532	13218	0.89	0.03
0.002500	10028	10385	121	9315	10032	0.93	0.03
0.003500	7415	7955	74	6979	7739	0.99	0.04
0.005000	10559	11008	100	9969	10717	0.93	0.03
0.008000	11096	11366	114	10424	11034	0.90	0.03
0.015000	10143	10776	116	9459	10438	0.98	0.03
0.030000	6527	6891	80	6055	6658	0.97	0.04
0.050000	2738	2866	35	2532	2764	0.96	0.06
0.080000	2375	2381	26	2222	2305	0.86	0.06
0.125000	1226	1120	13	1149	1082	0.68	0.08
0.175000	543	513	4	519	501	0.73	0.11
0.250000	480	413	8	433	390	0.61	0.12

Table 5.5: F_2^n/F_2^p averaged over Q^2 as a function of x. SAT with radiative corrections, Period I

x	Event yield			Empty subtracted		F_2^n/F_2^p	error
bin center	H_2	D_2	Empty	H_2	D_2		stat.
0.000150	126	109	5	97	89	0.64	0.27
0.000250	554	509	9	496	473	0.71	0.11
0.000400	2935	2380	36	2714	2257	0.49	0.04
0.000550	10358	6546	59	9994	6354	0.13	0.02
0.000695	1669	1575	24	1518	1497	0.77	0.07
0.000895	1282	1313	22	1148	1244	0.94	0.09
0.001500	5031	5218	61	4657	5028	0.94	0.04
0.002500	3745	3921	56	3404	3751	0.98	0.05
0.003500	2962	2909	29	2783	2819	0.82	0.05
0.005000	3909	4139	48	3612	3992	0.98	0.05
0.008000	4110	4296	47	3821	4154	0.95	0.05
0.015000	3798	3992	56	3457	3824	0.98	0.05
0.030000	2309	2391	29	2132	2305	0.94	0.07
0.050000	911	996	15	816	949	1.09	0.12
0.080000	800	818	13	722	779	0.94	0.12
0.125000	388	404	7	348	384	0.98	0.18
0.175000	189	207	2	177	201	1.03	0.23
0.250000	155	159	1	149	157	0.88	0.23

Table 5.6: F_2^n/F_2^p averaged over Q^2 as a function of x. SAT with radiative corrections, Period II

x	Event yield			Empty subtracted		F_2^n/F_2^p	error
bin center	H_2	D_2	Empty	H_2	D_2		stat.
0.000150	299	306	5	272	287	0.89	0.14
0.000250	1438	1457	19	1324	1383	0.87	0.07
0.000400	8078	6561	99	7496	6235	0.48	0.03
0.000550	28770	18338	176	27733	17784	0.13	0.01
0.000695	4696	4355	54	4380	4187	0.71	0.04
0.000895	3494	3665	48	3209	3515	0.96	0.05
0.001500	13742	14101	155	12828	13633	0.90	0.03
0.002500	10203	10650	121	9490	10290	0.94	0.03
0.003500	7594	8135	80	7121	7897	0.99	0.04
0.005000	10665	11201	102	10062	10899	0.94	0.03
0.008000	11236	11502	116	10552	11160	0.90	0.03
0.015000	10183	10847	119	9482	10497	0.99	0.03
0.030000	6531	6863	79	6063	6629	0.96	0.04
0.050000	2710	2846	32	2521	2752	0.96	0.06
0.080000	2373	2381	24	2231	2310	0.85	0.06
0.125000	1221	1155	12	1149	1119	0.74	0.08
0.175000	551	517	5	523	503	0.72	0.12
0.250000	498	433	9	446	407	0.63	0.14

Table 5.7: F_2^n/F_2^p averaged over Q^2 as a function of x. CAL trigger, Period II

x	Event yield			Empty subtracted		F_2^n/F_2^p	error
bin center	H_2	D_2	Empty	H_2	D_2		stat.
0.000007	2263	2273	25	2115	2200	0.86	0.06
0.000020	11248	11484	108	10609	11168	0.89	0.03
0.000040	8467	8723	101	7869	8427	0.92	0.03
0.000075	12959	13403	137	12148	13002	0.92	0.03
0.000150	13318	13759	198	12146	13179	0.94	0.03
0.000250	7426	7572	120	6716	7221	0.93	0.04
0.000400	8650	8796	90	8117	8533	0.88	0.03
0.000550	2801	2951	36	2588	2846	0.97	0.06
0.000695	3972	4018	41	3729	3898	0.87	0.05
0.000895	3007	3137	39	2776	3023	0.95	0.06
0.001500	7477	7641	71	7057	7433	0.89	0.03
0.000250	3237	3450	31	3053	3359	0.97	0.05
0.003500	1830	1898	17	1729	1848	0.91	0.07
0.005000	2107	2162	26	1953	2086	0.91	0.07
0.008000	2088	2073	19	1976	2017	0.83	0.06
0.015000	2014	2079	30	1836	1991	0.94	0.07
0.030000	1469	1454	26	1315	1378	0.88	0.08
0.050000	624	649	8	577	626	0.94	0.12
0.080000	462	509	7	421	489	1.09	0.15
0.125000	231	177	2	219	171	0.39	0.15
0.175000	75	85	0	75	85	1.03	0.33
0.250000	67	52	0	67	52	0.38	0.26

Table 5.8: F_2^n/F_2^p averaged over Q^2 as a function of x. SAT Period I and II combined

x bin center	F_2^n/F_2^p CAL cut	error	F_2^n/F_2^p RadCor	error
0.000150	0.876729	0.158876	0.838817	0.124753
0.000250	0.880088	0.0715525	0.824822	0.0578545
0.000400	0.908709	0.0440922	0.482129	0.0228881
0.000550	0.952012	0.0614078	0.131025	0.00947129
0.000695	0.942613	0.0456672	0.72214	0.0344202
0.000895	0.961809	0.0457547	0.959382	0.0455448
0.001500	0.896405	0.0216909	0.91286	0.0218553
0.002500	0.943888	0.0261097	0.952262	0.0265019
0.003500	0.921745	0.0289859	0.934459	0.0293811
0.005000	0.939295	0.0248158	0.952204	0.0252583
0.008000	0.911621	0.0240092	0.90919	0.0243973
0.015000	0.981364	0.0262125	0.98571	0.0271438
0.030000	0.961476	0.0324948	0.955106	0.0337592
0.050000	0.989617	0.051934	0.984882	0.054412
0.080000	0.86909	0.0522792	0.872088	0.0546184
0.125000	0.733488	0.0693039	0.784332	0.0746243
0.175000	0.778318	0.100553	0.784425	0.106676
0.250000	0.666615	0.109564	0.695666	0.119213

Table 5.9: Average Q^2 in each x bin. SAT and CAL trigger.

x	Average Q^2 (GeV^2)	
	CAL trig.	SAT
0.000004-0.00001	0.002	
0.00001-0.00003	0.005	
0.00003-0.00005	0.011	
0.00005-0.0001	0.022	
0.0001-0.0002	0.043	0.115
0.0002-0.0003	0.072	0.145
0.0003-0.0005	0.115	0.201
0.0005-0.0006	0.154	0.252
0.0006-0.00079	0.196	0.293
0.00079-0.001	0.252	0.344
0.001-0.002	0.373	0.437
0.002-0.003	0.631	0.561
0.003-0.004	0.867	0.668
0.004-0.006	1.250	0.857
0.006-0.010	2.034	1.277
0.010-0.020	3.853	2.383
0.020-0.040	7.845	4.928
0.040-0.060	12.858	8.125
0.060-0.100	20.863	12.219
0.100-0.150	32.917	18.634
0.150-0.200	50.957	24.143
0.200-0.300	74.440	35.588

5.3 The Q^2 dependence of the ratio

In order to examine the Q^2 dependence of the F_2^n/F_2^p ratio in each x bin the data were fitted with a linear function of $\ln(Q^2)$, $\frac{F_2^n}{F_2^p}(x_i, Q^2) = \beta_0(x_i) + \beta(x_i) \times \ln(Q^2)$, where i is the bin index. The fit parameters were obtained using a χ^2 minimization procedure. The $\ln(Q^2)$ dependence of the F_2^n/F_2^p ratio obtained using the CAL trigger data set is shown in figures 5.8- 5.10; each plot in the figures corresponding to a different x bin. The $\ln(Q^2)$ dependence of the SAT data set with electromagnetic rejection cuts is presented in figures 5.11- 5.13. In each one of the plots in these figures the

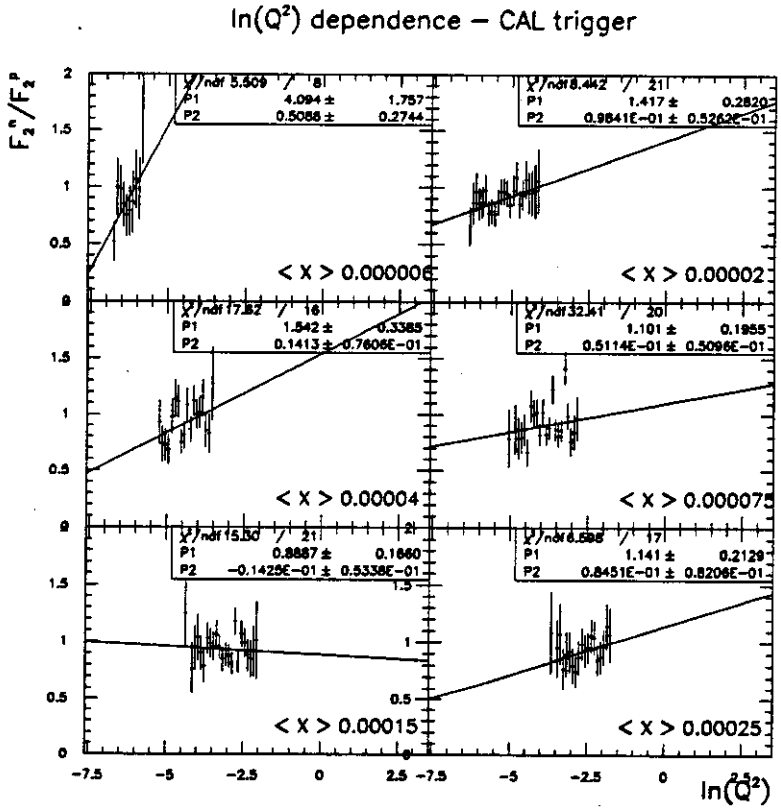

Figure 5.8: Logarithmic Q^2 dependence for fixed x - CAL trigger.

parameters obtained from the linear fit are listed. The figures are labeled with the

value of x at the center of the corresponding x bin. The results from the two analysis techniques are consistent; and within the statistical power of the measurement, there is no significant Q^2 dependence observed.

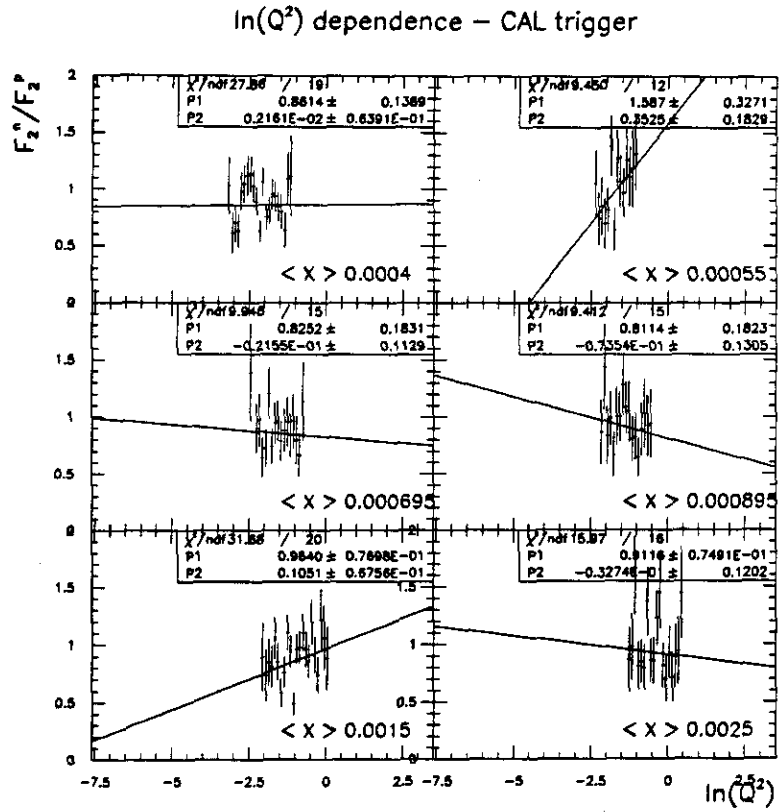

Figure 5.9: Logarithmic Q^2 dependence for fixed x - CAL trigger.

The measured logarithmic Q^2 slope is shown as a function of x in figure 5.14. The slopes $\beta(x_i)$ obtained from the analysis technique with the smallest systematic and statistical error in each x_i bin are plotted at the center of that bin. The E665 results are compared with the results of NMC [118], which are also consistent with no Q^2 dependence in the small-x region where both experiments have statistical power. The flat line plotted at the value $\beta = 0$ is drawn to guide the eye. The NMC results show significant negative slopes in the higher x region, $0.1 < x < 0.4$.

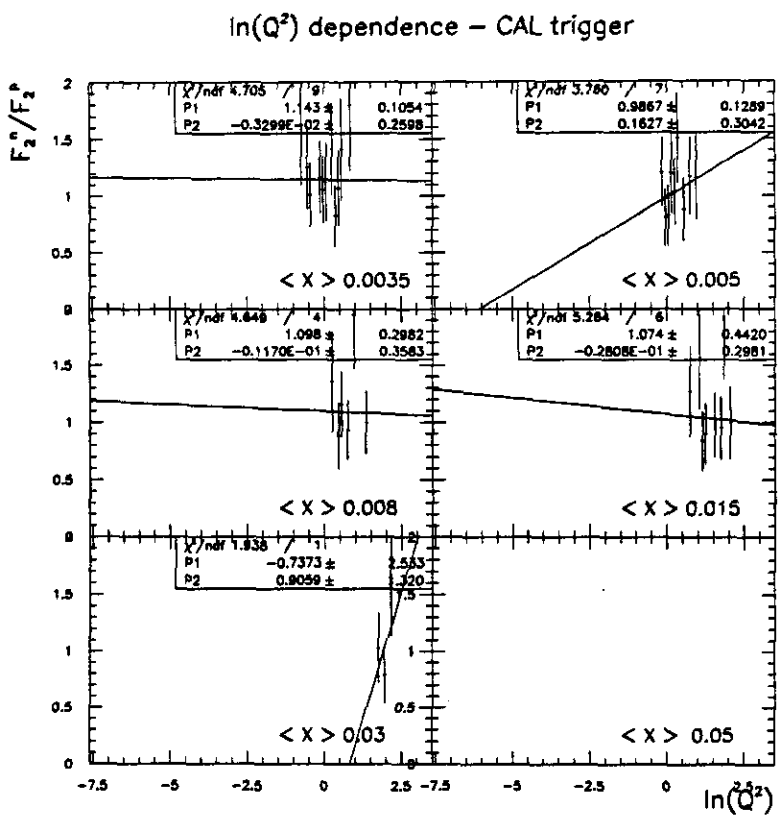

Figure 5.10: Logarithmic Q^2 dependence for fixed x - CAL trigger.

The results from the CAL trigger and the SAT with EM rejection analysis techniques are given in tables 5.10 and 5.11. For each technique the measured slopes (β), the intercepts at $Q^2 = 1GeV^2$ (β_0), and the χ^2 per degree of freedom of the fit are given for each x_i bin. In addition, the χ^2 per degree of freedom from a flat line fit is included (fit after setting $\beta = 0$). The logarithmic Q^2 dependence of the F_2^d/F_2^p ratio can be obtained from that of the F_2^n/F_2^p ratio. Since $F_2^d/F_2^p = \frac{F_2^n/F_2^p+1}{2}$, the logarithmic Q^2 slope β^d and the intercept β_0^d of the F_2^d/F_2^p ratio are given by the relations $\beta^d = 1/2\beta$ and $\beta_0^d = (\beta_0 + 1)/2$.

In order to verify that the apparatus did not introduce a target dependent bias in the Q^2 measurement, a series of tests have been performed. Reconstructed Monte Carlo events and reconstructed straight through beams were used to demonstrate that there are no systematic biases in the Q^2 measurement (section 4.6). In addition, the electron mass has been measured as a function of Q^2 from both targets, and this also showed no target dependent effect (appendix D).

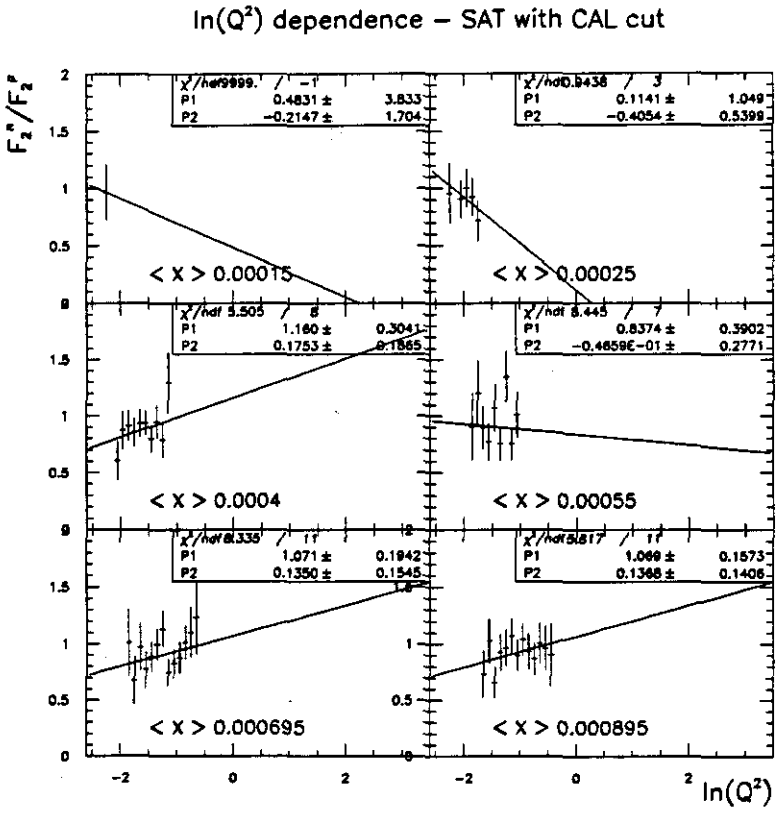

Figure 5.11: Logarithmic Q^2 dependence for fixed x - SAT with EM rejection.

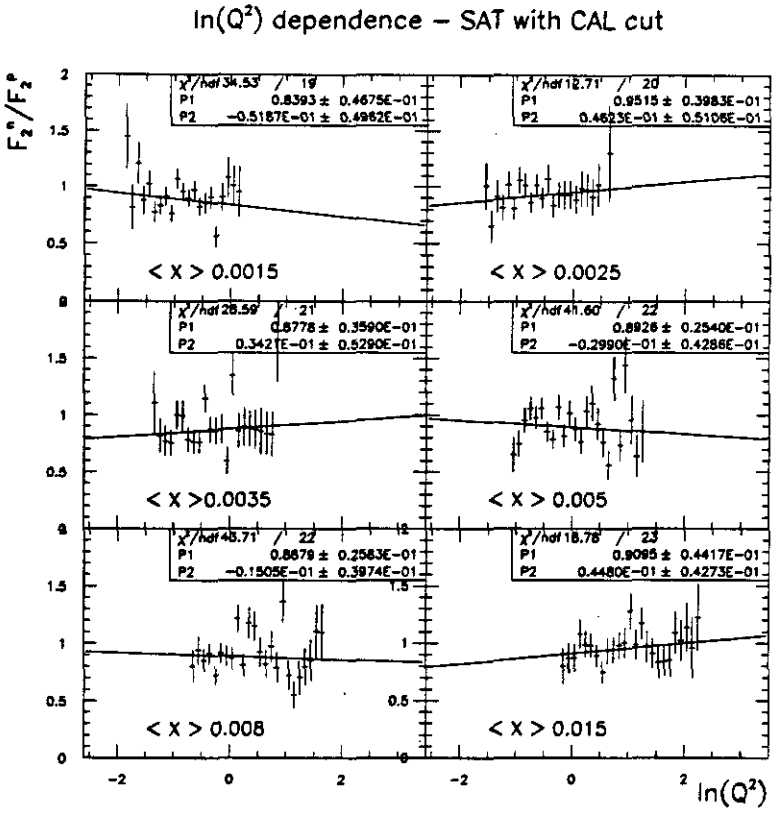

Figure 5.12: Logarithmic Q^2 dependence for fixed x - SAT with EM rejection.

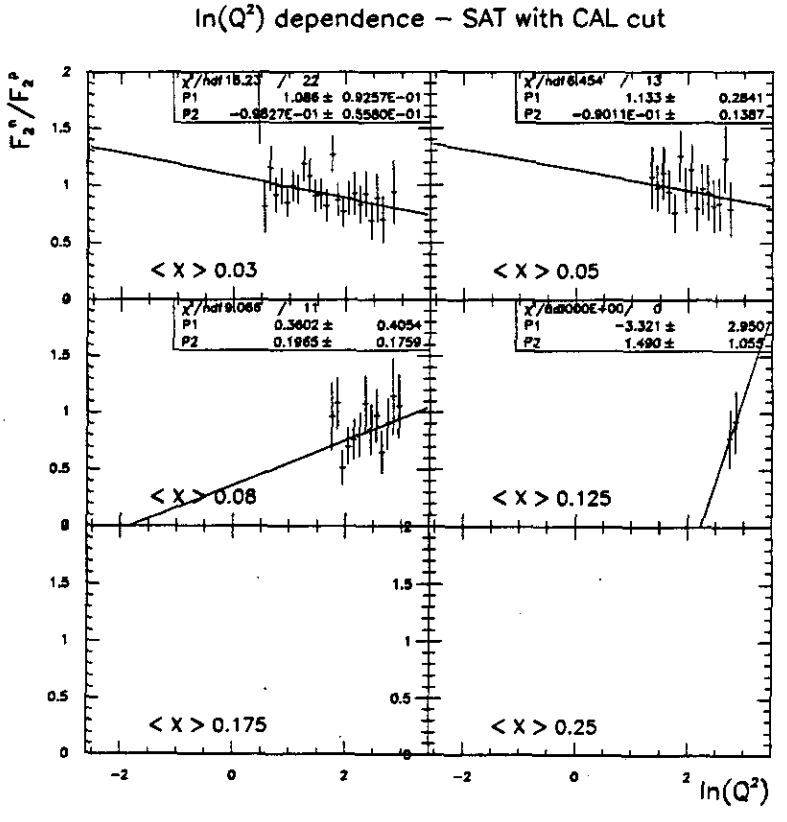

Figure 5.13: Logarithmic Q^2 dependence for fixed x - SAT with EM rejection.

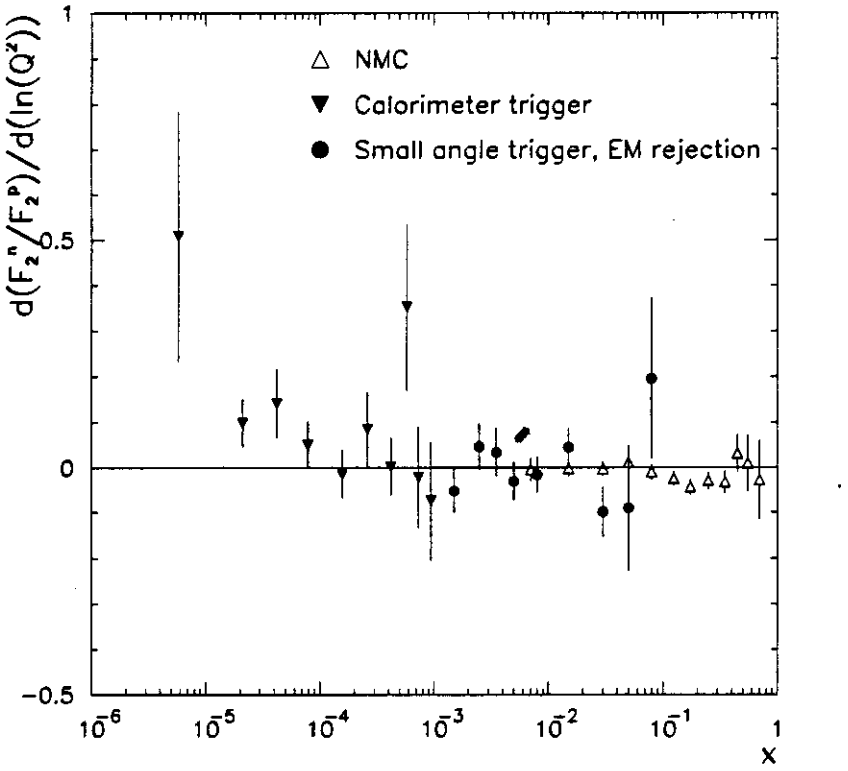

Figure 5.14: Logarithmic Q^2 slopes, as a function of x. The NMC result is also plotted.

Table 5.10: F_2^n/F_2^p as a function of Q^2, using the CAL trigger.

CAL trigger				
x	β	β_0	$\chi^2/ndof$	$\chi^2/ndof$ $\beta = 0$
0.000004-0.00001	0.508 ± 0.274	4.09 ± 1.75	0.69	0.98
0.00001-0.00003	0.098 ± 0.052	1.41 ± 0.28	0.40	0.53
0.00003-0.00005	0.141 ± 0.076	1.54 ± 0.34	1.10	1.20
0.00005-0.0001	0.051 ± 0.050	1.10 ± 0.19	0.62	1.52
0.0001-0.0002	0.014 ± 0.053	0.89 ± 0.17	0.73	0.68
0.0002-0.0003	0.085 ± 0.082	1.14 ± 0.21	0.38	0.42
0.0003-0.0005	0.002 ± 0.063	0.86 ± 0.14	1.42	1.37
0.0005-0.0006	0.352 ± 0.183	1.58 ± 0.33	0.79	1.00
0.0006-0.00079	-0.022 ± 0.112	0.83 ± 0.18	0.66	0.62
0.00079-0.001	-0.074 ± 0.130	0.81 ± 0.18	0.63	0.60
0.001-0.002	0.105 ± 0.068	0.96 ± 0.08	1.55	1.57
0.002-0.003	-0.033 ± 0.120	0.91 ± 0.08	1.00	0.94
0.003-0.004	-0.003 ± 0.260	1.14 ± 0.11	0.52	0.47
0.004-0.006	0.163 ± 0.340	0.99 ± 0.13	0.54	0.50
0.006-0.010	-0.012 ± 0.358	1.1 ± 0.30	1.16	0.92
0.010-0.020	-0.028 ± 0.298	1.1 ± 0.44	0.88	0.75
0.020-0.040	0.906 ± 1.320	-0.7 ± 2.55	1.90	1.20

Table 5.11: F_2^n/F_2^p as a function of Q^2, using the SAT.

SAT				
x	β	β_0	$\chi^2/ndof$	$\chi^2/ndof$ $\beta = 0$
0.0002-0.0003	-0.405± 0.539	1.16 ± 0.30	0.31	0.38
0.0003-0.0005	0.175± 0.186	0.83 ± 0.39	0.69	0.70
0.0005-0.0006	-0.047± 0.277	1.07 ± 0.19	1.20	1.04
0.0006-0.00079	0.135± 0.545	1.09 ± 0.16	0.76	0.75
0.00079-0.001	0.137± 0.140	0.84 ± 0.05	0.53	0.55
0.001-0.002	-0.052± 0.049	0.95 ± 0.04	1.78	1.73
0.002-0.003	0.046± 0.051	0.88 ± 0.04	0.64	0.63
0.003-0.004	0.034± 0.052	0.89 ± 0.03	1.33	1.29
0.004-0.006	-0.029± 0.042	0.89 ± 0.03	1.86	1.78
0.006-0.010	-0.015± 0.039	0.89 ± 0.03	11.95	1.80
0.010-0.020	0.045± 0.043	0.91 ± 0.04	0.81	0.81
0.020-0.040	-0.098± 0.056	1.08 ± 0.09	0.74	0.82
0.040-0.060	-0.090± 0.138	1.13 ± 0.28	0.50	0.49

Chapter 6

Summary and Conclusions

In this chapter the physics results of the measurement of the neutron to proton structure function ratio are summarized. The results are compared with predictions from models that include shadowing effects in the deuteron. The implication of the measurement to the experimentally estimated value of the Gottfried sum rule is also discussed.

6.1 Summary and Comparison with Shadowing models

The x and Q^2 dependence of the structure function ratio, F_2^n/F_2^p, from scattering of 470 GeV muons on hydrogen and deuterium targets, has been measured in the region $0.000004 < x < 0.3$ and $Q^2 > 0.001 GeV^2$. The ratio was extracted assuming no nuclear effects in the deuteron, $F_2^n/F_2^p = 2F_2^d/F_2^p - 1$, where F_2^d is the the per nucleon structure function of the deuteron. It was also assumed that $R^d = R^p$, where R is the ratio of the longitudinal to transverse polarization cross-sections of the virtual photon. With this assumption, the ratio of the deuteron to proton single-photon-exchange cross-sections is equal to the structure function ratio F_2^d/F_2^p. The

ratio F_2^n/F_2^p was found to be constant for $x < 0.01$ and to have no significant Q^2 dependence.

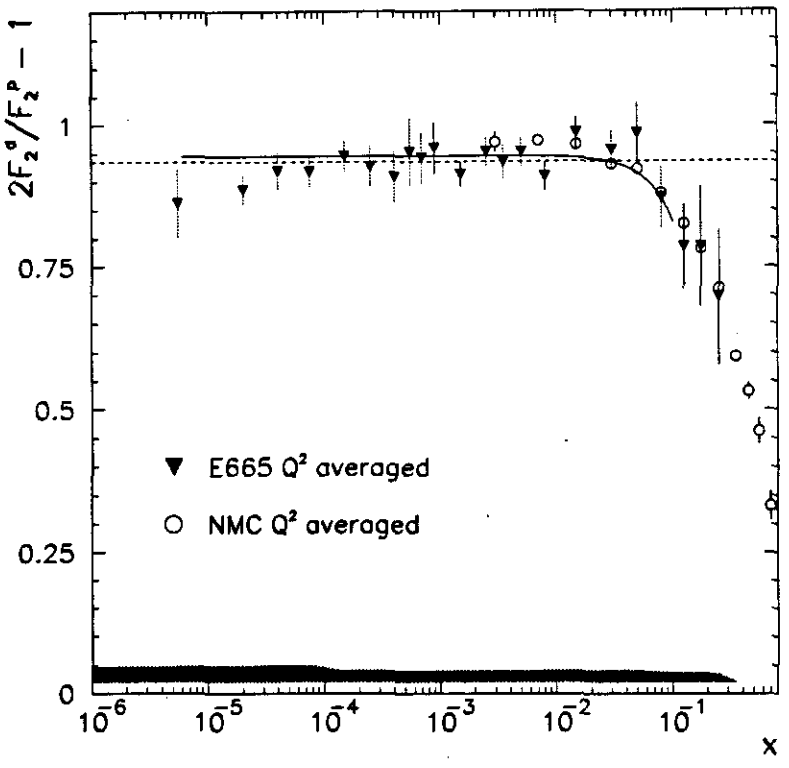

Figure 6.1: F_2^n/F_2^p ratio versus x, using the best points from each method. The solid line is the ratio prediction from Badełek and Kwieciński, including the shadowing effect, and the dashed line is a straight line fit to the E665 data, for $x < 0.01$.

In order to obtain the constant value of the ratio for $x < 0.01$, the measurement from the analysis technique with the smallest systematic and statistical error was used in each x bin. The results are shown in figure 6.1. The NMC points from [46] are also plotted, in order to emphasize the quantitative agreement between the two data sets. The value obtained from a straight line fit for $x \leq 0.01$ is 0.935 ± 0.008 (statistical error), with a χ^2 per degree of freedom of 0.83 (dashed line in figure 6.1).

Since $F_2^d/F_2^p = \frac{F_2^n/F_2^p+1}{2}$, the ratio F_2^d/F_2^p for $x < 0.01$, is then 0.968 ± 0.004 (statistical error), which means that the per nucleon structure function of the deuteron is 3.2% smaller than the structure function of a free nucleon. The data are compared to the prediction of the model of Badełek and Kwieciński, [11], which calculates the effects of nuclear shadowing in the deuteron. The curve in figure 6.1 (solid line) is from [43], where the prediction of the model for the ratio F_2^n/F_2^p including the shadowing effects is given in the E665 kinematic range. There is good agreement between the prediction of the model and the E665 data. Similar behaviour of the structure function ratio has been predicted by the model of Melnitchouk and Thomas [10]. In both models the shadowing effects in the deuteron are introduced by using the double-interaction formalism (see discussion in chapter 1). The vector meson contribution and the partonic contribution are both included. The two models differ in the way that the high and low Q^2 regions are connected, see [10] for a discussion. The prediction of the model of Melnitchouk and Thomas for F_2^d/F_2^p from [10] is shown in figure 6.2, and it is compared with the E665 results.

The x and Q^2 dependence of the structure function ratio F_2^n/F_2^p from the analysis techniques with the smallest systematic and statistical uncertainties are summarized in table 6.1. For each x bin the table includes the value of the ratio F_2^n/F_2^p with the statistical and systematic uncertainty, the average Q^2 for each bin, the Q^2 slope, and the method with which the measurement was obtained (the legends for the method are: CLT for the CAL trigger, STC for the SAT trigger with EM rejection, and STR for the SAT trigger with calculated radiative corrections). The ratio of the per nucleon structure function of the deuteron to that of the proton, F_2^d/F_2^p, can be obtained using the relation $F_2^d/F_2^p = \frac{F_2^n/F_2^p+1}{2}$.

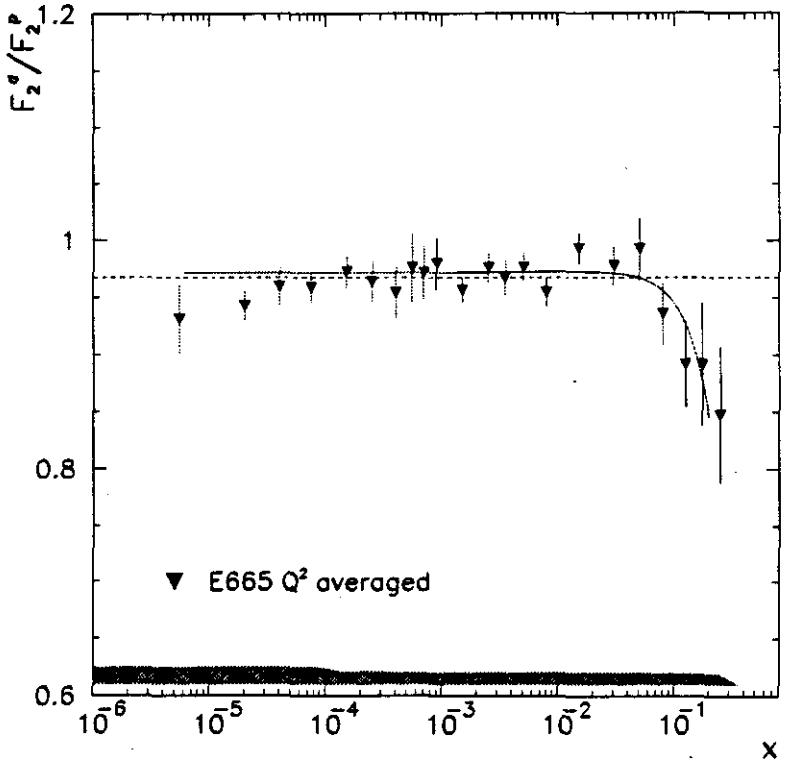

Figure 6.2: F_2^d/F_2^p ratio versus x, using the best points from each method. The solid line is the ratio prediction from Melnitchouk and Thomas, including the shadowing effect, and the dashed line is a straight line fit to the E665 data, for $x < 0.01$.

Table 6.1: F_2^n/F_2^p as a function of x and Q^2. $F_2^d/F_2^p = \frac{F_2^n/F_2^p+1}{2}$.

x	F_2^n/F_2^p	$< Q^2 >$	error		method	β	error
			stat.	syst.			
0.000004-0.00001	0.862	0.002	0.061	0.027	CLT	0.508	0.274
0.00001-0.00003	0.886	0.005	0.027	0.028	CLT	0.098	0.052
0.00003-0.00005	0.919	0.011	0.033	0.029	CLT	0.141	0.076
0.00005-0.0001	0.918	0.022	0.026	0.029	CLT	0.051	0.050
0.0001-0.0002	0.944	0.043	0.027	0.030	CLT	0.014	0.053
0.0002-0.0003	0.927	0.072	0.036	0.029	CLT	0.085	0.082
0.0003-0.0005	0.909	0.201	0.044	0.021	STC	0.002	0.063
0.0005-0.0006	0.952	0.252	0.061	0.022	STC	0.352	0.183
0.0006-0.00079	0.943	0.293	0.045	0.022	STC	-0.022	0.112
0.00079-0.001	0.959	0.344	0.045	0.021	STR	-0.074	0.130
0.001-0.002	0.913	0.437	0.022	0.020	STR	-0.052	0.049
0.002-0.003	0.952	0.561	0.027	0.021	STR	0.046	0.051
0.003-0.004	0.934	0.668	0.029	0.021	STR	0.034	0.052
0.004-0.006	0.952	0.857	0.025	0.021	STR	-0.029	0.042
0.006-0.010	0.909	1.277	0.024	0.020	STR	-0.015	0.039
0.010-0.020	0.986	2.383	0.027	0.022	STR	0.045	0.043
0.020-0.040	0.955	4.928	0.033	0.021	STR	-0.098	0.056
0.040-0.060	0.985	8.125	0.054	0.022	STR	-0.090	0.138
0.060-0.100	0.872	12.219	0.055	0.019	STR	0.196	0.175
0.100-0.150	0.785	18.634	0.074	0.017	STR		
0.150-0.200	0.784	24.143	0.107	0.017	STR		
0.200-0.300	0.700	35.588	0.119	0.016	STR		

6.2 Discussion and conclusions

In the first chapter of this thesis we examined the theoretical issues involved in the interpretation of the structure function ratio F_2^n/F_2^p in muon-nucleon inelastic scattering. In the high four-momentum transfer (Q^2) limit, where the quark-parton model is valid, the F_2^n/F_2^p ratio is related to the ratio of the down- and up-quark momentum distributions, and it can be used to measure the Gottfried sum rule that provides information about the light-flavor isospin symmetry of the nucleonic sea. The low-x measurements are of great importance, since most of the contribution to the sum rule comes from the low-x region. Furthermore, in this regime perturbative Quantum Chromo-Dynamics (pQCD) predicts that the Q^2 dependence of the structure function ratio can be at most logarithmic. This is a consequence of the logarithmic Q^2 dependence of the nucleon structure functions, as calculated within the framework of pQCD (see discussion in chapter 1). Even in the case of differences in the Q^2 evolution due to the different flavor contents of the neutron and the proton, the F_2^n/F_2^p ratio will have a slow logarithmic Q^2 dependence.

The above picture becomes more "colorful" if we allow Q^2 to become small enough that the strong coupling constant α_s becomes large. In this case the interactions among the partons in the nucleon during the scattering process become important, introducing a stronger Q^2 dependence to the structure functions (higher-twist effects, $\sim 1/Q^{2n-2}$, equation 1.23). The higher-twist effects are not calculable in pQCD and from their origin are flavor dependent, thus introducing a Q^2 dependence to the ratio. If Q^2 becomes even smaller, the perturbative expansion breaks down altogether and the Vector Meson Dominance (VMD) inspired [1] phenomenological description of the structure functions is the only one available (equation 1.26). This again introduces a strong Q^2 dependence to the structure functions and possibly to the ratio, in the low Q^2 region. In addition, the issue of nuclear shadowing in the deuteron, which

[1] This includes also the Generalized VMD (GVMD) models

arises naturally in the VMD picture and is a low-x phenomenon, has to be resolved. Also, Regge phenomenology predicts the equality of the neutron and proton structure functions in the low-x limit (cf. equation 1.30 and the discussion in chapter 1).

The previously existing high precision data from the NMC experiment [118] covered the region $x > 0.002$ and $Q^2 > 0.1GeV^2$. The NMC measurement of the Gottfried sum rule (using a Regge inspired extrapolation for the unmeasured x region) indicates that the nucleonic sea is not isospin symmetric [46]. The x region covered did not allow NMC to investigate deuterium shadowing. The measured Q^2 dependence in the NMC data (see figure 5.14) shows some higher-twist contribution in the higher-x region, but it is consistent with no effect in the lower-x region ($x < 0.1$) ([118] for a discussion).

The E665 results from the measurement presented in this thesis cover the region $0.000004 < x < 0.3$ and $Q^2 > 0.001GeV^2$, three orders of magnitude lower in x than NMC, and with higher average Q^2 in the overlap region. The structure function ratio F_2^n/F_2^p was obtained from the single-photon-exchange cross-section ratio assuming that $R^p = R^n$, where R is the ratio of the longitudinal to transverse polarization cross-sections of the virtual photon. The structure function ratio F_2^n/F_2^p, extracted without any consideration of nuclear effects in the deuteron, is constant for $x \leq 0.01$, and is found to be $0.935 \pm 0.008 \pm 0.034$, where the first number is the statistic error and the second the systematic error [2]. The ratio of the per nucleon structure function of the deuteron to that of the proton for $x \leq 0.01$, is then $F_2^d/F_2^p = 0.968 \pm 0.004 \pm 0.017$. This implies that the per nucleon structure function of the deuteron is smaller than the structure function of a free nucleon by $3.2\% \pm 1.7\%$. This can be an indication of shadowing of virtual photons on the deuteron. The E665 data match the predictions of phenomenological models that calculate the effect of nuclear shadowing in the deuteron ([11], [10]). Unfortunately, this is not the end of the story. These models

[2]The systematic error assigned is the largest value of the x dependent total systematic error presented in table 5.2 and in figure 5.7

rely on parametrizations of inclusive diffractive processes to calculate shadowing, so they are valid to the extent that Regge phenomenology concepts are valid. Of course, in that case we already have a prediction for the difference of the structure functions *of free nucleons*, $F_2^p - F_2^n \sim x^{1-0.5}$, so assuming that we have reached the Regge limit (see chapter 1) our measurement is indeed a confirmation of the existence of nuclear effects in the deuteron. In this case, the shadowing calculations should be used to correct all F_2^n measurements extracted from the deuteron (the size of the effect depends in general on x and Q^2). Since the shadowing effects decrease the structure function of the bound neutron compared to the structure function of the free neutron, the shadowing correction to the measured neutron structure function from the deuteron increases its value. Since the Gottfried integral is defined to be $S_G = \int_0^1 dx \, \frac{F_2^p(x) - F_2^n(x)}{x}$, the shadowing correction will decrease the integrand, thus reducing the value of the Gottfried sum rule. If the NMC data that were used to extract the Gottfried sum rule are corrected for shadowing, then the value of the sum rule will further *decrease* by $\sim 12\%$ [43]. This implies that the sea quark distributions are not flavor symmetric. This conclusion will affect the results of global analyses that extract parton distribution functions using structure function measurements, which will in turn affect the calculation of hard scattering cross-sections in ep, pp and $p\bar{p}$ collisions. The importance of the measurement of the ratio F_2^n/F_2^p on the determination of the parton distribution functions can be seen clearly in figure 6.3.

In this figure a comparison of the NMC, BCDMS, and EMC data with the ratio F_2^n/F_2^p constructed from existing parton distribution functions is shown (from [119]). The ratio is plotted at $Q^2 = M_W^2$, where M_W^2 is the mass of the W boson. It can be seen clearly that older sets of parton distribution functions which were not constrained by the recent NMC data, can be easily ruled out.

If, on the other hand, we choose to interpret our results as the measured difference of the free neutron to proton structure functions (disregarding nuclear effects in the deuteron), then our measurement shows that the neutron structure function is smaller

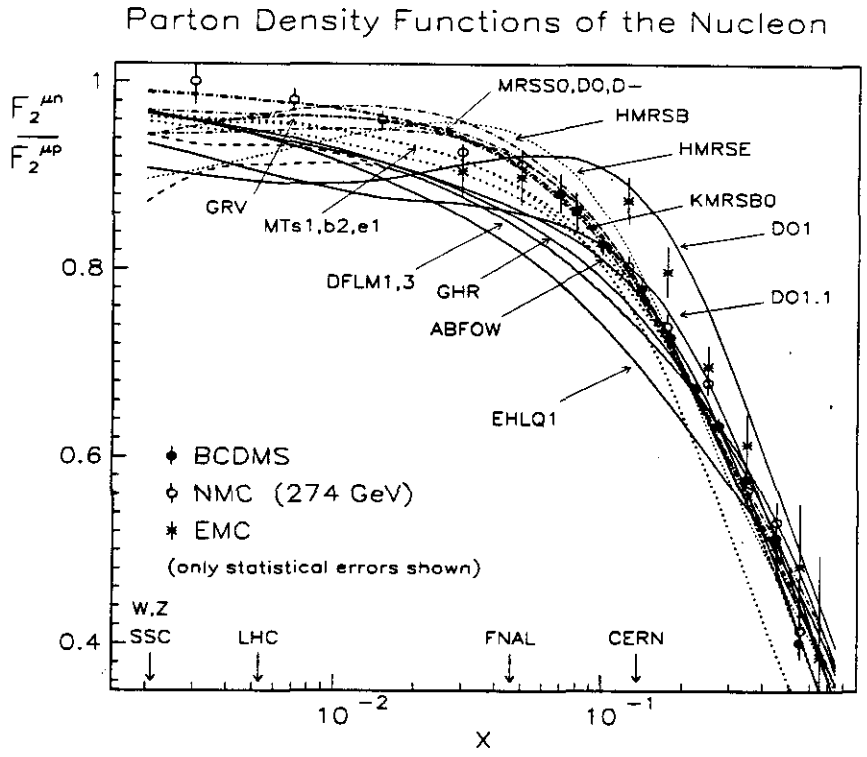

Figure 6.3: F_2^n/F_2^p **ratio. Comparison with Parton Distribution Functions from Global Structure Function Analysis.**

than the proton structure function, thus the value of the sum rule will increase. In order to make the last statement, we use the measurement of the Q^2 dependence of the structure function ratio. Since our results, and the NMC results, are consistent with no Q^2 dependence at the low x region, we can extrapolate our measurement to a high Q^2 value, where the structure functions have a parton-model interpretation. In this case the integral performed at fixed Q^2 will get a positive contribution from our result, and the sum rule value will increase.

The current sum rule picture could be clarified in the future by performing Drell-Yan experiments with protons on deuterium and hydrogen targets. The ratio $A_{DY} = \frac{\sigma_{pp}-\sigma_{pn}}{\sigma_{pp}+\sigma_{pn}}$ is directly related to the difference $\bar{d} - \bar{u}$ [120]. Also, if deuterons are used in the HERA collider, then the same low-x measurements will be performed at much higher Q^2, possibly further resolving the shadowing issue.

Appendix A

Liquid Targets for Run91

A.1 Density determination

A.1.1 Chemical composition

Different orientations of the two nuclear spins in the diatomic molecules of D_2 and H_2 give rise to the molecular modifications designated by the prefixes ortho and para. The equilibrium composition is temperature dependent. Close to the boiling point of liquid hydrogen (20.4 deg K) the concentrations are : ortho $\sim$ 0.21 % and para $\sim$ 99.79 % (equilibrium H_2). At 20.4 deg K the deuterium composition is $\sim$ 98 % ortho (equilibrium D_2). Most of the physical properties like vapor pressure, density of the liquid, etc. are mildly dependent upon the composition. The boiling point temperature in deg K for equilibrium H_2 is 20.27, for equilibrium D_2 is 23.52 and for hydrogen deuteride (HD) is 22.13 (at atmospheric pressure) from [121].

A.1.2 Measuring the E665 Liquid Target Densities

The target densities are derived indirectly from the measurement of the saturated vapor pressure in the cryogenic liquid reservoir (a description of the target setup and

geometry can be found in [60]). The vapor pressure was measured by a pressure to voltage transducer. The raw pressure has to be adjusted according to the pressure transducer calibration data [123]. The raw pressure values were recorded on the E665 raw data tapes from the EPICURE data logger. This datum is part of the 91 Spill Database record [69]. The information from each tape and for each spill is merged to create an n-tuple and it is checked for readout failures [94]. The data integrated over all Run blocks and after the transducer calibration correction are shown in figures A.1 and A.2, for D_2 and H_2 respectively.

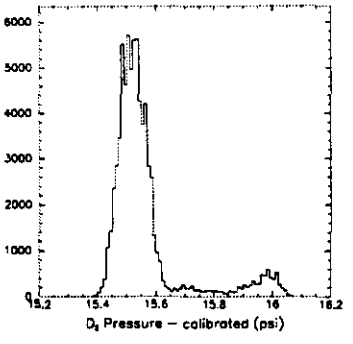

Figure A.1: D_2 Pressure

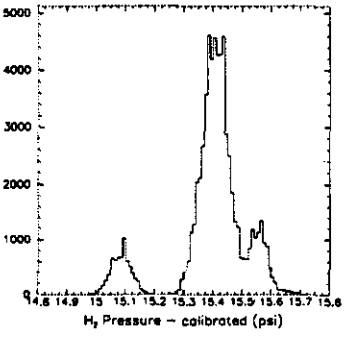

Figure A.2: H_2 Pressure

The Run dependence of the pressure values is shown in figure A.3 and figure A.4. The big fluctuations shown for some run blocks correspond to periods that either one

of the targets had problems. This was verified from the information found in the logbook of the experiment (Table A.1).

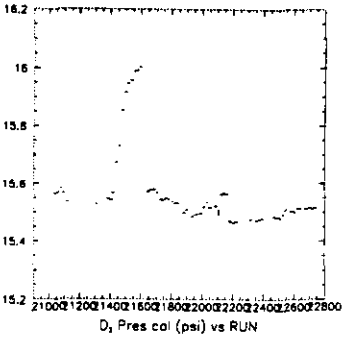

Figure A.3: D_2 Pressure vs Run

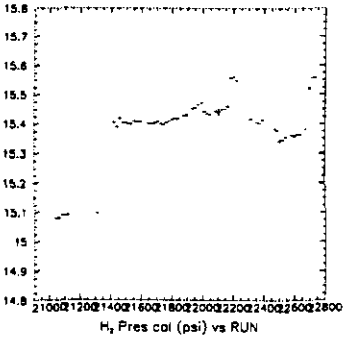

Figure A.4: H_2 Pressure vs Run

The target pressures are converted to temperatures using the parametrization for D_2 in equilibrium (from reference [121]) and the temperatures to density using the parametrizations from [124] as described in references [94] and [123]. The parametrizations for D_2 are:

$$\log_{10} P = a_0 + a_{-1}/T + a_1 \times T \tag{A.1}$$

where P and T are the pressure and temperature (mm Hg, deg Kelvin), $a_0 = 4.7367$,

$a_{-1} = -58.4440$, and $a_1 = 0.02670$.

$$\rho = (b_0 - T)/b_1 \tag{A.2}$$

where ρ and T are the density and temperature (gr/cm^3, Kelvin) and $b_0 = 86.981$ and $b_1 = 389.97$. For H_2 the parametrizations used are:

$$P = c_a^{c_0 + c_i/(T+c_b)+c_1 \times T} \tag{A.3}$$

where P and T are the pressure and temperature (atm, Kelvin) and $c_a = 10.$,$c_0 = 2.00062$, $c_i = -50.09708$, $c_b = 1.0044$ and $c_1 = 0.01748495$.

$$\rho = \rho_c + a_1 \times \delta^{0.38} + a_2 \times \delta + a_3 \times \delta^{1.33333} + a_4 \times \delta^{1.6666667} + a_5 \times \delta^2 \tag{A.4}$$

where ρ is in mol/cm^3, $\delta = T_c - T$, T_c is 32.976 degrees Kelvin and T is in Kelvin, ρ_c=0.01559 mol/cm^3, $a_1 = 7.3234603 \times 10^{-3}$,$a_2 = -4.407426 \times 10^{-4}$,$a_3 = 6.6207946 \times 10^{-4}$, $a_4 = -2.9226363 \times 10^{-4}$ and $a_5 = 4.00844907 \times 10^{-5}$.
The conversion factors for pressure units are: 1 mm Hg $\rightarrow$ 1 atm 1.3157895×10^{-3} and atm $\rightarrow$ psi 14.6960. It is worth emphasizing the fact that the densities are insensitive to small pressure changes. The slope for H_2 is 0.00025 gm/cm^3/psi and for D_2 is 0.00055 gm/cm^3/psi. The measured densities are shown in figure A.5 and figure A.6. The Run dependence is shown in figures A.7 and A.8. The arrows correspond to the bad Run Blocks listed in Table A.1 for either H_2 or D_2.

A.1.3 Results

After the Run blocks listed in Table A.1 are removed, the density distributions for the two targets are fitted to a gaussian shape. The result of the fit for the H_2 density is:

$\rho = 70.598 \pm 0.79164 \times 10^{-3}$ with $\sigma_\rho = 0.0160 \pm 0.40909 \times 10^{-4}$ (in g/cm^3).

The result of the fit for the D_2 density is:

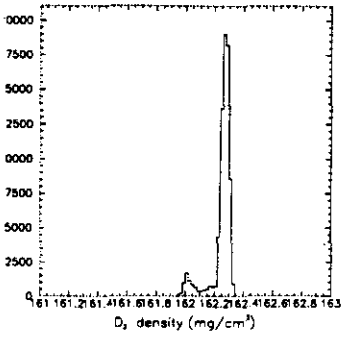

Figure A.5: D_2 Density

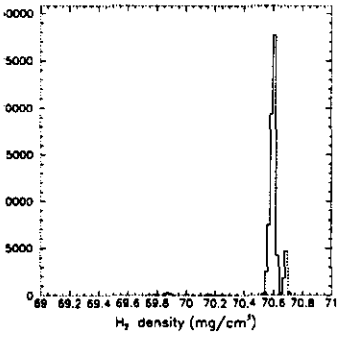

Figure A.6: H_2 Density

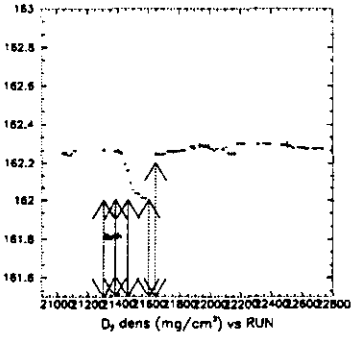

Figure A.7: D_2 Density vs Run

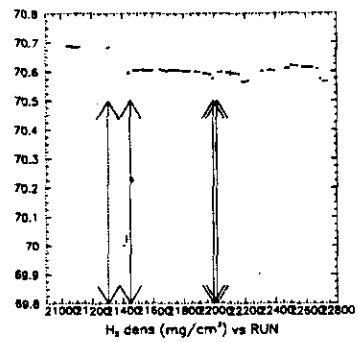

Figure A.8: H_2 Density vs Run

$\rho = 162.27 \pm 0.17169 \times 10^{-3}$ with $\sigma_\rho = 0.023666 \pm 0.52230 \times 10^{-4}$. The values are in g/cm^3.

The measured mean values of the pressures are $P = 15.409 \pm 0.00024$ for H_2 (in psi) and $P = 15.522 \pm 0.00021$ for D_2 (psi). The number of points entering these fits is $\sim$ 670000, since the Spill Database contains one pressure measurement per spill.

A.1.4 Systematic Errors

- Pressure to Density conversion. The resulting uncertainty of the conversion due to the different parametrizations is of the order of 0.3 % for D_2 and 0.04 % for H_2 ([124]).

- Pressure Transducer. The accuracy is quoted to be 0.11 % of the full reading (50 psi) ([123]). This gives a relative error in the density measurement $\sim$ 0.01 % for H_2 and D_2.

A.2 Measuring the Target Composition - Effects on the D_2 rate

A.2.1 Temperature determination

The chemical contents of the targets were analyzed using a boil-off test. Hydrogen deuteride (HD) in the D_2 target is the only impurity causing concern. The results for the D_2 composition from the Argonne Chemistry Lab are tabulated in Table A.2. The big difference between the last two measurements and the first one (and also the value for the 1990 Run Period) can be blamed on the D_2 target failure of the 6th of September 1991. For the 1991 Run Period the procedure used for the D_2 target was to collect the liquid in a tank and then reuse it to fill the target. The explanation for the large HD contamination after the 6th of September is that this tank was contaminated when the target liquid was collected after the target failed.

Since the D_2 is not pure the D_2 density computed from the measured vapor pressure is not correct since the pressure really corresponds to the D_2 and HD equilibrium mixture. The following procedure determines the correct D_2 density:

- A temperature T_i is obtained from the measured vapor pressure P_{meas}, using the D_2 P to T relation (equation A.1).
- This temperature is used with the parametrization (for HD)

$$\log_{10} P_{HD} = 5.04964 - \frac{55.2495}{T} + 0.01479 \times T \qquad \text{(A.5)}$$

  from [121] to find the vapor pressure P_{HD} (in mm Hg). Note that NMC [111] is using the same parametrization from [125] .
- The actual D_2 vapor pressure is computed from $nP_{meas} = n_{HD}P_{HD} + n_{D_2}P_{D_2}$, ($n = n_{HD} + n_{D_2}$ with n, n_{HD} and n_{D_2} being the number of moles). The HD molar volume is given by

$$U_{HD} = 24.886 - 0.30911T + 0.01717T^2 \qquad \text{(A.6)}$$

in $cm^3/mole$ from [125] and n_{D_2} is from equation A.2 converted to $moles/cm^3$. Note that the number of moles in the determination of the number n are converted to molar densities (dividing with the constant target volume V).

- From P_{D_2} a new T is found from equation A.1 and the procedure is repeated, until HD and D_2 are found to have the same T.

The first T measurement (T_i) was 23.718 deg K with $P_{meas} = 15.522$ psi. After a few iterations, for the first period (HD contamination of 4.2 %) the temperature is evaluated to be 23.602 deg K with $P_{D_2} = 15.061$ psi. The molar density from that value is 0.040346 moles/cm^3 and the mass density is 0.16225 gm/cm^3. For HD the molar density at 23.602 deg K is 0.039644 moles/cm^3.

The values for the second period (averaging the HD from the second and third measurements of Table A.2) starting with values $T = 23.718$ deg K and $P_{meas} = 15.522$ psi are: $T = 23.38163$ deg K, $P_{D_2} = 14.049$ psi and molar density 0.040487 moles/cm^3 and the mass density 0.16309 gm/cm^3 for the target D_2. For HD the molar density is 0.039788 moles/cm^3. The error from averaging measurements 2 and 3 of Table A.2 is $\sim$ 0.53 % . The results for the two periods (after the iterative procedure) are presented in Table A.3.

A.2.2 neutron scattering rate from the D_2 target

Two terms (α and β in the following formula), which are related to the deuterium target composition are required in order to obtain the relation between the scattering rate (R_{D_2}) from the target, as well as σ_p and σ_n, the proton and neutron cross sections (see [126]). The molar densities of electrons, protons and neutrons in the target are:

$$n_e = n_p = 2(1-f)n_{D_2} + 2fn_{HD} \tag{A.7}$$

$$n_n = 2(1-f)n_{D_2} + 1fn_{HD} \tag{A.8}$$

where n_{D_2} and n_{HD} are the molar densities of D_2 and HD respectively and f is the HD fraction per volume in the target. These are evaluated from equation A.2 converting to $moles/cm^3$ and equation A.6, using $n_{HD}=1/U_{HD}$.

Assuming that σ from the actual D_2 target is the sum of σ_p and σ_n (weighted with the molar densities for p and n in the target), the scattering rate is:

$$R = LN_A N_{flux}(n_p\sigma_p + n_n\sigma_n) = LN_A N_{flux} n_0(\alpha\sigma_n + \beta\sigma_p) \qquad (A.9)$$

where $n_0 = 2n_{D_2}$.

The results for the two different periods (the first period and the average of the second and the third periods as defined in Table A.2) are given in Table A.3.

A.2.3 Systematic error from the target composition determination

The total systematic error due to the target quantities in the cross-section measurement has a contribution from the pressure to density conversion (calibration, conversion parametrizations - section 1 of this appendix) and a contribution from the HD contamination correction (measurement of f - section 2). This last error affects both the determination of n_{D_2} and n_p, n_n from equation A.9. The fractional errors on each quantity are given below.

- $\delta_{n_{H_2}}/n_{H_2} = 0.05\%$. This is the error of the H_2 molar densisty.
- $\delta_{n_{D_2}}/n_{D_2} = \sqrt{0.31\% + 0.53\%} = 0.58\%$. This is the error of the D_2 molar densisty. The second number is the effect of the HD contamination correction (see section 2 of this appendix). The 2 errors are independent, so they add in quadrature.
- $\delta_f/f = 6.0\%$. This is the error assigned to the evaluation of the HD per volume fraction. The assumption is that there are 2 periods in the D_2 target composition, before and after the target problems. There are 2 measurements of the

target composition for period 2 (the 2 last 1991 values from Table A.2). The mean value is used as the f value for period 2 and the error on the mean as the error in f due to the chemical analysis method ($\delta_f = 0.006$).

From equations A.7 and A.8, the error in the number of neutrons and number of protons in the D_2 target depends on the error in f and the error in n_{D_2}. The errors are correlated since the value of n_{D_2} depends on f.

$$\delta_{n_i} = \sqrt{(\frac{\partial n_i}{\partial f}\delta_f)^2 + (\frac{\partial n_i}{\partial n_{D_2}}\delta_{n_{D_2}})^2 + 2\frac{\partial n_i}{\partial f}\frac{\partial n_i}{\partial n_{D_2}}\delta_f\delta_{n_{D_2}}} \tag{A.10}$$

with i=p or n, $\frac{\partial n_p}{\partial n_{D_2}} = \frac{\partial n_n}{\partial n_{D_2}} = 2(1-f)$, $\frac{\partial n_p}{\partial f} = -2n_{D_2} + 2n_{HD}$ and $\frac{\partial n_n}{\partial f} = -2n_{D_2} + n_{HD}$. Substituting these expressions in equation A.10, results in:

$$\delta_{n_p} = \sqrt{((-2n_{D_2} + 2n_{HD})\delta_f)^2 + (2(1-f)\delta_{n_D})^2 + 8(1-f)(-n_{D_2} + n_{HD})\delta_f\delta_{n_D}} \tag{A.11}$$

$$\delta_{n_n} = \sqrt{((-2n_{D_2} + n_{HD})\delta_f)^2 + (2(1-f)\delta_{n_D})^2 + 4(1-f)(-2n_{D_2} + n_{HD})\delta_f\delta_{n_D}} \tag{A.12}$$

The result is $\delta_{n_p} = 0.0004275 moles/cm^3$ and $\delta_{n_n} = 0.00019 moles/cm^3$. These errors correspond to $\delta_\alpha = 0.24$ % and δ_β 0.53 % . In order to find the normalization error from equation A.9 we need to know σ_p and σ_n. For the σ_n/σ_p ratio, with N_H and N_D the number of events from each target, N_f^H and N_f^D the number of beams, and given the equal lengths of the 2 targets we have ($n_H = 2n_{H_2}$):

$$\sigma_n/\sigma_p = \frac{1}{\alpha}(\frac{N_D n_H N_f^H}{N_H n_0 N_f^D}) - \frac{\beta}{\alpha} \tag{A.13}$$

Calling $A \equiv \frac{1}{\alpha}(\frac{N_D n_H N_f^H}{N_H n_0 N_f^D})$ and $r \equiv \sigma_n/\sigma_p$, the error due to the determination of the target composition is given by:

$$\delta_r = \sqrt{(\frac{\partial r}{\partial \alpha}\delta_\alpha)^2 + (\frac{\partial r}{\partial \beta}\delta_\beta)^2 + (\frac{\partial r}{\partial n_H}\delta_{n_H})^2 + +2(\frac{\partial r}{\partial \alpha}\frac{\partial r}{\partial \beta}\delta_\alpha\delta_\beta)} \tag{A.14}$$

Note that the n_0 that appears in equation A.13 is a scale factor. The effect of the error in the n_0 measurement has been taken into account in the α and β error calculation.

The derivatives are : $\frac{\partial r}{\partial \alpha} = -\frac{(A-\frac{\beta}{\alpha})}{\alpha}$, $\frac{\partial r}{\partial \beta} = -1/\alpha$ and $\frac{\partial r}{\partial n_H} = \frac{(A+\frac{\beta}{\alpha})}{n_H}$. Substituting these expressions to equation A.14 we get:

$$\delta_r = \sqrt{((A-\frac{\beta}{\alpha})\frac{\delta_\alpha}{\alpha})^2 + (\frac{\beta}{\alpha}\frac{\delta_\beta}{\beta})^2 + ((A+\frac{\beta}{\alpha})\frac{\delta_{n_H}}{n_H})^2 + +2(A-\frac{\beta}{\alpha})\frac{\beta}{\alpha}\frac{\delta_\alpha}{\alpha}\frac{\delta_\beta}{\beta}} \qquad \text{(A.15)}$$

which for $A \sim 2$ and $\frac{\beta}{\alpha} \sim 1$, gives $\delta_{\sigma_n/\sigma_p} \sim .85\%$.

Table A.1: Run 91 Liquid Target Performance vs Run Block

Run Blocks	Time	H_2 status	D_2 status
20935-21304	07jul91-12aug91	OK	OK
21305-21382	12aug91-20aug91	no	no
21383-21428	20aug91-24aug91	no	OK
21429-21449	24aug91-25aug91	OK	OK
21450-21463	25aug91-27aug91	no	OK
21464-21600	27aug91-06sep91	OK	OK
21601-21642	06sep91-15sep91	OK	no
21643-21990	15sep91-21oct91	OK	OK
21991-22009	21oct91-25oct91	no	OK
22015-22726	25oct91-08jan92	OK	OK
———	15oct91 move	targets	2cm east
———	18nov91 swap	targets	—

Table A.2: Run 91 D_2 Target Composition

Date	H_2	HD (f)	D_2
06sep91	0.0042	0.032	0.963
15nov91	0.0080	0.088	0.906
08jan92	0.0021	0.100	0.898
run 90	0.0006	0.044	0.955

Table A.3: Density and Scattering rate

Period	n_{H_2} moles/cm^3	n_{D_2} moles/cm^3	n_{HD} moles/cm^3	α	β
I	0.035022	0.040346	0.039644	0.98372	0.99944
II	0.035022	0.040487	0.039788	0.95219	0.99838

Appendix B

Normalization Database Structure

The 1991 Normalization Database files (91DBS) contained four different types of records. There was one header record (*WDxxxx, xxxx was the tape number) and one Summary record (*ED). For each spill there was an EPICURE record (*EP) and a Scaler record (*SC). The contents of these records were as follows:

1. Header: Tape name (from the PTMVE input control file), Run Number (NRUN), Spill Number (NSPILL), date and time.

2. Epicure (*EP): NRUN, NSPILL, time, the current readings of the CCM, CVM and NMRE magnets, and the target pressure readings of the H_2 and D_2 targets. These pressure measurements were recorded both at the supply line and at the ventilation line. Also recorded were the reference pressure and the currents of the beam collimator (HNM3CH) and the beam stop (HNM2BS), and the monitoring current for the magnets.

3. Scaler (*SC): NRUN, NSPILL, decoder errors, spill scaler channels, the event scaler channels integrated over the Spill and per target event statistics. The event scaler resets were compared to the trigger bit information, and if they did not match errors were flagged. All the event scaler channels were recorded

(integrated over the spill). There were several channels recorded from the spill scalers. These included all information corresponding to the event scalers, the gated and ungated beam signals the prescaled RF signal and the number of Rbeam triggers [69]. The number of events per trigger and per target were also reported.

4. Summary (*ED): Reported the total count of partially concatenated events per trigger and a summary of all decoder errors per trigger and per target.

The 91DBS software used the trigger mask to identify the different type of data acquisition events and the synchronization was done with the Begin Of Spill (BOS) events [69].

Appendix C

PTMVE n-tuple Structure

The physics trigger n-tuple was filled if either $\nu > 25$ GeV or $\theta > 0.0002$ rad and $\delta\nu/\nu < 0.5$, $\nu > 0$.

The contents of each ntuple word and the name tag of each word are given in the following list. For entries where more than one quantity is packed in a word, the number of bits used for each quantity are given in parentheses.

Physics ntuple (ID = 1)

1. NRUN: Run number.
2. NEVENT: Event number.
3. NSPILL: Spill number (bison 64).
4. TRIGGER: Trigger bits.
5. TGTBIT - bitted -
   - TARGET: (1-4) Target/beam tune.
   - NVTX: (5-8) Number of vertices.
   - FSMUON: (9-12) Number of Forward Spectrometer muons (including scattered muon.

- LPROY: (13-16) Number of Y projections in the Muon Detector.
- LPROZ: (17-20) Number of Z projections in the Muon Detector.
- BMSIGN: (21) Charge of beam track (0=-,1=+).
- MUSIGN: (22) Charge of muon track (0=-,1=+).

6. SBTBIT - bitted -
   - SBT1: (1-4) Number of SBT hits on the 1st beam track.
   - SBT2: (5-8) Number of SBT hits on the 2nd beam track.
   - SBT3: (9-12) Number of SBT hits on the 3rd beam track.
   - SBT4: (13-16) Number of SBT hits on the 4th beam track.
   - SBT5: (17-20) Number of SBT hits on the 5th beam track.
   - NBEAM: (21-24) Number of beam tracks.
7. TOFBIT - bitted -
   - TOFTOP: (1-12) TOF top.
   - TOFBOT: (13-24) TOF bottom.
8. GBSAT: Gated SAT beam since last SAT trigger.
9. GBSVS: Gated LAT beam since last SVS trigger.
10. GBSVW2: Gated LAT beam since last SVSWAM2 trigger.
11. GBCVT: Gated LAT beam since last CVT trigger.
12. GBCAL: Gated CAL beam since last CAL trigger.
13. EBEAM: Beam momentum.
14. Q2: Q^2 of the event.

15. NU: ν of the event.

16. THETA: θ of the event.

17. PHI: ϕ of the event.

18. YBJ: y_{Bj} of the event.

19. XBJ: x_{Bj} of the event.

20. W2: W^2 of the event.

21. EREBEAM: Error on the beam momentum of the event.

22. ERQ2: Error on Q^2 of the event.

23. ERNU: Error on ν of the event.

24. ERTHETA: Error on θ of the event.

25. ERPHI: Error on ϕ of the event.

26. ERYBJ: Error on y_{Bj} of the event.

27. ERXBJ: Error on x_{Bj} of the event.

28. ERW2: Error on W^2 of the event.

29. VTXBIT -bitted -

    - VTXTYP: (1-5) Primary vertex type.
    - NFTP0: (6-10) Number of positive fitted tracks (no cuts).
    - NFTN0: (11-15) Number of negative fitted tracks (no cuts).
    - NCLP0: (16-20) Number of positive close tracks (no cuts).
    - NCLN0: (21-25) Number of negative close tracks (no cuts).

30. XVTX: X position of vertex.
31. YVTX: Y position of vertex.
32. ZVTX: Z position of vertex.
33. ERXVTX: Error in X position of vertex.
34. PROBVX: Vertex probability.
35. MXVTX: $\mu - \mu$ only vertex X position.
36. MERXVT: $\mu - \mu$ only vertex X position error.
37. MPROBV: $\mu - \mu$ only vertex probability.
38. YBEAM: Y of beam at X=-16.000 m (Extrapolate the beam track from the last keyplane to X=-16.000 mm).
39. ZBEAM: Z of beam at X=-16.000m.
40. YPBEAM: Y' of beam at X=-16.000m.
41. ZPBEAM: Z' of beam at X=-16.000m.
42. YPMUIN: Y' of beam at vertex.
43. ZPMUIN: Z' of beam at vertex.
44. YPMUOUT: Y' of muon at vertex.
45. ZPMUOUT: Z' of muon at vertex.
46. XMULAST: X of muon at last keyplane on track.
47. YMULAST: Y of muon at last keyplane on track.
48. ZMULAST: Z of muon at last keyplane on track.

49. YPMULAST: Y' of muon at last keyplane on track.

50. ZPMULAST: Z' of muon at last keyplane on track.

51. YMUPTM: Y of muon at X=18.400 (Extrapolate the muon detector track associated with the scattered muon to X=18.400m).

52. ZMUPTM: Z of muon at X=18.400m.

53. YPMUPTM: Y' of muon at X=18.400m.

54. ZPMUPTM: Z' of muon at X=18.400m.

55. TRKBIT -bitted-

    - NCLP1: (1-5) Number of positive close tracks (after cuts).
    - NCLN1: (6-10) Number of negative close tracks (after cuts).
    - NNRP1: (11-15) Number of positive near tracks (after cuts).
    - NNRN1: (16-20) Number of negative near tracks (after cuts).
    - NHALO: (21-24) Number of halo tracks.

    Near track definition: fitted (using normalized distance to the vertex) OR distance of closest approach less than 1 cm. Halo definition: track momentum larger than 999.9 GeV and for the close tracks track momentum larger than the beam momentum OR (distance $\times$ track momentum $>$ 5 and track momentum $>$ 100 GeV).

56. LHADP: Signed momentum of the leading hadron.

57. LHADPT: Transverse momentum of the leading hadron.

58. LHADDC: Distance from the closest calorimeter cluster.

59. LHADEC: Energy of the closest calorimeter cluster.

60. NCLBIT -bitted-

    - NCLUS: (1-5) Multiplicity number of the calorimeter clusters.
    - ECAL: (6-24) Total energy in the calorimeter.

61. ECLBIT -bitted-

    - ECLUS1: (1-12) Energy of the most energetic calorimeter cluster.
    - ECALC: (13-24) Total calorimeter energy corrected for saturation.

62. EBIG: Sum of the energy of clusters with $E_{cal}/\nu > 0.35$.

63. ZFLOW: $\sum_{i=1}^{N} Z_i^2 \times E_i/E_{cal}$, where the sum runs over the number of calorimeter clusters, Z_i is the Z-coordinate of the center of the cluster and E_i is the energy of the cluster.

64. PLNRTY: $\frac{(\vec{P_{beam}} \times \vec{P_{fs}}) \cdot \vec{P_{clus1}}}{|\vec{P_{beam}}||\vec{P_{fs}}||\vec{P_{clus1}}|}$, where $\vec{P_{beam}}$ and $\vec{P_{fs}}$ are the three-momentum of the beam and scattered muon and $\vec{P_{clus1}}$ is the three-momentum of the largest reconstructed calorimeter cluster (assuming that the origin was at the interaction point.

65. PLNBIT1: Bit map showing chamber planes on the muon track.

    - bits: 1-16 VDC
    - bits: 17 PCV
    - bits: 18 PCN
    - bits: 19-23 PCF
    - bits: 24 PSC

66. PLNBIT2: Bit map showing chamber planes on the muon track.

    - bits: 1-2 DCA/B

- bits: 3 PSA
- bits: 4 MUON
- bits: 5 PBT
- bits: 6 VA PROCESSOR
- bits: 7 VB PROCESSOR
- bits: 8 VD PROCESSOR
- bits: 9 VS PROCESSOR

67. HODBIT: Bit map showing hodoscopes planes on the muon track. Bit map: 1-7 SBT,8-9 SUM,10 SVS, 11-18 SMS,19-22 SPM 23-24 SSA.

68. PBTBIT -bitted-

    - NPBTUN: (1-5) Number of unused PBT hits.
    - CLUS1Y: (6-13) unsigned Y position of largest cluster in cm.
    - SIGN1Y: (14) sign of Y position of largest cluster.
    - CLUS1Z: (15-22) unsigned Z position of largest cluster in cm.
    - SIGN1Z: (23) sign of Z position of largest cluster.

69. DECBIT1: Bits reporting the decoder errors.

70. DECBIT2: Bits reporting the decoder errors and the match type of scattered muon.

71. TRGBIT: Software trigger simulation information (bitted).

72. CHSQMAT: χ^2 of the muon match.

73. SLRSML: Bits about the spill monitor 24 buckets.

74. SLRLNG: Bits about the spill monitor 184 buckets.

75. YMUPSA: Y of muon at last keyplane on the muon track.

76. ZMUPSA: Z of muon at last keyplane on the track.

77. YPMUPSA: Y' of muon at last keyplane on track.

78. ZPMUPSA: Z' of muon at last keyplane on track.

79. BITSEG: matched and unmatched VDC segments and Forward Spectrometer lines.

80. BITFVT: SAT trigger floating veto fingers.

Rbeam ntuple (ID = 2)

1. NRUN: Run number.

2. NEVENT: Event number.

3. NSPILL: Spill number (bison 64).

4. TRIGGER: Trigger bits.

5. TGTBIT - bitted -

   - TARGET: (1-4) Target/beam tune.
   - NVTX: (5-8) Number of vertices.
   - FSMUON: (9-12) Number of Forward Spectrometer muons (including scattered muon.
   - LPROY: (13-16) Number of Y projections in the Muon Detector.
   - LPROZ: (17-20) Number of Z projections in the Muon Detector.
   - BMSIGN: (21) Charge of the beam track (0=-,1=+).
   - MUSIGN: (22) Charge of the muon track (0=-,1=+).

6. SBTBIT - bitted -
    - SBT1: (1-4) Number of SBT hits on the 1st beam track.
    - SBT2: (5-8) Number of SBT hits on the 2nd beam track.
    - SBT3: (9-12) Number of SBT hits on the 3rd beam track.
    - SBT4: (13-16) Number of SBT hits on the 4th beam track.
    - SBT5: (17-20) Number of SBT hits on the 5th beam track.
    - NBEAM: (21-24) Number of beam tracks.
7. TOFBIT - bitted -
    - TOFTOP: (1-12) TOF top.
    - TOFBOT: (13-24) TOF bottom.
8. GBRSAT: Gated SAT beam since the last RSAT trigger.
9. GBRLAT: Gated LAT beam since the last RLAT trigger.
10. GBRCAL: Gated CAL beam since the last RCAL trigger.
11. EBEAM: Beam momentum.
12. Q2: Q^2 of the event.
13. NU: ν of the event.
14. THETA: θ of the event.
15. PHI: ϕ of the event.
16. EREBEAM: Error on the beam momentum of the event. If no primary vertex found, then report the error on the momentum of the first beam track.
17. ERQ2: Error on Q^2 of the event.

18. ERNU: Error on ν of the event.

19. ERTHETA: Error on θ of the event.

20. ERPHI: Error on ϕ of the event.

21. YBEAM: Y-coordinate of the beam. The beam track was extrapolated from the last keyplane to X=-16.000m. The beam reported is the one fitted to the primary vertex; if no vertex was found then use the first beam found.

22. ZBEAM: Z of beam at X=-16.000m.

23. YPBEAM: YP of 1st beam at X=-16.00m.

24. ZPBEAM: ZP of 1st beam at X=-16.00m.

25. YMUPTM: Y of muon at X=18.400 (Extrapolate the muon detector track associated with the scattered muon to X=18.400m).

26. ZMUPTM: Z of muon at X=18.400m.

27. YPMUPTM: Y' of muon at X=18.400m.

28. ZPMUPTM: Z' of muon at X=18.400m.

29. EBMLSTF: Momentum of the beam attached to the primary vertex. If no vertex was found, the first beam found was used. This is information from the track fitting phase (LSTF bank).

30. EMULSTF: Momentum of the Forward Spectrometer muon attached to the primary vertex. If no vertex was found, the first muon found was used. (LSTE bank).

31. PLNBIT1: Bit map showing chamber planes on the muon track.

32. PLNBIT2: Bit map showing chamber planes on the muon track.

33. HODBIT: Bit map showing hodoscope planes on the muon track. The bit map for the last 3 entries is the same as the bit map for the physics n-tuple described above.

34. PBTBIT -bitted-

    - NPBTUN: (1-5) Number of unused PBT hits.
    - CLUS1Y: (6-13) unsigned Y position of the largest cluster in cm.
    - SIGN1Y: (14) sign of Y position of the largest cluster.
    - CLUS1Z: (15-22) unsigned Z position of the largest cluster in cm.
    - SIGN1Z: (23) sign of Z position of the largest cluster.

35. DECBIT1: Bits reporting the decoder errors.

36. DECBIT2: Bits reporting the decoder errors and the match type of the scattered muon.

37. TRGBIT: Software trigger simulation information (bitted).

38. SLRSML: Bits about the spill monitor 24 buckets.

39. SLRLNG: Bits about the spill monitor 184 buckets.

Appendix D

Muon-electron elastic scattering cross-section ratio

The large muon-electron elastic scattering contribution to the measured inclusive event rate can be used to validate the relative target and beam normalization measurements [1]. If the normalization is accurate, then the ratio of the muon-electron ($\mu - e$) elastic scattering cross-section measured using the deuterium target to that measured using the hydrogen target, should be one. Furthermore, the apparatus may be checked for any target dependent reconstruction bias by measuring the Q^2 dependence of the measured electron mass (m_e) as a function of the target.

The procedure to perform the above measurements is simple. Since the process is elastic, the kinematics are constrained: $1 = Q^2/2m_e\nu$. In the inclusive x distribution, the $\mu - e$ events are expected to appear as a peak centered at $x = m_e/M = 0.000545$, where $M = 0.93827GeV$ is the mass of the proton [2]. The width of the distribution

[1]The muon-electron elastic events can also be used to check absolute cross-section measurements. An analysis using the data from the 1990 run of the experiment is presented in reference [127].

[2]This is because we define the Bjorken scaling variable, $x \equiv x_{Bj} = Q^2/2M\nu$, for the muon-nucleon scattering process (ie. we use the mass of the proton)

corresponds to the experimental resolution plus the effects of bremsstrahlung photon radiation. The total event yield from $\mu - e$ elastic scattering can be determined from a fit to the x distribution around the position of the peak; and the mass can be determined from the position of the center of the peak.

The SAT data set from Period II was used for this study. The events were selected using the same selection criteria as those used for the SAT sample described in chapter 4. In addition, the following cuts were applied in order to enhance the $\mu - e$ content of the sample and to remove the contribution of $\mu - e$ radiative events that distort the event kinematics:

- 1 negative and 0 positive tracks were required in the event.
- The negative track was required to be associated with a calorimeter cluster. The center of the cluster was required to be within a distance of 3 cm of the track projection in the calorimeter.
- The energy of the track was required to be at least 95% of the total available energy in the event (ν).

After making all cuts, the event distribution as a function of x obtained from both the H_2 and the D_2 targets, is shown in figure D.1. A double gaussian function is fit to the data, the results of the fit are given in the figure. Using the parameters of the gaussian that corresponds to the $\mu - e$ peak to determine the number of events from each target we obtain the cross-section ratio ($\pm$ statistic $\pm$ systematic error):

$$\frac{\sigma^D_{\mu-e}}{\sigma^H_{\mu-e}} = \frac{N^D_{\mu-e} \times N^H_{beam} \times n^H_e}{N^H_{\mu-e} \times N^D_{beam} \times n^D_e} = 1.017 \pm 0.012 \pm 0.013$$

Here $N_{\mu-e}$ is the number of $\mu - e$ events, and N_{beam} is the number of muons and is determined from the number of RSAT beams from table 4.6. The electron molar density n_e is taken from table A.3. The systematic error is the taken from the normalization analysis presented in chapter 1 and appendix A. The beam normalization

uncertainty is added in quadrature to the target normalization uncertainty. This result confirms the accuracy of the relative beam and target normalization of the two targets.

The same double gaussian fits are performed to the x distributions of the two targets for five different Q^2 bins. The bin edges are: $0.1, 0.14, 0.2, 0.27, 0.37, 0.5$, in GeV^2. The results are shown in figures D.2 and D.3 for the H_2 target, and in figures D.4 and D.5 for the D_2 target. The measured electron mass from the two targets is shown in the upper plot of figure D.6 as a function of Q^2 (the mass of the electron is obtained from the mean of the gaussian corresponding to the peak and the mass of the proton, M). The ratio of the measured mass as a function of Q^2 is shown in the bottom plot of figure D.6. The ratio is fitted to a linear function in Q^2 and the results of the fit are given in figure D.6. The ratio measurement shows no significant Q^2 dependence.

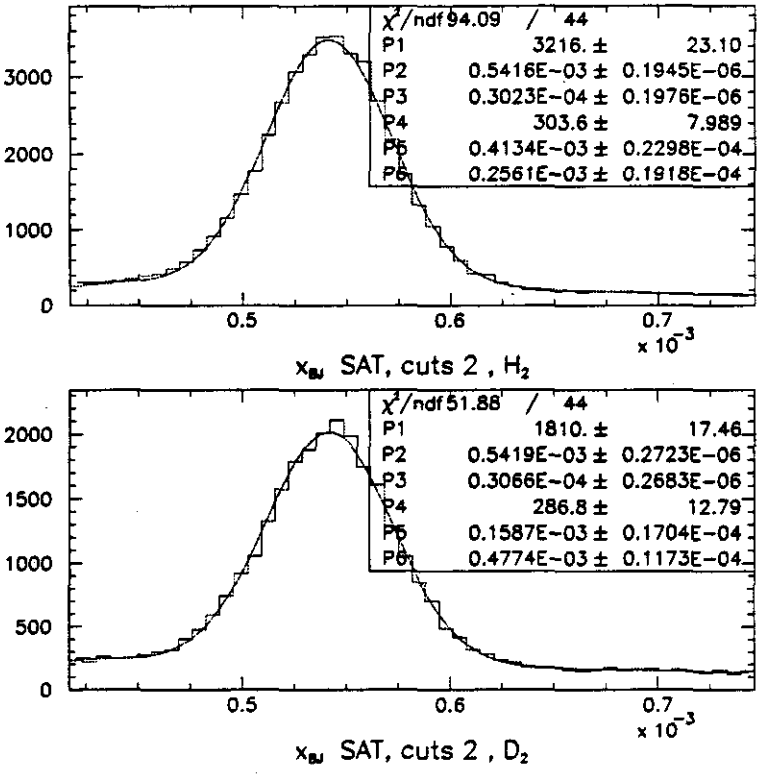

Figure D.1: $\mu - e$ selection x distribution for H_2 (upper plot) and D_2.

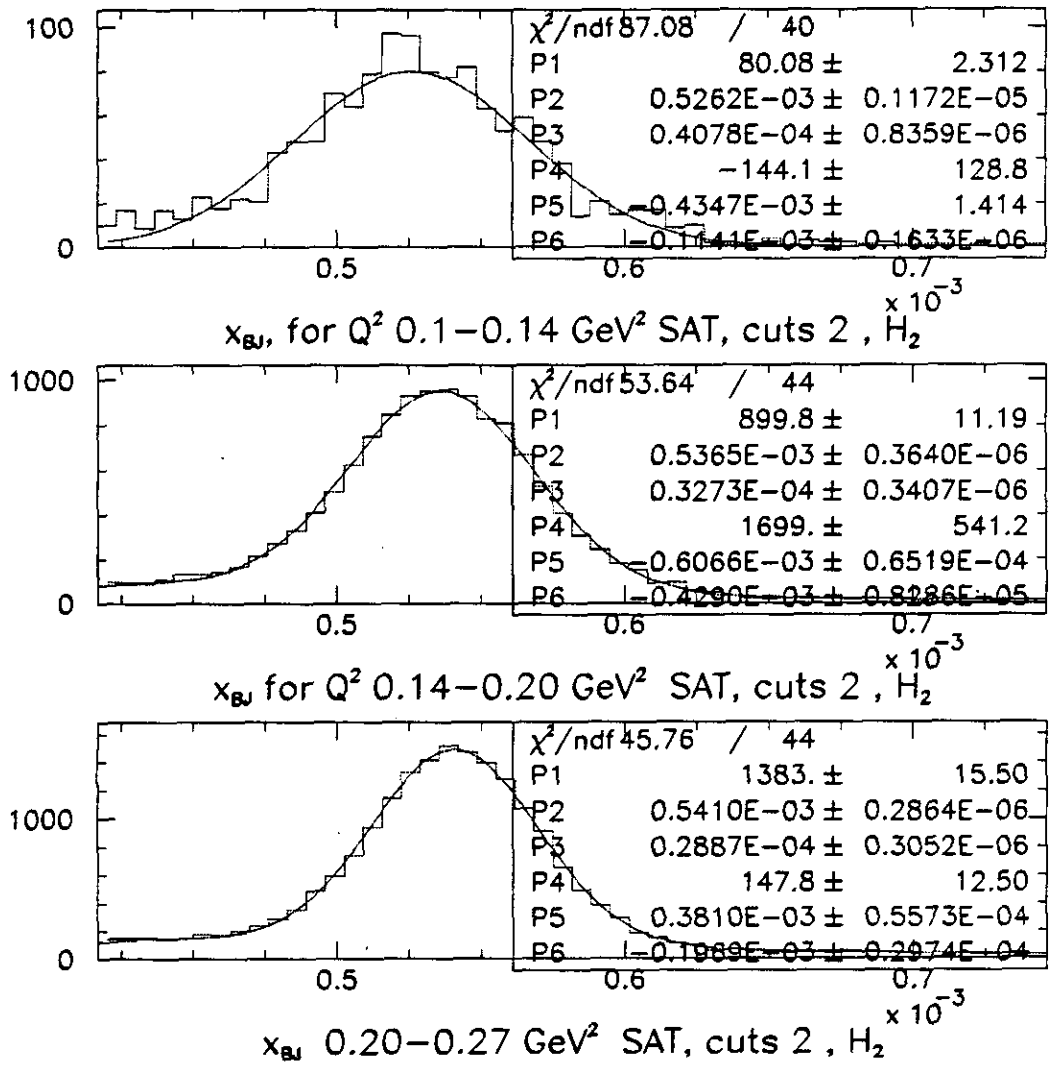

Figure D.2: $\mu - e$ selection x distribution in Q^2 bins for H_2.

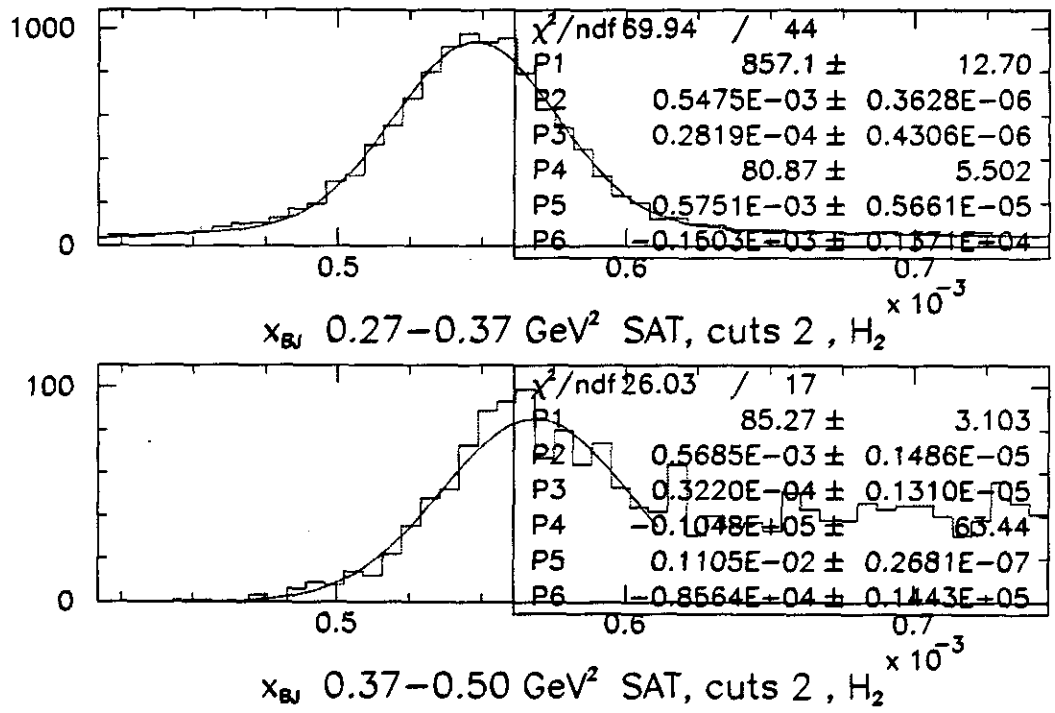

Figure D.3: $\mu - e$ selection x distribution in Q^2 bins for H_2.

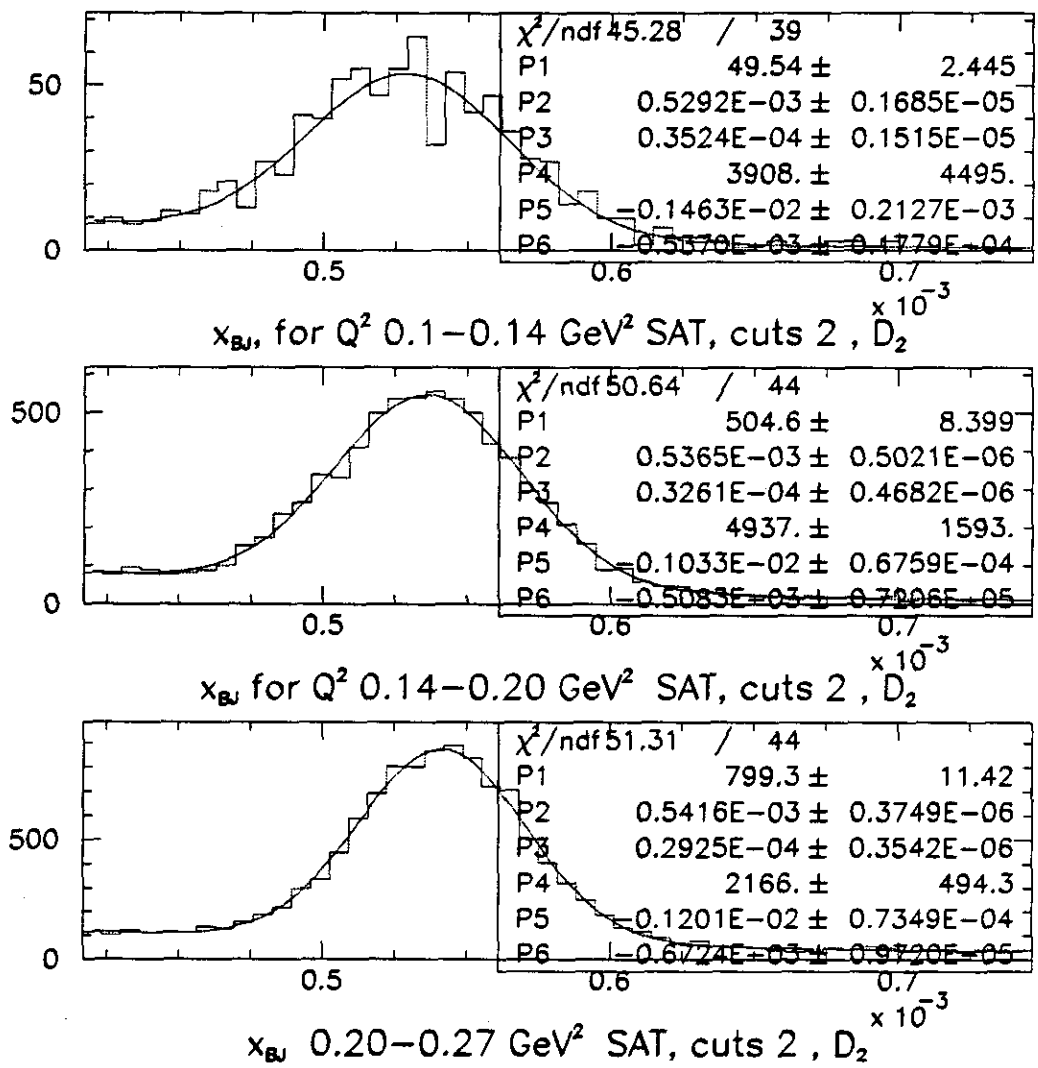

Figure D.4: $\mu - e$ selection x distribution in Q^2 bins for D_2.

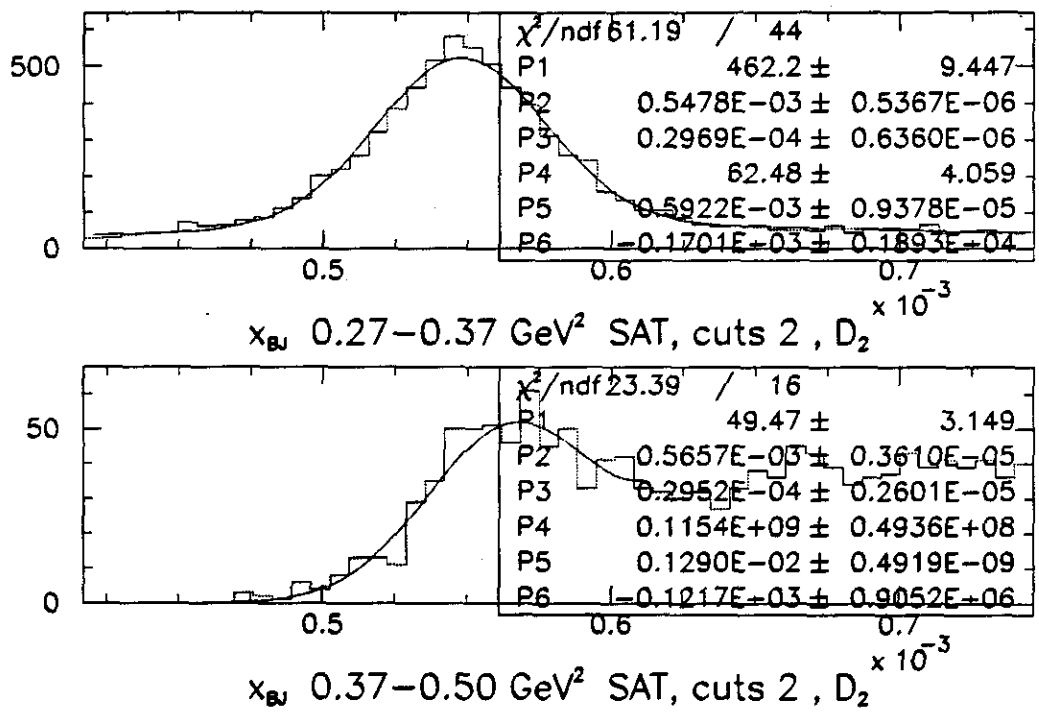

Figure D.5: $\mu - e$ selection x distribution in Q^2 bins for D_2.

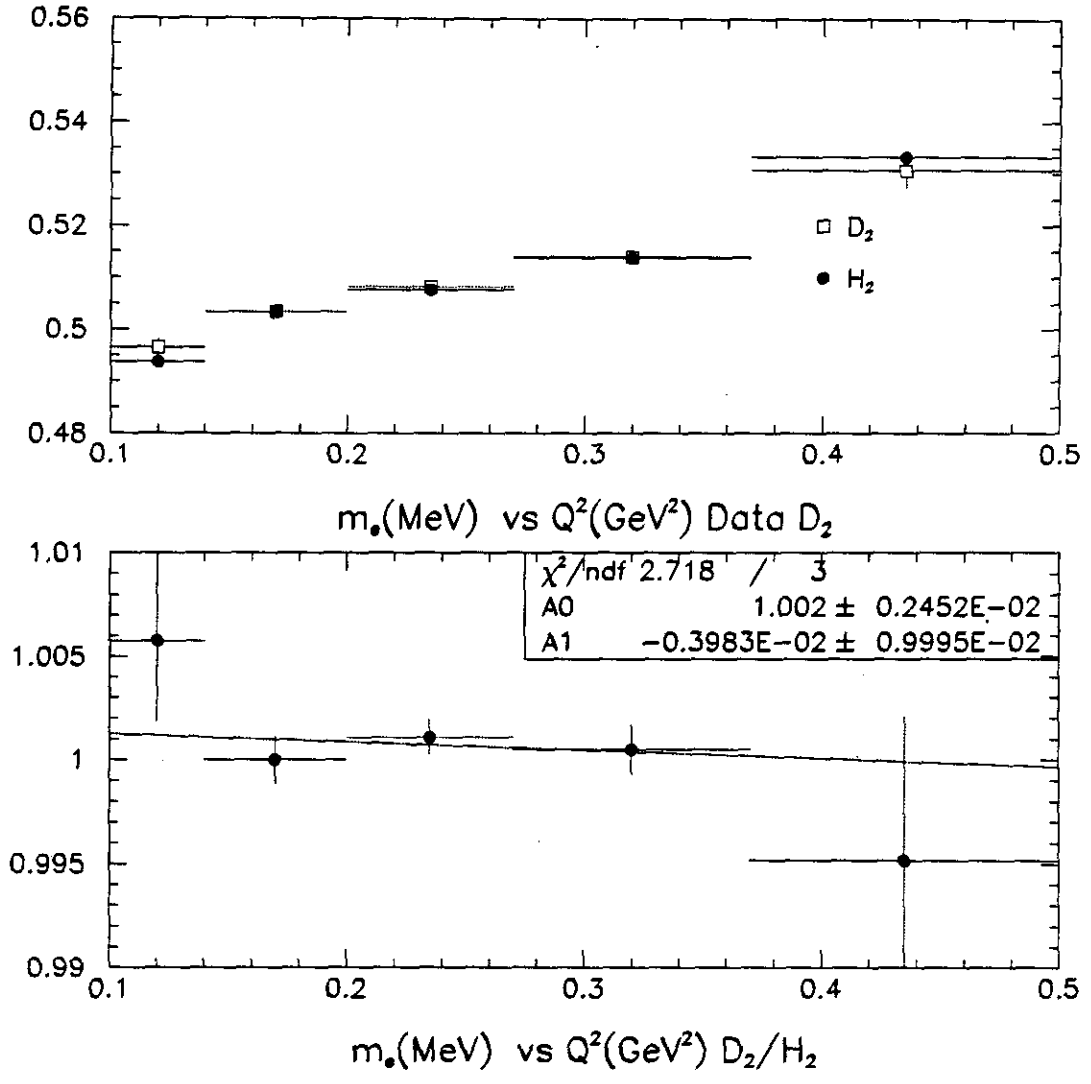

Figure D.6: The Q^2 dependence of the measured electron mass for H_2 and D_2 (upper plot) and for the ratio D_2/H_2.

Appendix E

Glossary

This Appendix contains a glossary of terms that are specific to the 665 experiment, and a few acronyms commonly used in high energy physics. The acronyms or terms that are used only locally in a chapter section are not included. All the detectors and triggers used by the 665 experiment are described in chapter 2 (table 2.1 contains a summary of the characteristics of each detector).

Beam Spectrometer: The component of the E665 apparatus which measured the momenta of the incoming muons, before their interaction with the experimental target.

CAL: The Electromagnetic Calorimeter.

CAL trigger: A trigger based on the Electromagnetic Calorimeter.

CCM: The Chicago Cyclotron Magnet. A dipole magnet used in the E665 Forward Spectrometer.

CVM: The Cern Vertex Magnet. A dipole magnet used in the E665 Forward Spectrometer. This was the magnet closest to the experimental target.

DC: Drift chambers.

DIS: Deep Inelastic Scattering. Inelastic scattering where the 4-momentum transfer squared and the energy transfer are very large compared to the mass squared of the target nucleon and the mass of the target nucleon respectively.

E665: Fermilab Experiment 665.

ECAL or $ECAL_{total}$: The total energy reported by the Electromagnetic Calorimeter in an event.

ECLUS1 or E_{clus1} : The value of the energy deposited in the largest Calorimeter energy cluster in an event.

EM: Electromagnetic.

FERRAD: A computer program used to calculate QED radiative corrections.

Forward Spectrometer: The Spectrometer located downstream of the experimental target. The Forward Spectrometer measured the momenta of the outgoing particles.

FS: Forward Spectrometer.

MT: Empty target vessel.

MTliq: Empty liquid target vessel.

MWPC: Multiwire Proportional Chamber.

NMRE: The dipole magnet used in the Beam Spectrometer to bend the trajectories of the incoming muons.

PBT: Beam Tagging Proportional Chambers. The MWPCs used in the Beam Spectrometer to reconstruct the trajectories of the incoming muons.

PC, PCF, PCN, PCV: MWPCs used in the Forward Spectrometer (see chapter 2).

PSA: A small MWPC responsible for covering the tracking of charged particles that remained close to the beam phase space region.

PTM: Proportional Tubes for the Muon identification. Used in the Muon detector downstream of the hadron absorber, in order to reconstruct muon tracks.

PTMVE: Pattern Recognition, Track Fitting, Muon Matching, Vertex Finding, and Electromagnetic Calorimeter analysis. The E665 offline reconstruction program.

QCD: Quantum Chromo-Dynamics. The quantum field theory that describes the Strong Interactions.

QED: Quantum Electro-Dynamics. The quantum field theory that describes the Electromagnetic Interactions.

RBEAM: Random Sampling of the Beam trigger (prescaled).

RCAL: Random Sampling of the Beam of the CAL trigger (prescaled).

RF: Radio Frequency. The Fermilab accelerator uses RF cavities with a frequency of 53.1 MHz.

RSAT: Random Sampling of the Beam of the Small Angle Trigger (prescaled).

SAT: Small Angle Trigger. An E665 muon veto trigger.

SBT: Beam Tagging Scintillators. Scintillator arrays that were part of the Beam Spectrometer. The SBTs were used in the trigger logic, and in the determination of the timing of the incoming muons.

SMS: Small Muon Scintillator. Scintillator array located downstream of the absorber. The SMS detector covered the beam region and it was used in triggering and in identifying muons that remained in the beam profile.

SPM: Large Muon Scintillators. Scintillator array located downstream of the absorber. The SPM detector covered the region outside of the beam profile and it was used in triggering and muon detection.

SSA: Small Scintillator Array. The SAT veto element located in front of the hadron absorber.

SUM: Scintillator Upstream Muon. Scintillator Array located upstream of the absorber. The SUM detector was used in triggering.

SVS: Small Veto Scintillator. Scintillator Array located downstream of the absorber. The SVS was used in triggering.

Z_{clus}: The Z coordinate of the center of a calorimeter energy cluster.

ZFLOW or Z_{flow}: A quantity that measures the calorimeter energy flow out of the bending plane of the E665 spectrometer. $Z_{flow} = \frac{\sum_{Nclus} Z^2_{clus} E_{clus}}{ECAL_{total}}$. The sum is over all the Nclus calorimeter energy clusters.

VDC: Vertex Drift Chambers. Drift Chambers located inside the CVM magnet.

Bibliography

[1] R. Hofstadter, L.I. Schiff *Nucleon Structure*, Proc. Inter. Conf. at Standford, Standford Univ. Press, 1964.

[2] J.I. Friedman, H. W. Kendal and R. E. Taylor, *Rev. Mod. Phys.* **63**, (1991) 573.

[3] R. P. Feynmann, Photon hadron interactions, Benjamin Press, New York (1972).

[4] J.D. Bjorken, *Phys. Rev.* **179** (1969) 1547.

[5] J.D. Bjorken and E. A. Paschos, *Phys. Rev.* **185** (1969) 197.

[6] K. Gottfried, *Phys. Rev. Lett.* **18** (1967) 1174.

[7] J.J. Aubert et al., *Nucl. Phys.* **B293** (1987) 740.

[8] A. C. Benvenuti et al., *Phys. Lett.* **B223** (1989) 485; *ibid* **B237** (1990) 592.

[9] M.R. Adams, et al., *Nucl.Inst. Methods* **A291** (1990) 533.

[10] W. Melnitchouk and A.W. Thomas, *Phys. Rev.* **D47** (1993) 3783; *Phys. Lett.* **B317** (1993) 437.

[11] B. Badełek and J. Kwieciński, *Nucl. Phys.* **B370** (1992) 278; *Nucl. Phys. B (Proc. Suppl.)* **29A** (1992) 30.

[12] B. Badełek, K. Charchuła, M. Krawczyk and J. Kwieciński, *Rev. Mod. Phys.* **64** (1992) 927.

[13] F. Halzen and A. D. Martin, *Quarks and Leptons: An Introductory Course in Modern Particle Physics*, John Wiley and Sons, 1984.

[14] S. D. Drell, SLAC Preprint No. SLAC-PUB-5720 (1992).

[15] F.E. Close, *Quarks and Leptons*, J. Wiley & Sons, New York, 1984.

[16] M.D. Mestayer et al., it Phys. Rev. **D27** (1983) 285.

[17] M. Gell-Mann, *Phys. Lett.* **8** (1964) 218.

[18] G. Altarelli and G. Parisi, *Nucl. Phys.* **B126** (1977) 298; E. Reya, *Phys. Rep.* **69** (1981) 195; G. Altarelli, *Phys. Rep.* **81** (1982) 1.

[19] CTEQ Collaboration FERMILAB Preprint No. FERMILAB-PUB-93-094 (1993).

[20] D.A.Ross and C.T.Sachrajda, *Nucl. Phys.* **B149** (1979) 497.

[21] R. G. Roberts, *The Structure of the Proton. Deep Inelastic Scattering*, Cambridge University Press, Cambridge, 1990.

[22] P. Renton, *Electroweak Interactions*, Cabridge University Press, New York, 1990.

[23] B. Badełek and J. Kwieciński, Warsaw University Preprint No. IFD/1/1994 (1994).

[24] K. Charchuła, et al., DESY Preprint No. DESY 90-019 (1990).

[25] T. H. Bauer et al., *Rev. Mod. Phys.* **50** (1978) 261.

[26] G. Shaw, *Phys. Rev.* **D47** (1993) 3676.

[27] G. Grammer Jr and J. D. Sullivan, in *Electromagnetic Interactions of Hadrons*, edited by A. Donnachie and G. Shaw, Plenum, New York, 1978, Vol.2.

[28] G. A. Schuler and T. Sjöstrand, *Nucl. Phys.* **B407** (1993) 425.

[29] P.D.B. Collins, *An Introduction to Regge Theory and High Energy Physics*, Cambridge University Press, Cambridge, 1977.

[30] A. Donnachie and P.V. Landshoff, *Phys. Lett.* **B296** (1992) 227.

[31] D.R. Yennie, S. Frautchi and H. Suura, *Ann. Phys. (N.Y.)* **13** (1961) 379.

[32] J.Ashman, et.al., *Phys.Lett.* **B202** (1988) 603; M.Arneodo, et.al., *Phys.Lett.* **B211** (1988) 493.

[33] M. Arneodo, *Phys. Rep.* **240** (1994) 301.

[34] M.R. Adams et al., *Phys.Rev. Lett.* **68** (1992) 3266.

[35] Yu. L. Dokshitzer et al., *Basics of Perturbative QCD*, Editions Frontières, Gif–sur–Yvette, 1991.

[36] R.J.Glauber, *Phys.Rev.* **100** (1955) 242; R. J. Glauber, in *Lectures in Theoretical Physics*, edited by W. E. Brittin and L. G. Dunham, Wiley Interscience, New York, 1959, Vol.I, p.315.

[37] V.Franco and R.J.Glauber, *Phys.Rev.* **142** (1966) 1195; E.S.Abers, H.Burkhardt, V.L.Teplitz and C.Wilkin, *Nuov.Cim.* **42** (1966) 365.

[38] N.N.Nikolaev and V.I.Zakharov, *Phys.Lett.* **55B** (1975) 397.

[39] A.H.Mueller and J.Qiu, *Nucl.Phys.* **B268** (1986) 427; J.Qiu, *Nucl.Phys.* **B291** (1987) 746.

[40] E.L.Berger and J.Qui, *Phys.Lett.* **206B** (1988) 141; F.E.Close, J.Qui and R.G.Roberts, *Phys.Rev.* **D40** (1989) 2820; J. Kwieciński, A.D.Martin, W.J.Stirling and R.G.Roberts, *Phys.Rev.* **D40** (1990) 3645.

[41] G.Ingelman and P.E.Schlein, *Phys.Lett.* **152B** (1985) 256;

[42] A.Donnachie and P.V.Landshoff, *Phys.Lett.* **B185** (1987) 403; A.Donnachie and P.V.Landshoff, *Phys.Lett.* **B191** (1987) 309. J.Bartels and G.Ingelman, *Phys.Lett.* **B235** (1990) 175.

[43] B. Badełek and J. Kwieciński, *Phys. Rev. D, Rapid Communications* **50** (1994) R4.

[44] V. Barone et al., *Phys. Lett.* **B321** (1994) 137.

[45] NMC; P. Amaudruz et al., *Nucl. Phys.* **B273** (1992) 3.

[46] NMC; M. Arneodo et al., preprint CERN-PPE/93-117 (Revised Version) and *Phys. Rev., Rapid Communications*, **D50** (1994) R1.

[47] P. Amaudruz, et al., *Phys. Lett.* **B295** (1992) 159; Erratum Oct. 26th, 1992; Erratum April 19th, 1993.

[48] V. R. Zoller, *Phys. Lett.* **B279** (1992) 145; *Z. Phys.* **C54** (1992) 425.

[49] M.R. Adams et al., *Phys. Lett.* **B309** (1993) 477.

[50] L.W. Whitlow et al., *Phys. Lett.* **B250** (1990) 193.

[51] P. Amaudruz et al., *Phys. Lett.* **B294** (1992) 120.

[52] T. Granier, to appear in the Proceedings of the XXIX Rencontre de Moriond, *QCD and High Energy Interactions*, March 1994, Méribel, France.

[53] H. Schellman, *Preliminary Final Design for Vertex Tracking System,* E665 Internal Report VS023.

[54] Nickerson, R., Pipkin, F., and Wilson, R., *Upstream Trigger Wall and Trigger Timing for 1989 Run,* E665 Internal Report BT062, August, 1988.

[55] R.D. Kennedy, *Measurement of the Ratio of the Neutron and Proton Structure Function F_2 in Inelastic Muon Scattering*, dissertation, University of California, San Diego, 1992.

[56] R. Guo, *The Study of Bose-Einstein Correlation in Deep Inelastic μ-Nucleon and μ-Nucleus Scattering at 465 GeV/c*, dissertation, University of Illinois at Chicago, 1994.

[57] T.J. Carroll, *Observation of Nuclear Shadowing at low x_{Bj} in Carbon, Calcium and Lead*, dissertation, University of Illinois at Chicago, 1994.

[58] A. Malensek and J.G. Morfin, *The Tevatron Muon Beam: A High Inensity Beam With Well-Defined Polarization*, Fermilab Technical Report TM 1193 2966.0, July 1983.

[59] P. Spentzouris, and H. Schellman, *E665 Proton Calibration Run Part II*, E665 Internal Report AN153, 1992.

[60] E.R Kinney, *Results of August 1990 survey of E665 targets*, E665 Internal Report AN088, 1991.

[61] E.R Kinney, *E665 Target Control Software Users Guide, Version 2.1*, E665 Internal Report OL031, 1990.

[62] Nickerson, *Electronics for the New Back Veto*, E665 Internal Report BT082, March, 1989.

[63] Nickerson, R., *Brief Documentation of the E665 EM Calorimeter*, E665 Internal Report EM012, October, 1985.

[64] A.V. Kotwal, dissertation, Harvard University, in preparation.

[65] Mark Adams and Timothy J. Carroll, *SAT Trigger Processor Users Guide*, E665 Internal Report SW192, 1992.

[66] Geesaman, D., et al., *IEEE Trans. Nucl. Sci.* **36** (1989) 1528.

[67] E. Berman, et al., *IEEE Trans. Nucl. Sci.* **34** (1987) 763.

[68] D.M. Berg, et al., *IEEE Trans. Nucl. Sci.* **32** (1985) 1368.

[69] P. Spentzouris, *Per Spill Database from 91 production,* E665 Internal Report AN198, 1993.

[70] P. Spentzouris, *Read Event Correlation Modules in the Begin and End of Spill Event Records,* E665 Internal Report OL030, 1991.

[71] Kennedy, R.D., *RUN90 spill scaler normalization: Inputs and results to date,* E665 Internal Report AN100, May 9, 1991.

[72] Jaffe, David E., *Proposed event scalers for RUN91,* E665 Internal Report BT092, May 3, 1991.

[73] Kobrak, Hans, *Implementation of David Jaffe's Event Scaler Scheme,* E665 Internal Report BT093, May 25, 1991.

[74] J. J. Ryan, *Particle Production in Deep Inelastic Muon Scattering,* dissertation, Massachusetts Institute of Technology, 1991.

[75] A. Salvarani, *Forward Hadron Production in Muon Deep Inelastic Scattering at 490 GeV from Deuterium and Xenon,* dissertation, University of California, San Diego, 1991.

[76] Wittek, Wolfgang, *Inclusion of multiple Coulomb scattering in the beam reconstruction,* E665 Internal Report SW178, September 25, 1991.

[77] Bhatti, A., Wittek, W., Wolbers, S., *The E665 Vertex Processor; Version 9.0,* E665 Internal Report SW071, August 15, 1990.

[78] Schmitt, Michael, *A modification to Nickerson's pad clustering routine,* E665 Internal Report EM017, July 15, 1991.

[79] M.H. Schmitt, *Deep Inelastic Exclusive ρ^0 Production using 485 GeV Muons,* dissertation, Harvard University (USA), 1991.

[80] P. Spentzouris, *Forward Spectrometer Alignment,* E665 Internal Report AN169, 1992.

[81] P. Spentzouris, *E665 Proton Calibration Run – Part III,* E665 Internal Report AN196, 1993.

[82] Melanson, H., *E665 DC Calibration, Pass 1,* E665 Internal Report FS027, December 4, 1988.

[83] Melanson, H., *E665 DC Calibration, Pass 2,* E665 Internal Report AN059, December 6, 1989.

[84] Kotwal, Ashutosh, *RUN90 Calorimeter Alignment,* E665 Internal Report AN172, January 13, 1993.

[85] Ashutosh Kotwal, *Preliminary RUN90 calorimeter calibration using electron beam data,* E665 Internal Report AN181, March 23, 1993.

[86] P. Spentzouris, *Beam alignment,* E665 Internal Report AN167, 1992.

[87] Schellman, H., *The E665 Proton Calibration Run – Part I,* E665 Internal Report AN152 December 3, 1991.

[88] Ashutosh Kotwal, *The Run Dependence of the Calorimeter Pressure, Temperature, High Voltage and Gas Composition for RUN91,* E665 Internal Report AN189, May 5, 1993.

[89] Ashutosh Kotwal, *RUN91 Calorimeter Correction for gas gain variation,* E665 Internal Report AN199, November 10, 1993.

[90] Stephen Wolbers, *RUN91 PTMV Production I – Code,* E665 Internal Report SW205, October 1, 1993.

[91] Stephen Wolbers, *RUN91 PTMV Production II – Code Updates,* E665 Internal Report SW213, January 20, 1994.

[92] M. Fausey et al. *CPS and CPS Batch Reference Guide: Version 2.7.0,* Fermi National Accelerator Laboratory Computing Publication GA0008, 1992.

[93] Kaufman, Sheldon, and Wolbers, Stephen, *cps, the farms, and E665* E665 Internal Report SW184, January 31, 1992.

[94] John Novak and Panagiotis Spentzouris, *Ntuple generating program for the 91 per spill database,* E665 Internal Report AN197, 1993.

[95] P. Spentzouris, *Efficiency studies using mu+e- from RUN90,* E665 Internal Report AN149, 1992.

[96] P. Spentzouris, *Efficiency studies using mu+e- from RUN90,* E665 Internal Report AN179, 1993.

[97] A. Arvidson, Barbara Badełek, *The Gamrad program,* NMC Internal Report NMC/92/5, 1992.

[98] J. Drees, *Radiative Corrections and hadron distributions in deep inelastic mu-p scattering,* EMC Internal Report EMC/78/24, April, 1978.

[99] T. Sjöstrand, *Comp. Phys. Comm.* **27** (1982) 243.

[100] R. Brun, et al., *GEANT: Simulation program for particle physics experiments. User guide and reference manual,* CERN Computing Division Report CERN-DD/78/2, 1978.

[101] Stephen Wolbers, *The E665 Second Stage Monte Carlo,* E665 Internal Report MC010, February 1, 1991.

[102] F.W. Brasse, et al., *Nucl. Phys.* **B110** (1976) 413.

[103] F.W. Brasse, et al., *Nucl. Phys.* **B39** (1972) 421.

[104] A. Donnachie and P.V. Landshoff, *Z.Phys.***C61** (1994) 139.

[105] Ashutosh Kotwal, *Constructing a Trial F2p,* E665 Internal Report AN207, January 5, 1994.

[106] L.W. Mo and Y.S. Tsai, *Rev. Mod. Phys.* **41** (1969) 205.

[107] M. Gari and W. Kruempelmann, *Z. Phys.* **A 332** (1985) 689.

[108] AN151 Melanson, Harry L., *A first look at sigma(n)/sigma(p) from the Run 91 data,* E665 Internal Report AN151, October 30, 1991.

[109] Y.S. Tsai, SLAC Report PUB-848, 1971.

[110] Ch. Scholz, computer program *FERRAD,* Version 35 (NMC Collaboration)

[111] M. Arneodo, *Measurement of the Structure Function Ratio F_2^{He}/F_2^D and a Comparison with Existing Data and Theoretical Models on Nuclear Effects in Deep Inelastic Scattering,* dissertation, Princeton University, Princeton 1992.

[112] K.P. Schuler, *A PROPOSED NEW TECHNIQUE FOR POLARIZED ELECTRON POLARIZED NUCLEON SCATTERING,* in *Lausanne 1980, Proceedings, High-energy Physics With Polarized Beams and Polarized Targets,* 460-462.

[113] D.F. Geesaman, *FERRAD, GAMRAD, AND TERAD - Dueling Radiative Corrections - II,* E665 Internal Report AN143, February 17, 1992.

[114] D.F. Geesaman, *Dueling Radiative Corrections – IV; Calculations with the same Structure Functions Detailed Differences,* E665 Internal Report AN159, June 30, 1992.

[115] B. Badełek et al. *Radiative Correction Schemes in Deep Inelastic Muon Scattering,* TSL-ISV-94-0092, Feb 1994.

[116] P. Spentzouris, *Measurement of the Bremsstrahlung event rate relative to the total event rate as a check of the Radiative Correction Calculations,* E665 Internal Report AN206, 1994.

[117] J.J. Aubert, et al. *Zeit.Phys.* **C10** (1981) 101.

[118] P. Amaudruz, et al., *Nucl. Phys.* **B371** (1992) 3.

[119] H. Plothow-Besch, *A Library of all available Parton Density Functions of the Nucleon, the Pion and the Photon and the corresponding α_s calculations,* preprint CERN–PPE/92–123, 1992.

[120] S.D. Ellis and W.J. Stirling, *Phys.Lett.* **B256** (1991) 258.

[121] Russel B. Scott, *Cryogenic Engineering,* D. Van Nostrand Company, INC.

[122] P. Spentzouris, *H_2 and D_2 target densities for 91,* E665 Internal Report AN203, 1994.

[123] D. Allspach, *Calibration of E665 liquid target readouts,* E665 Internal Report AN102.

[124] Uwe Ecker, *Determination of the liquid target densities in the E665 Run 1987,* E665 Internal Report AN025, 1988.

[125] R.J Tapper, *Tables of Vapour Pressure and Molar Volume for Liquid Hydrogen and Deuterium,* Rutherford Laboratory.

[126] H. Schellman, *Effects of HD Contaminations in the D_2 Target,* E665 Internal Report AN118.

[127] P. Spentzouris, *Cross-section measurement for $\mu - e$ elastic scattering from RUN90,* E665 Internal Report AN180, 1993.

[128] P. Amaudruz, et al., *Phys.Rev.Lett.* **66** (1991) 2712.

[129] M. Glück, et al., *Z.Phys.C* **53** 127 (1992).